

JYU DISSERTATIONS 460

Jasper Parkkila

Quantifying the Transport Properties of Quark-Gluon Plasma through Measurement of Higher Harmonic Flow and Their Non-Linear Response

CERN-THESIS-2021-209
19/11/2021



UNIVERSITY OF JYVÄSKYLÄ
FACULTY OF MATHEMATICS
AND SCIENCE

JYU DISSERTATIONS 460

Jasper Parkkila

Quantifying the Transport Properties of Quark-Gluon Plasma through Measurement of Higher Harmonic Flow and Their Non-Linear Response

Esitetään Jyväskylän yliopiston matemaattis-luonnontieteellisen tiedekunnan suostumuksella
julkisesti tarkastettavaksi marraskuun 19. päivänä 2021 kello 12.

Academic dissertation to be publicly discussed, by permission of
the Faculty of Mathematics and Science of the University of Jyväskylä,
on November 19, 2021 at 12 o'clock noon.



JYVÄSKYLÄN YLIOPISTO
UNIVERSITY OF JYVÄSKYLÄ

JYVÄSKYLÄ 2021

Editors

Ilari Maasilta

Department of Physics, University of Jyväskylä

Timo Hautala

Open Science Centre, University of Jyväskylä

Copyright © 2021, by Author and University of Jyväskylä

ISBN 978-951-39-8932-3 (PDF)

URN:ISBN:978-951-39-8932-3

ISSN 2489-9003

Permanent link to the online version of this publication: <http://urn.fi/URN:ISBN:978-951-39-8932-3>

Abstract

The elusive goal of heavy-ion physics is to understand the transport properties of the quark-gluon plasma (QGP), the form of nuclear matter at extreme temperatures, that prevailed in the first few microseconds after the Big Bang. Transport coefficients, such as the temperature dependent specific shear viscosity η/s and specific bulk viscosity ζ/s , can be constrained with the help of flow measurements. The higher harmonic flow observables and their non-linear responses to the initial state anisotropy have shown compelling potential to constrain the transport properties due to their high sensitivity to various stages of heavy-ion collisions.

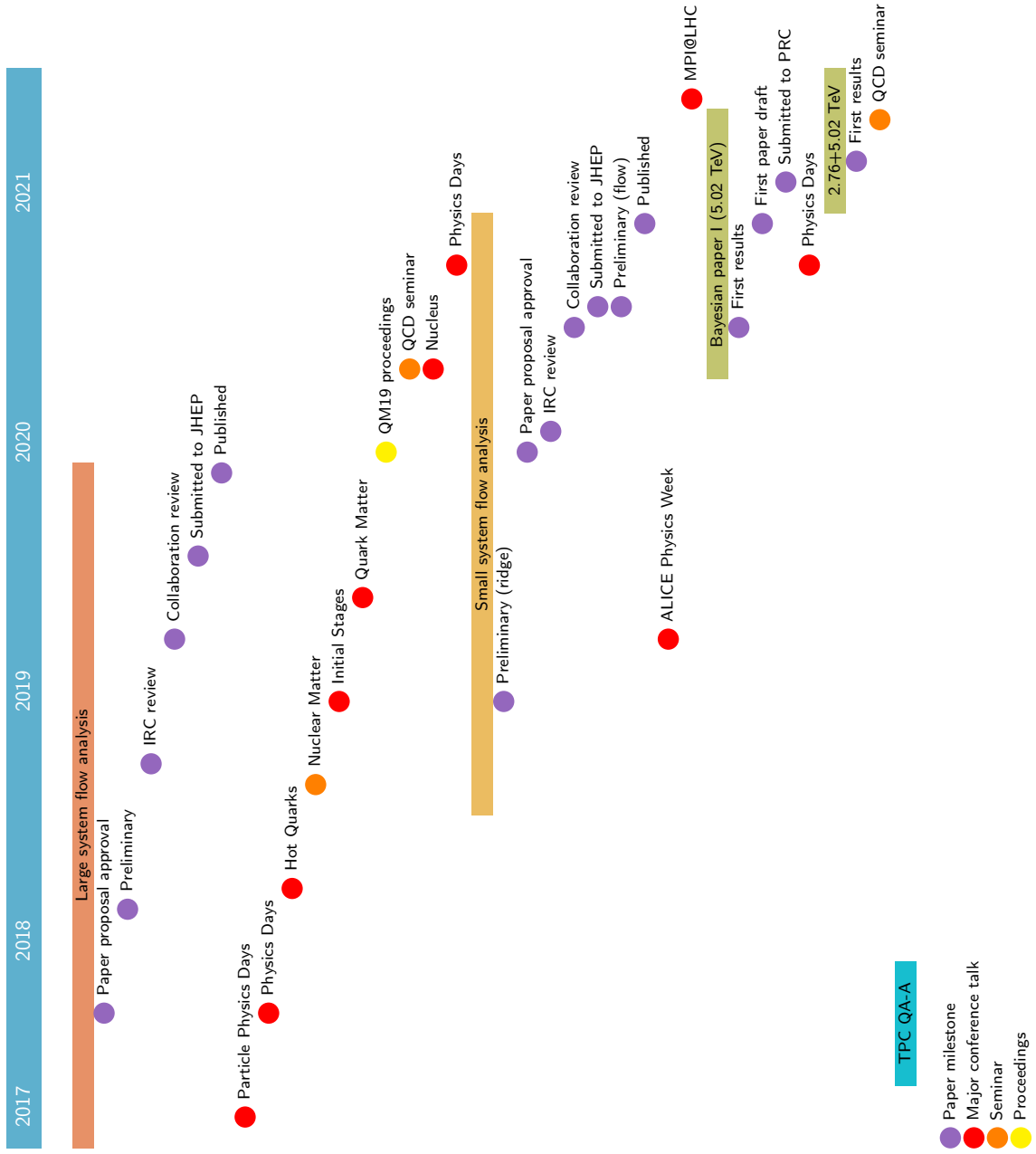
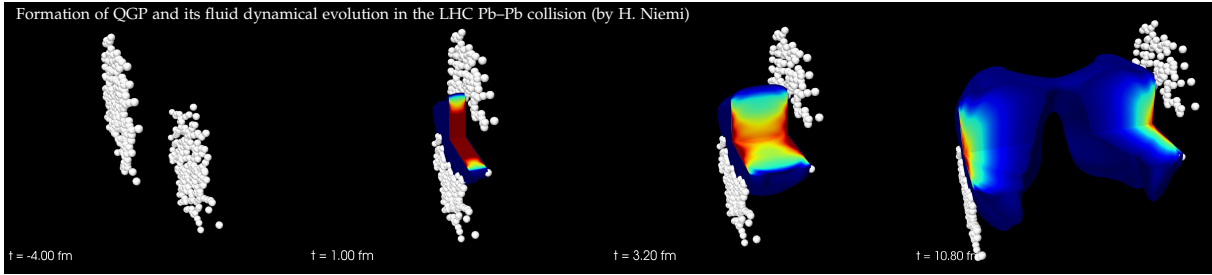
In this thesis, the measurements of higher harmonic flow up to the ninth order, and their non-linear flow modes up to the seventh harmonic in Pb–Pb collisions with ALICE at CERN-LHC are presented. These measurements are utilized in a Bayesian analysis to constrain the QGP properties and initial conditions of such collisions. In addition, the sensitivities of the high harmonic flow observables to various model parameters are quantified for the first time. This work suggests that a more dynamical picture of the initial conditions is needed to improve the understanding of the uncertainties of the extracted QGP properties or the model building blocks.

Tiivistelmä

Raskasionifysiikan tavoitteena on ymmärtää kvarkki-gluoniplasman (QGP), aikaisen maailmankaikkeuden ensihetkiä vallinneen ydinaineen äärimmäisen lämpötilan olo-
muodon kuljetusominaisuuksia. Kuljetuskertoimia, kuten lämpötilasta riippuva ominaisleikkausviskositeetti η/s sekä ominaisbulkkiviskositeetti ζ/s , voidaan rajata flowmittausten avulla. Korkeamman kertaluvun harmoniset flow observaabelit sekä näiden epälineaarinen vaste alkutilan anisotrooppisuuteen ovat osoittaneet tehokkuutta kuljetuskertoimien rajaamiseksi johtuen observaabelien korkeasta herkkyudesta raskasionitörmäyksen eri vaiheisiin.

Tämä työ esittää korkeamman harmonisen flow:n mittaukset yhdeksänten kertaluokkaan, sekä näiden epälineaariset moodit seitsemänten kertaluokkaan Pb–Pb törmäyksissä ALICE-kokeessa CERN-LHC:lla. Mittauksia hyödynnetään Bayesian analyysissä QGP:n ominaisuuksien sekä törmäyksen alkutilan rajaamiseksi. Tämän yhteydessä kvantifioidaan korkeamman harmonisen flow-observaabelien herkkyys hydrodynaamisen mallin eri parametreihin. Työn tulokset viittaavat dynaamisen alkutilamallin tarpeeseen QGP:n ominaisuuksien tai mallien parametrien epävarmuuksien ymmärtämiseksi.

Author	Jasper Parkkila University of Jyväskylä Jyväskylä, Finland
Supervisors	Adjunct Prof. Kim Dong Jo University of Jyväskylä Jyväskylä, Finland Adjunct Prof. Sami Räsänen University of Jyväskylä Jyväskylä, Finland
Reviewers	Prof. ShinIchi Esumi Tsukuba University Tsukuba, Japan Prof. Jiangyong Jia Stony Brook University New York, USA
Opponent	Prof. William Allen Zajc Columbia University New York, USA



Preface

Following an intense but rewarding period of four years at the ALICE group at University of Jyväskylä, HIP and CERN, I present you with this thesis describing the work conducted and results achieved during my doctoral training. This page is dedicated to the people I gratefully acknowledge for their vital and highly valued contribution towards this academic achievement.

First and foremost, I am highly grateful to my supervisor Dong Jo Kim for his uncompromising guidance for my work and personal development, as well as his utmost patience and dedication, which has enabled me to reach further as an independent researcher than I ever could have asked for. I am also greatly thankful to Sami Räsänen, whose guidance and support has been invaluable in work, life and various, clearly out-of-hand situations.

I am obliged to the following people who provided guidance, support or their contribution to the work presented in this thesis: William Allen Zajc for agreeing to be my opponent on the public defense of my thesis; ShinIchi Esumi and Jiangyong Jia for their review and valuable feedback on my thesis; Kari Eskola, Tuomas Lappi and Harri Niemi for their steering group support and/or useful discussions on the papers and hydrodynamic calculations; Anthony Timmins, Naghmeh Mohammadi, Alice Ohlson and Jurgen Schukraft for their careful review and/or feedback on the analysis; You Zhou for his contribution and paper review; Sudhir Raniwala, Jan Fiete Grosse-Oetringhaus, and Alexandru Florin Dobrin as the internal review committee for their extensive paper review as well as instructive discussions; Erik Brücken, Timo Hilden and Essi Kangasaho for introducing me to the workflow at the TPC upgrade project, as well as for the collegial atmosphere at the Helsinki detector laboratory.

I extend my deepest gratitude to my colleagues and peers at the ALICE group in Jyväskylä, both past and present, for the positive and inspiring working environment. Special thanks go to Anna Önerstad for her help and feedback on the final paper and following my guidance efficiently, as well as Oskari Saarimäki for comments on the analysis throughout my time. I have been also grateful to participate in untrammled discussions with the QCD theory group at the department regularly.

Finally, I am grateful to my parents and family, Julia Vauterin, Juha Parkkila, Juha Pyrhönen and Anne Tikkanen, for their support and encouragement. I am thankful to my friends for their advice, especially to my dearest friend Shirajum Monira, for standing by my side. I acknowledge CSC - IT Center for Science in Espoo, Finland, for the allocation of the computational resources and University of Jyväskylä and Helsinki Institute of Physics for the funding I received during my doctoral training.

–Jasper Parkkila
November 2021

List of publications

This thesis is composed of an introduction and the following scientific articles. The contribution of the author is outlined for each item.

1. **ALICE** Collaboration, S. Acharya *et al.*, “Higher harmonic non-linear flow modes of charged hadrons in Pb–Pb collisions at $\sqrt{s_{\text{NN}}} = 5.02$ TeV,” *JHEP* **05** (2020) 085, arXiv:2002.0633 [nucl-ex]

As the chair and main writer of the paper committee in ALICE, the author has prepared the analysis, measured and verified the results for the higher harmonics and their non-linear flow modes.

2. J. E. Parkkila, A. Onnerstad, and D. J. Kim, “Bayesian estimation of the specific shear and bulk viscosity of the quark-gluon plasma with additional flow harmonic observables,” *Phys.Rev.C* **104** (2021) 054904

As the principal investigator, the author has setup a Bayesian parameter estimation framework and integrated it with the analysis framework used in item [1]. The author has conducted the analysis against the new high harmonic observables, and is the main writer of the analysis and results parts of the paper.

3. **ALICE** Collaboration, S. Acharya *et al.*, “Long- and short-range correlations and their event-scale dependence in high-multiplicity pp collisions at $\sqrt{s} = 13$ TeV,” *JHEP* **05** (2021) 290, arXiv:2101.03110 [nucl-ex]

As a member of the paper committee, the author has verified the measurements as an independent check and contributed to the calculations of the systematic uncertainties.

Contents

Acknowledgements

1	Introduction	10
1.1	Quark-gluon plasma	11
1.2	Ultrarelativistic heavy-ion physics	12
1.2.1	Fundamental concepts	13
1.2.2	Constraints of the medium properties	15
1.3	Thesis aim and outline	18
2	Theoretical modeling	20
2.1	Relativistic hydrodynamics	20
2.1.1	Transport coefficients	22
2.2	The initial state of heavy-ion collisions	23
2.2.1	Initial condition models	24
2.2.2	Pre-equilibrium dynamics	30
2.2.3	Particlization	30
2.3	Parameter estimation	31
2.3.1	Analysis and model setup	31
3	Experimental observables	33
3.1	Anisotropic flow	33
3.2	Multi-particle correlations	34
3.2.1	Two-particle correlations	34
3.2.2	Higher orders and cumulants	35
3.3	Quantifying non-linear flow	37
3.3.1	Flow decomposition and mode coupling	37
3.4	Flow vector frameworks	40
3.4.1	Generic formulas	41
4	Experimental Setup	43
4.1	CERN	43
4.2	Large Hadron Collider	43
4.2.1	LHC experiments	46
4.3	ALICE	47
4.3.1	Tracking detectors	48
4.4	TPC upgrade	50
4.4.1	GEM based readout chambers	50
4.4.2	Quality assurance of GEM foils	51

5	Analysis	54
5.1	Experimental Setup and Data Analysis	54
5.1.1	Event Selection	54
5.1.2	Track Selection	55
5.2	Analysis verification	56
5.2.1	Closure test with AMPT simulation	57
5.2.2	Monte-Carlo test	57
5.3	Systematics	60
5.3.1	Summary of systematic uncertainties	61
6	Results	65
6.1	Measurement of the higher harmonic observables	65
6.2	Estimation of the transport properties	66
7	Conclusions	70

Chapter 1

Introduction

Our universe was created at a moment known as the Big Bang, around 14 billion years ago. One millionth of a second after the Big Bang, the universe consisted of plasma so extremely dense and hot, that no atomic nucleus or nucleon could exist in it. This plasma was composed of quarks and gluons, a type of elementary particles which together form nuclear constituents. Of these elementary particles, the gluon, according to the Standard Model of particle physics and quantum chromodynamics (QCD), mediates the strong interaction force through which the quarks may interact. It is our understanding, that the strong force ties together the quarks, which in turn can make up the nucleons and the atomic nuclei.

Quark-gluon plasma (QGP) is an extremely hot and dense form of matter, where the hadronic states of its constituents deconfine, thus freeing the internal quarks and gluons. Under normal conditions, neither quarks nor gluons have ever been observed as free particles, rather they are always found in bound states called hadrons, which also form the ordinary matter we see everywhere around us. However, in temperatures more than one tenth of a million times the core of sun, observations suggest that a phase transition takes place from the confined hadronic state to a plasma state of freely moving quarks and gluons.

The fundamental objective of this research is to contribute to and advance our understanding of the role the strong force has in the complex interplay between the four fundamental forces of nature that together govern the interaction between matter and energy, and ultimately, to contribute towards to formation of a grand, unifying theory of modern physics. A primary objective of the research is to determine the strength and nature of the strong interaction force. Particularly, we look at the interaction dynamics in the subatomic world to better understand the creation and evolution of all matter in our universe [4].

In its properties as a freely flowing deconfined and strongly interacting matter, QGP presents a rich environment providing a catalyst for advanced research. By no means is the research into QGP straightforward, as the temperature needed to reach the state of deconfinement is beyond anything in nature. QGP can be produced in high energy particle accelerator laboratories by colliding heavy-ions, although consequently only in the size of an atomic nucleus, and for a sustained period of merely ~ 30 yoctoseconds (3×10^{-23} s). The experiments do not see the QGP itself, only the resulting hadronic particles that are formed once the QGP cools down. The behaviour of the QGP is then probed through various observables that are constructed

from these particles.

In this thesis, I will present the measurement methodology and results of advanced observables relating to the evolution of the QGP under laboratory conditions. The results, complemented by model parameter estimation, will contribute to a better understanding of the dynamics of the plasma state of nuclear matter. First, I will give a brief introduction into heavy-ion physics, which covers the state-of-the-art research on QGP. In my introduction, I will present the main challenges and advancements of current research in the field. At the end of Chapter 1, I will present the research aim of my thesis, followed by an outline of the structure of the thesis.

1.1 Quark-gluon plasma

QGP as a state of nuclear matter was first introduced more than 45 years ago, when it was predicted that the asymptotic freedom of QCD, i.e., the weakening of the coupling between two strongly interacting particles at high energy scales, would lead to such state of deconfinement [5, 6]. In the QGP state, the constituent quarks and gluons are no longer confined into hadronic states, rather they can move and traverse freely within the plasma.

The existence of QGP had gained widespread scientific acceptance already during the first years of 21st century following the experiments conducted at the Brookhaven National Laboratory (BNL) RHIC (Relativistic Heavy-Ion Collider) [7] particle accelerator. In the experiment, it was observed that the response, i.e. the observed expansion of matter in a heavy-ion collision exhibited a particular kind of anisotropy that could not be accounted to any other effects when compared to smaller collision systems [8]. Discovery of the anisotropy was highly pivotal, as the anisotropy could be readily attributed to the expansion of a fluid-like matter acting under the influence of pressure gradients. Such observations widely confirmed the existence of the QGP phase of matter, triggering extensive studies in order to study its properties.

Several experiments preceded the RHIC era studies, and the search for QGP had been going on ever since the first heavy-ion capable particle colliders started their operation at the Lawrence Berkeley National Laboratory (BEVALAC) [9] and the Joint Institute for Nuclear Research in Dubna [10], capable of accelerating ions up to energies of 1 GeV/nucleon pair. Followed by these pioneering experiments, more progress was made when the Super Proton Synchrotron (SPS) at CERN and the Alternating Gradient Synchrotron (AGS) at BNL, Brookhaven were deployed almost simultaneously in 1986, providing center-of-mass energies of 18 and 5 GeV/nucleon pair [11], respectively. Due to low beam energies, none of the experiments could bring any clear evidence about the existence of QGP.

Later in 1994 the first indication of the QGP phase was observed, when the SPS was brought to be capable of accelerating heavier lead (Pb) ions at 17 GeV/nucleon pair. Especially the year 2000 was marked by significant developments, during which the first “compelling evidence” of QGP formation from the SPS was reported [8]: the expansion and the anisotropy of the expanded medium. Most notably this was also the year when the RHIC was brought online at BNL.

Today, the vast majority of research is conducted at the Large Hadron Collider (LHC) [12] at CERN, which presently is the most powerful particle accelerator in the

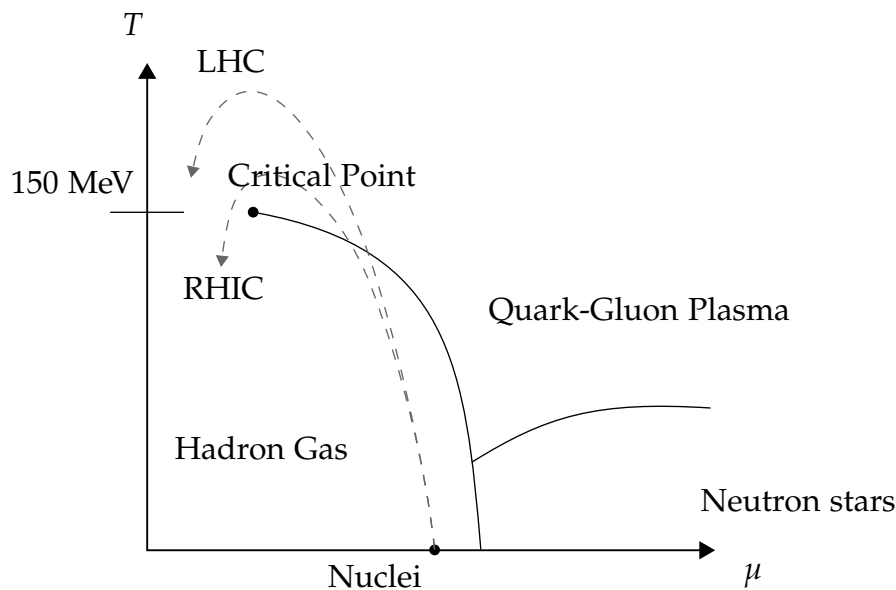


Figure 1.1: Phase diagram of the QCD. Here μ is the baryonic chemical potential characterizing the imbalance between quarks and the antiquarks (in arbitrary scale), and T is the temperature in MeV. The phase of the nuclei, in form of ordinary matter, are plotted at the bottom of the diagram. In a high-energy collision experiment, the temperature within the nuclei rapidly increases upon collision between two nuclei, resulting in a cross-over phase transition from confined nuclear matter into plasma state. A transition of the nuclei to the plasma state in RHIC and LHC experiments is sketched with dashed-line arrows.

world. During 2015 and 2018, LHC accelerated Pb–Pb beams up at 5.02 TeV/nucleon pair – well over the energy required to induce a phase transition from hadronic state of matter to QGP. Analogously to ordinary matter, one may sketch a phase diagram for the QCD matter, where “QCD matter” is used to refer to both hadronic matter and QGP. Figure 1.1 presents such diagram, outlining the conditions for the different phases of QCD matter. The diagram also plots the hypothetical location of the critical point, which has been obtained with QCD lattice¹ calculations. Based on the QCD lattice calculations [13], the temperature of the critical point is expected to be around $T_c \approx 150 \sim 175$ MeV, or roughly $2 \cdot 10^{12}$ K.

1.2 Ultrarelativistic heavy-ion physics

Heavy-ion physics, a branch of high-energy nuclear and particle physics, focuses on narrowing down the features and behaviour of the QGP. Notably this comprises especially the transport properties such as the shear- and bulk viscosities, denoted η and ζ , that are related to the interaction strengths between the constituent particles [14]. Of particular interest are the temperature-dependent features of the shear viscosity to entropy ratio $\eta/s(T)$ and bulk viscosity to entropy ratio $\zeta/s(T)$. Current data indicates that the η/s of the QGP at its critical point T_c is the lowest known shear viscosity to entropy ratio among all known substances at their respective critical points, close

¹A discretized subsidiary of the QCD gauge theory used in computer assisted calculations.

to the universal lower bound $\eta/s = 1/(4\pi) \approx 0.08$. As the critical point marks the lowest value of $\eta/s(T)$, determination of the precise value of $\eta/s(T_c)$ also implies the discovery of the critical point of the QCD matter [13].

The production of QGP in laboratory conditions relies on heavy-ion colliders. In modern colliders, bunches of heavy-ions such as ^{208}Pb or ^{129}Xe are accelerated to opposing ultrarelativistic velocities, after which they are collided. Extreme thermal energy breaks the structure of the nuclei, and phase transition takes place to a plasma state. Immediately after, the pressure gradients within the plasma will force it to expand and consequently cool down in a stage called *freeze-out*. During this process, the broken bonds of the quark constituents are reformed, creating various new hadronic particles. It is important to understand that the momentum built by the expanding matter is conserved and carried over to the particles as soon as they are formed. Therefore, an observed anisotropy in the final stage particle spectrum reflects the same transverse momentum distribution present in the QGP matter before the freeze-out.

The process can also be drawn on the phase diagram in Fig. 1.1. The phase of the still intact nucleus is plotted at a low-temperature limit and medium baryonic chemical potential. During the initial stages of the collision, the nuclear matter quickly thermalizes, crossing it over the phase boundary into the QGP regime. During the expansion at high temperatures, the system passes over the critical point, and eventually hadronizes into various final products. Unlike the phase transition from hadronic matter to QGP, hadronization is not an instant process. While the hadronization takes place, QGP and hadronic matter briefly coexist, which is expected from the bypassing of the critical point.

At the present, direct observation of the QGP is not possible. Instead, observations rely on the collective behaviour and patterns of the resulting final state hadrons. As the QGP hadronizes, the resulting particles may scatter and decay via weak and electromagnetic interactions. In a detector laboratory, long lived and energetic particles are capable of reaching the tracker and detector structures built around the designated collision point. Therefore, experiments are able to reconstruct the azimuthal angle and momentum distribution of final-state particles each collision event produces.

1.2.1 Fundamental concepts

In order to characterize the resulting particle distribution, it will be useful to decompose the signal into easily quantifiable basic components. For this task, a harmonic representation will be very suitable. Particularly, this is achieved by adopting Fourier series [15,16]:

$$\frac{dN}{d\phi} \propto 1 + 2 \sum_{n=1}^{\infty} v_n \cos(n(\phi - \psi_{\text{RP}})), \quad (1.1)$$

Here v_n are the flow coefficients, which represent the magnitude of each harmonic that make up the azimuthal distribution. Furthermore, ϕ is the azimuthal angle of an individual particle, and ψ_{RP} is the reaction plane, indicating the azimuthal orientation of the collision system. This form of representation is also particularly useful for characterizing the various modes of anisotropy observed in the experiments. A high v_2 indicates a strong elliptic anisotropy, while v_3 refers to a triangular expansion.

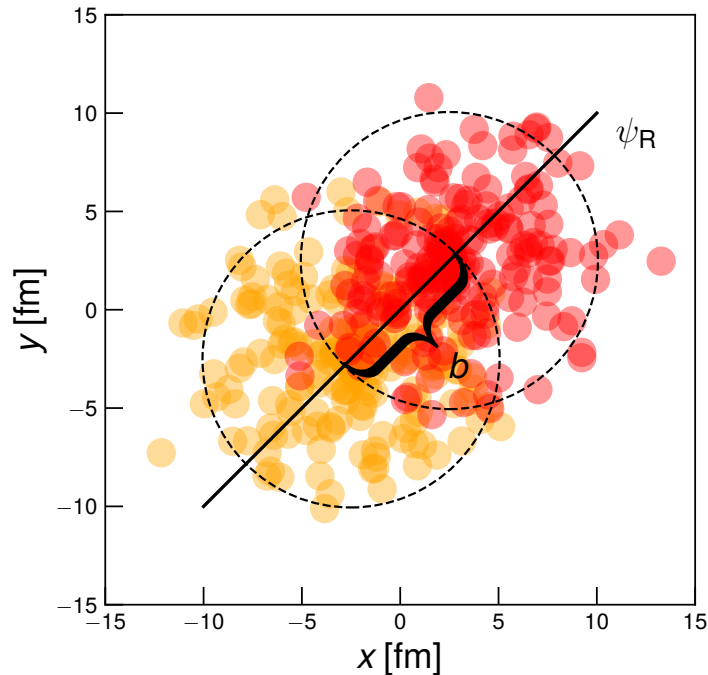


Figure 1.2: Schematic representation of a heavy-ion collision system. The overlapping and colliding nucleons in the middle define the participant region.

Correspondingly, higher harmonics pick up more finely structured signals. A more detailed introduction to anisotropic flow and its properties will be given in Chapter 3.

Figure 1.2 presents a schematic view of a collision system between two heavy-ions, along with a geometrical representation of the various quantities. Two nuclei are pictured colliding along the beam axis, with their centers separated by a distance defined by an impact parameter b . A reaction plane with an angle ψ_R is the plane that passes through the centers of both nuclei, perpendicularly to the transverse plane fixed by the x and y coordinates. In this example, the nuclei hit each other only partially, with the colliding area in the middle called the participant region.

Although of little use in experimental heavy-ion physics, the concepts of impact parameter and reaction plane are very typical parameters in theoretical modeling, where initial collision geometries strongly dictate the extent to which each physical process contributes to overall collision event. Therefore, it will be useful to define further quantities not only describing the geometry and arrangement of the nuclei, but also quantifying the structure of the actual matter inside the collision system.

Figure 1.2 further demonstrates how the nucleons might be located inside the nuclei, and how they might overlap within the participant region. Locations of the nuclei are known to fluctuate randomly from one event to another, and no collision system is the same even with identical b and ψ_{RP} . In the participant region, nucleons from the two nuclei collide with each other, and are the so-called participant nucleons.

In this case, the participant nucleons define a spatial symmetry among themselves. The symmetry is represented by a participant plane angle Φ [17, 18]. Analogously to the reaction plane ψ_R of the final state spectrum in Eq. (3.5), the participant plane can help define the initial state characterization with a quantity called eccentricity ε_n . One

such definition of eccentricity is given as

$$\varepsilon_n e^{in\Phi_n} \equiv - \frac{\int_{\Omega} dr d\varphi r^n e^{in(\varphi - \Phi_n)} \varepsilon(r, \varphi)}{\int_{\Omega} dr d\varphi r^n \varepsilon(r, \varphi)}. \quad (1.2)$$

Here $\varepsilon(r, \varphi)$ is the energy density at distance r from the system's center of mass and azimuthal angle φ . Similarly to the flow coefficients v_n , eccentricity ε_n characterizes the initial state anisotropies in terms of harmonic orders n . The integrations is over the interaction area Ω . Note that in Eq. (1.2) each order has its own corresponding participant plane, i.e. $\Phi \rightarrow \Phi_n$. This is to take account the presence of the initial state fluctuations, which can be shown to break the alignment of the symmetries between harmonic orders. Similar treatment is thus given for the final state decomposition in Eq. (3.5); $\psi_R \rightarrow \psi_n$. Here ψ_n are called the symmetry planes.

1.2.2 Constraints of the medium properties

As mentioned, direct observation of the QGP is not possible for now, and therefore the examination is limited to theoretical modeling of the collision process. A theoretical model for the dynamics of the QGP takes the initial state of the collision system as an input, for example $\varepsilon(r, \varphi)$, which the model then using some physical or phenomenological framework evolves into the system's final state. One example of such model is the class of hydrodynamical models [19], which by construction involve transport coefficients such as $\eta/s(T)$ and $\zeta/s(T)$ in order to characterize the momentum transport within the medium. A hydrodynamical model describes the collective motion of a fluid in terms of energy and momentum conservation within small discrete fluid elements. This will be described more in detail in Chapter 2. The input, i.e. the initial state represented by $\varepsilon(r, \varphi)$, will in turn be generated event-by-event by an initial state model, which aims to model the initial conditions as realistically as possible. In hydrodynamical modeling of heavy-ion collisions, the transport coefficients $\eta/s(T)$ and $\zeta/s(T)$ are *free* parameters of the theory, meaning that their values can only be determined by constraining them with comparisons to experimental data.

Flow harmonics v_2 and v_3

It has been well established by hydrodynamical calculations that the lower harmonic v_n for $n = 2, 3$ are to a good approximation linearly related to the corresponding orders of the initial state eccentricity, i.e., $v_n \propto \varepsilon_n$, $n = 2, 3$. Assuming that the initial state of a heavy-ion collision is truthfully represented by the initial state model, and can therefore be correctly characterized by the $\varepsilon_{2,3}$, the relation $v_n \propto \varepsilon_n$ together with the comparison of calculated v_n to the measured ones could act as a primary constraint for the η/s used by the theory. However, there are some major problems with this strategy.

Firstly, if we denote the connection between v_n and ε_n more explicitly as $v_n e^{in\psi_n} = k \varepsilon_n e^{in\Phi_n}$, one can realize that the scale k at which v_n is proportional to ε_n is not known. This leads to a situation where it is possible to have multiple representations of initial states that all satisfy this relation, and at the same time, after evolving the system to its final state with some set of transport coefficients, produce the same v_n . In other words, we do not actually know how the correct representation of initial conditions

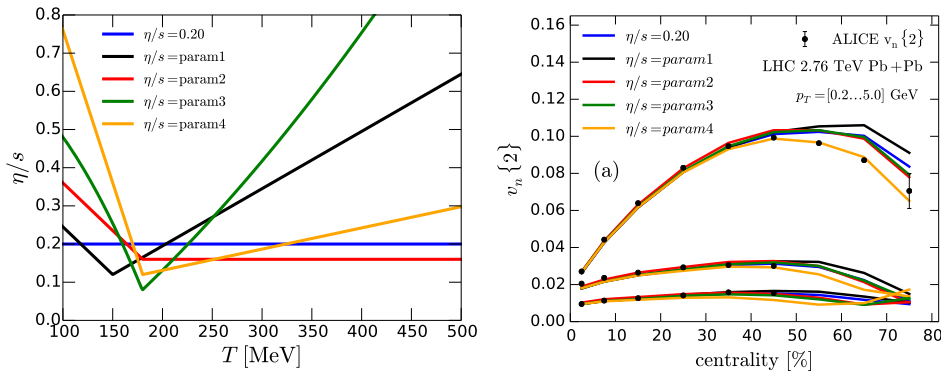


Figure 1.3: Various temperature dependence parameterizations of $\eta/s(T)$ (left) with their corresponding reproductions of v_n (right). The v_n exhibit a very low sensitivity to variations of strongly temperature dependent parameterizations [18]. Reprinted with permission from the American Physical Society.

look like, as it is not possible to have a corresponding experimentally measured ε_n unlike v_n , to which to compare. This is known as the initial state uncertainty, which leads into reproduction of measured v_n with many possible parameterizations of η/s .

The other issue with v_2 and v_3 is that they do not have enough constraining power to accurately constrain the temperature dependence of $\eta/s(T)$ [18]. Figure 1.3 illustrates this problem. The left side presents various parameterizations of $\eta/s(T)$. On the right side, the corresponding v_n calculations are shown. It is clear that with the same set of initial conditions, it is possible to have very drastic changes in the temperature dependence of $\eta/s(T)$, while having barely noticeable change in the v_n outcome. Consequently, one can state that the sensitivity of the low harmonic v_n , as far as $n \leq 3$ is concerned, to the temperature dependence of the transport coefficients is very low.

Higher harmonics and flow correlations

On the other hand, investigation of the higher harmonics $n \geq 4$ has contributed to major advancements in the overall state of the research. While still largely insensitive to the temperature dependence, higher harmonic v_n generally provide better sensitivity to the average values of η/s . This is largely due to the fact that higher frequency waveforms experience more viscous damping as they propagate through the medium. Furthermore, the unique properties of the higher harmonic flow in general can provide powerful constraints for the transport coefficients, including the temperature dependence, as will be demonstrated.

Unlike the second and third harmonic flow, the higher harmonic flow $n \geq 4$ can no longer be approximated by a linear relation to its corresponding initial state eccentricity ε_n [20]. Instead, studies have shown that the higher harmonic flow receives contributions not only from the response to ε_n , but also from lower harmonics in varying strengths. In other words, one can expect to find correlations within the harmonic orders, and it should be possible to quantify these correlations in some way.

These correlations were quantified for the first time by the development and mea-

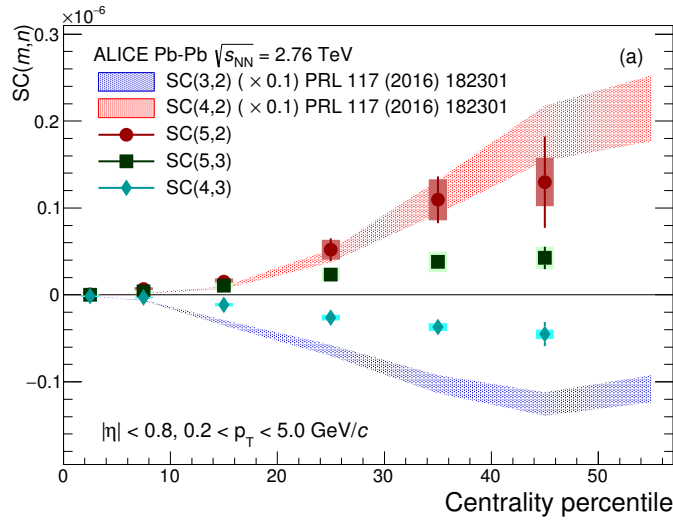


Figure 1.4: Symmetric cumulants (SC) measured by ALICE in Pb–Pb at $\sqrt{s_{\text{NN}}} = 2.76$ TeV [21]. Several pairs of harmonics show either strong correlation or anti-correlation with their positive or negative signs of the SC, respectively. With positive correlation between m and n , it is likely that for a higher than average v_m emerging from a single event, the v_n is also found larger than the corresponding event average. Likewise, the opposite holds for an anti-correlation, i.e. a symmetric cumulant with negative sign.

surement of the so-called symmetric cumulants (SC) [21–24], a set of observables which quantify the strengths of the correlations between magnitudes of various flow harmonics v_n . Measurements of some of these correlations by ALICE Collaboration are shown in Fig. 1.4. From the results, strong correlations between the flow harmonics can be observed most clearly in the peripheral collisions, with some correlations such as $\langle v_4 v_2 \rangle$ much stronger than the others, for example $\langle v_4 v_3 \rangle$.

A particularly interesting attribute of the symmetric cumulants is their ability to discriminate between the temperature dependent parameterizations of viscous hydrodynamics, and therefore also between the medium and hadronic stage effects [22]. Consequently, the correlations between the flow harmonics prove to be much stronger constraint for the temperature dependence of the transport coefficients than v_n alone. When used together, the potential to accurately narrow down the $\eta/s(T)$ and $\zeta/s(T)$ increases significantly.

Non-linear flow

Recent advancements over the years have made it possible to not only quantify the strength of the correlations between the flow harmonics, but also to actually determine the components and magnitudes of the cross-harmonic contributions to the higher harmonics. Such contributions will be referred to as the non-linear flow. In quantifying the cross-harmonic response to the ε_n , the flow is decomposed into linear- and non-linear contributions v_n^{L} and v_n^{NL} , respectively, where the former should retain a linear relation to a particularly defined eccentricity ε'_n , i.e. $v_n^{\text{L}} \propto \varepsilon'_n$. The non-linear nature of the higher harmonics comes from the observed non-linearity of the lower

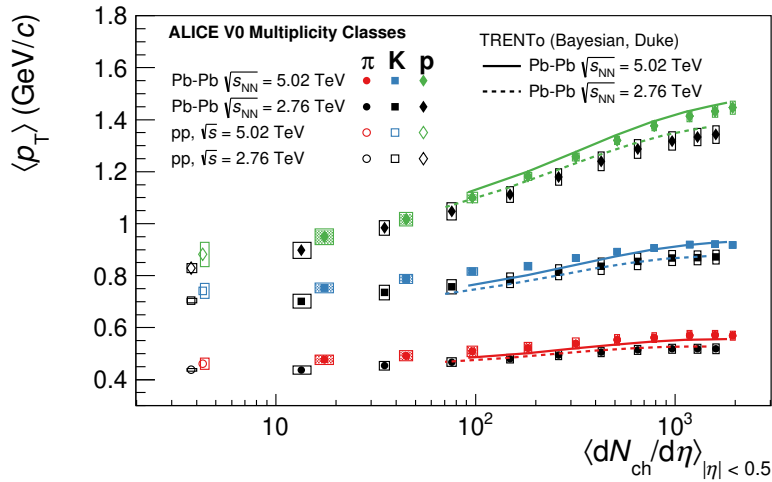


Figure 1.5: Transverse momentum of identified particles measured by ALICE [25]. The accompanying model comparisons quantitatively test the understanding of the current theories.

harmonic contributions. For example, it turns out that v_4 receives major contributions from the second order ε_2^2 , in addition to ε_4 . The strong dependence of v_4 on the second harmonic is also reflected by the symmetric cumulants in Fig. 1.4, where a clear positive $\langle v_4 v_2 \rangle$ through SC(4,2) is observed. The sensitivity of the non-linear flow mode observables to $\eta/s(T)$ especially around the freeze-out temperature is significant. As a result, by constraining the model parameters against the non-linear observables we may obtain new understanding of the medium properties. The measurements of the non-linear flow up to seventh harmonic order were published recently [1], and the results of this research work make also the most important contribution to this thesis.

Particle yields and energy production

The measurements of the particle yields and energy produced in collisions provide equally vital constraints to model calculations. Of particular interest are the charged and identified particle multiplicities $dN_{\{ch,\pi^\pm,K^\pm,p^\pm\}}/d\eta$ and mean transverse momentum $\langle p_{T,\{ch,\pi^\pm,K^\pm,p^\pm\}} \rangle$ (see Fig. 1.5), which together enable the mapping of the specific bulk viscosity $\zeta/s(T)$ and initial conditions. Recent measurements by the ALICE collaboration cover the charged and identified particle multiplicities in Pb–Pb collisions at the center of mass energy of 5.02 TeV per nucleon [26], as well as the mean transverse momentum [25].

1.3 Thesis aim and outline

Since research has advanced understanding of the hydrodynamic picture of the heavy-ion collisions, the non-linear flow has been an integral part of the theory of collectivity in these systems. The main focus of this thesis is on the measurement of the non-linear flow modes in Pb–Pb collisions along with the higher harmonic flow coefficients. The central aim of my thesis is to present and demonstrate the use of a new sophisticated

set of observables that can provide highly sensitive constraints for advanced model calculations in the search of the temperature dependence of $\eta/s(T)$ and $\zeta/s(T)$ as well as other parameters. In an additional study, I perform a Bayesian analysis with the hydrodynamical model framework by including the new observables measured during my research work. This thesis sets to contribute to advancement in the theory of heavy ion collisions by developing a method of reproduction of the non-linear flow observables in model calculations while simultaneously both predicting the basic observables, such as particle yields, energy production and the simple flow observables, and quantifying the sensitivities of observables.

This thesis is structured as follows. Chapter 2 introduces the modeling and the key theoretical concepts of our understanding of QGP. This includes the hydrodynamical model, and various initial state and transport related properties of the matter. In Chapter 3, the observables of the experimental analysis are presented. The discussion involves the introduction of the anisotropic flow, and several of the advanced flow observables used to constrain the QGP properties. Chapter 4 is dedicated to the description of the hardware and the experimental setup, in particular the ALICE detector facilities at CERN. Chapter 5 discusses the analysis procedure, verification, and systematics, after which Chapter 6 presents the results of this thesis. Finally, a summary of the results is given in Chapter 7.

Chapter 2

Theoretical modeling

A significant portion of present-day physics research relies on advanced computer models. Computer models and simulations enable physicists to test assumptions, make predictions and discoveries on increasingly complicated physical systems, especially where interaction with a real world system is not possible. Heavy-ion physics is no exception. As the observations of an event in particle and nuclear physics are limited to detector readings, caused by long-lived final state particles, the only way to understand the event is to try to model it based on existing understanding, and observe how the model replicates the results of a real world event.

The best approach to modeling the heavy-ion collisions is to split the collision process into separate, distinct phases. In such an approach, each stage of the collision is described by an individual, specially designed theoretical model. This description is then successively transferred to the following stage of the collision. The stages are commonly governed by the initial stage, the QGP phase, hadronization and the hadronic scattering with the QGP phase lasting about $\tau \sim 5$ to $8 \text{ fm}/c$. An illustration of the collision stages is presented in Fig. 2.1.

Relativistic hydrodynamics is a widely used and successful approach to heavy-ion collision modeling. The application of hydrodynamics in particle physics originates from the early attempts on analyzing collective particle motion as a result of proton-proton (pp) collisions [27,28]. Most importantly, the hydrodynamic model emphasizes the transversely anisotropic expansion of the system over the isotropic one that can be expected from an ideal gas [29]. Since the first experimental evidence of the fluid-like evolution of QGP [8], the importance of the hydrodynamics model in heavy-ion physics has been significant, and it has since been refined to model the dynamics of the QGP to impressive levels of accuracy.

2.1 Relativistic hydrodynamics

In this section, a brief overview on the hydrodynamic model is given based on Ref. [19]. A general hydrodynamic description relies on the energy and momentum conservation laws of the fluid dynamics. At the relativistic limit, the local energy-momentum conservation can be written as

$$\partial_\mu T^{\mu\nu}(x) = 0. \quad (2.1)$$

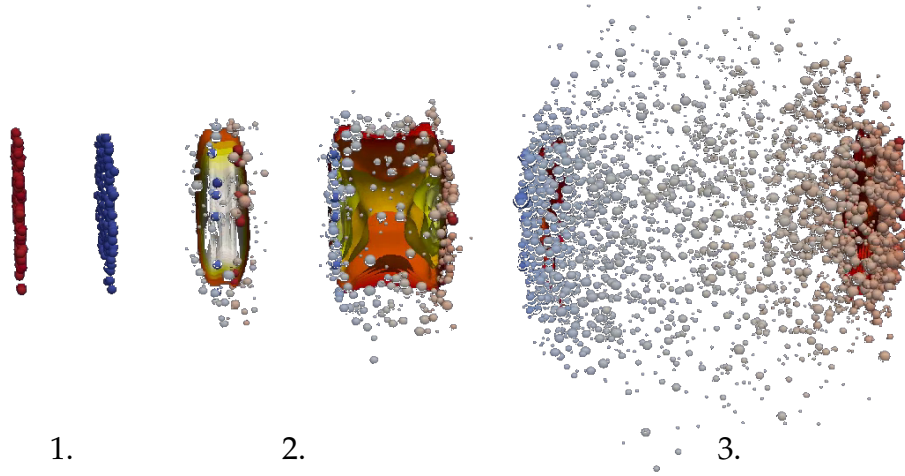


Figure 2.1: Stages of heavy-ion collision using hydrodynamic description. **1.** Two approaching Pb-ions at $\tau < 0$ fm/c. **2.** QGP after initial conditions at $\tau \gtrsim 1$ fm/c. **3.** Hadronization and hadronic scattering at $\tau \gtrsim 5 \sim 10$ fm/c. MADAI Collaboration, Hannah Petersen and Jonah Bernhard.

In order to maintain the conservation of various charges, another set of equations is enforced. This is governed by the continuity equations

$$\partial_\mu J_i^\mu(x) = 0. \quad (2.2)$$

Equation 2.2 represents a general case for multi-component systems, where different types of charges are conserved for $i =$ baryon number, strangeness, electric charge, etc. By defining a projection transverse to the 4-velocity

$$\Delta^{\mu\nu} = g^{\mu\nu} - u^\mu u^\nu \quad (2.3)$$

i.e. $\Delta^{\mu\nu} u_\nu = 0$, the charge current in Eq. (2.2) can be expressed as

$$J^\mu = nu^\mu + q^\mu, \quad (2.4)$$

where $q^\mu = \Delta^{\mu\nu} J_\nu$ is the charge flow, characterizing the local diffusion of the fluid. The energy momentum tensor becomes [19]

$$T^{\mu\nu} = \epsilon u^\mu u^\nu - (P + \Pi)\Delta^{\mu\nu} + \pi^{\mu\nu}, \quad (2.5)$$

where ϵ is the energy density and $P = P(\epsilon, n)$ the equation of state, relating the quantities together with the pressure P and thus closing the system of equations. The shear pressure $\pi^{\mu\nu}$ and the bulk pressure Π , encode the essential transport properties of the relativistic fluid. The full form of the various components is omitted for brevity. The viscous pressures are evolved with Israel-Stewart relaxation-type of equations up

to the Navier-Stokes limit, where the quantities are reduced to

$$\begin{aligned}\pi^{\mu\nu} &\sim 2\eta\nabla^{\langle\mu}u^{\nu\rangle} \\ \Pi &\sim -\zeta\partial_\mu u^\mu \\ q^\mu &\sim \kappa\nabla^\mu\frac{\mu}{T},\end{aligned}\tag{2.6}$$

where $\nabla^\mu = \Delta^{\mu\nu}\partial_\nu$. From this limit, one identifies the fundamental transport coefficients: the shear viscosity η and bulk viscosity ζ in addition to a diffusion coefficient κ . Together with the equation of state $P(\epsilon, n)$, the transport coefficients dictate the behaviour and response of the fluid under various events, distinguishing the fluid from another.

2.1.1 Transport coefficients

Shear viscosity

Shear viscosity, denoted as η , is a measure for the fluid's resistance to deformation, i.e. shear stress [14]. The higher the shear viscosity, the more "thick" the fluid will appear and the slower it will also flow under pressure. A low viscosity fluid will internally have stronger interactions within its constituents, and the constituents will thus travel shorter distances while exchanging momentum with others.

The viscosity of the QGP under hydrodynamic description manifests correspondingly to the viscosity of any other ordinary fluid. Heavy-ion physics is most interested in the specific shear viscosity, the shear viscosity over entropy density ratio η/s . In this form, the η/s is also a probe for the critical point of the QGP: generally the minimum η/s is found at the critical point of the substance (see Fig. 2.2). The relation to the entropy density s makes the comparison of the viscosity of different substances also convenient, as the entropy density cancels out the relation to the density of the matter.

Bulk viscosity

Bulk viscosity ζ depicts the fluid's resistance to expansion and compression [14]. The bulk viscosity has a direct effect on the radial expansion of the medium, and the attenuation of sound in it. As the fluid expands or contracts, in most substances a particular energy is needed to rearrange the microscopic structure in order to accommodate for the change in volume. As with the shear viscosity, the bulk viscosity in heavy-ion physics is given per unit entropy density, i.e. ζ/s .

Current understanding of the QGP transport coefficients

The current measurements of QGP shear viscosity over entropy density η/s are precise enough to rank it as the lowest value ever recorded among all fluids. With a value somewhere between ~ 0.08 to ~ 0.20 [31, 32, 32], the η/s of QGP can be considered very small and almost zero, making it resemble an ideal "perfect" fluid. Remarkably, anti-de Sitter/conformal field theory (AdS/CFT) calculations place the universal minimum value of η/s at $1/(4\pi) \approx 0.08$ [33].

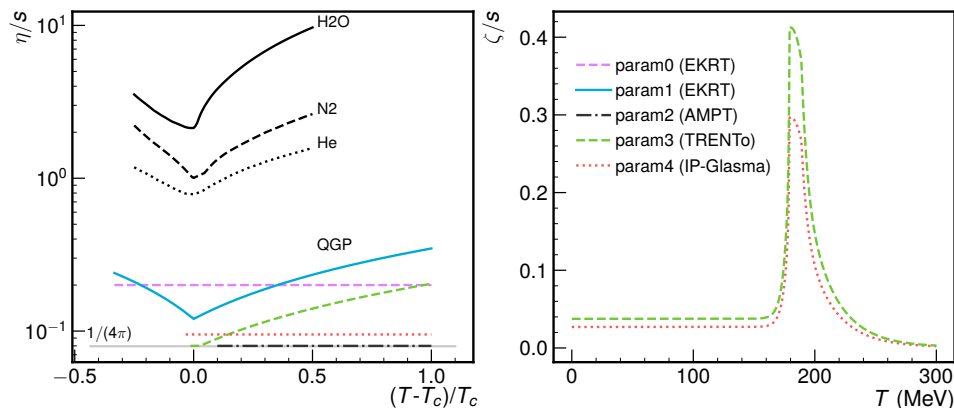


Figure 2.2: Temperature dependent parameterizations for the specific shear viscosity $\eta/s(T)$ and bulk viscosity $\zeta/s(T)$ [1]. $\eta/s(T)$ for various common substances have been added for comparison [30]. The minimum η/s expected to be around the critical point, approximately $T_c \approx 150 \sim 175$ MeV [13].

For many ordinary fluids, the η/s is known to be dependent on the underlying thermodynamic conditions, especially temperature [30]. There are hints that the η/s of the QGP exhibits a similar dependency, although the exact form of the said dependency is still unknown. Generally, the minimum $\eta/s(T)$ is found at the critical temperature $T = T_c$ of the substance. Based on the findings from atomic and molecular data, it is expected that the minimum $\eta/s(T)$ is found at the critical temperature also for the QGP [13].

On the left of Fig. 2.2, several parameterizations of transport coefficients based on the current knowledge of QGP are presented [1], along with the curves for ordinary water, nitrogen and helium [30]. Candidates for the QGP $\eta/s(T)$ include several temperature dependent parameterizations with the minimum found at the critical temperature T_c , as well as several temperature constant parameterizations around $0.08 \lesssim \eta/s \lesssim 0.2$. The parameterizations are specific to their model calculations, which have all been tuned to reproduce the charged hadron multiplicity, low- p_T spectra and several experimentally measurable low harmonic flow observables. The model uncertainty is clearly visible here, as the parameterizations vary significantly from each other. A more detailed discussion on the models and how they are tuned will be given in later sections.

Until recently, the contribution of the bulk viscosity over entropy density ζ/s in case of QGP was considered negligible, and generally left out from the calculations, i.e. $\zeta/s \sim 0$. Recently however, the importance of this effect has become more pronounced, as the simultaneous reproduction of some observables without it would seem not possible [34, 35]. A nonzero ζ/s has been deemed necessary around the critical temperature T_c .

2.2 The initial state of heavy-ion collisions

Initial state models provide the initial conditions for the hydrodynamic evolution, assigning the energy density of the initial state. In numerical terms, this translates to

the generation of the initial values on a lattice to act as the initial conditions for the differential equations of hydrodynamics. The initial condition model will take care of everything from shaping the geometry of the collision to energy density deposition, and finally pre-equilibrium dynamics after which the hydrodynamic model will work on the generated initial state [19].

A typical initial condition model can be divided into a number of distinct steps, each varying in complexity and on the underlying physical assumptions. The fundamental steps for initial conditioning may in many cases be stated as such:

1. Initialization of the layout for the collision system.
2. Placement of the nucleons according to a nuclear density distribution.
3. Determination of nucleon participants by a binary collision probability.
4. Assignment of a shape and density for each participant nucleon.
5. Evaluation of the nuclear thickness and energy density deposition in the participant region.
6. Free streaming and/or pre-equilibrium dynamics.

2.2.1 Initial condition models

MC-Glauber

In a simple nuclear model, the external geometry of a nuclei is roughly defined by a circular area with an effective radius $R = r_0 A^{1/3}$, also called nuclear radius [36]. Here $r_0 = 1.275$ fm, and A is the mass number. In a collision system of two heavy ions, the relative distance between the centers of the two nuclei on the azimuthal plane, defined as the impact parameter \mathbf{b} , is randomized or chosen according to the desired centrality of the collision. A random impact parameter may be drawn from the distribution $d\sigma/db = 2\pi b$. The orientation of the system is also random in real-life experiments, so it will be desirable to choose a random orientation between 0 and 2π radians.

The positions of the nucleons inside the nucleus fluctuate and distribute according to a nuclear density distribution. In a basic modeling approach described here, one of the first steps is to determine the positions of these nucleons, which in a later stage give a rise to the nuclear energy density. A straightforward approach is to sample the nuclear density distribution for each nucleon. A nuclear density distribution $\rho(r)$ is proportional to the mean field potential of the nucleus as a function of distance r from its center. The most common potential is the Woods-Saxon [37] potential given by

$$V(r) = -\frac{V_0}{1 + \exp\left(\frac{r-R}{a}\right)}, \quad (2.7)$$

where a characterizes the surface thickness of the nucleus, representing the falloff of the potential towards the edge of the nucleus. Such potential for a lead ion has been plotted in Fig. 2.3. Depending on the level of approximation, the mean field potentials

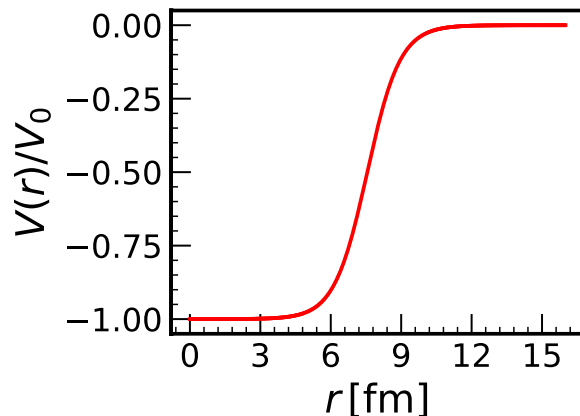


Figure 2.3: Woods-Saxon for ^{208}Pb , with $r_0 = 1.275$ fm and $a = 0.7$ fm.

for protons and neutrons can also be employed separately, more accurately taking into account the Coulomb potential of the protons, and the skin effect for neutrons.

From Eq. (2.7), the nuclear density is obtained proportionally $\rho(r) \propto V(r)$, which radial probability distribution $P(r) \propto r^2\rho(r)$ is then sampled to distribute the nucleons for the two nuclei of the collision system. Figure 1.2 presents a one example result of such placement. In such scenario, the positions of the nucleons are assumed to be uncorrelated, i.e. they are placed independently of each other. As the nucleons are not to freely overlap each other too closely, often a minimum distance of the order ~ 1 fm may be enforced to improve the realism of the model.

Once distributed, it is now possible to finalize the shape of the two incoming nuclei. For this and the following steps, the geometrical properties of the nucleons themselves, such as the size and density profile, should be defined. While there have been measurements of the size and shape of the proton for example, it is not known if and how these individual properties are related to the initial conditions of a heavy-ion collision. Often, this connection is quantified by leaving it as a free parameter of the theory, in other words as an unknown constant to be determined by fitting it to the experimental data. It can be assumed that the shape and placement of the nucleons follow some physical distribution. For a single nucleon, the density is given by the Fermi-distribution [38]

$$\rho_{\text{nucleon}}(r) = \rho_0 \frac{1 + w \left(\frac{r}{R}\right)^2}{1 + \exp\left(\frac{r-R}{a}\right)}. \quad (2.8)$$

Here, w is the width of the nucleon, and the other parameters work analogously to Eq. (2.7). Other distributions are also often used, such as the Gaussian distribution, possibly along with some modifiers to represent the fluctuations in density. The density of the individual nucleons is summed up to make up the density $\rho(x, y, z)$ for both of the two nuclei.

With the density assigned, we now define the nuclear thickness to represent the transverse profile of the nuclei A and B as

$$T_{A,B}(x, y) = \int dz \rho_{A,B}(x, y, z) = \sum_i^{N_{A,B}} \int dz \rho_{A,B,\text{nucleon}}^{(i)}(x, y, z). \quad (2.9)$$

Here, $N_{A,B}$ are the *participant* count for each nuclei, meaning only nucleons that participate in one or more binary collisions contribute to the nuclear thickness $T_{A,B}$. A nucleon collides with another according to a probability $P_{ij} \sim p(\rho_{A;\text{nucleon}}^{(i)}, \rho_{B;\text{nucleon}}^{(j)})$, which is often defined with a hard disk

$$r \leq \frac{\sigma_{\text{NN}}}{\pi}, \quad (2.10)$$

for which there is not distinction between heads-on or peripheral nucleon-nucleon collision, or with a more smooth Gaussian or an Eikonal type overlap function.

The goal of the initial condition model is now to convert the given nuclear thickness T_A and T_B into energy density $\epsilon \sim f(T_A, T_B)$. Different models have various different assumptions on the physical mechanisms of the energy production, leading to different predictions.

For the basic MC-Glauber model [36], the energy deposition scheme is very simple: a sum and a product of the two thicknesses, to model the energy density of the nuclear matter and the individual nucleon-nucleon collisions, respectively:

$$\epsilon \sim T_A + T_B + \alpha T_A T_B. \quad (2.11)$$

Here, α is a phenomenological variable to control the relative strength of the energy deposition for the nucleon-nucleon collisions.

MC-KLN

MC-KLN is a Color Glass Condensate (CGC) [39] field theory based saturation model for the initial conditions [40, 41]. A saturation picture states that the number of produced partons saturates proportionally to the square of the parton transverse momentum Q^2 , and the area of the nucleus. This happens because as the momentum of a parton increases, based on the uncertainty principle the larger will also be the area it occupies on the Lorentz contracted nucleus disk. At some point with a sufficient number of partons they start to overlap and interact with each other, preventing further increase of parton density. The momentum at which this happens is called the saturation scale, denoted as Q_s . The energy deposit is proportional to the produced gluon density

$$\epsilon \sim \frac{dN_g}{dyd^2r_\perp} \sim Q_{s,\text{min}}^2 \left[2 + \log \left(\frac{Q_{s,\text{max}}^2}{Q_{s,\text{min}}^2} \right) \right], \quad (2.12)$$

where $Q_{s,\text{min}}^2 \propto T_{\min(A,B)}$ and $Q_{s,\text{max}}^2 \propto T_{\max(A,B)}$.

EKRT

EKRT is a saturation model with collinearly factorized pQCD minijet production [18, 42]. The energy deposition in the EKRT model is driven by a production of saturated low- p_T partons, and higher energy partonic jets, also known as minijets. The initial minijet transverse energy density in a rapidity window Δy above a transverse momentum scale $p_0 \gg \Lambda_{\text{QCD}}$ is given by

$$\frac{dE_T}{d^2\mathbf{x}_\perp} = T_A(\mathbf{x}_\perp) T_B(\mathbf{x}_\perp - \mathbf{b}) \sigma \langle E_T \rangle_{p_0, \Delta y, \beta}, \quad (2.13)$$

where $\sigma\langle E_T\rangle_{p_0,\Delta y,\beta}$ is the minijet cross section, given by $\sigma\langle E_T\rangle_{p_0,\Delta y,\beta} = \int_0^{\sqrt{s_{NN}}} dE_T E_T \frac{d\sigma}{dE_T}$. Here $\frac{d\sigma}{dE_T}$ is obtained as phase-space integrations of NLO ($2 \rightarrow 2$) and ($2 \rightarrow 3$) partonic scattering cross sections. In case of EKRT, the nuclear thickness $T_{A,B}$ includes all nucleons from the two nuclei, as opposed to only participant nuclei determined by a collision probability. In other words, every nucleon is treated as a participant while generating the initial nuclear thickness.

The contribution of the minijets diminish at transverse momenta $p_T < p_0$, and the higher-order partonic scattering processes ($3 \rightarrow 2$) etc. start to dominate over the conventional low order processes. Given a saturation condition $\frac{dE_T}{d^2x_\perp dy}(2 \rightarrow 2) \sim \frac{dE_T}{d^2x_\perp dy}(3 \rightarrow 2)$, a saturation criterion for the minijet transverse energy density production can be written as

$$\frac{dE_T}{d^2x_\perp dy} = \frac{K_{\text{sat}}}{\pi} p_0^3 \Delta y, \quad (2.14)$$

where p_{sat} is the saturation momentum, which in MC implementation will be pre-computed for $K_{\text{sat}}, \beta = \text{const}$.

After relating the minijet production (2.13) to the saturation criterion (2.14), a numerical determination for the saturation scale p_0 can be conducted. With $p_{\text{sat}} \equiv p_0$, the expression for the energy density is

$$\epsilon \sim \frac{K_{\text{sat}}}{\pi} p_{\text{sat}}^3 (K_{\text{sat}}, \beta; T_A, T_B). \quad (2.15)$$

Figure 2.4 presents the energy density profile generated by the EKRT, while Fig. 2.5 shows the parameterized saturation momentums as a function of nuclear thickness.

TRENTo

Different initial condition models produce a wide range of different initial conditions, which translates to large variations in model predictions for the hydrodynamic transport coefficients. As a result, it may not be possible to fully distinguish the variations in the initial conditions from the QGP medium properties. TRENTo (Reduced Thickness Event-by-event Nuclear Topology) [43] aims to address this by removing the convoluted physical assumptions from the energy deposition, and reduce the representation to a parameterized function of the nuclear thickness. Such parameterization straightforwardly enables one to constrain the initial conditions simultaneously with the medium properties, and get a phenomenological idea of the true shape of the initial conditions.

For each nucleon-nucleon collision candidate between the nuclei A and B, TRENTo evaluates the probability of a collision by

$$P_{ij} = 1 - \exp\left(-\sigma_{gg} \int dx dy \int dz \rho_{A,\text{nucleon}}^{(i)} \int dz \rho_{B,\text{nucleon}}^{(j)}\right), \quad (2.16)$$

where σ_{gg} is an effective parton-parton interaction cross-section, scaled by the total nucleon-nucleon cross-section σ_{NN} . A nucleon contributes to the thickness only if the evaluation of probability in Eq. (2.16) returns positive.

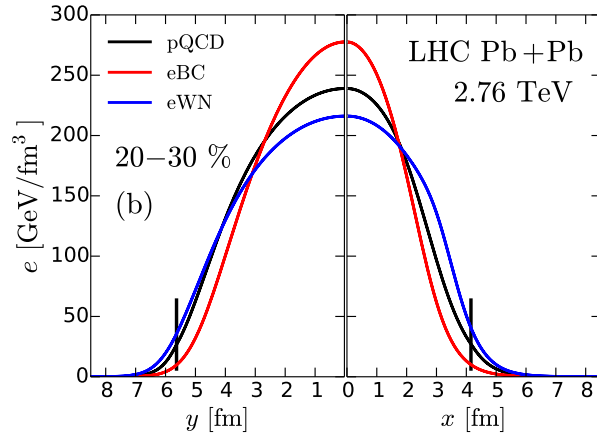


Figure 2.4: Energy density profile from EKRT with $K_{\text{sat}} = 0.63$, $\beta = 0.8$ at $\tau_0 = 0.204$ of Bjorken pre-thermal free streaming [18]. Reprinted with permission from the American Physical Society.

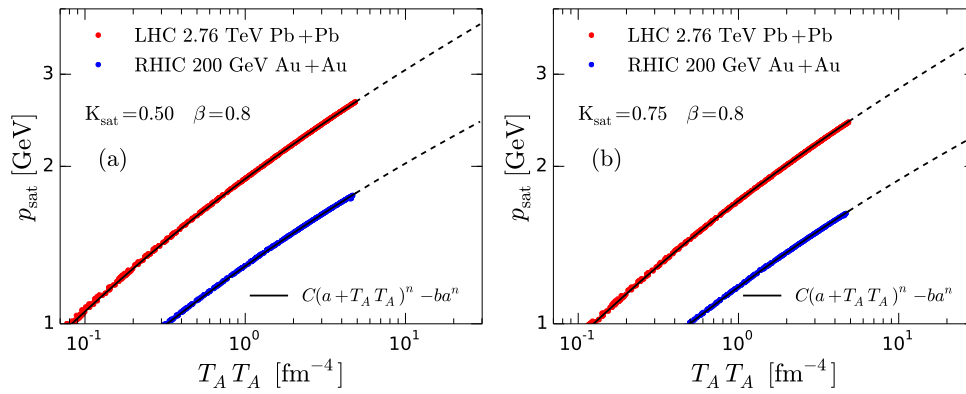


Figure 2.5: EKRT saturation momentum p_{sat} parameterizations for $K_{\text{sat}} = 0.5$ (left) and $K_{\text{sat}} = 0.75$ (right) [18]. Reprinted with permission from the American Physical Society.

To model the varying number of partons each nucleon-nucleon collision may produce, TRENTo incorporates fluctuations for the nucleon densities, which leads to a fluctuated thickness

$$\tilde{T}_{A,B} = \sum_i^{N_{A,B}} w_{A,B}^{(i)} \int dz \rho_{A,B,\text{nucleon}}^{(i)}(x, y, z). \quad (2.17)$$

For each nucleon, a weight $w_{A,B}^{(i)}$ is sampled from a gamma distribution

$$P_\kappa(w) = \frac{w^{\kappa-1} \kappa^\kappa}{\Gamma(\kappa)} e^{-\kappa w}. \quad (2.18)$$

The final energy density is derived from the reduced thickness

$$\epsilon \sim \left(\frac{\tilde{T}_A^p + \tilde{T}_B^p}{2} \right)^{\frac{1}{p}}, \quad (2.19)$$

where p is a dimensionless parameter, called the energy deposition parameter. By adjusting p , T_RENTo can reproduce many other models (see Fig. 2.6 and Fig. 2.7).

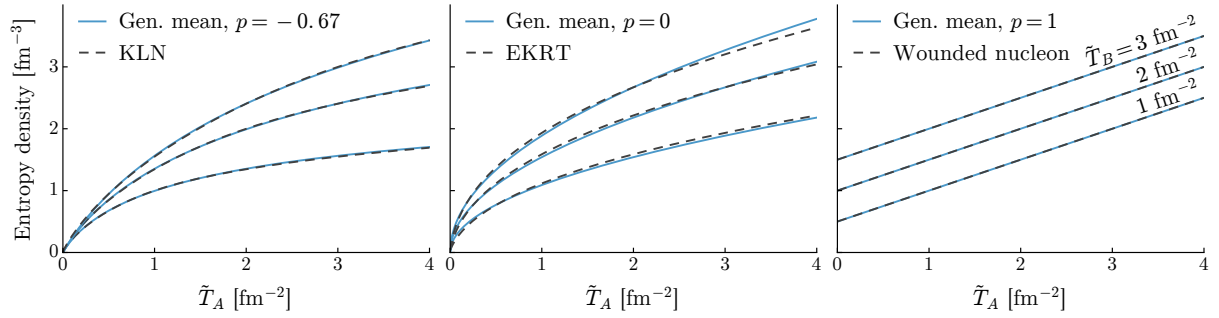


Figure 2.6: Initial entropy density profile predicted by KLN (left), EKRT($K = 0.64$, $\beta = 0.8$) (middle) and wounded nucleon model (right) compared to T_RENTo [44]. Reprinted with permission from the American Physical Society.

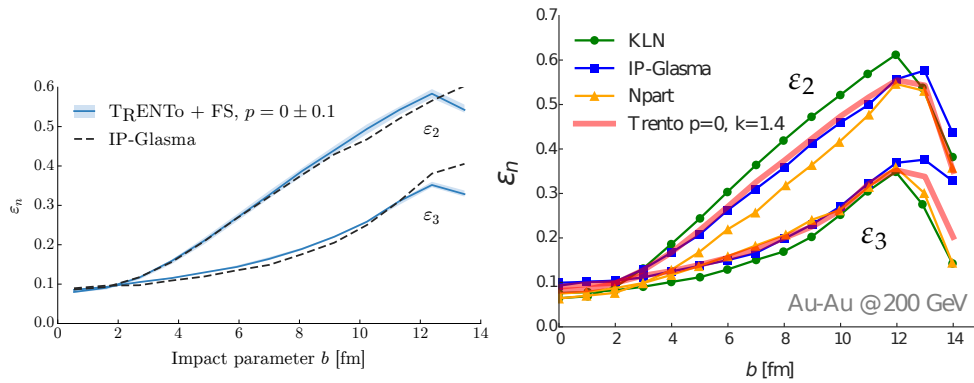


Figure 2.7: Eccentricity from T_RENTo with $p = 0$, $k = 1.6$ and nucleon width $w = 0.4$ (Gaussian) vs. other models as a function of impact parameter [44]. Reprinted with permission from the American Physical Society.

IP-Glasma

IP-Glasma is a successful initial state model, which encompasses a combination of CGC impact parameter dependent saturation model (IP-Sat) and classical Yang-Mills model of the initial gluon fields [45]. Unlike with the other models presented so far, IP-Glasma does not express the energy density in terms of $T_{A,B}$. Instead, IP-Glasma samples the nucleon positions from a Fermi distribution, after which the color charge density $g^2\mu_{A,B}^2(x, \mathbf{x}_\perp)$ is obtained proportionally to the summed saturation scales Q_s^2 provided by IP-Sat model for each nucleon. The color charges ρ^a are then sampled from the Gaussian distribution

$$\langle \rho_{A,B}^a(\mathbf{x}_\perp) \rho_{A,B}^b(\mathbf{y}_\perp) \rangle = g^2\mu_{A,B}^2(x, \mathbf{x}_\perp) \delta^{ab} \delta^{(2)}(\mathbf{x}_\perp - \mathbf{y}_\perp), \quad (2.20)$$

and the gluon fields determined by solving the classical Yang-Mills equations

$$[D_\mu, F_{\mu\nu}] = J^\nu, \quad (2.21)$$

where $J^\nu = \delta^{\nu\pm} \rho_{A,B}(x^\mp, \mathbf{x}_\perp)$ is the color current. The energy density ϵ is derived from the gluon fields, and evolved to a starting time of the hydrodynamic stage. Figure 2.8 presents an initial energy density profile from the IP-Glasma in comparison to simpler models. The resulting eccentricity from the IP-Glasma model are shown in Fig. 2.9.

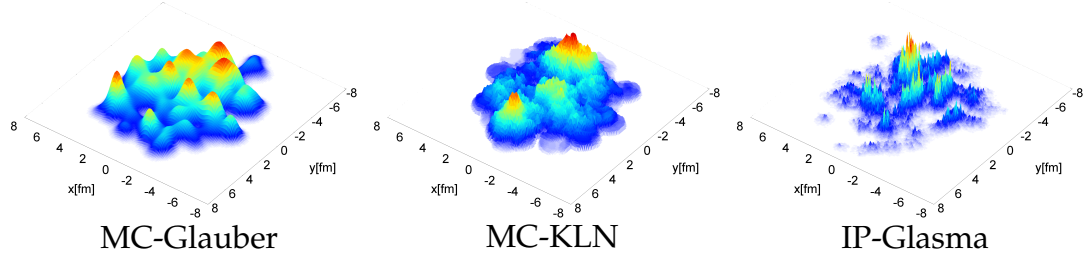


Figure 2.8: Visualisation of the initial energy density profile from MC-Glauber, MC-KLN and IP-Glasma models [45]. Reprinted with permission from the American Physical Society.

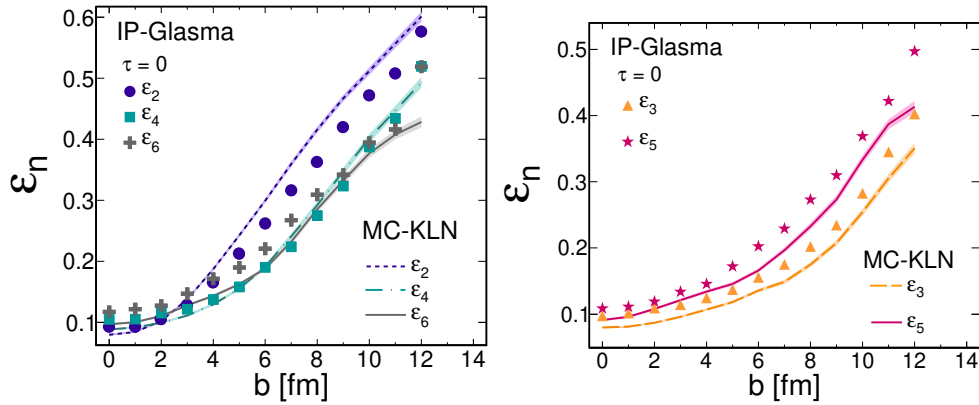


Figure 2.9: Eccentricity from IP-Glasma versus MC-KLN as a function of impact parameter [46]. Reprinted with permission from the American Physical Society.

2.2.2 Pre-equilibrium dynamics

In general, a hydrodynamic description assumes that the medium has reached a thermal equilibrium. According to present knowledge [47], in heavy-ion collisions the resulting QGP thermalizes quickly, within $\tau \sim 1 \text{ fm}/c$, making hydrodynamics applicable fairly early-on after the initial collision. Before this threshold however, a comparatively unknown dynamical process takes the matter distributed according to the initial energy density profile into thermal equilibrium. Freestreaming model [47] attempts to achieve this by modeling the QGP constituents at the initial stages of the collision as freely moving partons according to collisionless Boltzmann equation, after which the interactions are gradually introduced once the system gets more diluted.

2.2.3 Particlization

At a certain temperature, upon expanding to a sufficient volume and cooling down, the QGP constituents can no longer maintain a state of deconfinement. Consequently,

rebonding of the partonic constituents will gradually take place forming various types of hadrons. This process, known as particlization or hadronization, is generally modeled using the Cooper-Fry description, in which particles are sampled from the hypersurface of the hydrodynamic evolution according to [48]

$$E_p \frac{dN_n}{d^3p} = \frac{1}{(2\pi\hbar)^3} \int_{\Sigma} p \cdot d^3\sigma(x) f_n(x, p), \quad (2.22)$$

where Σ is the surface of condensation and $f_n(x, p)$ the phase-space distribution for a hadron species. In determining the final state and the time of hadronization, one may typically employ a specific switching temperature T_{switch} for which the freeze-out should take place. Although the use of a switching temperature is common, alternative methods based on expansion and scattering rates have also been proposed [49,50].

2.3 Parameter estimation

Models generally represent unknown constants or relations in nature through a set of parameters to quantify the observations. As mentioned, a hydrodynamic model typically employs transport parameters such as $\eta/s(T)$ and $\zeta/s(T)$, while an initial condition model might deal with parameters controlling nucleon size and energy deposition scale.

Parameter estimation refers to a model calibration process, in which the parameters of the model are tuned for the model to optimally reproduce the experimental results. Recently, a method based on Bayesian statistics has been used increasingly widely [2, 51–59]. A Bayesian parameter estimation is a process that finds the optimal configuration for a vector of parameters \mathbf{x} , against the experimental data denoted by \mathbf{y} using the Bayes' theorem

$$P(\mathbf{x}|\mathbf{y}) \propto P(\mathbf{y}|\mathbf{x})P(\mathbf{x}), \quad (2.23)$$

where the likelihood $P(\mathbf{y}|\mathbf{x})$ quantifies how well the model describes the data, and the prior $P(\mathbf{x})$ contains the initial knowledge on the parameters. During the optimization, the process extracts probability distributions for the optimal values of the parameters. A more detailed description of the process can be found in Ref. [55,57].

2.3.1 Analysis and model setup

In this thesis, I conduct a parameter estimation using the higher harmonic observables I have measured (detailed in Chapter 3). The parameter estimation will be done using a modified Bayesian parameter estimation framework provided by the authors of Ref. [57]. The model itself is composed of the following models:

- TRENTo initial conditions [55,57]
(4 parameters: nucleon attributes and energy deposition)
- freestreaming pre-equilibrium dynamics [47,60]
(1 parameter: time scale)

- OSU 2+1D viscous hydrodynamics (aka. VISHNew) [61,62]
(8 parameters: components of the transport parameterizations)
- UrQMD hadronic afterburner [63,64]
(no estimated parameters).

The associated number of tuned parameters is noted for each model, bringing the total number of parameters to 13. The majority of the parameters make up the parameterizations for the specific shear and bulk viscosities, which in this study can be written as [57]

$$(\eta/s)(T) = (\eta/s)(T_c) + (\eta/s)_{\text{slope}}(T - T_c) \left(\frac{T}{T_c} \right)^{(\eta/s)_{\text{crv}}} \quad (2.24)$$

and

$$(\zeta/s)(T) = \frac{(\zeta/s)_{\text{max}}}{1 + \left(\frac{T - (\zeta/s)_{\text{peak}}}{(\zeta/s)_{\text{width}}} \right)^2} \quad (2.25)$$

respectively. Details of the analysis are provided in [2] attached to this thesis, and the results are summarized in Chapter 6. The goal of this analysis is to find an improved parameterization that is able to reproduce the new higher harmonic flow observables simultaneously with the existing lower harmonic ones, and additionally to evaluate the sensitivity of these new observables against various transport coefficients and evaluate possible model shortcomings found in the process.

Chapter 3

Experimental observables

In heavy-ion physics, meaningful observations are quantified through the measurement of particle-level observables, which in turn allows one to evaluate the model performance in a quantitative manner. This is achieved by comparing the measured observables to those predicted by the model calculations. In this chapter, I will introduce the concept of anisotropic flow, which is used to quantify the effects of the medium expansion. Using the flow concept, I will further derive the standard flow observables used in characterizing the collective phenomena at the low- p_T region.

3.1 Anisotropic flow

As the expanding medium cools down, the fluid momentum is carried over to the particles that form during the freeze-out stage. Distributions of these particles therefore reflect the expansion of the medium itself, and provide valuable information on the early stages of the collision dynamics. Anisotropy of the particle distribution has been regarded as early evidence of the formation of the QGP, and the characterization of this anisotropy is essential to further quantify the medium effects.

A modern and standard characterization of the anisotropy decomposes the azimuthal particle distribution in terms of a Fourier expansion [15]:

$$f(\varphi) = \frac{a_0}{2\pi} + \frac{1}{\pi} \left(\sum_{n=1}^{\infty} a_n \cos(n\varphi) + \sum_{n=1}^{\infty} b_n \sin(n\varphi) \right), \quad (3.1)$$

where $a_n = \int_{-\pi}^{\pi} f(\varphi) \cos(n\varphi) d\varphi = \sum_{\nu} f(\varphi_{\nu}) \cos(n\varphi_{\nu})$ and $b_n = \int_{-\pi}^{\pi} f(\varphi) \sin(n\varphi) d\varphi = \sum_{\nu} f(\varphi_{\nu}) \sin(n\varphi_{\nu})$. Here the sums have been placed in the limit of a finite number of particles, ν denoting the index of an individual particle. One may then introduce a symmetry-plane angle $-\frac{\pi}{n} < \psi_n < \frac{\pi}{n}$, s.t. $\omega_n = \sqrt{a_n^2 + b_n^2}$, and therefore $a_n = \omega_n \cos(n\psi_n)$ and $b_n = \omega_n \sin(n\psi_n)$. Inserting these in to Eq. (3.1), we have

$$f(\varphi) = \frac{a_0}{2\pi} + \frac{1}{\pi} \sum_{n=1}^{\infty} \omega_n (\cos(n\psi_n) \cos(n\varphi) + \sin(n\psi_n) \sin(n\varphi)), \quad (3.2)$$

where $\cos(n\psi_n) \cos(n\varphi) + \sin(n\psi_n) \sin(n\varphi) = \cos(n(\varphi - \psi_n))$. The total number of particles is given by $a_0 = \omega_0 \cos(0\psi_0) = \omega_0 = \int_{-\pi}^{\pi} \frac{dN}{d\varphi} d\varphi = N$. As a result, the

expansion can be expressed as

$$f(\varphi) = \underbrace{\frac{\omega_0}{2\pi}}_{\frac{N}{2\pi}} \left(1 + \sum_{n=1}^{\infty} 2 \underbrace{\frac{\omega_n}{\omega_0}}_{\equiv v_n} \cos(n(\varphi - \psi_n)) \right), \quad (3.3)$$

where we have defined v_n as the magnitude of each harmonic contribution.

The v_n , also known as the flow coefficients, characterize the shape and anisotropy of the underlying event. The successive harmonics starting from v_2 represent the various modes of the expansions. For example, v_2 represents the eccentricity of an elliptic distribution, which can describe the ellipse-like anisotropic expansion emerging especially in a peripheral collision, where the participant region is highly almond-shaped. Likewise, v_3 represents the triangular modes one might observe in an asymmetric collision system. In the presence of event-by-event collision geometry fluctuations, one can always expect to observe a significant v_3 [65]. It can be shown, that the value of the flow coefficients can be explicitly obtained by [16]

$$v_n = \langle \cos(n(\varphi - \psi_n)) \rangle, \quad (3.4)$$

where the brackets $\langle \rangle$ denote an average over all particles. The anisotropic flow, and therefore the v_n , fluctuate event-by-event and as a result experiments generally report the values of v_n as well as other observables as an average over a large sample of events, which then corresponds to an expectation value for the flow coefficient over a distribution of event specific values. This fluctuation is currently attributed to the random spatial configuration of the nuclear constituents at the time of collision.

The azimuthal distribution in Eq. (3.3) can be equivalently written in terms of exponential complex quantities:

$$f(\varphi) = \frac{N}{2\pi} \sum_{n=-\infty}^{\infty} v_n e^{-in(\varphi - \psi_n)} = \frac{N}{2\pi} \sum_{n=-\infty}^{\infty} V_n e^{-in\varphi}, \quad (3.5)$$

where $V_n \equiv v_n e^{in\psi_n}$. It also follows from Eq. (3.4) that $V_n = \langle e^{in\varphi} \rangle$. This quantity is particularly useful as it not only includes the magnitude of the flow harmonic, but also its direction. The V_n will be used extensively in the later sections of this chapter where more advanced flow observables will be introduced.

3.2 Multi-particle correlations

3.2.1 Two-particle correlations

Advanced and modern flow analysis relies on multi-particle correlations, in which pairs, triplets or higher number of particles coming from a single event are correlated on the azimuthal-plane in order to calculate various flow observables. Equation (3.4) presented a valid expression to calculate the flow coefficients based on the particle azimuthal angles and the event symmetry-planes. However, due to its dependence on the symmetry-plane, the practical use this expression is severely limited. Only particle azimuthal angles are readily available in experimental analysis, and the event-plane

estimates of the symmetry-planes are generally not up to the modern standard in terms of accuracy to make Eq. (3.4) applicable [66].

A multi-particle approach presents a solution by operating solely on the particle azimuthal angles and not involving unobtainable or difficult to measure quantities. In case of two-particle correlations, the approach begins by forming a pair distribution from the product of two single particle distributions in Eq. (3.5). The pair distribution can be written as [67–69]

$$f_{\Delta}(\varphi) = \Delta N \left(1 + \sum_{n=1}^{\infty} 2 \underbrace{\langle v_n^a v_n^b \rangle}_{v_{n\Delta}} \cos(n(\varphi_a - \varphi_b)) \right) = \Delta N \sum_{n=-\infty}^{\infty} \underbrace{\langle v_n^a v_n^b \rangle}_{v_{n\Delta}} e^{-in(\varphi_a - \varphi_b)}. \quad (3.6)$$

Here $v_{n\Delta} = v_n^2$. The event v_n can then be obtained by calculating a two-particle correlation

$$v_n^2 + \delta_2 = \langle 2 \rangle_{n|n} = \langle \cos(n(\varphi_a - \varphi_b)) \rangle = \langle e^{-in(\varphi_a - \varphi_b)} \rangle. \quad (3.7)$$

The brackets denote an average over all pairs of particles, excluding the case where particle pairs with itself. A notation $\langle 2 \rangle_{n|n}$ has been employed to indicate a second-order correlation with with harmonics n and $-n$ (with the pipe $|$ separating positive and negative terms). In this case, the expression for the v_n has no ψ_n -dependence, which makes it readily available in an experimental setting. An additional term δ_2 has been introduced on the left side, uncorrelated to v_n , describing an inevitable *nonflow* contribution that emerges from azimuthal correlations determined by other sources than the anisotropic flow, such as resonance decays and jet contributions. Such contribution is regarded as a non-negligible experimental uncertainty, and common methods to reduce its impact will be discussed in this chapter.

3.2.2 Higher orders and cumulants

The multi-particle correlations can be extended to arbitrarily high orders. A generic multi-particle correlation can be written as

$$\langle m \rangle_{n_1, n_2, \dots, n_m} = \langle \cos(n_1 \varphi_1 + n_2 \varphi_2 + \dots + n_m \varphi_m) \rangle. \quad (3.8)$$

Again, only combinations of distinct particles are averaged in order to avoid self-correlation bias, also known as the autocorrelation. Only isotropic correlators will have non-zero values, i.e. the correlators for which a condition $n_1 + n_2 + \dots + n_m = 0$ is satisfied.

The higher and lower order correlations together provide a valuable mechanism to nonflow suppression of the of the lower orders [70]. In an approach known as the cumulant method, the nonflow is suppressed by a subtraction of a combination of lower order correlations from a higher order correlation. The resulting high order correlation, which as a result is insensitive to the nonflow of the lower orders, is called

a cumulant. The flow constructed from the cumulants up to the eighth order are

$$\begin{aligned}
v_n\{2\}^2 + \delta_2 &= \langle 2 \rangle_{n|n}, \\
v_n\{4\}^4 + \delta_4 &= -\left(\langle 4 \rangle_{n,n|n,n} - 2\langle 2 \rangle_{n|n}^2 \right), \\
v_n\{6\}^6 + \delta_6 &= \frac{1}{4} \left(\langle 6 \rangle - 9\langle 4 \rangle \langle 2 \rangle + 12\langle 2 \rangle^3 \right), \\
v_n\{8\}^8 + \delta_8 &= -\frac{1}{33} \left(\langle 8 \rangle - 16\langle 6 \rangle \langle 2 \rangle - 18\langle 4 \rangle^2 \right. \\
&\quad \left. + 144\langle 4 \rangle \langle 2 \rangle^2 - 144\langle 2 \rangle^4 \right).
\end{aligned} \tag{3.9}$$

The curly brackets denote the order of the cumulant. For brevity, the harmonics denoted by $n, \dots | n, \dots$ have been omitted from the notation starting from the sixth order, as the harmonic is always same. Generally, the lower order nonflow dominates over the higher in magnitude. The mechanism of the nonflow subtraction in Eq. (3.9) becomes clear if we decompose the multi-particle correlations into their independent contributions, as demonstrated in Ref. [70]. For the fourth order

$$\begin{aligned}
&\langle \cos(n(\varphi_1 + \varphi_2 - \varphi_3 - \varphi_4)) \rangle \\
&= \langle \cos(n(\varphi_1 - \varphi_3)) \rangle \langle \cos(n(\varphi_2 - \varphi_4)) \rangle \\
&+ \langle \cos(n(\varphi_1 - \varphi_4)) \rangle \langle \cos(n(\varphi_2 - \varphi_3)) \rangle \\
&+ \langle 4 \rangle_{n,n|n,n} - 2\langle 2 \rangle_{n|n}^2 + \delta_4,
\end{aligned} \tag{3.10}$$

where the two-particle correlations give rise to the second order non-flow according to Eq. (3.7) and are consequently subtracted by $2\langle 2 \rangle^2$ of the cumulant.

The cumulants therefore provide a reliable set of flow observables, insensitive to the lower order nonflow. Their mechanism of nonflow suppression also forms a basis for a number of prominent observables, such as the symmetric cumulants (SC) [21,22]. A definition of a two-harmonic symmetric cumulant looks very similar to $v_n\{4\}$ in Eq. (3.9):

$$\begin{aligned}
\text{SC}(m, n) &\equiv \langle v_m^2 v_n^2 \rangle - \langle v_m^2 \rangle \langle v_n^2 \rangle \\
&= \langle \cos(m\varphi_1 + n\varphi_2 - m\varphi_3 - n\varphi_4) \rangle \\
&- \langle \cos(m(\varphi_1 - \varphi_3)) \rangle \langle \cos(n(\varphi_2 - \varphi_4)) \rangle.
\end{aligned} \tag{3.11}$$

The symmetric cumulants measure the correlations between the magnitudes of the flow harmonics, and are particularly sensitive to the temperature dependence of the $\eta/s(T)$ [2,22]. A large positive value implies a strong correlation between two harmonics; for example a large positive $\text{SC}(4, 2)$ suggests that for a larger than average v_2 for an event, it is likely that v_4 has exceeded its average as well. Correspondingly, a negative SC implies an anti-correlation. A normalized symmetric cumulant refers to a quantity scaled by a correlation of flow coefficients:

$$\text{NSC}(m, n) = \frac{\text{SC}(m, n)}{\langle v_m^2 \rangle \langle v_n^2 \rangle} = \frac{\langle v_m^2 v_n^2 \rangle}{\langle v_m^2 \rangle \langle v_n^2 \rangle} - 1. \tag{3.12}$$

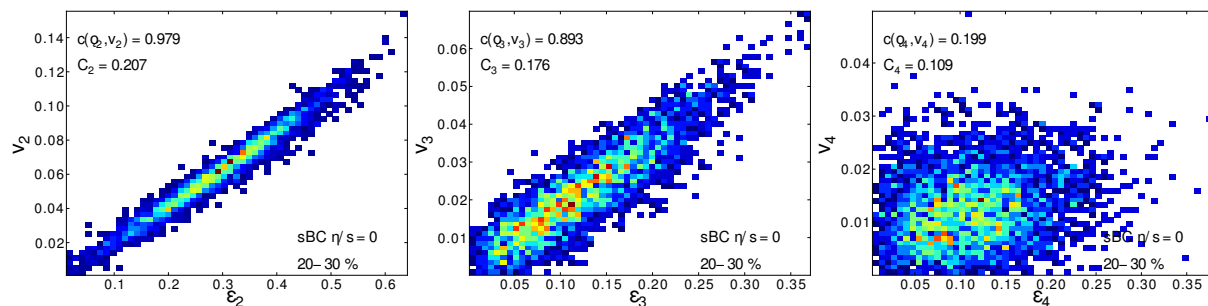


Figure 3.1: Hydrodynamic calculations of v_n plotted with respect to the corresponding initial state eccentricity ε_n [20]. The consequent correlations for the second and third harmonics are approximately linear, while for the fourth harmonic the linearity breaks down. Reprinted with permission from the American Physical Society.

NSC provides means to explore correlations between the flow harmonics without the expected dependence on the magnitude of the flow coefficients.

Recently, the symmetric cumulants have also been extended to higher orders [23], and are capable of measuring the correlations between three or more flow harmonics, while also being even less affected by the nonflow bias. Many of the harmonic correlations arise due to the non-linearities in the flow response [22]. Formalism for the non-linear flow will be explored in the following sections.

3.3 Quantifying non-linear flow

The concept of the non-linearity in anisotropic flow arises from the observations that for higher harmonics, the approximately linear correlations found between the initial state eccentricity and flow are no longer seen. This is illustrated by hydrodynamical calculations shown in Fig. 3.1 [20]. One can see that the linear relation $\varepsilon_n \propto v_n$ clearly breaks down at the fourth harmonic. From the measurements of the symmetric cumulant $SC(4, 2)$ shown in Fig.1.4, we know that there is a strong correlation between the fourth and second harmonics, which is likely to be explained by the very prominent non-linear relation between ε_4 and v_4 . In this section, I will describe a formalism to further quantify the non-linear relations between various flow harmonics. This formalism forms the basis of the measurements in this thesis that will be presented in the final chapters.

3.3.1 Flow decomposition and mode coupling

A linear relation between ε_n and v_n can be explicitly expressed by

$$v_n e^{in\psi_n} = k \varepsilon_n e^{in\Phi_n}, \quad (3.13)$$

where k is a scaling factor. From the discussion above, we know that this is to a good approximation valid for $n \leq 3$. A qualitative analysis done in Ref. [71] indicates that an improved estimate for the higher harmonics can be obtained by adding a higher

order non-linear term. A trial indicates that such estimator for the fourth harmonic is a combination of ε_4 and ε_2^2 terms, i.e.

$$v_4 e^{in\psi_4} = k\varepsilon_4 e^{4i\Phi_4} + k'\varepsilon_2^2 e^{4i\Phi_2}. \quad (3.14)$$

Similarly, for the fifth harmonic,

$$v_5 e^{in\psi_5} = k\varepsilon_5 e^{5i\Phi_5} + k'\varepsilon_2 e^{2i\Phi_2} \varepsilon_3 e^{3i\Phi_3}. \quad (3.15)$$

The estimators in Eq. (3.14) and (3.15) provide a reasonable approximation across a wider centrality range, as opposed to (3.13) which gives a poor estimate in mid-central and peripheral collisions [71]. As a result, the higher harmonic flow can be expressed as a superposition of linear and non-linear contributions.

We then proceed to express the estimators in terms of the final state flow. Substituting the second harmonic estimator in Eq. (3.13) to Eq. (3.14), we get

$$v_4 e^{in\psi_4} = v_{4,L} e^{4i\psi_4} + \frac{k'}{k'^2} v_2^2 e^{2i\psi_2}. \quad (3.16)$$

Here $v_{4,L}$ denotes the fourth harmonic linear contribution. The linear contribution retains a linear relation to a cumulant-defined initial state anisotropy [72]

$$v_{4,L} e^{4i\psi_4} \propto \varepsilon_4' e^{i4\Phi_4'} = \varepsilon_4 e^{i4\Phi_4} + \frac{3\langle r^2 \rangle^2}{\langle r^4 \rangle} \varepsilon_2 e^{i4\Phi_2}, \quad (3.17)$$

whereas the total contribution for $n = 2, 3$ is linearly related to the classical definition in Eq. (1.2). Recalling that $V_n \equiv v_n e^{in\psi_n}$, one may rewrite the Eq. (3.16) as

$$V_4 = V_{4,L} + \chi_{4,22} V_2^2, \quad (3.18)$$

where $\chi_{4,22}$, called non-linear flow mode coefficient, has been chosen to quantify the non-linear response. The corresponding flow decomposition for a number of higher harmonics can be obtained similarly [73]

$$\begin{aligned} V_5 &= V_{5,L} + \chi_{5,23} V_2 V_3, \\ V_6 &= V_{6,L} + \chi_{6,222} V_2^3 + \chi_{6,33} V_3^2 + \chi_{6,24} V_2 V_{4,L}, \\ V_7 &= V_{7,L} + \chi_{7,223} V_2^2 V_3 + \chi_{7,34} V_3 V_{4,L} + \chi_{7,25} V_2 V_{5,L}, \\ V_8 &= V_{8,L} + \chi_{8,2222} V_2^4 + \chi_{8,233} V_2 V_3^2 + \mathcal{E}(V_{4,L}, V_{5,L}, V_{6,L}). \end{aligned} \quad (3.19)$$

Starting from the sixth harmonic, the number of possible lower harmonic contributions increases, which translates to added terms including those for the lower harmonic linear contributions. Here $\mathcal{E}(\dots)$ depicts the many higher harmonic linear contributions for the V_8 .

The linear and non-linear parts are separable, assuming that the respective contributions are uncorrelated [74], i.e. $\langle (V_2^*)^2 V_{4L} \rangle \simeq \langle V_2^2 V_{4L}^* \rangle \simeq 0$. Here the brackets denote an average over large sample of events and $*$ a complex conjugate. The assumption was experimentally tested in Ref. [75]. By mean-squaring the relations in

Eq. (3.19) over all events, and using the non-correlation, one derives an explicit expression for the linear part as

$$\underbrace{\langle |V_{4L}|^2 \rangle}_{\langle v_{4,L} \rangle}^{\frac{1}{2}} = \left(\underbrace{\langle |V_4|^2 \rangle}_{\langle v_4^2 \rangle} - \underbrace{\chi_{4,22}^2 \langle |V_2|^4 \rangle}_{\langle v_{4,NL}^2 \rangle} \right)^{\frac{1}{2}}. \quad (3.20)$$

The event-averaged linear contribution $\langle v_{4,L} \rangle$ is therefore experimentally measurable. One can further identify the non-linear contribution $\langle v_{4,NL}^2 \rangle \equiv \chi_{4,22}^2 \langle |V_2|^4 \rangle$ from Eq. (3.20). An expression for $\chi_{4,22}^2$ can be derived by multiplying Eq. (3.18) by $V_2^{(*2)}$:

$$\begin{aligned} V_4 &= V_{4,L} + \chi_{4,22} V_2^2 | \cdot V_2^{(*2)} \\ V_4 V_2^{(*2)} &= V_{4,L} V_2^{(*2)} + \chi_{4,22} V_2^2 V_2^{(*2)} \\ \langle V_4 V_2^{(*2)} \rangle &= \chi_{4,22} \langle |V_2|^4 \rangle \\ \chi_{4,22} &= \frac{\langle V_4 V_2^{(*2)} \rangle}{\langle |V_2|^4 \rangle} \\ &= \frac{\langle \langle \cos(4\varphi_1 - 2\varphi_2 - 2\varphi_3) \rangle \rangle}{\langle \langle \cos(2\varphi_1 + 2\varphi_2 - 2\varphi_3 - 2\varphi_4) \rangle \rangle} \\ &= \frac{\langle \langle 3 \rangle_{4,-2,-2} \rangle}{\langle \langle 4 \rangle_{2,2,-2,-2} \rangle}. \end{aligned} \quad (3.21)$$

Similar treatment can be given to higher harmonics in Eq. (3.19). The mode coupling coefficient for the fifth harmonic can be written as

$$\begin{aligned} \chi_{5,23} &= \frac{\langle V_5 V_2^* V_3^* \rangle}{\langle |V_2|^2 | |V_3|^2 \rangle} \\ &= \frac{\langle \langle \cos(5\varphi_1 - 2\varphi_2 - 3\varphi_3) \rangle \rangle}{\langle \langle \cos(2\varphi_1 + 3\varphi_2 - 2\varphi_3 - 3\varphi_4) \rangle \rangle} \\ &= \frac{\langle \langle 3 \rangle_{5,-2,-3} \rangle}{\langle \langle 4 \rangle_{2,3,-2,-3} \rangle}. \end{aligned} \quad (3.22)$$

The magnitude of the non-linear contribution for the fourth harmonic can be then written as $v_{4,22} \equiv \chi_{4,22}^2 \langle |V_2|^4 \rangle$, where we have defined $v_{4,22}$ as the harmonic projection of the fourth harmonic onto the direction of the second. While the $v_{n,mk}$ has the ability to describe, or in the best case predict the magnitude of the non-linear flow contribution, the $\chi_{n,mk}$ quantifies the strength of the non-linear response between harmonic orders. An important benchmark of a theory is its ability to predict the magnitude of v_n and $\chi_{n,mk}$ simultaneously.

For completeness, one more set of observables will be introduced, call the symmetry-plane correlations. As the name suggests, the symmetry-plane correlations measure the correlations between the directions of various flow harmonics. The lowest harmonic, measuring the correlation between fourth and second harmonic symmetry-planes, is defined as [76]

$$\rho_{4,22} = \frac{\langle V_4 V_2^{(*2)} \rangle}{\sqrt{\langle |V_4|^2 \rangle \langle |V_2|^4 \rangle}} = \frac{v_{4,22}}{v_4}. \quad (3.23)$$

The symmetry-plane correlations will be measured alongside the other observables. Techniques on how to practically measure these observables constructed from multi-particle correlations will be discussed next. Table 3.1 presents a summary of various observables and what they measure.

Table 3.1: Summary of flow observables and their properties.

Name	Symbol	Measure	Particular observed sensitivity
Flow coefficients	v_n	System expansion and anisotropy of the flow	Average $\langle \eta/s \rangle$ and $\zeta/s(T)$ peak
(Normalized) Symmetric cumulants	(N)SC(m, n)	Correlation between magnitudes of flow harmonics	$\eta/s(T)$ temperature dependence
Linear and non-linear contributions	$v_{n,L}, v_{n,mk}$	Magnitude of the linear and non-linear contributions to the v_n	(not tested)
Non-linear flow mode coefficients	$\chi_{n,mk}$	Quantification of the non-linear response	$\eta/s(T)$ at the freeze-out temperature
Symmetry-plane correlations	$\rho_{n,mk}$	Correlations between the directions of flow harmonics	(not observed)

3.4 Flow vector frameworks

Multiple methods to measure the correlations from particle azimuthal angles have been developed over the course of heavy-ion research. A traditional method in measuring the flow coefficients has been to use Eq. (3.3), either with reaction plane ψ_R or symmetry-planes ψ_n , directly i.e. by first estimating the orientation of the symmetry-plane with an event-plane estimate, evaluating Eq. (3.3), and finally correcting the result by calculating the event-plane resolution. This method, known as the event-plane method [16, 66], suffers from various biases and is not practical in measuring more advanced flow observables described in the previous section. Instead, efficient methods for calculating multi-particle correlations according to Eq. (3.8) will be examined.

A major practical issue with this Eq. (3.8) is the computational cost of calculating it, unless circumvented somehow. This is apparent by explicitly writing the expression for the average [77]:

$$\langle m \rangle_{n_1, n_2, \dots, n_m} = \frac{\sum_{\substack{k_1, k_2, \dots, k_m=1 \\ k_1 \neq k_2 \neq \dots \neq k_m}}^M w_{k_1} w_{k_2} \dots w_{k_m} \cos(n_1 \varphi_{k_1} + n_2 \varphi_{k_2} + \dots + n_m \varphi_{k_m})}{\sum_{\substack{k_1, k_2, \dots, k_m=1 \\ k_1 \neq k_2 \neq \dots \neq k_m}}^M w_{k_1} w_{k_2} \dots w_{k_m}} \quad (3.24)$$

where w_j are individual particle weights to correct for a non-uniform detector acceptance. On a machine, this translates to a total of m nested loops, i.e. a highly expensive $\mathcal{O}(M^m)$ algorithm, which becomes impossible to calculate repeatedly over a large number of events in a brute force approach.

3.4.1 Generic formulas

A better approach is to find the expressions of $\langle m \rangle_{n_1, n_2, \dots, n_m}$ in terms of products of sums of linear complexity. For this purpose, one first defines a flow vectors, also known as the Q-vector as [78]

$$Q_{n,p} = \sum_{k=1}^M w_k^p \cos(in\varphi_k), \quad (3.25)$$

so that $Q_{-n,p} = Q_{n,p}^*$. An approximate result for a correlation can be obtained by multiplying and normalizing the Q-vectors together, in which case the result will be biased by autocorrelations. This bias is generally non-negligible and needs to be removed. Furthermore, such approach does not correctly account for the weights for a non-uniform detector acceptance. I will therefore limit the discussion to the presentation of the complete and unbiased solutions used in the measurements in this thesis.

Multi-particle correlations without η -gap

The following solutions are given by the generic framework [77]. A two particle correlator, for which the autocorrelation has been removed and the detector non-uniform acceptance correctly treated, can be written as

$$\langle 2 \rangle_{n_1, n_2} = \frac{Q_{n_1,1} Q_{n_2,1} - Q_{n_1+n_2,2}}{Q_{0,1}^2 - Q_{0,2}}. \quad (3.26)$$

A three-particle correlator, used extensively by the non-linear flow mode observables, one can write as

$$\begin{aligned} \langle 3 \rangle_{n_1, n_2, n_3} &= Q_{n_1,1} Q_{n_2,1} Q_{n_3,1} - Q_{n_1+n_2,2} Q_{n_3,1} - Q_{n_2,1} Q_{n_1+n_3,2} \\ &\quad - Q_{n_1,1} Q_{n_2+n_3,2} + 2Q_{n_1+n_2+n_3,3} \\ &\quad / (Q_{0,1}^3 - 3Q_{0,2} Q_{0,1} + 2Q_{0,3}). \end{aligned} \quad (3.27)$$

Finally, a four-particle correlation, found in symmetric cumulants and for some very high harmonic non-linear flow observables, is

$$\begin{aligned} \langle 4 \rangle_{n_1, n_2, n_3, n_4} &= Q_{n_1,1} Q_{n_2,1} Q_{n_3,1} Q_{n_4,1} - Q_{n_1+n_2,2} Q_{n_3,1} Q_{n_4,1} - Q_{n_2,1} Q_{n_1+n_3,2} Q_{n_4,1} \\ &\quad - Q_{n_1,1} Q_{n_2+n_3,2} Q_{n_4,1} + 2Q_{n_1+n_2+n_3,3} Q_{n_4,1} - Q_{n_2,1} Q_{n_3,1} Q_{n_1+n_4,2} \\ &\quad + Q_{n_2+n_3,2} Q_{n_1+n_4,2} - Q_{n_1,1} Q_{n_3,1} Q_{n_2+n_4,2} + Q_{n_1+n_3,2} Q_{n_2+n_4,2} \\ &\quad + 2Q_{n_3,1} Q_{n_1+n_2+n_4,3} - Q_{n_1,1} Q_{n_2,1} Q_{n_3+n_4,2} + Q_{n_1+n_2,2} Q_{n_3+n_4,2} \\ &\quad + 2Q_{n_2,1} Q_{n_1+n_3+n_4,3} + 2Q_{n_1,1} Q_{n_2+n_3+n_4,3} - 6Q_{n_1+n_2+n_3+n_4,4} \\ &\quad / (Q_{0,1}^4 - 6Q_{0,1}^2 Q_{0,2} + 3Q_{0,2}^2 + 8Q_{0,1} Q_{0,3} - 6Q_{0,4}). \end{aligned} \quad (3.28)$$

All Q-vectors can be numerically calculated in one loop over the particle azimuthal angles, and the implementation stays optimal.

Multi-particle correlations with η -gap

While the correlators above resolve the issues of autocorrelation and non-uniform acceptance, they might still be sensitive to nonflow effects in experimental setting. Observables such as the cumulants and the symmetric cumulants inherently resolve the nonflow issue with their nonflow suppressing construction. However, large majority of the observables including the v_n and the non-linear flow modes do not have the nonflow suppressing properties and they are affected by the nonflow that comes with the correlators in Eq. (3.26)–(3.28) [12].

Studies have shown [79] that vast majority of the nonflow arises from the short-range correlations by resonance decays and jet contributions, in other words at the low pseudorapidity (η) region. A straightforward solution is therefore to ensure that no pair or higher order combination of particles are correlated within this small- η region. This is achieved by a splitting of the event into subevents, separated by one or more η -gaps, effectively excluding the η -region prone to nonflow from the analysis.

It has been shown [80] that two subevents is generally sufficient to remove the major nonflow contribution, as most of the time possible sources of nonflow produce particles within these two subevents only, regardless of how many are used. Any remaining contribution can be further removed by increasing the number of subevents, however, studies have shown the benefit to be very minor. As a consequence, the nonflow arising in some higher order correlations such as the three-particle correlator will be considered negligible. The magnitude of these small contributions are estimated with studies of systematic uncertainty.

In case of two subevents separated by one η -gap, one will calculate two Q-vectors using Eq. (3.25), one for negative η -region and another for positive η -region, including particles only from that side. The corresponding Q-vectors for the two regions will be interchangeably labeled $Q_{n,p}^A$ and $Q_{n,p}^B$. The addition of a η -gap will result in modified expression for the correlators. For two-particle correlator, the expression becomes

$$\langle 2 \rangle_{n_1, n_2}^{\text{Gap}} = \frac{Q_{n_1,1}^A Q_{n_2,1}^B}{Q_{0,1}^A Q_{0,1}^B}, \quad (3.29)$$

for which the autocorrelation is taken care by the η -gap, and need not to be explicitly subtracted. The higher correlations still need a subtraction of the autocorrelation. A three-particle correlator for which $n_1 = n_2 + n_3$ can be written as

$$\langle 3 \rangle_{n_1, n_2, n_3}^{\text{Gap}} = \frac{Q_{n_1,1}^A Q_{n_2,1}^B Q_{n_3,1}^B - Q_{n_1,1}^A Q_{n_2+n_3,2}^B}{Q_{0,1}^A ((Q_{0,1}^B)^2 - Q_{0,2}^B)}. \quad (3.30)$$

The four-particle correlator for $n_1 = n_2 + n_3 + n_4$ is

$$\begin{aligned} \langle 4 \rangle_{n_1, n_2, n_3, n_4}^{\text{Gap}} = & Q_{n_1,1}^A Q_{n_2,1}^B Q_{n_3,1}^B Q_{n_4,1}^B - Q_{n_1,1}^A Q_{n_2+n_3,2}^B Q_{n_4,1}^B \\ & - Q_{n_1,1}^A Q_{n_3,1}^B Q_{n_2+n_4,2}^B - Q_{n_1,1}^A Q_{n_2,1}^B Q_{n_3+n_4,2}^B \\ & + 2Q_{n_1,1}^A Q_{n_2+n_3+n_4,3}^B \\ & / (Q_{0,1}^A ((Q_{0,1}^B)^3 - 3Q_{0,2}^B Q_{0,1}^B + 2Q_{0,3}^B)). \end{aligned} \quad (3.31)$$

In the measurements for this thesis, equations (3.29)–(3.31) shall be used for all observables. The symmetric cumulants, although not measured in this work, use equations (3.28) and (3.26).

Chapter 4

Experimental Setup

4.1 CERN

Established in 1954, The European Organization for Nuclear Research (CERN) is the operator of the largest particle physics and accelerator laboratory in the world. Located in the vicinity of Geneva near the border between France and Switzerland, the laboratory employs more than 2500 personnel, with over 12000 visiting scientists each year. The operation of CERN is supported by its present 23 member states.

4.2 Large Hadron Collider

The Large Hadron Collider (LHC) [82] is the main accelerator ring of CERN. With a circumference of 26.7 km, it is currently the largest operational particle accelerator in the world, capable of delivering single beams in counter rotating two beam pipes with half the energy of up to 14 TeV and 5.02 TeV per nucleon for protons and heavy-ions, respectively. LHC has a design luminosity of $10^{34} \text{ cm}^{-2}\text{s}^{-1}$, which has already been exceeded a number of times with the record being about double this value. The key parameters for LHC are summarized in table 4.1 [83].

LHC can not accelerate particles from standstill to ultra-relativistic velocities on its own. Rather, particle beams undergo several pre-acceleration stages before their injection into the main ring for final acceleration. LHC receives its beams from the smaller and predecesing Super Proton Synchrotron (SPS), in which the protons are accelerated to 450 GeV before their injection to LHC. SPS, in turn, is supplied by Proton Synchrotron (PS) with beam energies of 25 GeV. Depending on the type of beam, this chain of acceleration stages is then retraced from PS to PS Booster (1.4 GeV) in case of protons, and finally to the linear accelerator LINAC2 (50 MeV) that accelerates the particles provided by a proton source. During heavy-ion physics runs, PS is supplied by Low Energy Ion Ring (LEIR) before initially accelerated by the corresponding linear accelerator LINAC3 from the ion source.

The acceleration of particles in LHC is based on its RF cavities along the accelerator ring [84]. When the oscillation of the electromagnetic fields produced by the RF cavities is synchronized with the circulation of the charged particles in the ring, the particles experience a net forward acceleration. Entry of the particle bunches must therefore be synchronized properly in order to begin the acceleration. During the

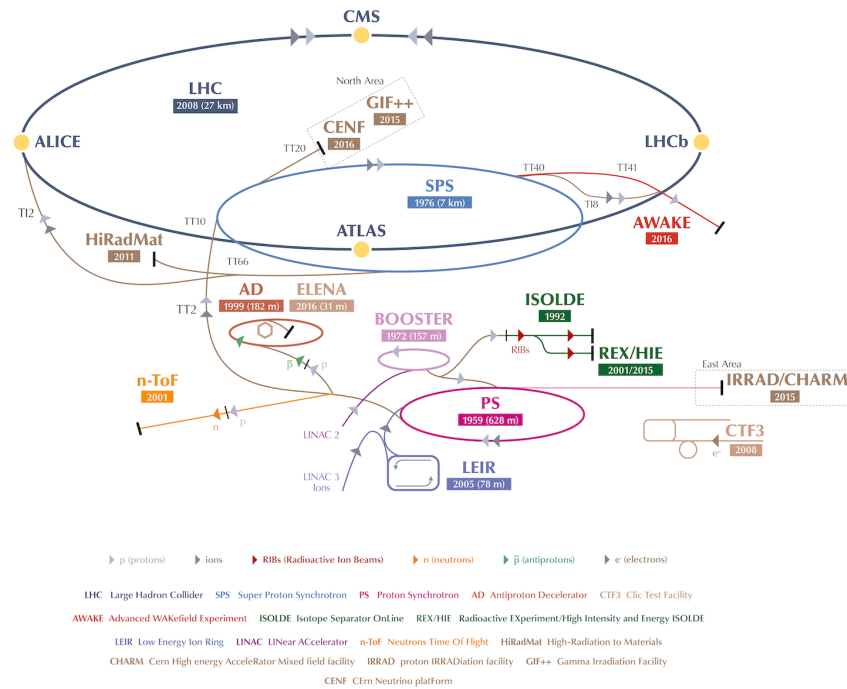


Figure 4.1: CERN collider complex [81].

Table 4.1: LHC key design parameters. [83]

Parameter	Value
Circumference	26.7 km
Dipole operating temperature	1.9 K
Main RF System	400.8 MHz
No. of magnets	9300
No. of dipoles	1232
No. of quadrupoles	858
Nominal energy, protons	7 TeV
Momentum at injection	450 GeV/c
Peak magnet dipole field	8.33 T
Minimum distance between bunches	~7 m
Bunch spacing	25 ns
Design Luminosity	$10^{34} \text{ cm}^{-2} \text{ s}^{-1}$
No. of bunches / proton beam	2808
Beam lifetime	10 h
No. of collisions per second	600 millions
Beta function β^*	0.55 m

runs, the oscillation of the RF cavities is tuned for a certain particle species to achieve specific energies. When a particle approaches the target energy, the accelerating force on the particle diminishes. Likewise, a particle with too much energy during some phase of the acceleration will get decelerated. As a result, the particles will get accelerated in distinct bunches, of which in LHC there can by design be simultaneously 2808. The RF cavities in LHC oscillate at the frequency of 400.8 MHz, resulting in a

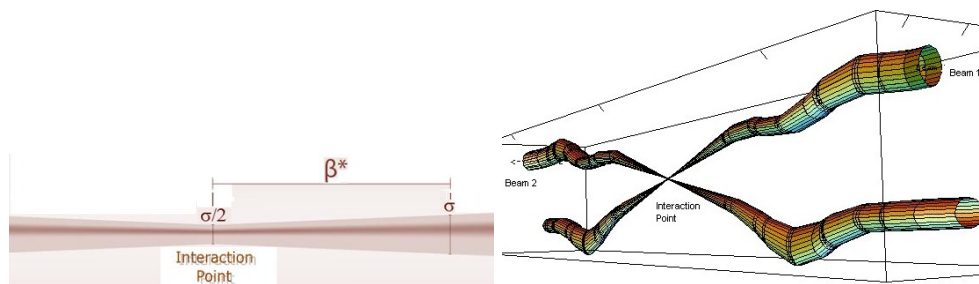


Figure 4.2: β^* (left) and the beam crossing at the interaction point (right) [88].

theoretical bunch separation of 2.5 ns. In practice however, only 10% of the detector bunch capacity is used, increasing the actual separation to 25 ns.

The beam in the accelerator is guided with powerful superconducting electromagnets. In order to maintain the circular orbit, LHC has 1232 dipole magnets, each producing a 8.33 T magnetic field required by a 7 TeV proton beam [85]. Additionally, LHC has 858 quadrupole magnets to keep the beam focused while traveling inside the accelerator pipe, and a further 7210 higher multipole magnets for beam adjustment, totaling the number of magnets in LHC to 9300.

To describe the confinement of a particle bunch in the beam, a quantity called beam emittance ε is used [86,87]. The smaller the beam emittance, the more confined the particle bunch, i.e. distances between the particles are smaller and their energies are closer between each other. Emittance defines the smallest area $A = \pi\varepsilon$ a beam can be squeezed through [87]. A highly confined bunch is more easily able to pass through the beam transport system, and more likely to collide with the opposite beam at the interaction point. The emittance can be used to express a so-called amplitude function:

$$\beta = \frac{\pi\sigma^2}{\varepsilon}, \quad (4.1)$$

where σ is the cross-sectional size of the bunch. The amplitude function at the interaction point is referred to as β^* . At the experiments, the β^* is minimized in order to yield the highest possible collision rate. The collision rate can be expressed by luminosity

$$\mathcal{L} \sim \frac{fN^2}{4\varepsilon\beta^*} \quad (4.2)$$

A high luminosity at the interaction point is therefore achieved by providing large particle bunches of population N , at low emittance while maximizing the frequency at which these bunches arrive.

β^* must be accurately controlled to maximize the luminosity and to also avoid significant imbalances between the experiments. Future regimes of operations and the upgrade to the high luminosity LHC (HL-LHC) will run at lower β at 0.15 m and higher luminosities [89].

Figure 4.3 presents the integrated (cumulative) luminosity of LHC in 2018 during the last proton physics runs before Long Shutdown 2 (LS2) [90]. The achieved luminosity at the end of the run corresponds to the highest luminosity reached so far.

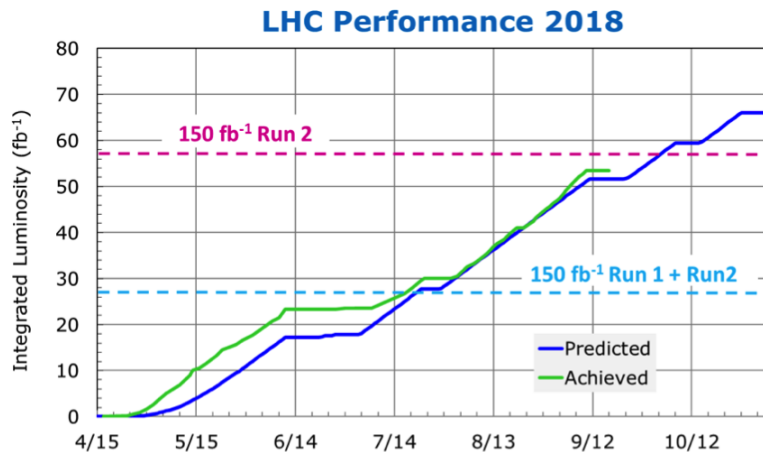


Figure 4.3: LHC performance before LS2 [90].

4.2.1 LHC experiments

LHC provides beams to a total of four large experiments along its accelerator ring: ALICE [91, 92], ATLAS [93], CMS [94] and LHCb [95]. Out of these, ALICE (A Large Ion Collider Experiment) is the only experiment primarily dedicated to heavy ion physics. The foremost contribution of ALICE is the study of properties of the strongly interacting matter, quark-gluon plasma.

On the other hand, ATLAS (A Toroidal LHC ApparatuS) and CMS (Compact Muon Solenoid), the two largest experiments at CERN, are multipurpose experiments designed to be capable of a wide range physics experiments. The measurements from the ATLAS and CMS experiments cover a vast array of topics. The most well known contribution is the discovery of the Higgs boson in 2012 [96, 97].

Finally, LHCb (LHC beauty) serves to study the physics of the bottom “beauty” quark. Above all, this involves the measurement of CP violation parameters with decays of hadrons via the bottom quark. One of the major contributions of LHCb is the confirmation of $B_s^0 \rightarrow \mu^+ \mu^-$ decay [98, 99], which is a verification of one of the mechanisms predicted by the Standard Model.

Furthermore, LHC houses three smaller experiments: LHCf [100], TOTEM [101] and MoEDAL [102]. LHCf (LHC forward) is located at point 1 alongside with the ATLAS experiment, where it emulates cosmic rays by particles emitted forward at the ATLAS interaction point. TOTEM (TOTAl Elastic and diffractive cross section Measurement) is located at point 5 together with CMS, where it operates on the production from the CMS interaction point at small angles for various cross-section measurements. MoEDAL is stationed at point 8 by the LHCb experiment. The aim of the MoEDAL experiment is to detect and measure signals of hypothetical magnetically charged particles.

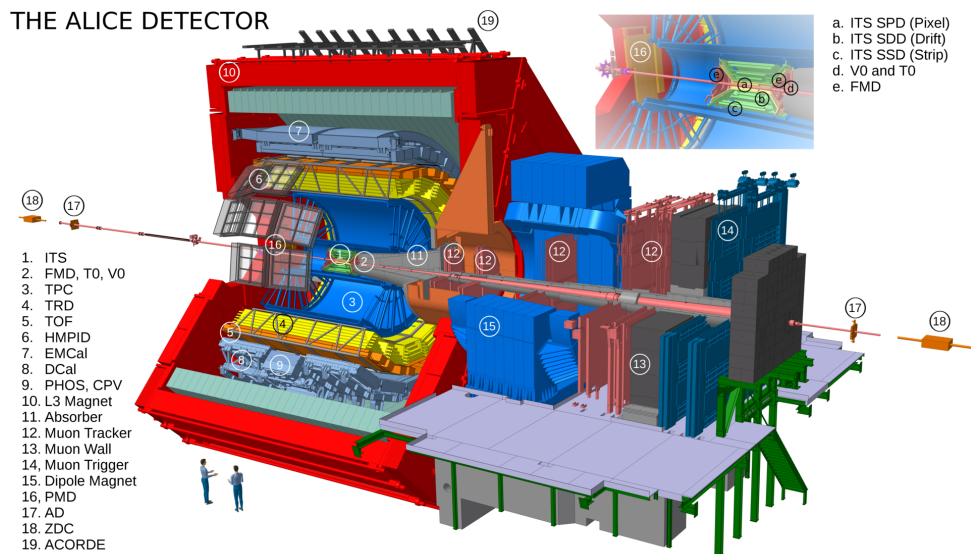


Figure 4.4: Schematic view of the ALICE detector during Run 2.

4.3 ALICE

ALICE (A Large Ion Collider Experiment) is the dedicated heavy-ion experiment at LHC. The primary design goals of the ALICE detector subsystems are the readiness for the very high number of particles produced in simultaneously colliding heavy ions, high momentum resolution especially at low- p_T regions, and superior particle identification capabilities [91, 92].

Figure 4.4 presents a schematic overview of the ALICE detector. During Run 2, the ALICE detector consisted of 24 individual detectors for various purposes and physics analyses. Ordered from the inner center towards the outer layers, some of the notable innermost detectors utilized in this thesis are

- Inner Tracking System (ITS) [91, 103, 104]
- V0 [105]
- Time Projection Chamber (TPC) [106]
- Time of Flight (TOF) [107].

The layered arrangement of the detectors from the center close to the interaction point up to the outer ranges of the structure ensures that as much information as possible is captured from the particles produced in an event. The tracking detectors are located closest to the center in order to accurately locate the primary interaction vertex, as well as to have a high quality representation of the charged particle tracks. Placement of the tracking detectors in the inner layers also ensures that the loss of particles due to interaction in the detectors is minimized before reaching the outer layer detectors. Since the loss of particles is low in the particle identification detectors, they are placed immediately after the tracking detectors. On the other hand, calorimeters are located on the outer layer, since the particle energy is measured by absorption, and thus, loss of the particle. The V0 detectors are used for selecting minimum bias

events and for the determination of the collision centrality. TOF information is used to remove background events from beam interactions with the residual gas molecules in the beam pipe and pileup events. The main role and features of the listed detectors are described in the following sections and in Ref. [1,3] attached to this thesis. More detailed description of the tracking detectors TPC and ITS is given in following sections.

4.3.1 Tracking detectors

ALICE operates on several high granularity tracking detectors, designed to handle extremely high particle multiplicities produced in heavy ion collisions. In the original design before LHC started, the tracking system was prepared to handle an estimated 8000 charged particles per rapidity unit, although the real value turned out much smaller, around 1600.

Time Projection Chamber (TPC)

The main tracking detector in ALICE is the Time Projection Chamber (TPC) [106], which is supported by the Inner Tracking System (ITS) [103,104] composed of a few detector subsystems. The purpose of the TPC is to provide an accurate 3-dimensional track representation for as many particles as possible. Information from the TPC enables one to determine the momentum at which a particle was emitted, as well as identification details based on its energy loss and curvature in the magnetic field.

The TPC is a large $5 \times 5 \text{ m}^2$ cylindrical gas detector filled with 90 m^3 of Ne/CO₂/N₂ (90/10/5) gas mixture. The operation of the TPC is based on the ionizing effect of the particles that traverse through its gas volume. As the particles travel through the TPC, they ionize the fill gas, leaving behind a trail of electrons separated from their gas molecules. A longitudinal 400 V/cm electric field created by a 100 kV potential in both sides of the TPC cage will accelerate the electrons towards the end plates, projecting them on to a 2D-location (r, φ) corresponding to the original point of ionization (r, φ, z) . At the end of the plates, the anode wires of the Multi-Wire Proportional Chamber (MWPC) based detectors measure the number of avalanching electrons after the amplification. Since the drift velocity of the electrons in the electric field is mostly constant due to their collisions with the gas molecules, a time of drift can be obtained, which then translates to a distance giving the z -coordinate of the interaction. The maximum drift time of the electrons in a 100 kV potential is about $94 \mu\text{s}$, which poses a significant bottleneck in the maximum achievable luminosity. Figure 4.5 presents the structure of the TPC field cage.

The particle detectors at the end plates are arranged in 18 sectors. Each sector in turn consists of four readout chambers, with two inner (IROC) and two outer readout chambers (OROC). There are 159 of these chambers in radial direction between the inner radius of the detector 0.85 m to the outer 2.5 m. During Run 2, these detectors were based on the Multi-Wire Proportional Chamber (MWPC) technology [108], which has been applied in several TPC trackers prior that of ALICE.

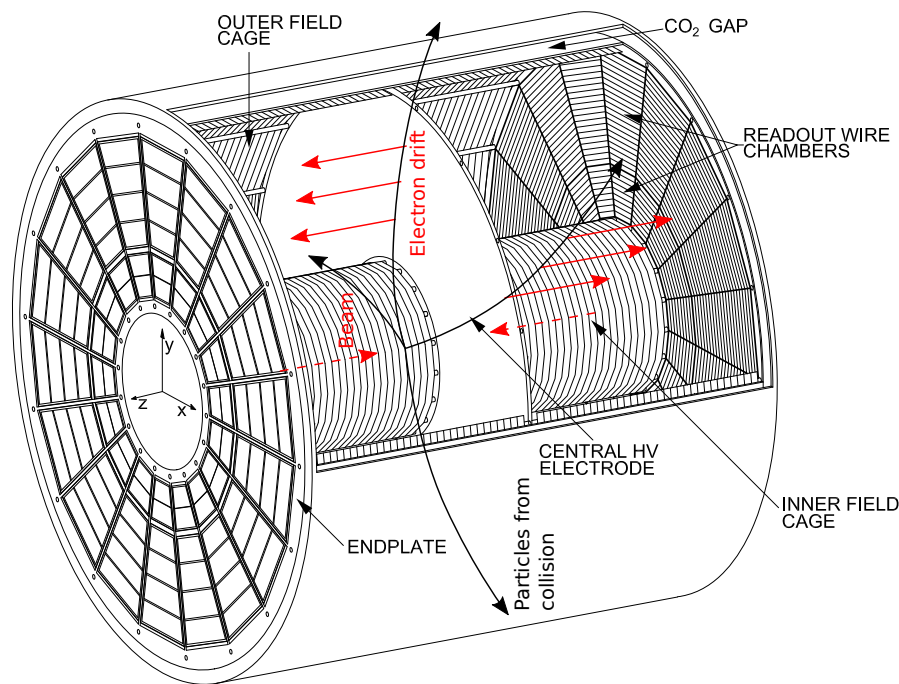


Figure 4.5: TPC field cage [106]. The particles emitted from the collision events are sketched with black arrows. The electron drift from the gas ionization used to track these particles is drawn in red arrows. Reprinted with permission from Elsevier.

Inner Tracking System (ITS)

The Inner Tracking system (ITS) [103,104] is an array of silicon based detectors located closest to the interaction point and encapsulated by the TPC. The ITS is responsible for the primary and secondary vertex reconstruction, triggering input, as well as high resolution particle tracking within close proximity of the interaction point, thus assisting TPC for an improved overall track reconstruction performance.

Out of the total six layers of ITS detectors, three groups of two layers each serve also a specialized purpose. The innermost two layers, Silicon Pixel Detectors (SPD), consist of a highly dense matrix of 8192 silicon detector diode cells, which provide a sufficient two-dimensional resolution to resolve the extremely large particle track density observed at a minimum range of 3.9 cm to heavy ion collisions. The following two layers, Silicon Drift Detectors (SDD), operate on a slightly different principle. In this case, particle hits within its total of 260 silicon drift cells can be accurately located by measuring the resulting charge carrier drift time and velocity within the cell. Additionally, SDD provides a particle identification (PID) capability through the measurement of the number of charge carriers corresponding to some dE/dx of the passing particle. Like SPD, the SDD provides highly accurate particle tracking capable of resolving high particle track densities. The last two layers of the ITS are the Silicon Strip Detectors (SSD). The SSD is constructed from a grid of $2.61 \cdot 10^6$ intervening silicon strips, which signal a particle hit similarly as the silicon pixels. The location of a particle hit is obtained from the intersection point of two unaligned, overlapping silicon strips. As with SDD, dE/dx information is provided by counting the charge

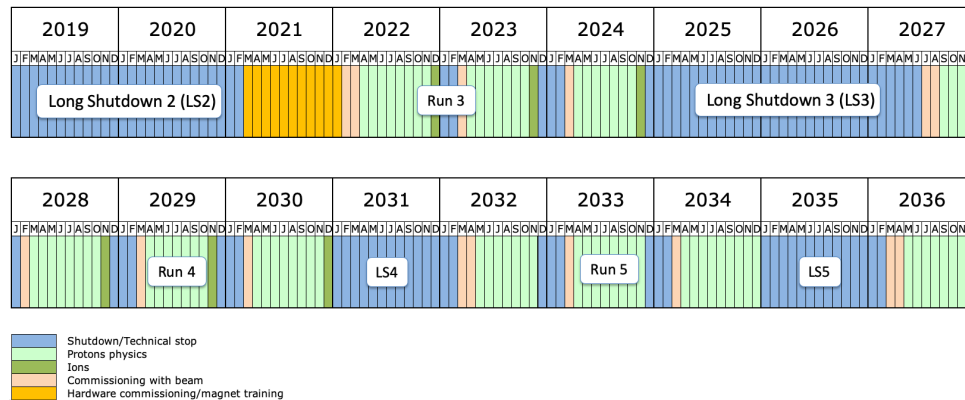


Figure 4.6: The LHC long term schedule [109]. Commissioning for the Run 3 is expected to end at the end of 2021, while Run 3 data taking with proton physics may start 2022. The first heavy-ion run during Run 3 is expected to take place at the end of 2022.

carriers. Together with SDD, the SSD provides a total of four layers of energy loss and PID measurement within the ITS. The SSD also plays a vital role in matching the particle tracks with those recorded by the TPC, forming the prerequisites for hybrid tracking between ITS and TPC.

4.4 TPC upgrade

Figure 4.6 presents the LHC running schedule [109]. The beginning of 2022 will mark the end of Long Shutdown 2 (LS2), and the LHC and ALICE experiment will enter the Run 3 data taking period (2022-2024). Several detector subsystems will be upgraded, including improved readout electronics and DAQ systems. During the 2-year shutdown period, the improvements done on the LHC will enable it to run at almost designed collision systems. The primary effect of the upgrade projects is the significantly improved luminosity, which allows physicists to perform increasingly higher-precision measurements with an order of 100 times larger data that can be collected.

A major upgrade of the ALICE Time Projection Chamber (TPC) will increase the readout rate of the detector by about two orders of magnitude. The current readout, based on multi-wire proportional-chamber (MWPC) technology [108], will not be able to cope with increased interaction rates. In order to remedy this, the MWPCs will be replaced with multi-stage gas electron multiplier (GEM) chambers [110,111].

4.4.1 GEM based readout chambers

The current MWPC based system limits the readout rate to 3.5 kHz [112]. However, an interaction rate of 50 kHz is expected for the Pb–Pb periods after the luminosity upgrade of the LHC during LS2. In order to operate the experiment at these interaction rates, the MWPC based TPC readout chambers will be replaced by GEMs, allowing a continuous readout of the TPC [111]. The details of this upgrade are described in [113]. The key elements of the upgrade and quality assurance of the GEM foils

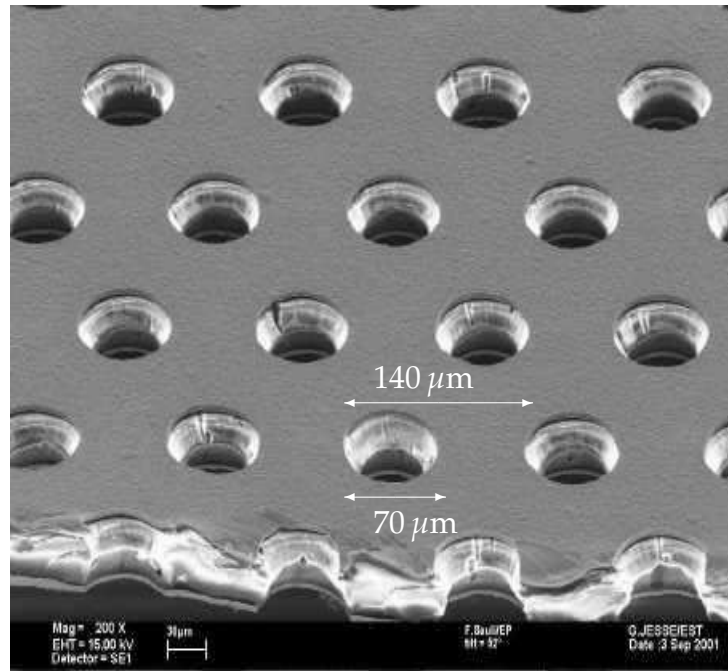


Figure 4.7: Scanning electron microscope (SEM) picture of a GEM foil. [110, 114]. Reprinted from Ref. [110] with permission from Elsevier.

work that was performed by the author are summarized next.

Figure 4.7 presents a scanning electron microscope (SEM) picture of a GEM foil [110]. By construction, GEM is a $\sim 50 \mu\text{m}$ thick capton insulator foil layered between two, fractionally thin $\sim 5 \mu\text{m}$ conductive copper surfaces. The foil is etched to carry equally spaced microscopic holes at a density of $50\text{--}100 \frac{1}{\text{mm}^2}$, whose diameter $40\text{--}120 \mu\text{m}$ varies according to the requirements for the detector. Each foil is segmented into $18\text{--}24$ sectors in order to yield a good position resolution – between these sectors there are no holes. A potential difference of 200 V to 400 V between the conductive surfaces of the GEM foil is sufficient to cause an electron avalanche multiplication inside the holes. In the final assembly, there will be 4 layers of GEM foils. The foils are stacked such that the holes between the layers do not align. Furthermore, the density of the holes varies from one layer to another: the density is higher in the two middle layers, while the outer layers present a lower density. The purpose of this layering is to reduce ion backflow, which distorts the electric field in the drift volume thus possibly affecting the drift of the incoming further electrons.

4.4.2 Quality assurance of GEM foils

Before installing of the new GEM based detectors into the TPC cage and the eventual commissioning, flawless quality and operation of the manufactured foils has to be ensured. During the quality assurance (QA) phase of the production, the foil undergoes an extensive set of tests in order to find potential defects [115]. In the QA process, defective foils are discarded, while foils that pass the tests move forward to the installation phase. In this section, a brief overlook to the GEM QA process is given, and particularly to that performed at the Helsinki Detector Laboratory.

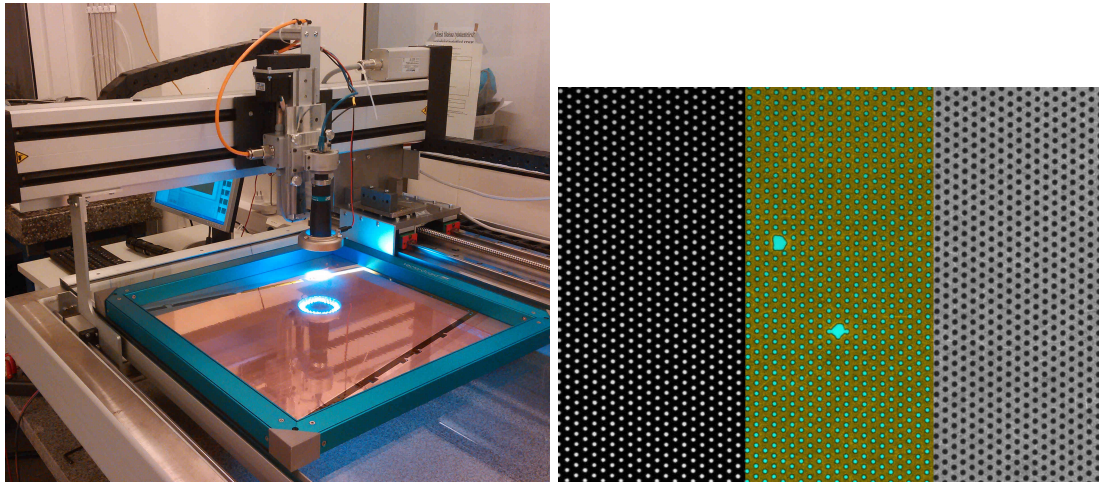


Figure 4.8: Left: High resolution optical scanner at the Helsinki Institute of Physics clean room. Right: An image taken by the optical scanner in two exposure mode. The left-most image presents the scan with background light only, while the right-side image represents the same scan with foreground light only. The combined image into two color channels is shown in the middle. Figure from [116].

Advanced quality assurance (QA-A)

The foils are manufactured at CERN, after which they are subjected to a basic quality assurance process (QA-B). During this step, the foils are optically inspected in order to find any major defects, as well as tested for leakage currents with high voltages. Once passed, the foils are sent forward for advanced QA testing (QA-A) at Helsinki Institute of Physics (HIP) or Wigner Research Centre in Budapest. Details of the QA-A process at HIP are given in Ref. [117]. I will briefly overview the QA-A process at HIP.

The QA-A primarily consists of high-resolution optical scan and a long term high voltage (HV) test. The high-resolution scan is able to distinguish the microscopic hole structure that is not visible during the basic QA. The optical scanning is performed by a scanning robot (pictured in Fig. 4.8 left) which sweeps through the entire area of the foil segments, photographing it 11.3×8.5 mm area at a time. The resulting imagery (Fig. 4.8 right) is then passed to a software filter for hole detection, and consequently analysed by a neural network based classification algorithm, trained to classify holes and defects. Based on the results, the foil is then passed or rejected by an entry to a foil measurement database, along with a map of the foil's surface attributes and defects. One such map is presented in Fig. 4.9, depicting the inner hole sizes of a foil. This important QA step ensures the uniformity and flawlessness in the hole sizes and arrangement, as these attributes are directly connected to the foil's gain properties.

During the HV test, the foil is subjected to a high voltage of at least 500 V. The test will last 5 to 12 hours for daytime or overnight testing, respectively. Each segment is individually monitored and measured for leakage currents. A failure is triggered if the current exceeds 160 pA at any point of the test. The foil may be retested after carefully cleaning it, however, a second failure often rejects the foil as defective, in which case it is sent back for repairing.

The workflow includes the operation of the scanning robot, as well as conduction

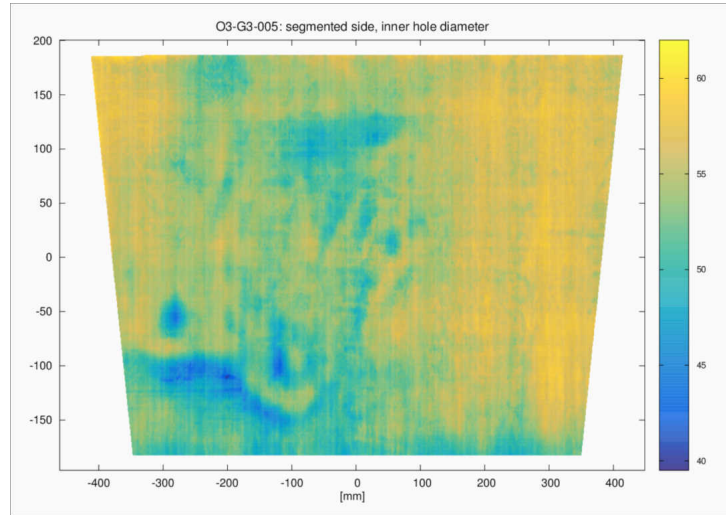


Figure 4.9: Polyimide hole diameters, also known as the inner hole diameter, mapped by the analysis on the foil imagery [117].

Table 4.2: QA criteria [115]. The criteria for the basic QA, conducted at CERN, is listed on the second column of the table. Optical and the long-term stability QA criteria are given in the subsequent columns. Finally, gain scanning QA criteria is given in the last column.

Criteria	Basic	Optical			Long-term stability	Gain scanning
	I_{leak}	inner/outer RMS	rim mean	inner/outer deviation	I_{leak}	uniformity
Green	< 500 pA	< 4 μm	< 15 μm	< 5 μm	< 500 pA	< 10%
Yellow	n/a	n/a	15-19 μm	5-10 μm	< 500 pA / non stable	> 10%
Orange	n/a	> 4 μm	> 19 μm	> 10 μm	n/a	n/a
Red	> 500 pA	n/a	n/a	n/a	> 500 pA	n/a

of the HV testing. Furthermore, the work includes maintaining and programming a foil map plotting and labeling software for information entry to the foil measurement database. Based on the QA results given by the HV test and the analysis of the foil imagery, the classification of the foil is given according to the QA criteria given in table 4.2 with a color code. Here, green color means that the foil has passed all tests, and qualifies to be installed on TPC for commissioning. Red color means that the foil has failed the basic QA, and will not be used. Finally, yellow and orange color means that the foil has failed the advanced QA, but could still be used if repaired, or if the green foils run out for installing.

At the time of writing this thesis, all foils have been installed to the ALICE TPC, and the upgraded tracking detector was installed in the experiment in August 2020, commissioned ready for Run 3 of data collection in 2022.

Chapter 5

Analysis

5.1 Experimental Setup and Data Analysis

In this chapter, the analysis datasets will be described, and the event and track selection outlined for each respective dataset. A summary of the datasets produced by ALICE is given in table 5.1. During Run 1 and Run 2 of LHC operation, several datasets consisting of pp, p–Pb, Pb–Pb and Xe–Xe collisions at various center of mass energies have been recorded. All experimental results introduced in this thesis are measured from the Pb–Pb heavy ion collision dataset recorded during Run 2 in 2015. While this 2015 dataset will be the primary focus in this thesis, I will also briefly describe the newer and larger 2018 Pb–Pb dataset which will be used in future analyses.

Table 5.1: Summary of datasets. The integrated luminosities are from ALICE.

Run 1 (2009-2013)			Run 2 (2015-2018)		
pp	0.90 TeV	$\sim [200]\mu b^{-1}$	pp	5.02 TeV	$\sim [1.3]pb^{-1}$
	2.76 TeV	$\sim [100]nb^{-1}$		13.00 TeV	$\sim [25]pb^{-1}$
	7.00 TeV	$\sim [1.5]pb^{-1}$	p–Pb	5.02 TeV	$\sim [3]nb^{-1}$
	8.00 TeV	$\sim [2.5]pb^{-1}$		8.16 TeV	$\sim [25]nb^{-1}$
p–Pb	5.02 TeV	$\sim [15]nb^{-1}$	Xe–Xe	5.44 TeV	$\sim [0.3]\mu b^{-1}$
Pb–Pb	2.76 TeV	$\sim [75]\mu b^{-1}$	Pb–Pb	5.02 TeV	$\sim [1]nb^{-1}$

5.1.1 Event Selection

The data sample consists of about 42M and 200M minimum bias Pb–Pb collisions (events) at $\sqrt{s_{NN}} = 5.02$ TeV recorded during Run 2 in 2015 and 2018, respectively. An event is triggered by combined signals from the two scintillator arrays, V0A and V0C [91, 105], covering the pseudorapidity intervals $2.8 < \eta < 5.1$ and $-3.7 < \eta < -1.7$, respectively. A primary vertex position less than 10 cm from the nominal interaction point along the beam axis for all reconstructed events is required. The event is discarded as pile-up if it does not fall in to the multiplicity correlation between V0 and the first SPD layer [91, 104]. For out-of-bunch pile-up removal a correlation between the multiplicity estimates from SPD with those imposed with a TOF readout is required.

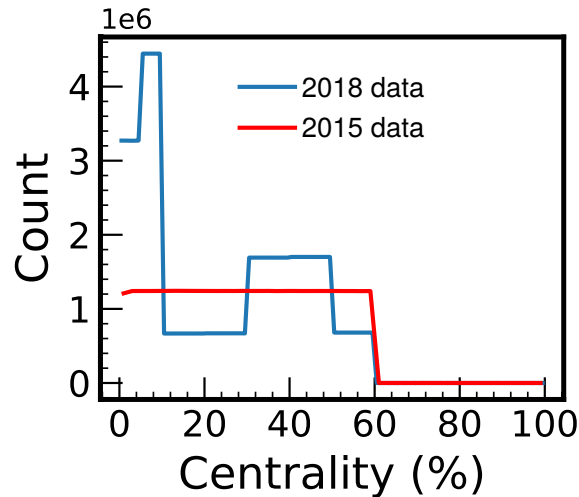


Figure 5.1: Centrality distribution between the 2015 and 2018 Pb–Pb datasets. In the case of the 2018 data, the centrality distribution has been corrected.

The centrality of the collision is determined based on information from the V0 arrays. The details of the centrality determination at ALICE are outlined in [118]. This analysis uses events only within the centrality range of 0 to 60%. The resulting centrality distribution for the 2015 and 2018 Pb–Pb data is presented in Fig. 5.1. In the case of the 2015 data, the centrality distribution is mostly flat. Due to centrality triggering, this is not the case for the 2018 data, where the number of events in each centrality class varies significantly. Because of this uneven centrality distribution of the 2018 data, a centrality flattening has been imposed by randomly rejecting events according to an inverse distribution specific to each centrality range.

5.1.2 Track Selection

The track reconstruction is based on combined information from the Time Projection Chamber (TPC) [91, 106] and the Inner Tracking System (ITS) [91, 104] in a tracking scheme called “hybrid” tracking. The contributions from the secondary particles are avoided by requiring the tracks to have a distance of closest approach (DCA) to the primary vertex of less than 3.2 cm and 2.4 cm in the longitudinal and transverse directions, respectively. Such a loose DCA track cut is chosen to improve the uniformity of the φ -distribution for the Q-vector calculation. At least 70 TPC space points are required for each track out of the maximum 159, as well as the average χ^2 per degree of freedom of the track fit to the TPC space points to be less than 2. Minimum two hits are required in the ITS. The unwanted effects of track reconstruction efficiency and contamination from secondary particles [119] are avoided by employing a HIJING simulation [120, 121] with GEANT3 [122] detector model to construct a p_T -dependent track weighting correction. The track reconstruction efficiency is approximately 65% at $p_T = 0.2 \text{ GeV}/c$ and 80% at $p_T > 1.0 \text{ GeV}/c$, while the contamination from secondaries is less than 10% and 5%, respectively. Efficiency, contamination and the final correction factor as a function of p_T in 20-40% centrality class are presented in Fig. 5.4. Only particle tracks within the transverse momentum interval $0.2 < p_T < 5.0 \text{ GeV}/c$

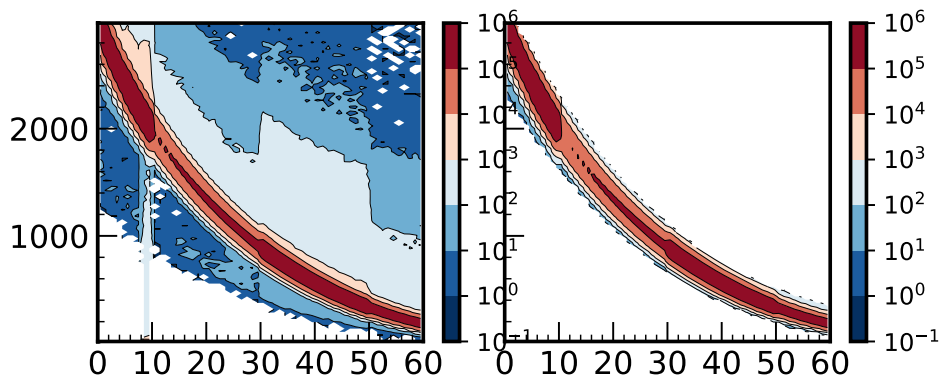


Figure 5.2: V0M and CL0 multiplicity correlation, before (left) and after (right) the outlier removal.

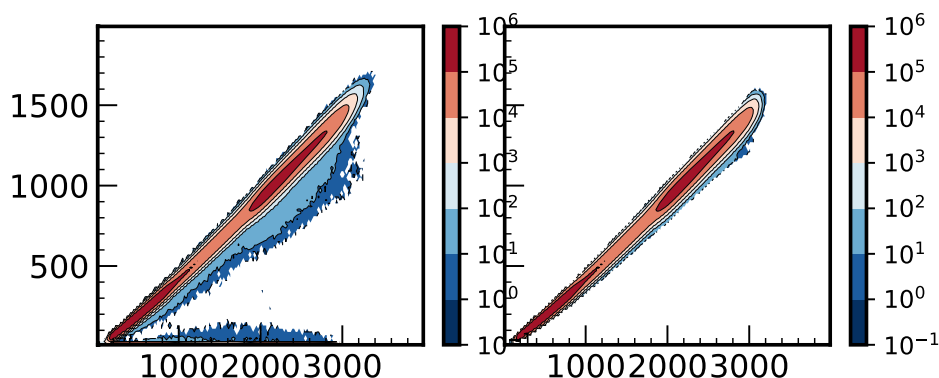


Figure 5.3: Out of bunch pile-up removal using filter bit 32 tracks and time of flight information.

and pseudorapidity range $0.4 < |\eta| < 0.8$ are considered. The low p_T -cut is to limit contributions due to weaker low- p_T reconstruction efficiency, while the upper bound limits contribution from energetic jets. A pseudorapidity gap $|\Delta\eta| > 0.8$ is used to suppress the non-flow.

5.2 Analysis verification

For a good assurance of the reliability of the results, I have verified the methods and the reconstruction of the flow observables with an AMPT [123,124] simulation, as well as a simple event generating Monte-Carlo code. Particularly, this verification is conducted to ensure the validity of the non-uniform acceptance (NUA) correction using particle weights on the Q-vectors as given in Eq. (3.25), and to test the presence of any reconstruction specific bias for high harmonic flow where very small magnitude for the quantities is expected.

The NUA correction is generally performed by inverting the initially measured φ -distribution, and then using the elements of the discrete distribution as particle weights. In this work, the φ -distribution, also denoted $\frac{dN}{d\varphi}(\eta, z_{\text{vtx}})$, is recorded as a function of η and the nominal interaction point z_{vtx} . The discretized inverse of this

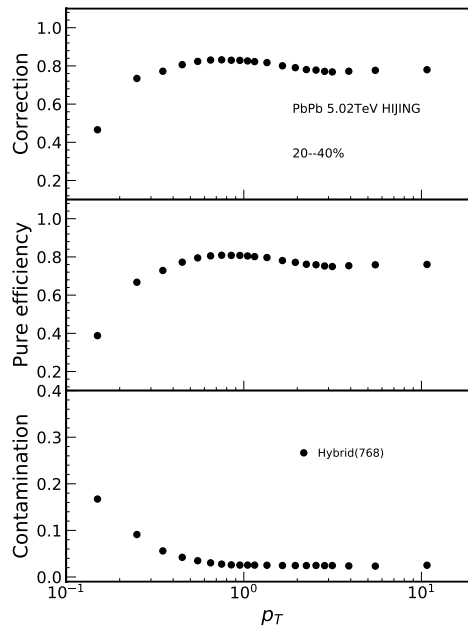


Figure 5.4: A pure efficiency, contamination, and final correction factor extracted from HIJING simulations are shown for various track selection modes in ALICE.

φ -distribution is referred to as correction map. The AMPT simulation verifies the implementation of the correction in a realistic setting with finite-resolution correction maps, whereas the simpler Monte-Carlo tests the correction and the reconstruction of the flow more analytically in high resolution.

5.2.1 Closure test with AMPT simulation

Flow reconstruction and the NUA correction is tested with an AMPT simulation which includes a detector level reconstruction for the particle tracks. In this scenario, an AMPT event-by-event simulation is first performed without any detector effects, i.e. with an ideal detector acceptance. After this, another run with same statistics is performed, but this time with the detector effects corresponding the real data production of 2015 Pb–Pb run. This AMPT run is then considered to produce *uncorrected* results with a similar φ -modulation one can observe in real data. The correction is performed by creating the correction maps based on the φ -distribution of the uncorrected run. After this, a final pass is performed over the AMPT production while utilizing the correction maps. The final pass produces the *corrected* results, which should compare to the original *true* AMPT results without any detector level reconstruction effects. The results are presented in Fig. 5.5, along with a comparison to the published v_n measurements [1]. The *true* AMPT v_n are recovered within uncertainty in every centrality class, except for 0–5% as seen in Fig. 5.5.

5.2.2 Monte-Carlo test

More accurately the methods can be tested with a simple Monte-Carlo, in which the aim is to recover the true v_n using flow reconstruction methods in such way that the results correspond to the known and given values of v_n . A simple Monte-Carlo

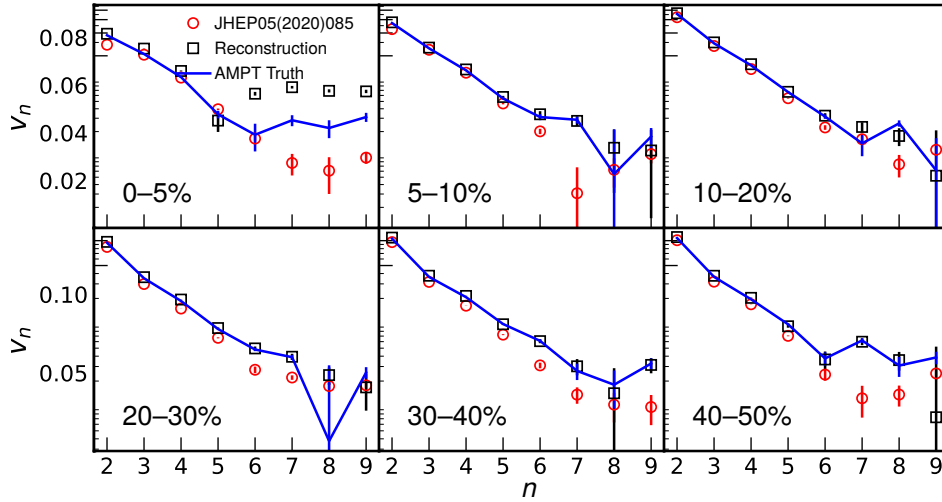


Figure 5.5: AMPT reproduction of v_n , with comparison between the truth values and the imposed detector level reconstruction. The measured values shown in red have been added as an additional insight on the real values of v_n .

(MC) implementation samples particles from the azimuthal distribution in Eq. (3.3) with random ψ_n , and fixed input v_n values, i.e. v_n -fluctuations are not necessarily included. The resulting φ -distribution, in which there are as many particles as one needs, can be modulated in order to test the NUA effects and reconstruction of the v_n in accordance to the input v_n values. Unlike with AMPT, generating a very large number of events with the simple MC method is much easier due to its inherent speed. This way, statistical fluctuations do not significantly bias the results, and testing the reconstruction of the very high harmonics is also possible.

The simple MC test was conducted as follows. A large number of events were generated with input v_n values corresponding to the measured spectra for $0.2 < p_T < 5.0 \text{ GeV}/c$ up to the seventh harmonic, while the higher harmonics $n \geq 8$ are chosen according to the power law $v_n \propto \exp(-k'n^2)$. The power law reproduces the exponential harmonic dependence observed for $n < 7$ [1]. This choice for the higher harmonics is to ensure that no potential artificial enhancement of v_n magnitude that might be induced by the reconstruction methods is left unnoticed. Furthermore, particle tracks were randomly rejected according to a probability distribution depicting an extreme gap in the detector acceptance, resulting in a heavily modulated φ -distribution. This modulation was then corrected in the Q-vectors with weights extracted from an analytical inverse modulation. The total number of tracks for each event is smoothly interpolated between the multiplicities of table 5.2 according to a randomly chosen centrality percentile. Each multiplicity of the table represents an average number of charged particles in respective centrality bins. The published values are the official and corrected measurements by ALICE Collaboration [26], while the rows labeled “Measured” are measured estimates from this work.

The results using the measured multiplicity events are presented in Fig. 5.6. In all cases, the input v_n are generally recovered up to the ninth harmonic order, and no artificial enhancement of the recovered v_n is observed in case of the damped input. In some cases, the successful recovery extends up to the eleventh harmonic. Significantly

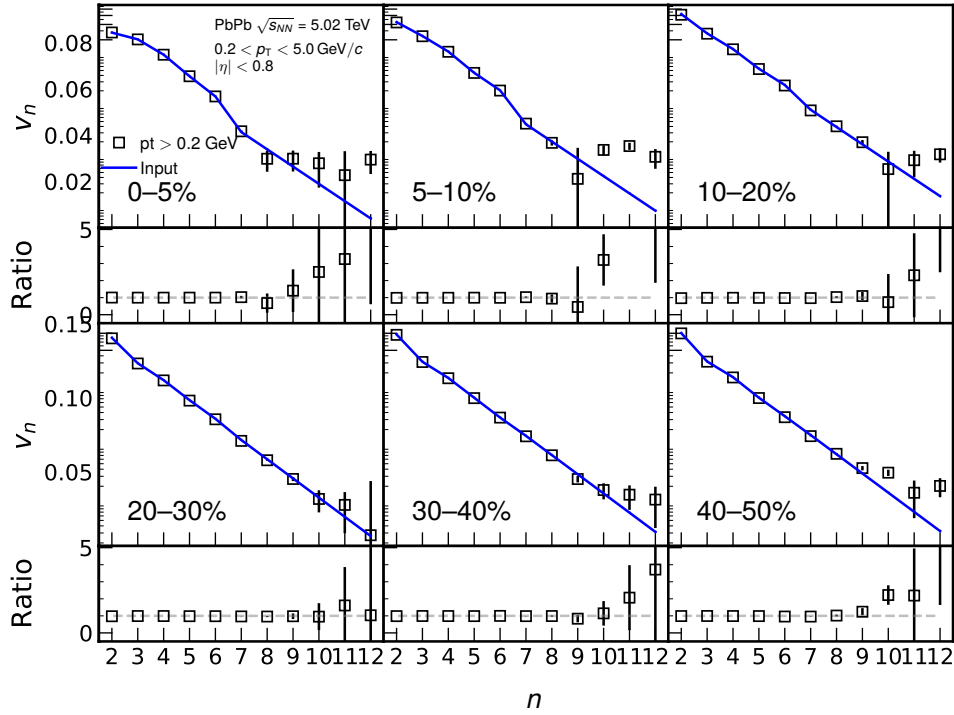


Figure 5.6: MC v_n for transverse momentum region $0.2 < p_T < 5.0 \text{ GeV}/c$. The blue line represents the input v_n extracted from the measurements up to $n = 9$. The higher harmonics $n > 9$ are obtained from the power law, resulting in exponentially damped input values, imitating the behaviour at lower harmonics.

increased statistics may confirm the recovery of these higher harmonics as well.

Figure 5.7 presents another case, where the input v_n has been fixed to a very low constant value corresponding to estimated (not measured) magnitude of v_{12} at $0.2 < p_T < 5.0 \text{ GeV}/c$ for all harmonic orders. As a result, only the phasor is varied according to the number of the harmonic. The results presented here with somewhat limited statistics do not confirm any bias of harmonic dependence.

Table 5.2: Input multiplicities measured by ALICE. For the measured multiplicities, asterisk (*) indicates that no efficiency correction was applied. The measured multiplicities have been obtained within TPC acceptance ranges, and further limited to $0.2 < p_T < 5.0, \text{ GeV}/c$ momentum range. For the published multiplicities [26], an efficiency correction has been applied. The published multiplicity covers the entire p_T -range, and a pseudorapidity range $-3.5 < \eta < 5.0$.

	0–5%	5–10%	10–20%	20–30%	30–40%	40–50%	50–60%
Published	1950	1603	1196	802	521	322	185
Measured	1247	1120	841	565	367	225	210
Measured*	989	888	667	448	291	178	101

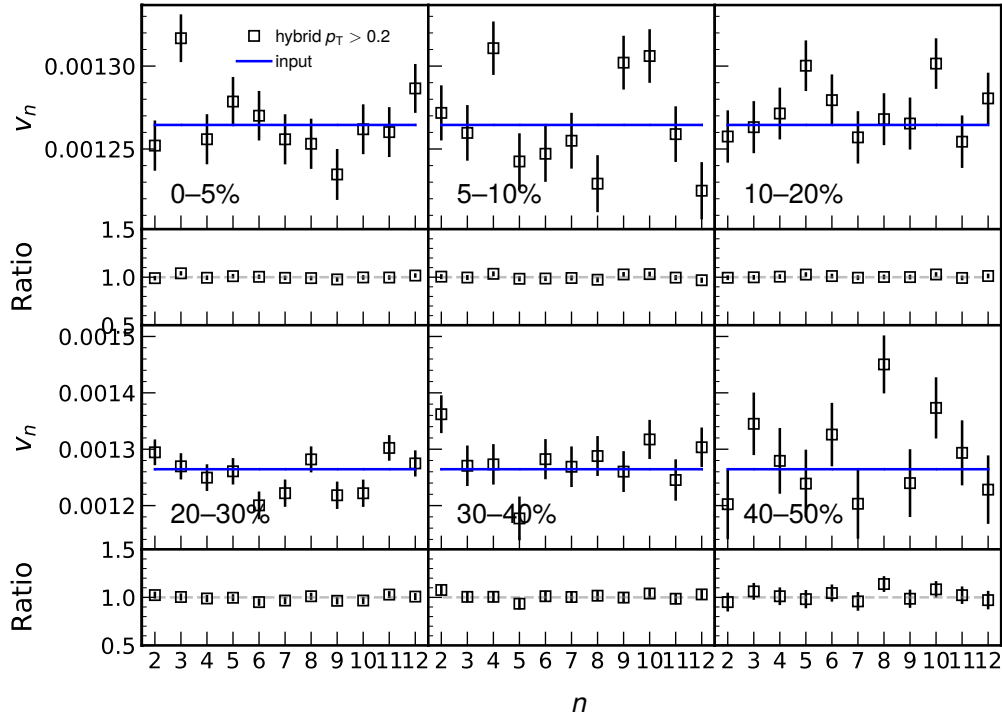


Figure 5.7: Reconstructed v_n with fixed input magnitude for all harmonics. A recovery of the flat input line within the limits of uncertainty implies no bias of harmonic dependence.

5.3 Systematics

Systematic uncertainty characterizes the uncertainty related to the experimental setup. Typically, a systematic error is assigned for each measured data point of an observable. The systematic uncertainties are estimated by individually varying the event and track selection criteria. The error is assigned by calculating a ratio between the data points for an observable over the centrality bins of the results of default (\mathbf{x}_{def}) and varied (\mathbf{x}_{sys}) configurations $\mathbf{R} = \mathbf{x}_{\text{sys}}/\mathbf{x}_{\text{def}}$, where \mathbf{R} is a vector of ratios. In order to rule out the statistically insignificant points from the systematic evaluation, a Barlow test [125] between the default and the varied configurations is conducted. For each data point, the Barlow test

$$\mathbf{B} = \frac{|\mathbf{x}_{\text{def}} - \mathbf{x}_{\text{sys}}|}{\sqrt{|\sigma_{\text{def}}^2 \pm \sigma_{\text{sys}}^2|}}. \quad (5.1)$$

is evaluated, where σ_{def} and σ_{sys} are the statistical uncertainties for the default and systematic variation data. The sign in the denominator is negative if the variation is a subset of the default configuration, and positive if the samples are independent. A result $\mathbf{B}_i > 1$ indicates a statistically significant point i , in which case the point will contribute to the systematic uncertainty. Those that contribute, will have a constant fitted through their ratio points \mathbf{R} to obtain the configuration specific uncertainty for an observable.

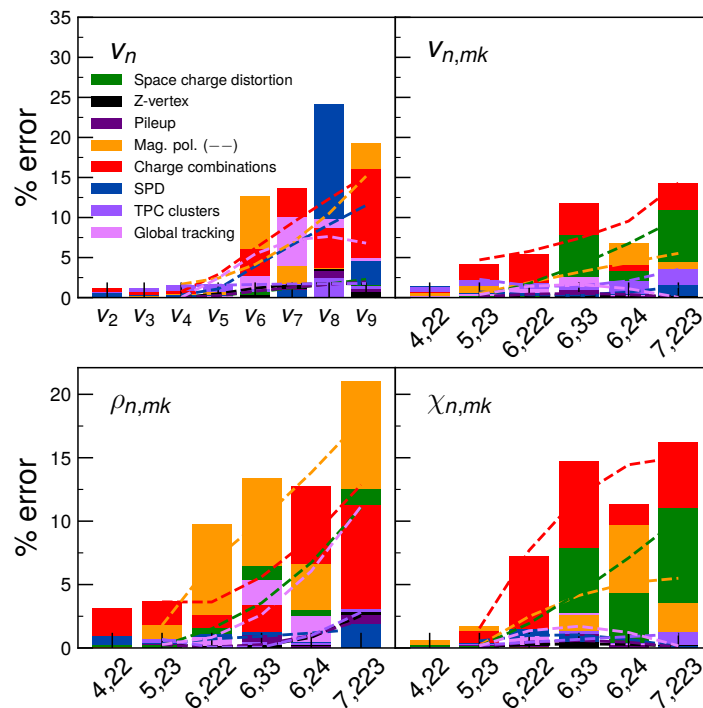


Figure 5.8: Systematic relative uncertainty plotted together for all configurations. Solid lines between the points help visualize the variations between the raw errors of different harmonics. The dashed lines plot the second order polynomial fits to the error values, intended to provide smoothed values to combat the relative large statistical fluctuations at high harmonics.

5.3.1 Summary of systematic uncertainties

Figure 5.8 presents the resulting relative systematic uncertainty for each observable and harmonic, obtained as a quadratic sum over the individual contributions, i.e. a sum over the fit constants minus one. The resulting uncertainties are given in terms of percentage error. The detailed values are presented in tables 5.3–5.6. While the systematic uncertainty is found consistently small at low harmonics, the higher harmonics show large variations from one harmonic to another. For this reason, a second order polynomial has been fitted through the error values, providing a new value smoothing the statistical variations. The smoothed values are used in the data plots, but not in the tables. The individual checks and their raw contribution are summarized below.

The sources of the systematic uncertainty can be roughly divided into event selection based uncertainty, centrality determination and tracking related uncertainties. Additionally, a nonflow estimation of the remaining contributions is assigned as a systematic uncertainty. For these measurements, I have considered two event selection related uncertainties. The z-vertex cut determines the distance the reconstructed events are allowed to have from the nominal interaction point. By default, only events reconstructed within 10 cm from the nominal interaction point are accepted. To estimate the significance of this choice, the rejection tolerance is decreased to 8 cm. The difference to the default configuration remains small for all observables. The sec-

Table 5.3: Systematic uncertainty of the flow coefficients. The uncertainties are given in percentages and are categorized into four groups: event selection, centrality determination, tracking and non-flow. The overall systematic uncertainty is obtained by summing in quadrature the uncertainties coming from each source. The resulting uncertainty is expressed in terms of percentages (%).

Type	v_2	v_3	v_4	v_5	v_6	v_7	v_8	v_9
Event Selection								
z-vertex cut	< 0.1	< 0.1	< 0.1	0.5	1.2	1.6	1.8	1.7
Pile-up rejection	< 0.1	< 0.1	< 0.1	0.2	0.8	1.3	1.7	2.0
Centrality Determination								
SPD	0.6	0.3	0.3	1.1	3.9	6.6	9.1	11.5
Tracking								
Magnetic field polarity	0.1	0.1	1.7	2.4	4.1	6.8	10.5	15.2
Tracking mode	0.1	0.2	< 0.1	2.4	5.4	7.2	7.6	6.8
Number of TPC space points	0.7	1.2	1.4	1.5	1.6	1.7	1.7	1.8
Space charge distortion	< 0.1	< 0.1	< 0.1	0.2	0.7	1.2	1.7	2.3
Non-flow								
Charge combinations ($--/++$)	1.1	0.7	0.8	2.9	6.2	9.3	12.3	15.2
Overall	1.5	1.4	2.4	4.9	10.3	15.4	20.4	25.6

Table 5.4: Relative systematic uncertainty of the harmonic projections $v_{n,mk}$.

Type	$v_{4,22}$	$v_{5,23}$	$v_{6,222}$	$v_{6,33}$	$v_{6,24}$	$v_{7,223}$
Event Selection						
z-vertex cut	0.1	0.1	0.2	0.3	0.2	0.1
Pile-up rejection	< 0.1	0.1	0.4	0.5	0.4	< 0.1
Centrality Determination						
SPD	1.5	0.7	0.3	0.3	0.7	1.4
Tracking						
Magnetic field polarity	0.5	0.5	1.9	3.2	4.4	5.5
Tracking mode	0.1	0.4	1.4	1.7	1.1	< 0.1
Number of TPC space points	3.8	2.3	1.5	1.4	2.1	3.5
Space charge distortion	0.2	0.1	1.8	4.0	6.7	9.9
Non-flow						
Charge combinations ($--/++$)	4.2	4.7	5.8	7.4	9.6	14.3
Overall	5.9	5.3	6.7	9.3	12.7	18.6

ond test evaluates the effect of the pile-up events on the results. The event selection consists of a primary vertex selection and an outlier removal based on V0 and CL0 multiplicity correlations. A further pile-up removal can be conducted by imposing an additional 4σ -cut on the multiplicity correlations, and by performing an out-of-bunch pile-up removal based on the CL0 multiplicity correlations with time of flight (TOF) information with another 4σ -cut. The pile-up is seen to have a low effect for every observable. Finally, one may estimate the uncertainties related to the method of centrality determination. An alternative centrality determination scheme is based on the information from the silicon pixel detectors (SPD). Any bias in the centrality deter-

Table 5.5: Relative systematic uncertainty of the symmetry plane correlations $\rho_{n,mk}$.

Type	$\rho_{4,22}$	$\rho_{5,23}$	$\rho_{6,222}$	$\rho_{6,33}$	$\rho_{6,24}$	$\rho_{7,223}$
Event Selection						
z-vertex cut	0.1	0.3	0.1	0.2	0.8	2.5
Pile-up rejection	0.1	0.3	0.1	0.3	1.0	2.2
Centrality Determination						
SPD	0.9	0.3	0.7	0.9	1.2	1.5
Tracking						
Magnetic field polarity	< 0.1	1.8	6.8	10.1	13.8	18.0
Tracking mode	0.1	0.3	0.8	2.6	6.1	11.2
Number of TPC space points	< 0.1	0.7	0.1	< 0.1	1.0	2.8
Space charge distortion	0.2	0.2	1.5	3.5	6.7	11.1
Non-flow						
Charge combinations (– – / + +)	3.1	3.6	3.6	5.6	8.7	12.9
Overall	3.3	4.2	7.9	12.4	18.8	27.5

Table 5.6: Relative systematic uncertainty of the non-linear flow mode coefficients $\chi_{n,mk}$.

Type	$\chi_{4,22}$	$\chi_{5,23}$	$\chi_{6,222}$	$\chi_{6,33}$	$\chi_{6,224}$	$\chi_{7,223}$
Event Selection						
z-vertex cut	< 0.1	0.1	0.3	0.3	0.3	0.1
Pile-up rejection	< 0.1	0.1	0.5	0.6	0.5	0.1
Centrality Determination						
SPD	0.2	0.6	1.0	1.0	0.7	0.1
Tracking						
Magnetic field polarity	0.6	0.2	2.5	4.1	5.1	5.5
Tracking mode	< 0.1	0.2	1.4	1.7	1.2	0.2
Number of TPC space points	< 0.1	0.2	0.5	0.7	0.9	1.1
Space charge distortion	0.2	0.1	1.9	4.4	7.1	10.1
Non-flow						
Charge combinations (– – / + +)	0.2	1.5	7.7	12.0	14.4	15.0
Overall	0.7	1.7	8.5	13.6	17.0	19.0

mination can be checked by comparing the SPD centrality determination against the default V0. Based on the results, it can be concluded that there are no considerable effects, except for very high harmonic flow coefficients with $n \geq 7$.

A large majority of the systematic checks comprises of the tracking related uncertainties. The ALICE magnet can be operated with either positive or negative solenoid magnetic field polarity. The polarity of the field affects the direction of the charged particle curvature, while also subjecting the detector itself to two possible field conditions. A subset of the dataset has been recorded with each configuration, and to investigate the effect of the polarity, an analysis on these two lists can be conducted separately as opposed to combining them as done for the default setting. Restricting the polarity has no significant effect for low harmonics. From $n \geq 6$, a considerable contribution arises for the flow coefficients, as well as for the symmetry plane cor-

relations starting from $\rho_{6,222}$. There are multiple methods on how the particle tracks are reconstructed. In this work, two methods are considered, one as a default, and another as a check of systematic uncertainty. The track reconstruction related uncertainty, referred to as tracking mode, was evaluated by comparing results obtained with different track reconstruction schemes, for which the role of the ITS (number of hits in its layers) is changed between the systematic configuration and compared to the default. In this case, the uncertainty is generally less than 15%, and a maximum of 20% is evaluated for $\rho_{7,223}$. Additionally, the track selection criteria was tightened by increasing the minimum number of TPC space points from 70 to 90, resulting in uncertainties around 1 to 3%. As the final systematic check on the particle tracking, I have checked the influence of the space charge distortion within the TPC. A multi-particle correlation with subevents can be calculated by either taking the first particle from the A-side of the detector and the other particles from the C-side, or vice versa. In a default configuration the correlators are calculated both ways, and the results are averaged. The space charge distortion effect is evaluated by not averaging the results, but by individually comparing the A or C-sided correlators to the default configuration. In case of v_n , the underlying two-particle correlation is not affected by space charge distortions. Other observables exhibit systematic uncertainty between 5 and 10% starting from the sixth harmonic order.

A final systematic check evaluates the contribution of the remaining nonflow effects. The like-sign technique, which correlates only charged particles of equal sign, is employed to investigate the magnitude of the remaining non-flow effects that were not suppressed by the two-subevent method. In order to investigate this remaining contribution, only particles with an equal charge sign are correlated, ignoring particles of the opposite sign from the analysis. Based on the results, the charge combinations pose the most significant error to the systematics.

Chapter 6

Results

6.1 Measurement of the higher harmonic observables

This chapter presents an overview of the most important results from my thesis work. For a detailed description and the complete set of all measurements, the reader is referred to Ref. [1], also attached to this thesis.

Over recent years, the accuracy and precision of equipment and methods has improved, which has enabled the measurement of the flow harmonics v_n in finer detail and higher harmonics [126–133]. This, in turn, has provided valuable information on the medium response, and in particular the medium properties in terms of both transport properties $\eta/s(T)$ and $\zeta/s(T)$, and the equation of state [14]. For this thesis, the main focus has been on achieving the measurement of higher harmonics, $n > 7$, while aiming at providing highly sensitive observables to medium properties, and thus contributing to increased knowledge and understanding of the different stages of heavy-ion collisions.

Figure 6.1 presents the flow coefficients up to the ninth harmonic in 0–5% and 40–50% centrality classes, representing the first measurement of the higher harmonics v_8 and v_9 at the LHC energies. A clear exponential damping of the flow coefficients up to the seventh harmonic can be observed, especially in the mid-peripheral collisions. However, the exponential relation becomes obscure at $n \sim 8$. Here, one can find a subtle enhancement of the magnitude of the v_8 with respect to the exponential trend. This enhancement in magnitude is even more visible at $n = 9$, and one can recognize a compelling hint of $v_9 \gtrsim v_8$, although not distinctly enough with respect to the limits of the uncertainties. This hint raises a possible existence of the acoustic peak, which might arise due to the distinct oscillation phase of the flow harmonics at the freeze-out – an effect that might be important for very low values of η/s [134]. The complete power spectra for all centrality classes can be found in Ref. [1].

Figure 6.2 shows the measured non-linear flow mode coefficients up to $\chi_{7,223}$. All of the coefficients exhibit a subtle centrality dependence, with the mid-central collisions generally showing the largest values. No significant beam energy dependence between $\sqrt{s_{\text{NN}}} = 5.02$ TeV and 2.76 TeV is observed. Most importantly, the measurements reveal the different magnitudes of non-linear response between the harmonics. For example, the response projected by the fifth harmonic $\chi_{5,23}$ is about twice as large as for the $\chi_{4,22}$. Similarly, the odd harmonic $\chi_{7,223}$ is measured significantly larger compared to the preceding sixth harmonic flow mode coefficients. The vari-

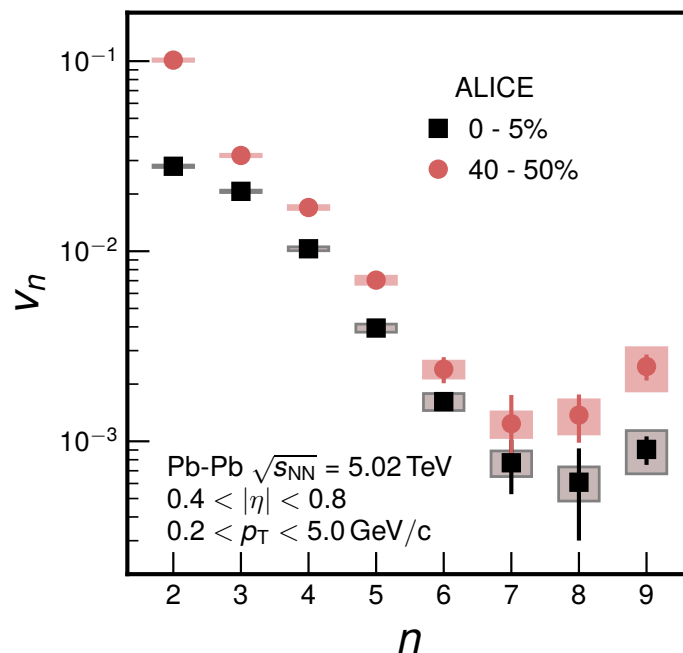


Figure 6.1: Flow coefficients v_n from the second harmonic up to the ninth harmonic in two centrality classes. The logarithmic scale highlights the exponential damping observed up until $n = 7$, after which the exponential dependence is broken.

ous model calculations show the sensitivity of the coefficients to the overall model setup [18, 135, 136]. The large deviation of the calculations to the data points at the fifth harmonic indicates an overall strong sensitivity of the $\chi_{5,23}$ compared to $\chi_{4,22}$. A detailed description of the results for the non-linear flow mode coefficients and the model setups and calculations are presented in Ref. [1].

6.2 Estimation of the transport properties

The results from the Bayesian parameter estimation along with the sensitivity analysis of the observables are summarized next. The parameter estimation includes the newly measured higher harmonic observables, particularly those of which the non-linear observables have previously not been used in such analysis. More specifically, this includes the v_n up to seventh harmonic [1], non-linear flow mode coefficients $\chi_{4,22}$, $\chi_{5,23}$, $\chi_{6,222}$ and $\chi_{6,33}$ [1], and the normalized symmetric cumulants up to NSC(4, 3) [24]. Furthermore, the analysis includes the charged and identified particle mean- p_T [25] and multiplicity production [26]. A complete and in-depth description of the analysis procedure is given in Ref. [2].

Figure 6.3 shows the final 90%-credibility region extracted from the posterior distributions for the specific shear $\eta/s(T)$ and bulk viscosity $\zeta/s(T)$ parameterizations, following the equations (2.24) and (2.25), respectively. In average, the resulting $\eta/s(T)$ is close to the AdS/CFT minimum limit $1/(4\pi)$ [33], and the temperature dependence is comparatively weak. On the other hand, the overall magnitude of the $\zeta/s(T)$ is found smaller than reported in the previous works [57, 137], implying that the added

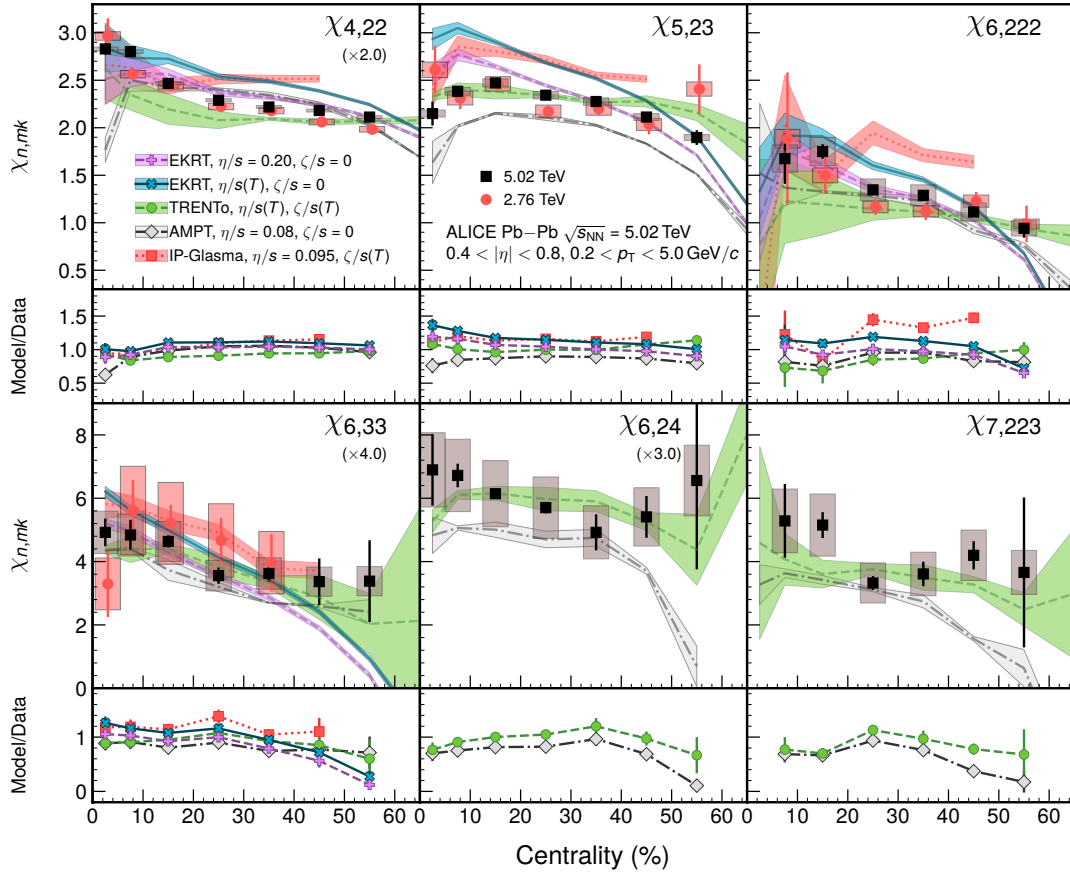


Figure 6.2: Non-linear flow mode coefficients up to $\chi_{7,223}$ [1]. The black squares represent the 5.02 TeV data points, while the red dots show the data points at 2.76 TeV center of mass energy [75]. The colored bands represent various theoretical calculations, discussed more in detail in Ref. [1].

observables favor lower values of $\zeta/s(T)$. The maximum $\zeta/s(T)$ represents an order of magnitude shift compared to the lattice QCD calculation [138] and the parameterizations used in [135,136]. A similar finding for the $\zeta/s(T)$ was reported in Ref. [139]. In spite of the added observables with the improved statistical uncertainties both on the experimental data and hydrodynamic calculations, the 90%-credibility region was not further improved compared to the previous analysis [57]. Further studies with the inclusion of the lower beam energy data will be performed in the near future. All in all, this analysis indicates that a more dynamical picture of the initial conditions is not an option but a necessity to complete the model building blocks, the initial stage, hydrodynamic evolution and the hadronic stage, of heavy-ion collisions.

As a final part of the computational analysis, a sensitivity analysis was conducted on the new observables. The analysis is done by choosing a parameter point \mathbf{x} corresponding to the optimal set of parameters found during the parameter estimation, shifting each parameter individually one at a time by a small displacement $\delta = 0.1$ to obtain a point $\mathbf{x}' = (x_1, x_2, \dots, (1 + \delta)x_j, \dots, x_p)$, and then evaluating the difference in

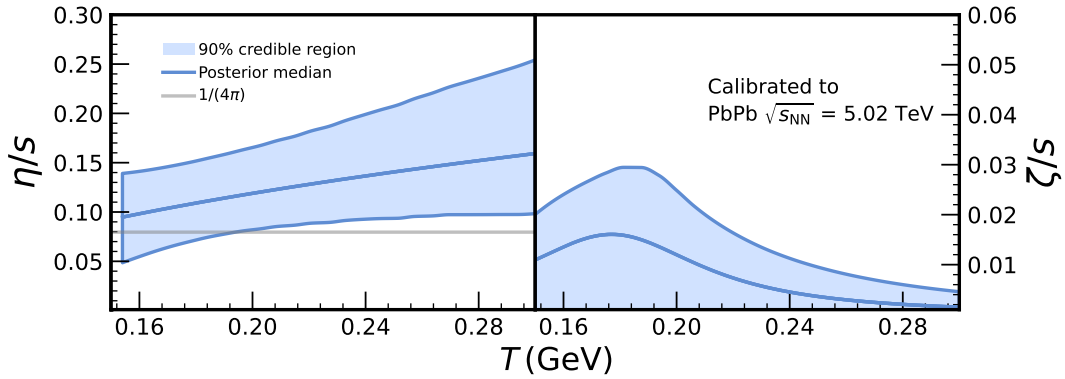


Figure 6.3: Posterior region for the specific shear (left) and bulk (right) viscosities. The blue line represents the median of the credible range Ref. [2].

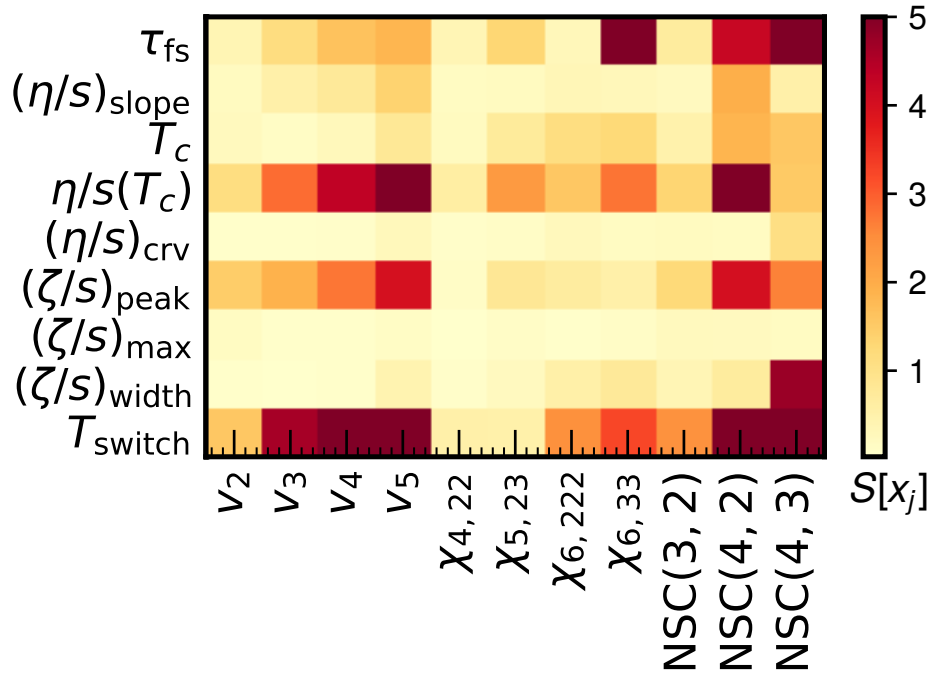


Figure 6.4: Sensitivity of the flow observables to freestreaming and transport parameters. White-yellowish colors, each corresponding to a combination of parameter and observable, represent low sensitivity while red colors indicate a strong dependence. For the complete list of model parameters and their descriptions, the reader is referred to Ref. [2].

the prediction for the observables by calculating a sensitivity index

$$S[x_j] = \frac{1}{\delta} \frac{|\hat{O}(\mathbf{x}') - \hat{O}(\mathbf{x})|}{\hat{O}(\mathbf{x})}, \quad (6.1)$$

where $\hat{O}(\mathbf{x})$ and $\hat{O}(\mathbf{x}')$ are the values of an observable at parameter points \mathbf{x} and \mathbf{x}' , respectively [137].

The results of the sensitivity analysis are presented in Fig. 6.4. One first observes the strong sensitivity of the flow coefficients v_n to the η/s at the critical temperature T_c , denoted $\eta/s(T_c)$, affirming that the v_n are mostly sensitive to the average values of η/s . As expected, the sensitivity increases with higher harmonics, with v_5 presenting a significantly stronger dependence on $\eta/s(T_c)$ compared to v_2 , for example. It is also found that the v_n provide a very good sensitivity to the temperature dependence of the specific bulk viscosity, as reflected by $(\zeta/s)_{\text{peak}}$. The non-linear flow mode coefficients on the other hand are known to be sensitive to the η/s at the freeze-out temperature [1,75]. This is confirmed by the observed sensitivity of the $\chi_{n,mk}$ to $\eta/s(T_c)$, as well as the critical temperature T_c . Only very subtle ζ/s dependence is observed. Interestingly, the sensitivity of the $\chi_{6,33}$ to the freestreaming time scale is also found much greater than for the previously examined other observables. Finally, the sensitivity of the normalized symmetric cumulants (NSC) is examined. Firstly, the results confirm the high sensitivity of the symmetric cumulants to the temperature dependence of $\eta/s(T)$, in particular of the slope $(\eta/s)_{\text{slope}}$, as well as T_c and $\eta/s(T_c)$. NSC(4,3) also exhibits dependence on the curvature of the η/s slope, denoted $(\eta/s)_{\text{crv}}$, as the only observable in the list. Secondly, the symmetric cumulants are strongly sensitive to the temperature dependence of $\zeta/s(T)$. The sensitivity to $(\zeta/s)_{\text{peak}}$ is comparable to that of the v_n , while additionally NSC(4,3) is found highly sensitive to the width of the ζ/s -peak, i.e. $(\zeta/s)_{\text{width}}$. All observables are found either moderately or strongly sensitive to the switching temperature between the hydrodynamic evolution and the hadronic scattering, T_{switch} .

Chapter 7

Conclusions

In summary, this thesis work has achieved and demonstrated the measurement of the highest flow harmonics, as well as their non-linear flow modes [1]. Furthermore, these measurements were utilized in a Bayesian parameter estimation for the first time [2]. The sensitivity of each observable to the hydrodynamic model parameters was evaluated as part of this work.

In my thesis I have shown that the measurement of very high harmonics and their non-linear flow modes is a key to constrain the model parameterization in hydrodynamic calculations. Up until this achievement, the inclusion of the higher harmonics $n \geq 5$ and sophisticated flow observables in a parameter estimation has been challenging due to the complexity of the measurement and limited access to computing power. However, this thesis research has succeeded in solving that challenge by using the same analysis framework as for the data analysis [1] and by exploiting the significant computing power available through the CSC computing center in Finland. While the model calculations have successfully predicted a wide range of lower harmonic observables, reproduction of the higher harmonics and advanced flow observables can provide a more stringent test of theory. Calibration of the model parameters to the newly measured observables provides us with the following interesting observations.

- (i) The temperature dependence of $\eta/s(T)$ is similar to what was obtained in [57]. On the other hand, we observe a stronger curvature of $\eta/s(T)$. This implies lower values of $\eta/s(T)$ at higher temperatures above T_c .
- (ii) Lower $(\zeta/s(T))_{\max}$ is favored in order to reproduce additional observables. The obtained $\zeta/s(T)$ is smaller than the ones reported in the previous studies [57, 137], and significantly lower compared to the value from lattice QCD calculation [138] and the parameterizations used in [135, 136].
- (iii) The switching temperature is higher than found in the previous studies, where on average T_{switch} is around ~ 0.150 GeV.
- (iv) As found in Ref. [1, 75, 140], the non-linear flow modes and the symmetric cumulants are sensitive to viscous corrections to the equilibrium distribution at hadronic freeze-out [73, 74, 141, 142] and seem to prefer the higher switching temperature.

- (v) The sensitivity analysis for the observables indicates that observables such as the symmetric cumulants and non-linear flow modes provide a highly potent constraining power. Consequently, the flow coefficients alongside the symmetric cumulants and non-linear flow mode can provide some of the strongest constraints for the temperature dependence of $\eta/s(T)$ and T_{switch} .

Despite the added observables and with the improved statistical uncertainties both on the experimental data and hydrodynamic calculations, the final credibility range was not reduced significantly. Improving aspects of the collision model by incorporating a nucleon substructure [143] in the initial conditions before the hydrodynamic takes place [144, 145], might help improve our understanding of the uncertainties of the extracted QGP properties and/or the model building blocks [2].

As it is known that understanding the initial state model is more important in the small system collisions, another aspect of this thesis work has been on improving the measurements in small collision systems. While there are some debates on physics conclusions for small system [146–149], the author made a significant contribution of the measurement on the event-scale dependence ridge studies with the highest pp collision energy data [3]. The results might open a new way of studying the flow in small systems in the future and will help to constrain the initial conditions both in small and large systems.

Bibliography

- [1] ALICE Collaboration, S. Acharya *et al.*, “Higher harmonic non-linear flow modes of charged hadrons in Pb-Pb collisions at $\sqrt{s_{\text{NN}}} = 5.02$ TeV,” *JHEP* **05** (2020) 085, arXiv:2002.00633 [nucl-ex].
- [2] J. E. Parkkila, A. Onnerstad, and D. J. Kim, “Bayesian estimation of the specific shear and bulk viscosity of the quark-gluon plasma with additional flow harmonic observables,” *Phys. Rev. C* **104** (Nov, 2021) 054904. <https://link.aps.org/doi/10.1103/PhysRevC.104.054904>.
- [3] ALICE Collaboration, S. Acharya *et al.*, “Long- and short-range correlations and their event-scale dependence in high-multiplicity pp collisions at $\sqrt{s} = 13$ TeV,” *JHEP* **05** (2021) 290, arXiv:2101.03110 [nucl-ex].
- [4] J. Rafelski, “Discovery of Quark-Gluon-Plasma: Strangeness Diaries,” *Eur. Phys. J. ST* **229** no. 1, (2020) 1–140, arXiv:1911.00831 [hep-ph].
- [5] J. C. Collins and M. J. Perry, “Superdense matter: Neutrons or asymptotically free quarks?,” *Phys. Rev. Lett.* **34** (May, 1975) 1353–1356. <https://link.aps.org/doi/10.1103/PhysRevLett.34.1353>.
- [6] E. V. Shuryak, “Quantum Chromodynamics and the Theory of Superdense Matter,” *Phys. Rept.* **61** (1980) 71–158.
- [7] J.-Y. Ollitrault, “Anisotropy as a signature of transverse collective flow,” *Phys. Rev.* **D46** (1992) 229–245.
- [8] U. W. Heinz and M. Jacob, “Evidence for a new state of matter: An Assessment of the results from the CERN lead beam program,” arXiv:nucl-th/0002042.
- [9] E. Lofgren *ACCELERATOR DIVISION ANNUAL REPORTS* no. LBL-3835, (12, 1972) . <https://publications.lbl.gov/islandora/object/ir%3A102869>.
- [10] A. Kovalenko, “Status of the Nuclotron,” *Proceedings, EPAC’94, London, June 1994* (1995) 161–164.
- [11] G. Martinez, “Advances in Quark Gluon Plasma,” 4, 2013. arXiv:1304.1452 [nucl-ex].
- [12] S. A. Voloshin, A. M. Poskanzer, and R. Snellings, “Collective phenomena in non-central nuclear collisions,” *Landolt-Bornstein* **23** (2010) 293–333, arXiv:0809.2949 [nucl-ex].

- [13] R. A. Lacey, N. N. Ajitanand, J. M. Alexander, P. Chung, W. G. Holzmann, M. Issah, A. Taranenko, P. Danielewicz, and H. Stoecker, "Has the QCD Critical Point been Signaled by Observations at RHIC?," *Phys. Rev. Lett.* **98** (2007) 092301, arXiv:nucl-ex/0609025 [nucl-ex].
- [14] D. A. Teaney, "Viscous Hydrodynamics and the Quark Gluon Plasma," arXiv:0905.2433 [nucl-th].
- [15] S. Voloshin and Y. Zhang, "Flow study in relativistic nuclear collisions by Fourier expansion of Azimuthal particle distributions," *Z. Phys.* **C70** (1996) 665–672, arXiv:hep-ph/9407282 [hep-ph].
- [16] A. M. Poskanzer and S. A. Voloshin, "Methods for analyzing anisotropic flow in relativistic nuclear collisions," *Phys. Rev.* **C58** (1998) 1671–1678, arXiv:nucl-ex/9805001 [nucl-ex].
- [17] D. Teaney and L. Yan, "Triangularity and dipole asymmetry in heavy ion collisions," *Phys. Rev.* **C83** (2011) 064904, arXiv:1010.1876 [nucl-th].
- [18] H. Niemi, K. J. Eskola, and R. Paatelainen, "Event-by-event fluctuations in a perturbative QCD + saturation + hydrodynamics model: Determining QCD matter shear viscosity in ultrarelativistic heavy-ion collisions," *Phys. Rev.* **C93** no. 2, (2016) 024907, arXiv:1505.02677 [hep-ph].
- [19] C. Gale, S. Jeon, and B. Schenke, "Hydrodynamic Modeling of Heavy-Ion Collisions," *Int. J. Mod. Phys. A* **28** (2013) 1340011, arXiv:1301.5893 [nucl-th].
- [20] H. Niemi, G. S. Denicol, H. Holopainen, and P. Huovinen, "Event-by-event distributions of azimuthal asymmetries in ultrarelativistic heavy-ion collisions," *Phys. Rev.* **C87** no. 5, (2013) 054901, arXiv:1212.1008 [nucl-th].
- [21] ALICE Collaboration, S. Acharya *et al.*, "Systematic studies of correlations between different order flow harmonics in Pb-Pb collisions at $\sqrt{s_{NN}} = 2.76$ TeV," *Phys. Rev. C* **97** no. 2, (2018) 024906, arXiv:1709.01127 [nucl-ex].
- [22] ALICE Collaboration, J. Adam *et al.*, "Correlated event-by-event fluctuations of flow harmonics in Pb-Pb collisions at $\sqrt{s_{NN}} = 2.76$ TeV," *Phys. Rev. Lett.* **117** (2016) 182301, arXiv:1604.07663 [nucl-ex].
- [23] C. Mordasini, A. Bilandzic, D. Karakoç, and S. F. Taghavi, "Higher order Symmetric Cumulants," *Phys. Rev. C* **102** no. 2, (2020) 024907, arXiv:1901.06968 [nucl-ex].
- [24] ALICE Collaboration, S. Acharya *et al.*, "Measurements of mixed harmonic cumulants in Pb–Pb collisions at $\sqrt{s_{NN}} = 5.02$ TeV," *Phys. Lett. B* **818** (2021) 136354, arXiv:2102.12180 [nucl-ex].
- [25] ALICE Collaboration, S. Acharya *et al.*, "Production of charged pions, kaons, and (anti-)protons in Pb-Pb and inelastic *pp* collisions at $\sqrt{s_{NN}} = 5.02$ TeV," *Phys. Rev. C* **101** no. 4, (2020) 044907, arXiv:1910.07678 [nucl-ex].

- [26] ALICE Collaboration, J. Adam *et al.*, “Centrality dependence of the pseudorapidity density distribution for charged particles in Pb-Pb collisions at $\sqrt{s_{NN}} = 5.02$ TeV,” *Phys. Lett. B* **772** (2017) 567–577, arXiv:1612.08966 [nucl-ex].
- [27] E. Fermi, “High Energy Nuclear Events,” *Progress of Theoretical Physics* **5** no. 4, (07, 1950) 570–583,
<https://academic.oup.com/ptp/article-pdf/5/4/570/5430247/5-4-570.pdf>.
<https://doi.org/10.1143/ptp/5.4.570>.
- [28] L. D. Landau, “On the multiparticle production in high-energy collisions,” *Izv. Akad. Nauk Ser. Fiz.* **17** (1953) 51–64.
- [29] I. M. Khalatnikov, “Some questions of relativistic hydrodynamics,” *Zh. Eksp. Teor. Fiz.* **27** (1954) 529–541.
- [30] L. P. Csernai, J. I. Kapusta, and L. D. McLerran, “On the Strongly-Interacting Low-Viscosity Matter Created in Relativistic Nuclear Collisions,” *Phys. Rev. Lett.* **97** (2006) 152303, arXiv:nucl-th/0604032.
- [31] T. Hirano, U. W. Heinz, D. Kharzeev, R. Lacey, and Y. Nara, “Hadronic dissipative effects on elliptic flow in ultrarelativistic heavy-ion collisions,” *Phys. Lett.* **B636** (2006) 299–304, arXiv:nucl-th/0511046 [nucl-th].
- [32] P. Romatschke and U. Romatschke, “Viscosity Information from Relativistic Nuclear Collisions: How Perfect is the Fluid Observed at RHIC?,” *Phys. Rev. Lett.* **99** (2007) 172301, arXiv:0706.1522 [nucl-th].
- [33] P. Kovtun, D. T. Son, and A. O. Starinets, “Viscosity in strongly interacting quantum field theories from black hole physics,” *Phys. Rev. Lett.* **94** (2005) 111601, arXiv:hep-th/0405231 [hep-th].
- [34] S. Ryu, J. F. Paquet, C. Shen, G. S. Denicol, B. Schenke, S. Jeon, and C. Gale, “Importance of the Bulk Viscosity of QCD in Ultrarelativistic Heavy-Ion Collisions,” *Phys. Rev. Lett.* **115** no. 13, (2015) 132301, arXiv:1502.01675 [nucl-th].
- [35] S. Ryu, J.-F. Paquet, C. Shen, G. Denicol, B. Schenke, S. Jeon, and C. Gale, “Effects of bulk viscosity and hadronic rescattering in heavy ion collisions at energies available at the BNL Relativistic Heavy Ion Collider and at the CERN Large Hadron Collider,” *Phys. Rev.* **C97** no. 3, (2018) 034910, arXiv:1704.04216 [nucl-th].
- [36] M. L. Miller, K. Reygers, S. J. Sanders, and P. Steinberg, “Glauber modeling in high energy nuclear collisions,” *Ann. Rev. Nucl. Part. Sci.* **57** (2007) 205–243, arXiv:nucl-ex/0701025 [nucl-ex].
- [37] R. D. Woods and D. S. Saxon, “Diffuse surface optical model for nucleon-nuclei scattering,” *Phys. Rev.* **95** (Jul, 1954) 577–578.
<https://link.aps.org/doi/10.1103/PhysRev.95.577>.

- [38] L. C. Chamon, B. V. Carlson, L. R. Gasques, D. Pereira, C. De Conti, M. A. G. Alvarez, M. S. Hussein, M. A. Candido Ribeiro, E. S. Rossi, Jr., and C. P. Silva, "Toward a global description of the nucleus-nucleus interaction," *Phys. Rev. C* **66** (2002) 014610, arXiv:nuc1-th/0202015.
- [39] F. Gelis, E. Iancu, J. Jalilian-Marian, and R. Venugopalan, "The Color Glass Condensate," *Ann. Rev. Nucl. Part. Sci.* **60** (2010) 463–489, arXiv:1002.0333 [hep-ph].
- [40] D. Kharzeev, E. Levin, and M. Nardi, "The Onset of classical QCD dynamics in relativistic heavy ion collisions," *Phys. Rev. C* **71** (2005) 054903, arXiv:hep-ph/0111315.
- [41] H.-J. Drescher, A. Dumitru, A. Hayashigaki, and Y. Nara, "The Eccentricity in heavy-ion collisions from color glass condensate initial conditions," *Phys. Rev. C* **74** (2006) 044905, arXiv:nuc1-th/0605012.
- [42] E. Molnar, H. Niemi, and D. H. Rischke, "Numerical tests of causal relativistic dissipative fluid dynamics," *Eur. Phys. J.* **C65** (2010) 615–635, arXiv:0907.2583 [nucl-th].
- [43] J. S. Moreland, J. E. Bernhard, and S. A. Bass, "Alternative ansatz to wounded nucleon and binary collision scaling in high-energy nuclear collisions," *Phys. Rev.* **C92** no. 1, (2015) 011901, arXiv:1412.4708 [nucl-th].
<http://qcd.phy.duke.edu/trento/>.
- [44] J. E. Bernhard, J. S. Moreland, S. A. Bass, J. Liu, and U. Heinz, "Applying Bayesian parameter estimation to relativistic heavy-ion collisions: simultaneous characterization of the initial state and quark-gluon plasma medium," *Phys. Rev.* **C94** no. 2, (2016) 024907, arXiv:1605.03954 [nucl-th].
- [45] B. Schenke, P. Tribedy, and R. Venugopalan, "Fluctuating Glasma initial conditions and flow in heavy ion collisions," *Phys. Rev. Lett.* **108** (2012) 252301, arXiv:1202.6646 [nucl-th].
- [46] B. Schenke, P. Tribedy, and R. Venugopalan, "Event-by-event gluon multiplicity, energy density, and eccentricities in ultrarelativistic heavy-ion collisions," *Phys. Rev. C* **86** (2012) 034908, arXiv:1206.6805 [hep-ph].
- [47] J. Liu, C. Shen, and U. Heinz, "Pre-equilibrium evolution effects on heavy-ion collision observables," *Phys. Rev. C* **91** no. 6, (2015) 064906, arXiv:1504.02160 [nucl-th]. [Erratum: *Phys.Rev.C* 92, 049904 (2015)].
- [48] F. Cooper and G. Frye, "Single-particle distribution in the hydrodynamic and statistical thermodynamic models of multiparticle production," *Phys. Rev. D* **10** (Jul, 1974) 186–189. <https://link.aps.org/doi/10.1103/PhysRevD.10.186>.
- [49] C. M. Hung and E. V. Shuryak, "Equation of state, radial flow and freezeout in high-energy heavy ion collisions," *Phys. Rev. C* **57** (1998) 1891–1906, arXiv:hep-ph/9709264.

- [50] H. Holopainen and P. Huovinen, "Dynamical Freeze-out in Event-by-Event Hydrodynamics," *J. Phys. Conf. Ser.* **389** (2012) 012018, arXiv:1207.7331 [hep-ph].
- [51] H. Petersen, C. Coleman-Smith, S. A. Bass, and R. Wolpert, "Constraining the initial state granularity with bulk observables in Au+Au collisions at $\sqrt{s_{NN}} = 200$ GeV," *J. Phys.* **G38** (2011) 045102, arXiv:1012.4629 [nucl-th].
- [52] J. Novak, K. Novak, S. Pratt, J. Vredevoogd, C. Coleman-Smith, and R. Wolpert, "Determining Fundamental Properties of Matter Created in Ultrarelativistic Heavy-Ion Collisions," *Phys. Rev. C* **89** no. 3, (2014) 034917, arXiv:1303.5769 [nucl-th].
- [53] S. Pratt, E. Sangaline, P. Sorensen, and H. Wang, "Constraining the Eq. of State of Super-Hadronic Matter from Heavy-Ion Collisions," *Phys. Rev. Lett.* **114** (2015) 202301, arXiv:1501.04042 [nucl-th].
- [54] E. Sangaline and S. Pratt, "Toward a deeper understanding of how experiments constrain the underlying physics of heavy-ion collisions," *Phys. Rev.* **C93** no. 2, (2016) 024908, arXiv:1508.07017 [nucl-th].
- [55] J. E. Bernhard, P. W. Marcy, C. E. Coleman-Smith, S. Huzurbazar, R. L. Wolpert, and S. A. Bass, "Quantifying properties of hot and dense QCD matter through systematic model-to-data comparison," *Phys. Rev. C* **91** no. 5, (2015) 054910, arXiv:1502.00339 [nucl-th].
- [56] U. W. Heinz and J. Liu, "Pre-equilibrium dynamics and heavy-ion observables," in *25th International Conference on Ultra-Relativistic Nucleus-Nucleus Collisions (Quark Matter 2015) Kobe, Japan, September 27-October 3, 2015*. Nucl. Phys. A, in press, 2015. arXiv:1512.08276 [nucl-th]. <https://inspirehep.net/record/1411488/files/arXiv:1512.08276.pdf>.
- [57] J. E. Bernhard, J. S. Moreland, and S. A. Bass, "Bayesian estimation of the specific shear and bulk viscosity of quark-gluon plasma," *Nature Physics* (2019) . <https://doi.org/10.1038/s41567-019-0611-8>.
- [58] J. Auvinen, K. J. Eskola, P. Huovinen, H. Niemi, R. Paatelainen, and P. Petreczky, "Temperature dependence of η/s of strongly interacting matter: Effects of the equation of state and the parametric form of $(\eta/s)(T)$," *Phys. Rev. C* **102** no. 4, (2020) 044911, arXiv:2006.12499 [nucl-th].
- [59] G. Nijs, W. van der Schee, U. Gürsoy, and R. Snellings, "Bayesian analysis of heavy ion collisions with the heavy ion computational framework Trajectum," *Phys. Rev. C* **103** no. 5, (2021) 054909, arXiv:2010.15134 [nucl-th].
- [60] W. Broniowski, W. Florkowski, M. Chojnacki, and A. Kisiel, "Free-streaming approximation in early dynamics of relativistic heavy-ion collisions," *Phys. Rev. C* **80** (2009) 034902, arXiv:0812.3393 [nucl-th].
- [61] H. Song and U. W. Heinz, "Causal viscous hydrodynamics in 2+1 dimensions for relativistic heavy-ion collisions," *Phys. Rev. C* **77** (2008) 064901, arXiv:0712.3715 [nucl-th].

- [62] H. Song and U. W. Heinz, "Multiplicity scaling in ideal and viscous hydrodynamics," *Phys. Rev. C* **78** (2008) 024902, arXiv:0805.1756 [nucl-th].
- [63] S. A. Bass *et al.*, "Microscopic models for ultrarelativistic heavy ion collisions," *Prog. Part. Nucl. Phys.* **41** (1998) 255–369, arXiv:nucl-th/9803035.
- [64] M. Bleicher *et al.*, "Relativistic hadron hadron collisions in the ultrarelativistic quantum molecular dynamics model," *J. Phys. G* **25** (1999) 1859–1896, arXiv:hep-ph/9909407.
- [65] B. Alver and G. Roland, "Collision geometry fluctuations and triangular flow in heavy-ion collisions," *Phys. Rev.* **C81** (2010) 054905, arXiv:1003.0194 [nucl-th]. [Erratum: *Phys. Rev.*C82,039903(2010)].
- [66] M. Luzum and J.-Y. Ollitrault, "Eliminating experimental bias in anisotropic-flow measurements of high-energy nuclear collisions," *Phys. Rev.* **C87** no. 4, (2013) 044907, arXiv:1209.2323 [nucl-ex].
- [67] S. Wang, Y. Z. Jiang, Y. M. Liu, D. Keane, D. Beavis, S. Y. Chu, S. Y. Fung, M. Vient, C. Hartnack, and H. Stoecker, "Measurement of collective flow in heavy ion collisions using particle pair correlations," *Phys. Rev. C* **44** (1991) 1091–1095.
- [68] R. A. Lacey *et al.*, "Multifragment azimuthal correlation functions: Probes for reaction dynamics in collisions of intermediate energy heavy ions," *Phys. Rev. Lett.* **70** (1993) 1224–1227.
- [69] PHENIX Collaboration, R. A. Lacey, "Elliptic flow measurements with the PHENIX detector," *Nucl. Phys. A* **698** (2002) 559–563, arXiv:nucl-ex/0105003.
- [70] N. Borghini, P. M. Dinh, and J.-Y. Ollitrault, "Flow analysis from multiparticle azimuthal correlations," *Phys. Rev. C* **64** (2001) 054901, arXiv:nucl-th/0105040.
- [71] F. G. Gardim, F. Grassi, M. Luzum, and J.-Y. Ollitrault, "Mapping the hydrodynamic response to the initial geometry in heavy-ion collisions," *Phys. Rev.* **C85** (2012) 024908, arXiv:1111.6538 [nucl-th].
- [72] D. Teaney and L. Yan, "Event-plane correlations and hydrodynamic simulations of heavy ion collisions," *Phys. Rev.* **C90** no. 2, (2014) 024902, arXiv:1312.3689 [nucl-th].
- [73] L. Yan and J.-Y. Ollitrault, " v_4, v_5, v_6, v_7 : nonlinear hydrodynamic response versus LHC data," *Phys. Lett.* **B744** (2015) 82–87, arXiv:1502.02502 [nucl-th].
- [74] D. Teaney and L. Yan, "Non linearities in the harmonic spectrum of heavy ion collisions with ideal and viscous hydrodynamics," *Phys. Rev.* **C86** (2012) 044908, arXiv:1206.1905 [nucl-th].
- [75] ALICE Collaboration, S. Acharya *et al.*, "Linear and non-linear flow modes in Pb-Pb collisions at $\sqrt{s_{NN}} = 2.76$ TeV," *Phys. Lett.* **B773** (2017) 68–80, arXiv:1705.04377 [nucl-ex].

- [76] Z. Qiu and U. Heinz, "Hydrodynamic event-plane correlations in Pb+Pb collisions at $\sqrt{s} = 2.76$ ATeV," *Phys. Lett.* **B717** (2012) 261–265, arXiv:1208.1200 [nucl-th].
- [77] A. Bilandzic, C. H. Christensen, K. Gulbrandsen, A. Hansen, and Y. Zhou, "Generic framework for anisotropic flow analyses with multiparticle azimuthal correlations," *Phys. Rev.* **C89** no. 6, (2014) 064904, arXiv:1312.3572 [nucl-ex].
- [78] P. Danielewicz and G. Odnyc, "Transverse Momentum Analysis of Collective Motion in Relativistic Nuclear Collisions," *Phys. Lett. B* **157** (1985) 146–150.
- [79] CMS Collaboration, S. Chatrchyan *et al.*, "Multiplicity and Transverse Momentum Dependence of Two- and Four-Particle Correlations in pPb and PbPb Collisions," *Phys. Lett. B* **724** (2013) 213–240, arXiv:1305.0609 [nucl-ex].
- [80] P. Huo, K. Gajdošová, J. Jia, and Y. Zhou, "Importance of non-flow in mixed-harmonic multi-particle correlations in small collision systems," *Phys. Lett. B* **777** (2018) 201–206, arXiv:1710.07567 [nucl-ex].
- [81] E. Mobs, "The CERN accelerator complex. Complexe des accélérateurs du CERN," <http://cds.cern.ch/record/2197559>. General Photo.
- [82] L. Evans and P. Bryant, "LHC machine," *Journal of Instrumentation* **3** no. 08, (Aug, 2008) S08001–S08001. <https://doi.org/10.1088/1748-0221/3/08/s08001>.
- [83] R. Schmidt *et al.*, "Protection of the CERN Large Hadron Collider," *New J. Phys.* **8** (2006) 290.
- [84] "LHC Machine," *JINST* **3** (2008) S08001.
- [85] LHC Magnet Team Collaboration, R. Perin and J. Vloagaert, "Magnets for the Large Hadron Collider," tech. rep., CERN, Geneva, Feb, 1994. <https://cds.cern.ch/record/260440>.
- [86] D. Boussard, "Schottky noise and beam transfer function diagnostics," <https://cds.cern.ch/record/168143>.
- [87] S. Baird, "Accelerators for pedestrians; rev. version," tech. rep., CERN, Geneva, Feb, 2007. <http://cds.cern.ch/record/1017689>.
- [88] "Collisions, LHC Machine Outreach." <http://lhc-machine-outreach.web.cern.ch/collisions.htm>. Accessed: 04.08.2021.
- [89] "HL-LHC Preliminary Design Report: Deliverable: D1.5," <https://cds.cern.ch/record/1972604>.
- [90] "LHC Report: The final days of Run 2." <https://home.cern/news/news/accelerators/lhc-report-final-days-run-2>. Accessed: 04.08.2021.

- [91] **ALICE** Collaboration, K. Aamodt *et al.*, “The ALICE experiment at the CERN LHC,” *JINST* **3** (2008) S08002.
- [92] **ALICE** Collaboration, B. B. Abelev *et al.*, “Performance of the ALICE Experiment at the CERN LHC,” *Int. J. Mod. Phys. A* **29** (2014) 1430044, arXiv:1402.4476 [nucl-ex].
- [93] **ATLAS** Collaboration, G. Aad *et al.*, “The ATLAS Experiment at the CERN Large Hadron Collider,” *JINST* **3** (2008) S08003.
- [94] **CMS** Collaboration, S. Chatrchyan *et al.*, “The CMS Experiment at the CERN LHC,” *JINST* **3** (2008) S08004.
- [95] **LHCb** Collaboration, J. Alves, A. Augusto *et al.*, “The LHCb Detector at the LHC,” *JINST* **3** (2008) S08005.
- [96] **CMS** Collaboration, S. Chatrchyan *et al.*, “Observation of a New Boson at a Mass of 125 GeV with the CMS Experiment at the LHC,” *Phys. Lett. B* **716** (2012) 30–61, arXiv:1207.7235 [hep-ex].
- [97] **ATLAS** Collaboration, G. Aad *et al.*, “Observation of a new particle in the search for the Standard Model Higgs boson with the ATLAS detector at the LHC,” *Phys. Lett. B* **716** (2012) 1–29, arXiv:1207.7214 [hep-ex].
- [98] **LHCb** Collaboration, R. Aaij *et al.*, “First Evidence for the Decay $B_s^0 \rightarrow \mu^+ \mu^-$,” *Phys. Rev. Lett.* **110** no. 2, (2013) 021801, arXiv:1211.2674 [hep-ex].
- [99] **LHCb** Collaboration, R. Aaij *et al.*, “Measurement of the $B_s^0 \rightarrow \mu^+ \mu^-$ branching fraction and effective lifetime and search for $B^0 \rightarrow \mu^+ \mu^-$ decays,” *Phys. Rev. Lett.* **118** no. 19, (2017) 191801, arXiv:1703.05747 [hep-ex].
- [100] **LHCf** Collaboration, O. Adriani *et al.*, “The LHCf detector at the CERN Large Hadron Collider,” *JINST* **3** (2008) S08006.
- [101] **TOTEM** Collaboration, G. Anelli *et al.*, “The TOTEM experiment at the CERN Large Hadron Collider,” *JINST* **3** (2008) S08007.
- [102] **MoEDAL** Collaboration, B. Acharya *et al.*, “Search for magnetic monopoles with the MoEDAL prototype trapping detector in 8 TeV proton-proton collisions at the LHC,” *JHEP* **08** (2016) 067, arXiv:1604.06645 [hep-ex].
- [103] **ALICE Collaboration** Collaboration, *ALICE Inner Tracking System (ITS): Technical Design Report*. Technical design report. ALICE. CERN, Geneva, 1999. <https://cds.cern.ch/record/391175>.
- [104] **ALICE** Collaboration, K. Aamodt *et al.*, “Alignment of the ALICE Inner Tracking System with cosmic-ray tracks,” *JINST* **5** (2010) P03003, arXiv:1001.0502 [physics.ins-det].
- [105] **ALICE** Collaboration, E. Abbas *et al.*, “Performance of the ALICE VZERO system,” *JINST* **8** (2013) P10016, arXiv:1306.3130 [nucl-ex].

- [106] J. Alme *et al.*, “The ALICE TPC, a large 3-dimensional tracking device with fast readout for ultra-high multiplicity events,” *Nucl. Instrum. Meth.* **A622** (2010) 316–367, arXiv:1001.1950 [physics.ins-det].
- [107] ALICE Collaboration, F. Carnesecchi, “Performance of the ALICE Time-Of-Flight detector at the LHC,” *JINST* **14** no. 06, (2019) C06023, arXiv:1806.03825 [physics.ins-det].
- [108] G. Charpak, R. Bouclier, T. Bressani, J. Favier, and C. Zupancic, “The Use of Multiwire Proportional Counters to Select and Localize Charged Particles,” *Nucl. Instrum. Meth.* **62** (1968) 262–268.
- [109] “Long term LHC schedule.”
<https://lhc-commissioning.web.cern.ch/schedule/LHC-long-term.htm>.
Accessed: 04.08.2021.
- [110] F. Sauli, “GEM: A new concept for electron amplification in gas detectors,” *Nucl. Instrum. Meth. A* **386** (1997) 531–534.
- [111] The ALICE Collaboration Collaboration, “Upgrade of the ALICE Time Projection Chamber,” tech. rep., Oct, 2013.
<https://cds.cern.ch/record/1622286>.
- [112] ALICE Collaboration, T. Gunji, “Future Upgrade and Physics Perspectives of the ALICE TPC,” *Nucl. Phys. A* **931** (2014) 1152–1157, arXiv:1408.3484 [physics.ins-det].
- [113] ALICE Collaboration, C. Lippmann, “Upgrade of the ALICE Time Projection Chamber,”.
- [114] A. Colaleo, A. Safonov, A. Sharma, and M. Tytgat, “CMS Technical Design Report for the Muon Endcap GEM Upgrade,” tech. rep., Jun, 2015.
<https://cds.cern.ch/record/2021453>.
- [115] T. Hildén, E. Brücken, J. Heino, M. Kalliokoski, A. Karadzhinova, R. Lauhakangas, E. Tuominen, and R. Turpeinen, “Optical quality assurance of GEM foils,” *Nucl. Instrum. Meth. A* **770** (2015) 113–122, arXiv:1704.06691 [physics.ins-det].
- [116] E. Brücken and T. Hildén, “GEM Foil Quality Assurance For The ALICE TPC Upgrade,” *EPJ Web Conf.* **174** (2018) 03004, arXiv:1704.06310 [physics.ins-det].
- [117] ALICE TPC upgrade Collaboration, J. E. Brücken and T. E. Hildén, “The GEM QA Protocol of the ALICE TPC Upgrade Project,” *PoS MPGD2017* (2019) 073, arXiv:1811.07043 [physics.ins-det].
- [118] ALICE Collaboration, B. Abelev *et al.*, “Centrality determination of Pb-Pb collisions at $\sqrt{s_{NN}} = 2.76$ TeV with ALICE,” *Phys. Rev.* **C88** no. 4, (2013) 044909, arXiv:1301.4361 [nucl-ex].

- [119] **ALICE Collaboration** Collaboration, “The ALICE definition of primary particles,” <https://cds.cern.ch/record/2270008>.
- [120] X.-N. Wang and M. Gyulassy, “HIJING: A Monte Carlo model for multiple jet production in p p, p A and A A collisions,” *Phys. Rev.* **D44** (1991) 3501–3516.
- [121] M. Gyulassy and X.-N. Wang, “HIJING 1.0: A Monte Carlo program for parton and particle production in high-energy hadronic and nuclear collisions,” *Comput. Phys. Commun.* **83** (1994) 307, arXiv:nucl-th/9502021 [nucl-th].
- [122] R. Brun, F. Bruyant, F. Carminati, S. Giani, M. Maire, A. McPherson, G. Patrick, and L. Urban, “GEANT Detector Description and Simulation Tool,”
- [123] Z.-W. Lin, C. M. Ko, B.-A. Li, B. Zhang, and S. Pal, “A Multi-phase transport model for relativistic heavy ion collisions,” *Phys. Rev. C* **72** (2005) 064901, arXiv:nucl-th/0411110.
- [124] J. Xu and C. M. Ko, “Pb-Pb collisions at $\sqrt{s_{NN}} = 2.76$ TeV in a multiphase transport model,” *Phys. Rev. C* **83** (2011) 034904, arXiv:1101.2231 [nucl-th].
- [125] R. J. Barlow, “Practical Statistics for Particle Physics,” *CERN Yellow Rep. School Proc.* **5** (2020) 149–197, arXiv:1905.12362 [physics.data-an].
- [126] **ALICE Collaboration**, K. Aamodt *et al.*, “Elliptic flow of charged particles in Pb–Pb collisions at 2.76 TeV,” *Phys. Rev. Lett.* **105** (2010) 252302, arXiv:1011.3914 [nucl-ex].
- [127] **ALICE Collaboration**, K. Aamodt *et al.*, “Higher harmonic anisotropic flow measurements of charged particles in Pb-Pb collisions at $\sqrt{s_{NN}}=2.76$ TeV,” *Phys. Rev. Lett.* **107** (2011) 032301, arXiv:1105.3865 [nucl-ex].
- [128] **ALICE Collaboration**, B. Abelev *et al.*, “Anisotropic flow of charged hadrons, pions and (anti-)protons measured at high transverse momentum in Pb-Pb collisions at $\sqrt{s_{NN}}=2.76$ TeV,” *Phys. Lett.* **B719** (2013) 18–28, arXiv:1205.5761 [nucl-ex].
- [129] **ALICE Collaboration**, B. B. Abelev *et al.*, “Elliptic flow of identified hadrons in Pb–Pb collisions at $\sqrt{s_{NN}} = 2.76$ TeV,” *JHEP* **06** (2015) 190, arXiv:1405.4632 [nucl-ex].
- [130] **ALICE Collaboration**, J. Adam *et al.*, “Higher harmonic flow coefficients of identified hadrons in Pb-Pb collisions at $\sqrt{s_{NN}} = 2.76$ TeV,” *JHEP* **09** (2016) 164, arXiv:1606.06057 [nucl-ex].
- [131] **ALICE Collaboration**, J. Adam *et al.*, “Anisotropic flow of charged particles in Pb-Pb collisions at $\sqrt{s_{NN}} = 5.02$ TeV,” *Phys. Rev. Lett.* **116** no. 13, (2016) 132302, arXiv:1602.01119 [nucl-ex].
- [132] **ALICE Collaboration**, S. Acharya *et al.*, “Searches for transverse momentum dependent flow vector fluctuations in Pb-Pb and p-Pb collisions at the LHC,” *JHEP* **09** (2017) 032, arXiv:1707.05690 [nucl-ex].

- [133] ALICE Collaboration, S. Acharya *et al.*, “Anisotropic flow of identified particles in Pb-Pb collisions at $\sqrt{s_{\text{NN}}} = 5.02$ TeV,” *JHEP* **09** (2018) 006, arXiv:1805.04390 [nucl-ex].
- [134] E. Shuryak, “The sounds of the Little and Big Bangs,” *Universe* **3** no. 4, (2017) 75, arXiv:1710.03776 [hep-ph].
- [135] W. Zhao, H.-j. Xu, and H. Song, “Collective flow in 2.76 A TeV and 5.02 A TeV Pb+Pb collisions,” *Eur. Phys. J.* **C77** no. 9, (2017) 645, arXiv:1703.10792 [nucl-th].
- [136] S. McDonald, C. Shen, F. Fillion-Gourdeau, S. Jeon, and C. Gale, “Hydrodynamic predictions for Pb+Pb collisions at 5.02 TeV,” *Phys. Rev.* **C95** no. 6, (2017) 064913, arXiv:1609.02958 [hep-ph].
- [137] JETSCAPE Collaboration, D. Everett *et al.*, “Multisystem Bayesian constraints on the transport coefficients of QCD matter,” *Phys. Rev. C* **103** no. 5, (2021) 054904, arXiv:2011.01430 [hep-ph].
- [138] A. Nakamura and S. Sakai, “Transport coefficients of gluon plasma,” *Phys. Rev. Lett.* **94** (2005) 072305, arXiv:hep-lat/0406009.
- [139] G. Nijs, W. van der Schee, U. Gürsoy, and R. Snellings, “A transverse momentum differential global analysis of Heavy Ion Collisions,” *Phys. Rev. Lett.* **126** no. 20, (2021) 202301, arXiv:2010.15130 [nucl-th].
- [140] ALICE Collaboration, S. Acharya *et al.*, “Systematic studies of correlations between different order flow harmonics in Pb-Pb collisions at $\sqrt{s_{\text{NN}}} = 2.76$ TeV,” *Phys. Rev.* **C97** no. 2, (2018) 024906, arXiv:1709.01127 [nucl-ex].
- [141] M. Luzum and J.-Y. Ollitrault, “Constraining the viscous freeze-out distribution function with data obtained at the BNL Relativistic Heavy Ion Collider (RHIC),” *Phys. Rev. C* **82** (2010) 014906, arXiv:1004.2023 [nucl-th].
- [142] M. Luzum, C. Gombeaud, and J.-Y. Ollitrault, “ v_4 in ideal and viscous hydrodynamics simulations of nuclear collisions at the BNL Relativistic Heavy Ion Collider (RHIC) and the CERN Large Hadron Collider (LHC),” *Phys. Rev. C* **81** (2010) 054910, arXiv:1004.2024 [nucl-th].
- [143] H. Mäntysaari, B. Schenke, C. Shen, and P. Tribedy, “Imprints of fluctuating proton shapes on flow in proton-lead collisions at the LHC,” *Phys. Lett. B* **772** (2017) 681–686, arXiv:1705.03177 [nucl-th].
- [144] W. van der Schee, P. Romatschke, and S. Pratt, “Fully Dynamical Simulation of Central Nuclear Collisions,” *Phys. Rev. Lett.* **111** no. 22, (2013) 222302, arXiv:1307.2539 [nucl-th].
- [145] P. Romatschke and U. Romatschke, *Relativistic Fluid Dynamics In and Out of Equilibrium*. Cambridge Monographs on Mathematical Physics. Cambridge University Press, 5, 2019. arXiv:1712.05815 [nucl-th].

-
- [146] M. Strickland, “Small system studies: A theory overview,” *Nucl. Phys. A* **982** (2019) 92–98, arXiv:1807.07191 [nucl-th].
- [147] C. Loizides, “Experimental overview on small collision systems at the LHC,” *Nucl. Phys. A* **956** (2016) 200–207, arXiv:1602.09138 [nucl-ex].
- [148] J. L. Nagle and W. A. Zajc, “Small System Collectivity in Relativistic Hadronic and Nuclear Collisions,” *Ann. Rev. Nucl. Part. Sci.* **68** (2018) 211–235, arXiv:1801.03477 [nucl-ex].
- [149] B. Schenke, “The smallest fluid on earth,” arXiv:2102.11189 [nucl-th].



ORIGINAL PAPERS

I

HIGHER HARMONIC NON-LINEAR FLOW MODES OF CHARGED HADRONS IN Pb- Pb COLLISIONS AT $\sqrt{s_{NN}} = 5.02$ TeV

by

ALICE Collaboration, S. Acharya et al. 2020

JHEP 05 (2020) 085, arXiv:2002.0633 [nucl-ex]

<https://arxiv.org/abs/2002.00633>

Reproduced with kind permission by Springer.

Higher harmonic non-linear flow modes of charged hadrons in Pb-Pb collisions at $\sqrt{s_{\text{NN}}} = 5.02$ TeV



ALICE

The ALICE collaboration

E-mail: ALICE-publications@cern.ch

ABSTRACT: Anisotropic flow coefficients, v_n , non-linear flow mode coefficients, $\chi_{n,mk}$, and correlations among different symmetry planes, $\rho_{n,mk}$ are measured in Pb-Pb collisions at $\sqrt{s_{\text{NN}}} = 5.02$ TeV. Results obtained with multi-particle correlations are reported for the transverse momentum interval $0.2 < p_{\text{T}} < 5.0$ GeV/ c within the pseudorapidity interval $0.4 < |\eta| < 0.8$ as a function of collision centrality. The v_n coefficients and $\chi_{n,mk}$ and $\rho_{n,mk}$ are presented up to the ninth and seventh harmonic order, respectively. Calculations suggest that the correlations measured in different symmetry planes and the non-linear flow mode coefficients are dependent on the shear and bulk viscosity to entropy ratios of the medium created in heavy-ion collisions. The comparison between these measurements and those at lower energies and calculations from hydrodynamic models places strong constraints on the initial conditions and transport properties of the system.

KEYWORDS: Heavy Ion Experiments

ARXIV EPRINT: [2002.00633](https://arxiv.org/abs/2002.00633)

Contents

1	Introduction	1
2	Formalism and observables	3
3	Experimental setup and data analysis	4
4	Systematic uncertainties	5
5	Results	8
6	Summary	16
A	List of observables	18
	The ALICE collaboration	26

1 Introduction

One of the primary goals in the ultra-relativistic heavy-ion collision programs at the Relativistic Heavy Ion Collider (RHIC) and the Large Hadron Collider (LHC) is to study the nuclear matter at extreme conditions. The pressure gradients in the strongly interacting matter, known as the Quark-Gluon Plasma (QGP), are believed to drive the hydrodynamic expansion observed through anisotropy in multi-particle correlations in high energy collisions at RHIC and the LHC [1, 2]. The anisotropic expansion of the medium, commonly referred to as anisotropic flow [1], can be characterized by a Fourier decomposition of the azimuthal particle distribution with respect to the reaction plane [3, 4]

$$\frac{dN}{d\varphi} \propto 1 + 2 \sum_{n=1}^{\infty} v_n \cos(n(\varphi - \psi_{\text{RP}})), \tag{1.1}$$

where the flow coefficient v_n is the magnitude of the n -th order flow, and the reaction plane ψ_{RP} defined by the beam direction and impact parameter which is defined as the distance between the centers of two colliding nuclei. Due to fluctuations in the initial state energy density profile, it is useful to define symmetry planes of different orders, where the n -th order plane ψ_n defines the orientation of the n -th order complex flow vector $V_n \equiv v_n e^{in\psi_n}$. The expansion of the azimuthal distribution about ψ_n also yields finite values of odd coefficients [5, 6]. Anisotropic flow measurements through two- and multi-particle azimuthal correlations [6–13] have provided important information on the medium response and in particular its transport coefficients such as the shear viscosity to entropy density ratio (η/s), bulk viscosity to entropy density ratio (ζ/s) and the equation of state [14]. Studies have shown the relativistic hydrodynamic nature of the medium [1, 2, 15–22], with η/s close to the AdS/CFT minimum $1/(4\pi)$ [23].

The initial state eccentricity, determined from the energy density profile, is obtained from the definition [5]

$$\varepsilon_n e^{in\Phi_n} = -\{r^n e^{in\varphi}\}/\{r^n\}, \quad n \geq 2, \quad (1.2)$$

where the curly brackets denote the average over the transverse plane, i.e. $\{\dots\} = \int dx dy e(x, y, \tau_0)(\dots)$, r is the distance to the system's center of mass, φ is the azimuthal angle, $e(x, y, \tau_0)$ is the energy density at the initial time τ_0 , and Φ_n is the participant plane angle, defining the spatial symmetry of the nuclear constituents in the participant region (see refs. [24, 25]). Hydrodynamic models demonstrate that the second and the third harmonic flow coefficients exhibit an almost linear dependence on the initial eccentricity coefficients ε_n [26]. Considering that the anisotropic expansion is a result of a hydrodynamic evolution governed by η/s , a measurement of the second and third harmonics combined with hydrodynamic calculations can constrain the properties of the medium. Several estimates for the limits of η/s were determined through measurements of elliptic flow coefficient v_2 [27–32] and their comparison with hydrodynamic calculations. Consequently, the early constraints placed the value of η/s between 0.08 to 0.16 [33–35]. However, the limited sensitivity of the elliptic flow to η/s and the large uncertainty in the initial state anisotropy inhibit a precise determination of the value of η/s [34, 36–38], and its temperature dependence, which was recently shown to be explorable during the second run of LHC [39, 40]. In addition, part of the anisotropic flow can also originate from the hadronic phase [41–43]. It has been shown in [43, 44] that the inclusion of the temperature dependent bulk viscosity $\zeta/s(T)$ in hydrodynamic simulation lead to a better description of the average transverse momentum of charged hadrons and on the elliptic flow coefficient. The effects of bulk viscosity should be considered when extracting any transport coefficient from the data [45–47].

Flow harmonics of order $n \geq 3$ reveal finer details of initial conditions [6, 8, 10, 11, 13], enabling to constrain η/s better [39, 40, 48, 49]. Higher flow harmonics $n > 3$ do not exhibit a linear response to the initial anisotropy [26] as a finite contribution is induced by the initial state anisotropy of the lower orders [50, 51]. For example, the fourth order flow vector V_4 gains contributions not only from the fourth order flow (linear flow mode), but also from the second order flow (non-linear flow mode). Starting from the V_n estimators studied in [50], the flow can be expressed as a vector sum of the linear and non-linear modes

$$\begin{aligned} V_4 &= V_{4L} + \chi_{4,22} V_2^2, \\ V_5 &= V_{5L} + \chi_{5,23} V_2 V_3, \\ V_6 &= V_{6L} + \chi_{6,222} V_2^3 + \chi_{6,33} V_3^2 + \chi_{6,24} V_2 V_{4L}, \\ V_7 &= V_{7L} + \chi_{7,223} V_2^2 V_3 + \chi_{7,34} V_3 V_{4L} + \chi_{7,25} V_2 V_{5L}, \\ V_8 &= V_{8L} + \chi_{8,2222} V_2^4 + \chi_{8,233} V_2 V_3^2 + \mathcal{E}(V_{4L}, V_{5L}, V_{6L}), \end{aligned} \quad (1.3)$$

where $\chi_{n,mk}$ is called non-linear flow mode coefficient, characterizing the non-linear flow mode induced by the lower order harmonics. The high order linear component is denoted by V_{nL} , while the many higher order linear couplings are depicted by $\mathcal{E}(\dots)$ for V_8 . The

V_{nL} is linearly related to a cumulant-defined anisotropy [52]

$$\varepsilon'_4 e^{i4\Phi'_4} = \varepsilon_4 e^{i4\Phi_4} + \frac{3\langle r^2 \rangle^2}{\langle r^4 \rangle} \varepsilon_2 e^{i4\Phi_2} \quad (1.4)$$

as opposed to the relation $v_n \propto \varepsilon_n$, where v_n is the magnitude of the total contribution and ε_n is given by eq. (1.2).

In earlier measurements performed by ALICE [53], the non-linear flow mode coefficients were measured up to the sixth harmonic order in Pb-Pb collisions at $\sqrt{s_{NN}} = 2.76$ TeV. It was indicated that the coefficients $\chi_{5,23}$ and $\chi_{6,33}$ are sensitive not only to η/s , but also to the distinctive energy density profiles generated by different initial conditions. It was observed that the hydrodynamic models with their respective initial conditions Monte-Carlo (MC)-Glauber [54, 55], MC-KLN [33, 56], and IP-Glasma [57]), are unable to reproduce these measurements, which indicates that the model tuning and η/s parameterization require further work.

In this paper, measurements of high order flow coefficients in Pb-Pb collisions at $\sqrt{s_{NN}} = 5.02$ TeV are presented. The flow coefficients v_n are measured up to the ninth harmonic, v_9 , extending the previous measurements of v_2-v_6 [58]. The data recorded during the 2015 heavy-ion run of the LHC allow the measurements of non-linear flow mode and correlations between symmetry planes to be extended. A total of six non-linear flow mode coefficients are measured, including the non-linear flow mode coefficient $\chi_{7,223}$, for which the sensitivity to η/s is expected to be significantly stronger than for the lower odd-harmonic coefficient $\chi_{5,23}$ [37, 59]. The results are compared with those in Pb-Pb collisions at $\sqrt{s_{NN}} = 2.76$ TeV [53] and various state of the art hydrodynamical calculations.

2 Formalism and observables

In order to separate the linear and non-linear contributions from eq. (1.3), one assumes the respective contributions to be uncorrelated [60]. For example for the fourth order V_4 , by mean-squaring the equations in eq. (1.3) and setting $\langle (V_2^*)^2 V_{4L} \rangle \simeq \langle V_2^2 V_{4L}^* \rangle \simeq 0$, the linear part can be derived

$$\underbrace{\langle |V_{4L}|^2 \rangle}_{v_{4L}}^{\frac{1}{2}} = \left(\underbrace{\langle |V_4|^2 \rangle}_{v_4^2} - \underbrace{\chi_{4,22}^2 \langle |V_2|^4 \rangle}_{v_{4,NL}^2} \right)^{\frac{1}{2}}. \quad (2.1)$$

Here $\langle \rangle$ denotes an average over all events and $*$ the complex conjugate. The magnitudes of the linear and non-linear flow coefficients are denoted with v_{4L} and $v_{4,NL}$, respectively.

The observables of the non-linear response mode are constructed from the projections of flow vectors on to the symmetry planes of lower harmonics [61, 62]. For $n = 4$, the magnitude of the non-linear response mode is given by

$$v_{4,22} = \frac{\Re(V_4(V_2^*)^2)}{\sqrt{\langle |V_2|^4 \rangle}} \approx \langle v_4 \cos(4\psi_4 - 4\psi_2) \rangle, \quad (2.2)$$

where $v_{4,22}^2 \equiv v_{4,NL}^2 \equiv \chi_{4,22}^2 \langle |V_2|^4 \rangle$. The right-hand side approximation holds if the low ($n = 2, 3$) and high order flow is weakly correlated. Only the fourth harmonic is shown here and the complete list of other harmonics are provided in appendix A.

The contributions from short-range correlations unrelated to the common symmetry plane, commonly referred to as “non-flow”, are suppressed by using the subevent method where the event is divided into two subevents separated by a pseudorapidity gap [4]. The underlying multi-particle correlation coefficient for subevent A is $v_{4,22}^A = \langle \langle \cos(4\varphi_1^A - 2\varphi_2^B - 2\varphi_3^B) \rangle \rangle / \langle \langle \cos(2\varphi_1^A + 2\varphi_2^A - 2\varphi_3^B - 2\varphi_4^B) \rangle \rangle^{1/2}$ as determined using eq. (2.2),¹ and a similar treatment is applied for the subevent B, for which $v_{4,22}^B$ is obtained by swapping B for A in the aforementioned expression. The final result is then the average of the results from subevents A and B.

The symmetry-plane correlations are defined as the ratio between the magnitude of the non-linear flow modes and flow coefficients [63]. For $n = 4$, one obtains

$$\rho_{4,22} = \frac{v_{4,22}}{v_4} \approx \langle \cos(4\psi_4 - 4\psi_2) \rangle. \quad (2.3)$$

A value close to zero indicates weakly correlated symmetry planes, while a value reaching one implies a strong correlation. The correlations between symmetry planes reflect those of the corresponding initial state participant planes [53, 64], therefore providing valuable information on the evolution of the QGP. Correlations between symmetry planes have been previously studied using the event-plane method [64, 65], *event plane* describing an experimentally approximated symmetry plane. However, these results depend on the event-plane resolution [66], which complicates the comparison between data and theoretical calculations. Recently, the ALICE Collaboration has measured symmetry-plane correlations [53]. It was found that the correlations of symmetry planes of higher harmonics with second and third order symmetry planes increased for less central collisions. Furthermore, the comparison with hydrodynamic calculations revealed the importance of final-state collective dynamics in addition to the initial-state density fluctuations [33] as it is known that the observation of correlated final state symmetry planes implies the existence of fluctuations in the initial state eccentricity vectors.

The fourth non-linear flow mode coefficient, with the aforementioned assumptions, is given by [59]

$$\chi_{4,22} = \frac{v_{4,22}}{\sqrt{\langle v_2^4 \rangle}}. \quad (2.4)$$

3 Experimental setup and data analysis

The data sample consists of about 42 million minimum bias Pb-Pb collisions at $\sqrt{s_{NN}} = 5.02$ TeV, recorded by ALICE [67, 68] during the 2015 heavy-ion run at the LHC. Detailed descriptions of the detector can be found in [67, 69, 70]. The trigger plus crossing of beam is provided by signals from the two scintillator arrays, V0A and V0C [67, 71], covering the pseudorapidity intervals $2.8 < \eta < 5.1$ and $-3.7 < \eta < -1.7$, respectively. A primary vertex position less than 10 cm in beam direction from the nominal interaction point is required. Pile-up events are removed by correlating the V0 multiplicity with the multiplicity from the first Silicon Pixel Detector (SPD) [67, 72] layer. To further remove pile-up events,

¹For practical usage, the self-correlation is recursively removed from three- and four-particle correlations, resulting in modified equations.

information from the Time-of-Flight (TOF) [73] detector is used: the multiplicity estimates from the SPD are correlated with those imposed with a TOF readout requirement. The centrality of the collision is determined using information from the V0 arrays. Further details on the centrality determination in ALICE are given in [74]. Only events in the centrality range 0% to 60% are used in the analysis.

The track reconstruction is based on combined information from the Time Projection Chamber (TPC) [67, 75] and the Inner Tracking System (ITS) [67, 72]. To avoid contributions from secondary particles, the tracks are required to have a distance of closest approach to the primary vertex of less than 3.2 cm and 2.4 cm in the longitudinal and transverse directions, respectively. Such a loose Distance of Closest Approach (DCA) track cut is chosen to improve the uniformity of the φ -distribution for the Q_n -vector calculation. Furthermore, each track is required to have at least 70 TPC space points out of the maximum 159, and the average χ^2 per degree of freedom of the track fit to the TPC space points to be less than 2. Minimum 2 hits are required in the ITS. In order to counteract the effects of track reconstruction efficiency and contamination from secondary particles [76], a HIJING simulation [77, 78] with GEANT3 [79] detector model is employed to construct a p_T -dependent track weighting correction. The track reconstruction efficiency is approximately 65% at $p_T = 0.2$ GeV/ c and 80% at $p_T > 1.0$ GeV/ c , while the contamination from secondaries is less than 10% and 5%, respectively. Only particle tracks within the transverse momentum interval $0.2 < p_T < 5.0$ GeV/ c and pseudorapidity range $0.4 < |\eta| < 0.8$ are considered. A pseudorapidity gap $|\Delta\eta| > 0.8$ is used to suppress the non-flow. The observables in this analysis are measured with multi-particle correlations obtained using the generic framework for anisotropic flow analysis [80].

4 Systematic uncertainties

The systematic uncertainties are estimated by varying criteria for selecting the events and tracks. The systematic evaluation is done by independently varying the selection criteria, and the results given by this variation are then compared to the default criteria given in section 3. The total uncertainty is obtained by assuming that the individual sources are uncorrelated, which are then quadratically summed.

Summaries of the relative systematic uncertainties are given in tables 1–4. Uncertainties stemming from the event selection criteria are estimated by changing the rejection based on the vertex position from 10 cm to 8 cm and by adjusting the pile-up rejection criteria. It is found that the contribution to the uncertainty is generally negligible, below 1%. An alternative centrality determination is employed using the event multiplicity estimates from the SPD layers. The uncertainty related to the centrality determination is less than 2% for all observables, except for v_7 to v_9 for which the uncertainty increases to 10%.

The ALICE detector can be operated with either positive or negative solenoid magnetic field polarity. The polarity of the field affects the direction of the charged particle curvature, while also subjecting the structural materials of the detector itself to either a positive or negative magnetic field. The default data set is composed of events recorded with both polarities. The results produced with exclusively either negative or positive magnetic field configurations deviate from the default by up to 15% in case of flow coefficients, and 28% for

Type	v_2	v_3	v_4	v_5	v_6	v_7	v_8	v_9
Event Selection								
z -vertex cut	< 0.1	< 0.1	< 0.1	0.5	1.2	1.6	1.8	1.7
Pile-up rejection	< 0.1	< 0.1	< 0.1	0.2	0.8	1.3	1.7	2.0
Centrality Determination								
SPD	0.6	0.3	0.3	1.1	3.9	6.6	9.1	11.5
Tracking								
Magnetic field polarity	0.1	0.1	1.7	2.4	4.1	6.8	10.5	15.2
Tracking mode	0.1	0.2	< 0.1	2.4	5.4	7.2	7.6	6.8
Number of TPC space points	0.7	1.2	1.4	1.5	1.6	1.7	1.7	1.8
Space charge distortion	< 0.1	< 0.1	< 0.1	0.2	0.7	1.2	1.7	2.3
Non-flow								
Charge combinations ($--/+ +$)	1.1	0.7	0.8	2.9	6.2	9.3	12.3	15.2
Overall								
Overall	1.5	1.4	2.4	4.9	10.3	15.4	20.4	25.6

Table 1. Relative systematic uncertainties of the flow coefficients. The uncertainties are given in percents and are categorized into four groups: event selection, centrality determination, tracking and non-flow. The overall systematic uncertainty is obtained by summing in quadrature the uncertainties from each source.

Type	$v_{4,22}$	$v_{5,23}$	$v_{6,222}$	$v_{6,33}$	$v_{6,24}$	$v_{7,223}$
Event Selection						
z -vertex cut	0.1	0.1	0.2	0.3	0.2	0.1
Pile-up rejection	< 0.1	0.1	0.4	0.5	0.4	< 0.1
Centrality Determination						
SPD	1.5	0.7	0.3	0.3	0.7	1.4
Tracking						
Magnetic field polarity	0.5	0.5	1.9	3.2	4.4	5.5
Tracking mode	0.1	0.4	1.4	1.7	1.1	< 0.1
Number of TPC space points	3.8	2.3	1.5	1.4	2.1	3.5
Space charge distortion	0.2	0.1	1.8	4.0	6.7	9.9
Non-flow						
Charge combinations ($--/+ +$)	4.2	4.7	5.8	7.4	9.6	14.3
Overall						
Overall	5.9	5.3	6.7	9.3	12.7	18.6

Table 2. Relative systematic uncertainties of the harmonic projections $v_{n,mk}$.

$\rho_{7,223}$. In order to estimate the non-flow contributions from resonance decays, the like-sign technique [2] which correlates exclusively either positively or negatively charged particles, is employed. The difference with respect to the results obtained by selecting all charged particles is assigned as a systematic uncertainty. In general, this uncertainty ranges from 2% to 15%. The effect from the space charge distortions in the TPC drift volume because

Type	$\rho_{4,22}$	$\rho_{5,23}$	$\rho_{6,222}$	$\rho_{6,33}$	$\rho_{6,24}$	$\rho_{7,223}$
Event Selection						
z -vertex cut	0.1	0.3	0.1	0.2	0.8	2.5
Pile-up rejection	0.1	0.3	0.1	0.3	1.0	2.2
Centrality Determination						
SPD	0.9	0.3	0.7	0.9	1.2	1.5
Tracking						
Magnetic field polarity	< 0.1	1.8	6.8	10.1	13.8	18.0
Tracking mode	0.1	0.3	0.8	2.6	6.1	11.2
Number of TPC space points	< 0.1	0.7	0.1	< 0.1	1.0	2.8
Space charge distortion	0.2	0.2	1.5	3.5	6.7	11.1
Non-flow						
Charge combinations ($--/++$)	3.1	3.6	3.6	5.6	8.7	12.9
Overall						
Overall	3.3	4.2	7.9	12.4	18.8	27.5

Table 3. Relative systematic uncertainties of the symmetry-plane correlations $\rho_{n,mk}$.

Type	$\chi_{4,22}$	$\chi_{5,23}$	$\chi_{6,222}$	$\chi_{6,33}$	$\chi_{6,224}$	$\chi_{7,223}$
Event Selection						
z -vertex cut	< 0.1	0.1	0.3	0.3	0.3	0.1
Pile-up rejection	< 0.1	0.1	0.5	0.6	0.5	0.1
Centrality Determination						
SPD	0.2	0.6	1.0	1.0	0.7	0.1
Tracking						
Magnetic field polarity	0.6	0.2	2.5	4.1	5.1	5.5
Tracking mode	< 0.1	0.2	1.4	1.7	1.2	0.2
Number of TPC space points	< 0.1	0.2	0.5	0.7	0.9	1.1
Space charge distortion	0.2	0.1	1.9	4.4	7.1	10.1
Non-flow						
Charge combinations ($--/++$)	0.2	1.5	7.7	12.0	14.4	15.0
Overall						
Overall	0.7	1.7	8.5	13.6	17.0	19.0

Table 4. Relative systematic uncertainties of the non-linear flow mode coefficients $\chi_{n,mk}$.

of the higher interaction rates is estimated by comparing results from different regions of the TPC, one for $\eta > 0$ and the other $\eta < 0$. The maximum uncertainty is evaluated less than 15%. The track reconstruction related uncertainty, referred to as tracking mode, is evaluated by comparing the results obtained with tracks for which the requirement for the number of hits in the ITS layers is changed. In this case, the uncertainty is generally less than 15%, and a maximum 20% is evaluated for $\rho_{7,223}$. Furthermore, the track selection criteria is tightened by increasing the minimum number of the TPC space points from 70 to 90, resulting in uncertainties around 1% to 3%.

5 Results

In this section, the measurements of the flow coefficients, the non-linear modes, symmetry-plane correlations and the non-linear flow mode coefficients are presented. They are compared with hydrodynamic calculations with various settings [25, 57, 81, 82]. The first calculation is based on an event-by-event viscous hydrodynamic model with EKRT initial conditions [25, 81] using a value of $\eta/s = 0.20$ (param0) and a temperature dependent $\eta/s(T)$ (param1). For both configurations, ζ/s is set to zero. The visualization of the model parameters can be found in figure 1. The second calculation employs the iEBE-VISHNU hybrid model [83] with AMPT [84–86] and T_RENTo [87] initial conditions. The $\eta/s = 0.08$ and $\zeta/s = 0$ are taken for param2, while the $\eta/s(T)$ and $\zeta/s(T)$ (param3), extracted using Bayesian analysis [45] (except for the normalization factors) from a fit to the final multiplicities of the charged hadron spectra in Pb-Pb collisions at $\sqrt{s_{\text{NN}}} = 5.02$, are used for the T_RENTo initial conditions. The third calculation uses the MUSIC model [88] with IP-Glasma [89] initial conditions with a value of $\eta/s = 0.095$ and $\zeta/s(T)$ (param4). Each of the $\eta/s(T)$ parameterizations is adjusted to reproduce the measured charged hadron multiplicity, the low- p_{T} region of the charged-hadron spectra, and v_n from central to mid-peripheral collisions up to the fourth harmonic at RHIC and the LHC [25, 44, 57, 84, 90–92]. The model configurations are summarized in table 5.

In figure 2, the measurements of the flow coefficients from v_2 to v_9 are presented. The first two coefficients up to v_6 have been extensively measured at RHIC and LHC [6–13], and more recently also v_7 [49]. The present analysis reports the first results on higher harmonic coefficients from v_7 to v_9 in ALICE, where v_8 and v_9 are measured for the first time at the LHC energies. The coefficients exhibit a modest centrality dependence, and their magnitude is similar to that of v_7 within statistical and systematic uncertainties. The measurements up to v_6 are compatible with those published previously [58].

Figure 2 also shows the comparison between the measured v_n and model calculations. The hydrodynamic calculations qualitatively reproduce the v_n measurements, and the overall model depiction is very good for v_2 and v_3 . For $n \geq 4$ however, the calculations show noticeable overestimations, especially in mid-peripheral collisions. For v_5 and v_6 , the data are well described by EKRT+param0, showing a better agreement than the temperature dependent EKRT+param1. The data are also described by AMPT+param2, for which the agreement for v_5 and v_6 is good in mid-central and mid-peripheral collisions. IP-Glasma+param4 and T_RENTo+param3 overestimate the measurements by a factor of 1.5~2. Values of v_7 are well estimated by AMPT+param2, and v_8 by both AMPT+param2 and T_RENTo+param3 within uncertainties. In other cases, the data are overestimated by the other models.

To study the dependence on the harmonic order of the anisotropy coefficients [97], figure 3 shows values of different coefficients as a function of n for all centralities. This presentation is particularly well suited in visualizing the harmonic dependence, and the acoustic scaling [97] observed across the harmonic orders. The decrease in v_n with increasing harmonic order up to $n = 7$ indicates viscous damping [97]. This means that the higher frequency waveform propagating through the medium should get more damped

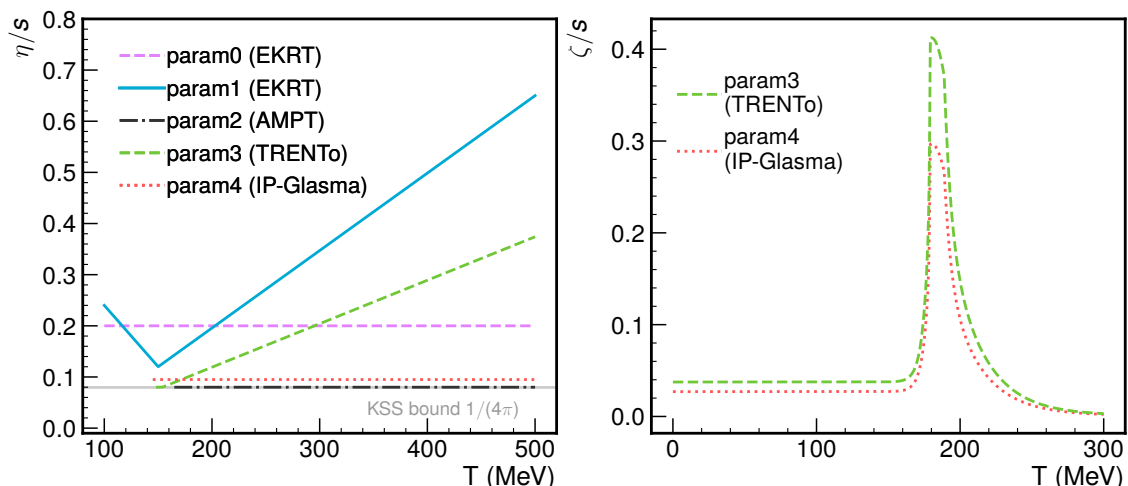


Figure 1. The five different parameterizations of η/s and ζ/s used for the different hydrodynamic model calculations are shown in the left and right panel. Note that the functional form of $\zeta/s(T)$ is the same for param3 and param4 and taken from eq. 5 in [45] motivated by refs. [43, 93–95]. For the parameters with T_RENTo initial condition, the ones based on identified yields are taken from table 4 in [45]. The ζ/s normalization factor used with IP-Glasma (T_RENTo) initial conditions is 0.9 (1.25). The models with $\zeta/s = 0$ are not shown on the right.

Model	Hydrodynamic code	Initial conditions	η/s	ζ/s
EKRT+param0 [25, 81]	EbyE [25, 96]	EKRT [25, 81]	0.20	0
EKRT+param1 [25, 81]	EbyE [25, 96]	EKRT [25, 81]	$\eta/s(T)$ [25]	0
AMPT+param2 [82]	iEBE-VISHNU [83]	AMPT [84–86]	0.08	0
T _R ENTo+param3 [82]	iEBE-VISHNU [83]	T _R ENTo($p = 0$) [87]	$\eta/s(T)$ [45, 82]	$\zeta/s(T)$ [45, 82]
IP-Glasma+param4 [57]	MUSIC [88]	IP-Glasma [89]	0.095	$\zeta/s(T)$ [57]

Table 5. Hydrodynamic model configurations. Shown are the key components such as initial condition models, and η/s and ζ/s parameterizations. With T_RENTo initial conditions, an entropy deposition parameter $p = 0$ [82] is used for all calculations.

until freeze-out takes place. In [98, 99] the viscosity effect is explained as the main contributor to the observed damping. It is speculated, that another driving factor is the phase of the oscillation itself, which also contributes to the magnitude at the time of freeze-out. The measurements show that there is a hint of $v_9 > v_8$, as also predicted in the acoustic model [97].

Figure 4 presents the higher order flow coefficients as well as their linear and non-linear flow modes up to the seventh order as a function of centrality. For the flow harmonics v_4 and v_5 , presented in panels (a) and (b), respectively, the non-linear contributions are small in central collisions, where the linear contribution is dominant. A weak centrality dependence is observed for the linear component. In case of v_4 , significant contributions from the second order arise in less central collisions. The v_5 coefficient, on the other hand, is largely induced by the low order v_2 and v_3 , indicated by the large $v_{5,23}$.

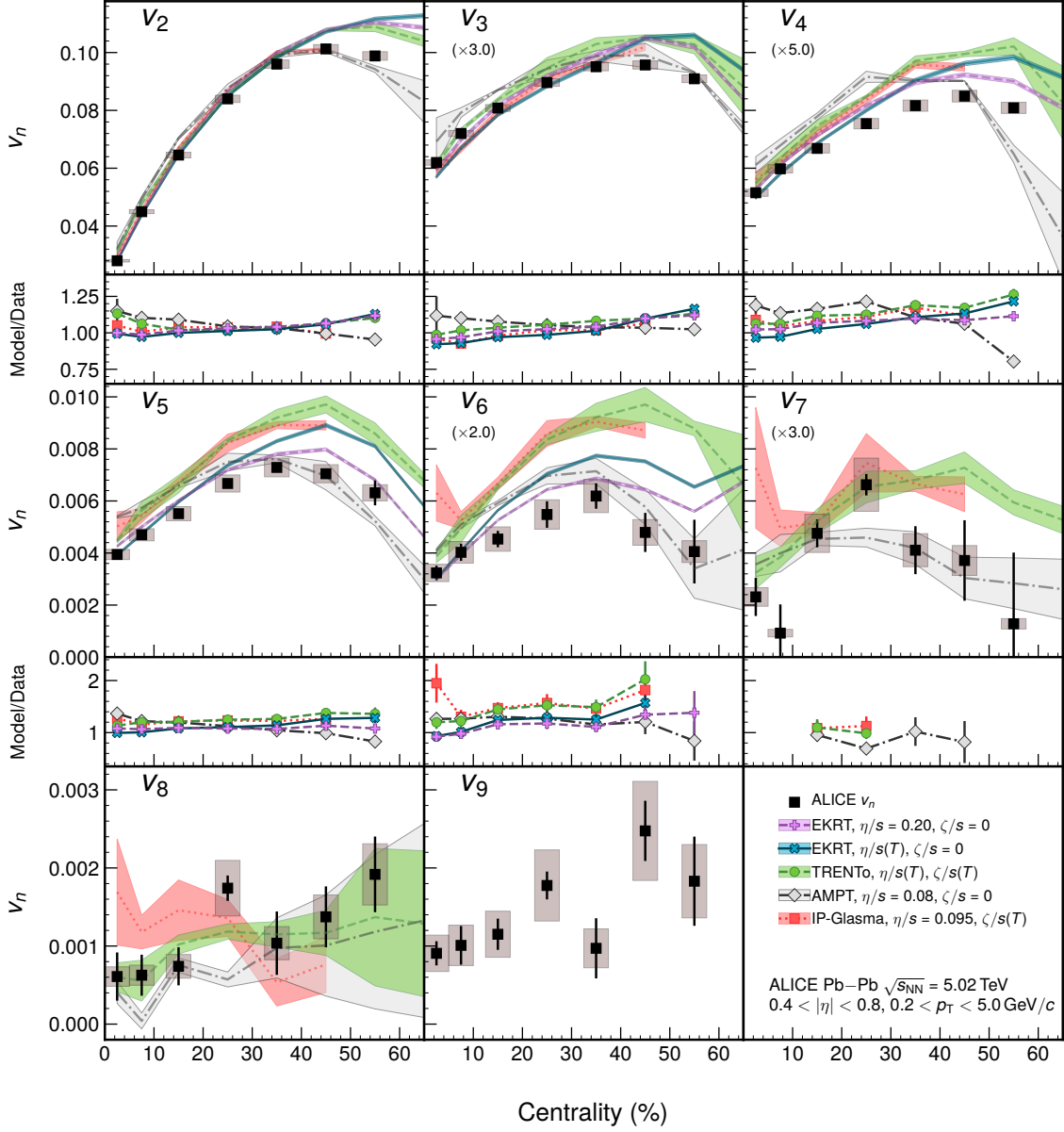


Figure 2. Flow harmonics up to the ninth order as a function of centrality, along with five different hydrodynamic calculations shown as color bands, each representing different configurations. For the black markers representing the measured data points, the systematic uncertainty is indicated by the gray patches around the markers. The bands indicate the extent of the uncertainty of the corresponding calculation. On the bottom part of each panel, the ratios between model calculations and the data are shown with symbols. Ratios with uncertainties larger than 1 are not shown in the ratio panel. For some panels, the points are scaled by an indicated factor for better visibility across the panels.

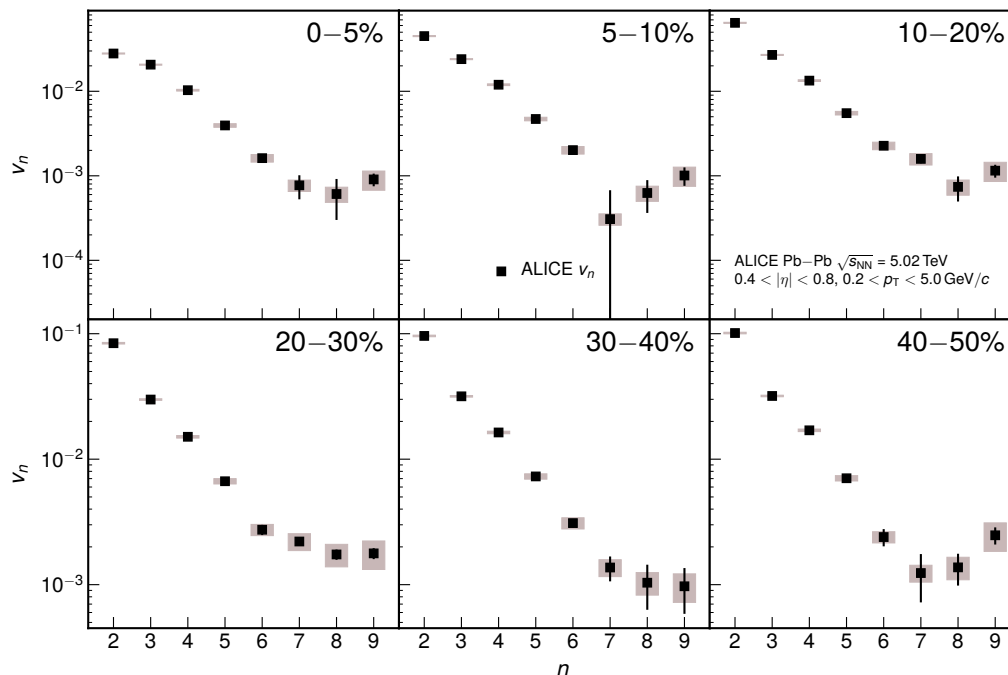


Figure 3. v_n as a function of the harmonic order n for various centrality intervals.

Panels (c) and (d) of figure 4 show the flow modes of v_6 and v_7 . Only the non-linear flow modes of v_6 and v_7 are presented. The $v_{6,222}$ increases from zero to approximately half of the total v_6 in mid-central collisions, while the other mode, $v_{6,33}$, has a much weaker centrality dependence. The relatively large magnitude of these flow modes imply strong contributions from the second and third order harmonics. Finally, $v_{6,24}$ follows the trend of the total magnitude. The magnitude of $v_{6,24}$ comes close to the total, which in turn suggests not only strong contributions from the second harmonic order, but also the fourth one. The $v_{6,24}$ induced by the fourth order is seen to be the dominant contribution to the sixth order from 10% centrality classes and higher. For the seventh order v_7 , there are three non-linear contributions, of which $v_{7,223}$ is measured. The centrality dependence is similar as with the v_6 coefficient, and there is a similar general trend as for the lower order harmonics among the non-linear flow modes.

The coefficients $\rho_{n,mk}$, quantifying the correlations amongst different symmetry planes, are presented as a function of centrality in figure 5. Except for $\rho_{6,33}$, all coefficients indicate an increase in correlation between symmetry planes with increasing centrality class of the collision. The measurements generally agree with the ones obtained at the lower energy. The $\rho_{6,222}$ is the only coefficient for which an energy dependence can be observed. The hydrodynamic calculations reproduce the measurements within the large theoretical uncertainties. For $\rho_{4,22}$, $\rho_{5,23}$, and $\rho_{6,222}$, TRENTo+param3 however underestimates the data in mid-central collisions.

Finally, the non-linear flow mode coefficients are presented in figure 6. Six coefficients are measured, of which four are compared with the lower beam energy results available

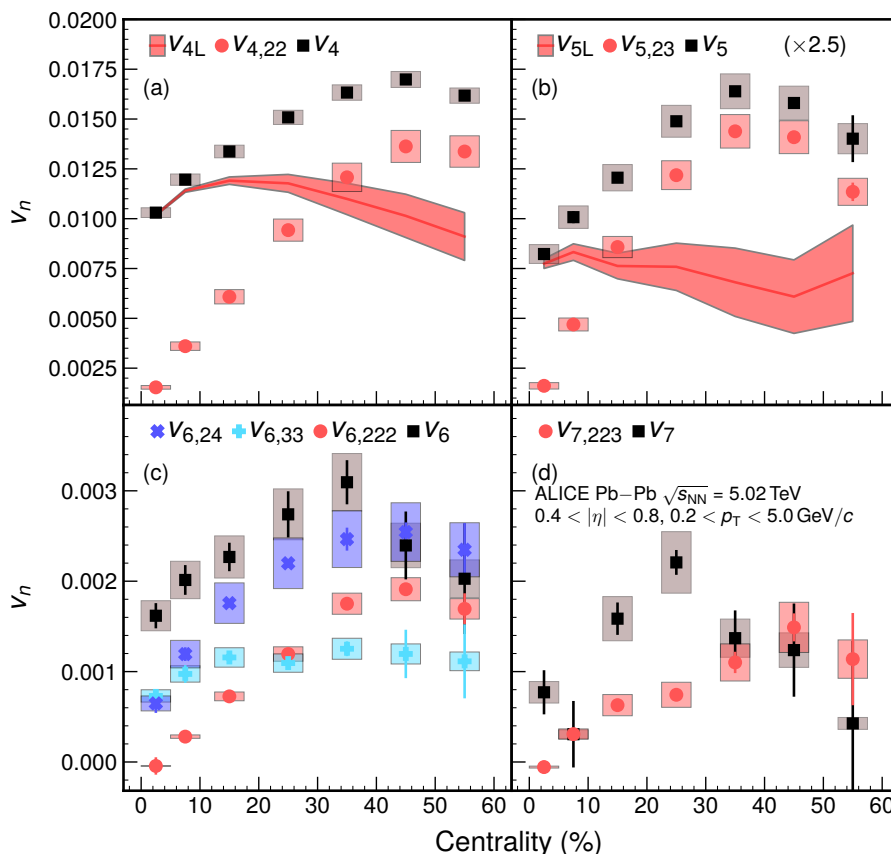


Figure 4. Linear and non-linear flow modes as a function of centrality. The total contribution measured in Pb-Pb collisions at $\sqrt{s_{\text{NN}}} = 5.02$ TeV is shown as black squares. Various non-linear contributions are presented in different red and blue colors, while the linear part, extracted from the aforementioned contributions, is shown as a red band. For panel (b), the data points are scaled by 2.5 for better visibility across the panels.

in [53]. For $\chi_{4,22}$ and $\chi_{5,23}$, the centrality dependence and overall magnitude agree well with the results from the lower beam energy. The centrality dependence of the new data is similar to the previous results: a larger value in more central collisions, decreasing close to unity towards 50% centrality.

All of the non-linear flow mode coefficients for the sixth harmonic agree with the previous measurements. The centrality dependence of $\chi_{6,222}$ is similar to the ones of the lower order coefficients, and the overall magnitude similar to $\chi_{4,22}$. As for $\chi_{6,33}$, no clear centrality dependence is observed within the current experimental uncertainties. Whereas the previous measurements are unable to distinguish between the magnitudes of $\chi_{6,222}$ and $\chi_{6,33}$, the current results show that $\chi_{6,222} > \chi_{6,33}$ across the whole centrality interval. For $\chi_{7,223}$, the overall magnitude is larger than for the other non-linear flow mode coefficients.

The hydrodynamic calculations for the non-linear flow mode coefficients show slightly more variation compared to the symmetry-plane correlations. As seen from the panels of figure 6, one observes the reproduction of the data points by EKRT+param0 up to

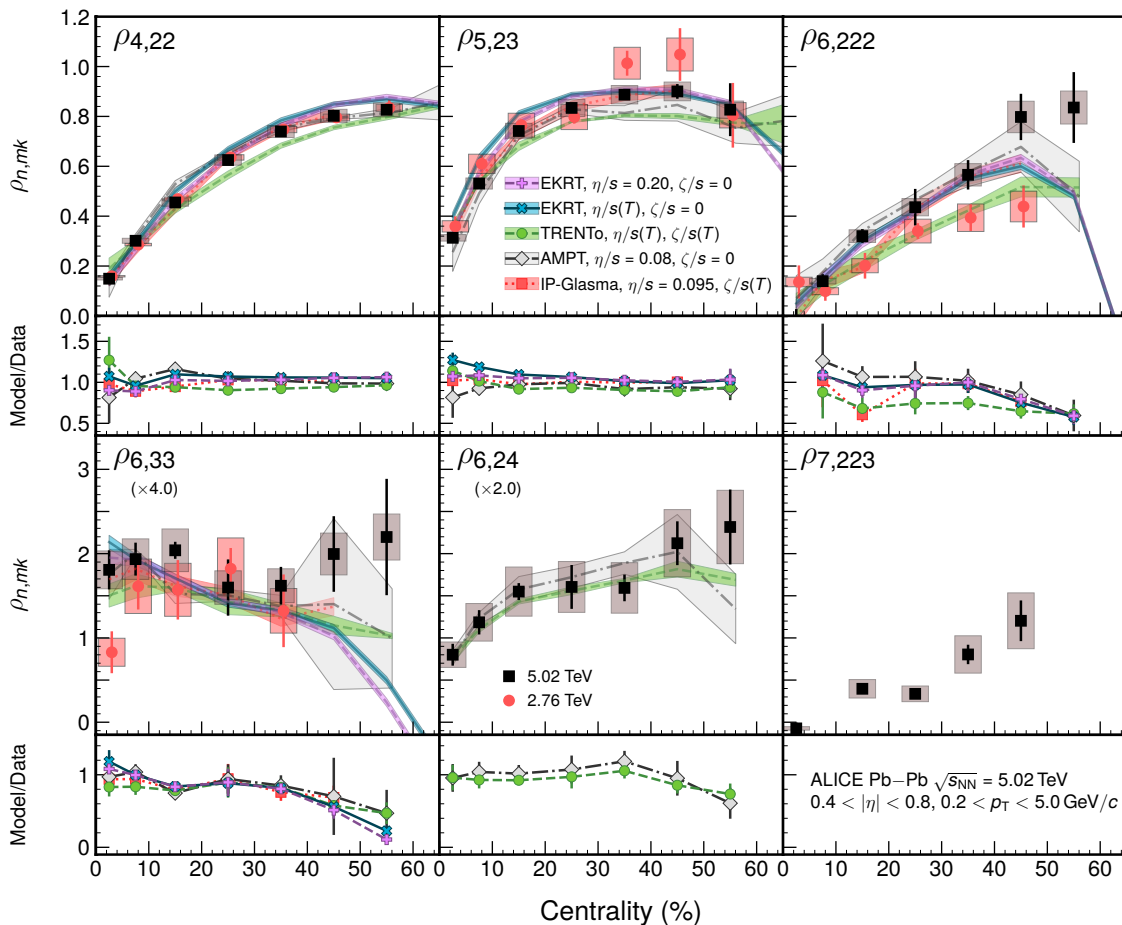


Figure 5. Symmetry-plane correlations as a function of centrality in Pb-Pb collisions at $\sqrt{s_{NN}} = 5.02$ TeV (black markers) compared with those in Pb-Pb collisions at $\sqrt{s_{NN}} = 2.76$ TeV [53], along with five different hydrodynamic calculations shown as color bands. On the bottom part of each panel, the ratios between model calculations and the data are shown. For some panels, the data points are scaled by an indicated factor for better visibility.

the modes of the sixth harmonic, and TRENTo+param3 in all harmonics. The EKRT+param1 calculations slightly overestimate the centrality dependence of the non-linear flow mode coefficients. It can be seen that the parameterizations of the EKRT presented here imply $\chi_{n,mk}$ across all harmonic orders to have sensitivity to η/s , whereas in the previous calculations in [53], weak η/s dependence was found for $\chi_{4,22}$ and $\chi_{6,222}$. The fifth order coefficient $\chi_{5,23}$ is expected to be quite sensitive to η/s in central collisions as can be seen from the difference of the predicted values from EKRT+param0 and EKRT+param1. The AMPT+param2 calculations underestimate the magnitude of some of the measured non-linear flow mode coefficients in various centrality classes, especially $\chi_{5,23}$, $\chi_{7,223}$ as well as $\chi_{6,24}$. The IP-Glasma+param4 calculations overestimate the measurements in some centrality intervals.

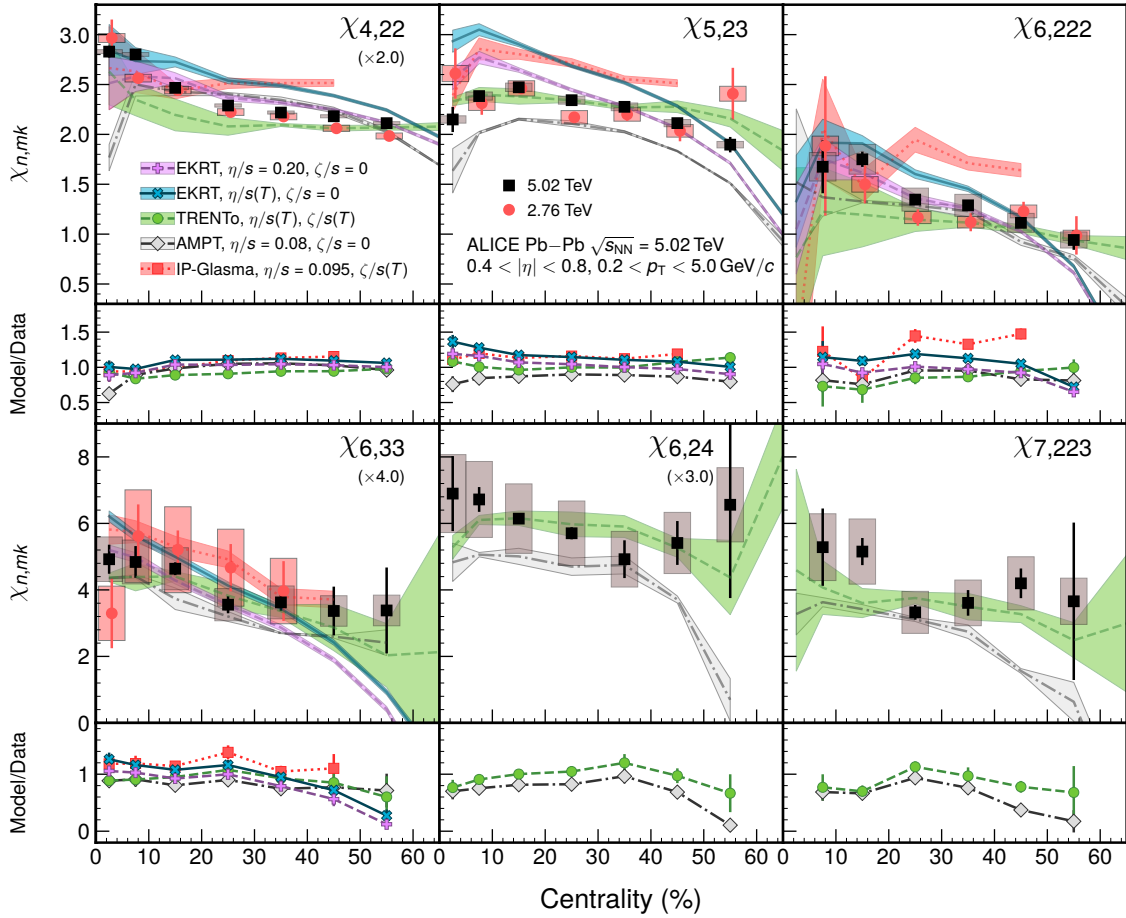


Figure 6. Non-linear mode coefficients as a function of centrality in Pb-Pb collisions at $\sqrt{s_{\text{NN}}} = 5.02$ TeV (black markers) compared with those from $\sqrt{s_{\text{NN}}} = 2.76$ TeV (red markers) [53], along with five different hydrodynamic calculations shown as color bands. On the bottom part of each panel, the ratios between model calculations and the data are shown. For some panels, the points are scaled by an indicated factor for better visibility across the panels.

The agreement between data and the model calculations is quantified by calculating the reduced χ^2/N_{dof} defined as

$$\chi^2/N_{\text{dof}} = \frac{1}{N_{\text{dof}}} \sum_{i=1}^{N_{\text{dof}}} \frac{(y_i - f_i)^2}{\sigma_i^2}, \quad (5.1)$$

where y_i and f_i are the values for data and calculations, respectively, and $\sigma_i^2 = \sigma_{i,\text{stat}}^2 + \sigma_{i,\text{syst}}^2 + \sigma_{f_i,\text{stat}}^2$ is the quadratic uncertainty in terms of statistical measurement $\sigma_{i,\text{stat}}$, model uncertainties $\sigma_{f_i,\text{stat}}$, and systematic uncertainties $\sigma_{i,\text{syst}}$ in centrality bin i . Here N_{dof} represents the number of data points across the centrality interval.

The χ^2/N_{dof} for the flow coefficients are presented in figure 7, panel (a). It is observed that IP-Glasma+param4 gives the best description of v_2 and v_3 compared to the other models, indicated by the overall low value of χ^2/N_{dof} . However, the overall performance

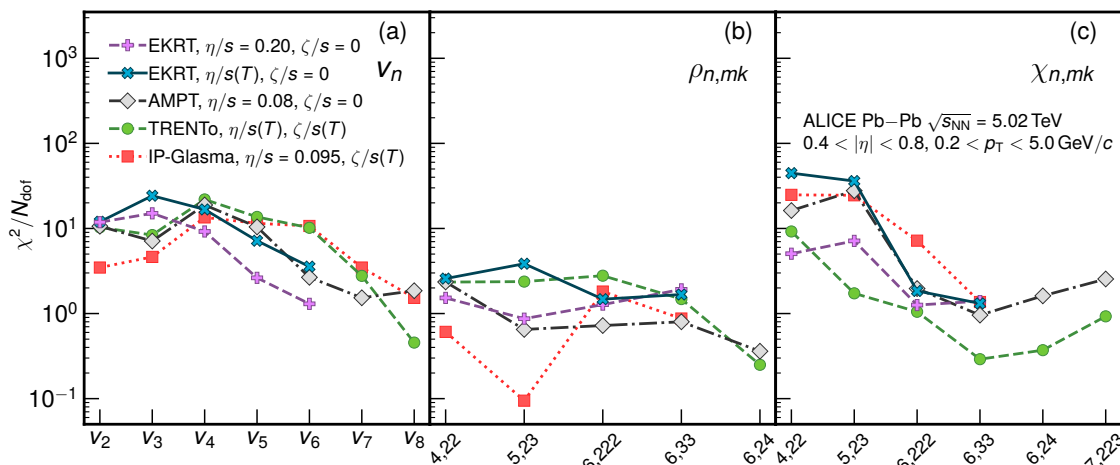


Figure 7. Overview of various model comparisons with data, quantified by χ^2/N_{dof} . Lower χ^2/N_{dof} represents a better overall description for a given observable.

of IP-Glasma+param4 is considerably worse at $n \geq 4$, for which the data are overestimated, as seen in figure 2. For v_4 to v_6 , EKRT+param0 gives the lowest value of χ^2/N_{dof} . In the case of EKRT+param1, the χ^2/N_{dof} is slightly worse than EKRT+param0. The χ^2/N_{dof} of TRENTo+param3 is very close to that of IP-Glasma+param4, indicating a comparable description of data between the two model configurations. At low harmonic orders, TRENTo+param3 performs slightly worse than IP-Glasma+param4. For $n \geq 4$, description of the data between these two models are comparable except for $n = 8$, where TRENTo+param3 clearly has a better magnitude and centrality depiction. Notably this can be seen for v_8 where the χ^2/N_{dof} value is the lowest across all models. Finally, the performance of AMPT+param2 can be considered good within the reported χ^2/N_{dof} values. It is noted that the magnitude of v_7 is best depicted by AMPT+param2 amongst the three models used.

The performance of the models with respect to the symmetry-plane correlations is quantified in panel (b) of figure 7. IP-Glasma+param4 has by far the best estimates of $\rho_{n,mk}$ for $\rho_{4,22}$ and $\rho_{5,23}$. For other models, the model depiction is comparable. In low harmonic orders, EKRT+param0 shows good agreement with the data, as well as AMPT+param2, which has the best agreement in higher harmonic orders. For TRENTo+param3, the agreement is slightly worse for $\rho_{5,23}$ and $\rho_{6,222}$.

The panel (c) of figure 7 shows the χ^2/N_{dof} for non-linear flow mode coefficients. As seen also in figure 6, TRENTo+param3 consistently provides the most successful overall description of the data. For other models the data are more frequently over- or underestimated. TRENTo+param3 estimates $\chi_{n,mk}$ better than it does the v_n coefficients, for which significant overestimation was present at almost every harmonic order (see figure 2). For EKRT+param0 the agreement is good, but the calculation over- or underestimates in some cases especially in most central or mid-peripheral collisions. Most of the observables are better described by the calculations using EKRT+param0 with a const $\eta/s = 0.2$ as compared to results from EKRT+param1 which uses a temperature dependent η/s value.

AMPT+param2 performs worse for low-order harmonics as it overpredicts the data in central and mid-central collisions. Of the five configurations, IP-Glasma+param4 describes the data worse in all harmonic orders.

The deviation of the calculated results from the measured value of each observable is of the same order of magnitude for the different models. Even where the model results show gross agreement with overall features in data, the values of χ^2/N_{dof} vary considerably from one harmonic order to another. Considering the χ^2/N_{dof} to be a goodness-of-fit estimate to validate any model, these variations suggest that the sensitivity of the different observables on the initial conditions, η/s , and ζ/s are reflected differently in the model calculations. Since the current uncertainties in the model calculations are large for higher order harmonics, the absolute χ^2 test should not be over-interpreted. Both, improved statistical uncertainties in the model calculations and different values of input parameters would be beneficial. However, large sets of calculations in many parameter spaces require substantial computing power. In order to constrain the model parameters Bayesian analysis can provide a plausible approach as demonstrated in [45, 47]. At present it is limited to low harmonic-order observables, and the extracted parameters have large uncertainties. Extending the Bayesian analysis to include the results in this paper will help reduce the uncertainties of the model parameters.

6 Summary

The measurements of anisotropic flow coefficients (v_n), non-linear flow mode coefficients ($\chi_{n,mk}$), and correlations among different symmetry planes ($\rho_{n,mk}$) in Pb-Pb collisions at $\sqrt{s_{\text{NN}}} = 5.02$ TeV are presented. The anisotropic flow coefficients are measured up to v_9 , where v_8 and v_9 are measured for the first time at LHC energies. It is observed that v_n decreases as n increases, observing n -ordered damping up to $n = 7$. The v_n is found to be enhanced for $n > 7$. The non-linear contribution becomes dominant towards peripheral collisions in all harmonic orders. The strength of the non-linear flow mode and the symmetry-plane correlations depends also on harmonic orders. The non-linear flow mode coefficients show a clear centrality and harmonic order dependencies and the strongest non-linear mode coefficients is observed for the fifth and seventh harmonic orders.

These results are compared with various hydrodynamic model calculations with different initial conditions, as well as different parameterizations of η/s and ζ/s . None of the models presented in this paper simultaneously describe the v_n coefficients, $\chi_{n,mk}$, or $\rho_{n,mk}$. Based on the model and data comparisons, among all the models, the event-by-event viscous hydrodynamic model with EKRT initial conditions and a constant $\eta/s = 0.2$ is observed to describe the data best, as far as the harmonics up to the sixth order are concerned. As a result further tuning is required to find the accurate parameterization of η/s and ζ/s . It is found that the different order harmonic observables presented in this paper have different sensitivities to the initial conditions and the system properties. These results allow further model parameters to be optimized and the initial conditions and the transport properties of nuclear matter in ultra-relativistic heavy-ion collisions to be better constrained.

Acknowledgments

The ALICE Collaboration would like to thank all its engineers and technicians for their invaluable contributions to the construction of the experiment and the CERN accelerator teams for the outstanding performance of the LHC complex. The ALICE Collaboration gratefully acknowledges the resources and support provided by all Grid centres and the Worldwide LHC Computing Grid (WLCG) collaboration. The ALICE Collaboration acknowledges the following funding agencies for their support in building and running the ALICE detector: A.I. Alikhanyan National Science Laboratory (Yerevan Physics Institute) Foundation (ANSL), State Committee of Science and World Federation of Scientists (WFS), Armenia; Austrian Academy of Sciences, Austrian Science Fund (FWF): [M 2467-N36] and Nationalstiftung für Forschung, Technologie und Entwicklung, Austria; Ministry of Communications and High Technologies, National Nuclear Research Center, Azerbaijan; Conselho Nacional de Desenvolvimento Científico e Tecnológico (CNPq), Financiadora de Estudos e Projetos (Finep), Fundação de Amparo à Pesquisa do Estado de São Paulo (FAPESP) and Universidade Federal do Rio Grande do Sul (UFRGS), Brazil; Ministry of Education of China (MOEC), Ministry of Science & Technology of China (MSTC) and National Natural Science Foundation of China (NSFC), China; Ministry of Science and Education and Croatian Science Foundation, Croatia; Centro de Aplicaciones Tecnológicas y Desarrollo Nuclear (CEADEN), Cubaenergía, Cuba; Ministry of Education, Youth and Sports of the Czech Republic, Czech Republic; The Danish Council for Independent Research — Natural Sciences, the VILLUM FONDEN and Danish National Research Foundation (DNRF), Denmark; Helsinki Institute of Physics (HIP), Finland; Commissariat à l’Energie Atomique (CEA), Institut National de Physique Nucléaire et de Physique des Particules (IN2P3) and Centre National de la Recherche Scientifique (CNRS) and Région des Pays de la Loire, France; Bundesministerium für Bildung und Forschung (BMBF) and GSI Helmholtzzentrum für Schwerionenforschung GmbH, Germany; General Secretariat for Research and Technology, Ministry of Education, Research and Religions, Greece; National Research, Development and Innovation Office, Hungary; Department of Atomic Energy Government of India (DAE), Department of Science and Technology, Government of India (DST), University Grants Commission, Government of India (UGC) and Council of Scientific and Industrial Research (CSIR), India; Indonesian Institute of Science, Indonesia; Centro Fermi — Museo Storico della Fisica e Centro Studi e Ricerche Enrico Fermi and Istituto Nazionale di Fisica Nucleare (INFN), Italy; Institute for Innovative Science and Technology, Nagasaki Institute of Applied Science (IIST), Japanese Ministry of Education, Culture, Sports, Science and Technology (MEXT) and Japan Society for the Promotion of Science (JSPS) KAKENHI, Japan; Consejo Nacional de Ciencia (CONACYT) y Tecnología, through Fondo de Cooperación Internacional en Ciencia y Tecnología (FONCICYT) and Dirección General de Asuntos del Personal Académico (DGAPA), Mexico; Nederlandse Organisatie voor Wetenschappelijk Onderzoek (NWO), Netherlands; The Research Council of Norway, Norway; Commission on Science and Technology for Sustainable Development in the South (COMSATS), Pakistan; Pontificia Universidad Católica del Perú, Peru; Ministry of Science and Higher Education and National Science Centre, Poland;

Korea Institute of Science and Technology Information and National Research Foundation of Korea (NRF), Republic of Korea; Ministry of Education and Scientific Research, Institute of Atomic Physics and Ministry of Research and Innovation and Institute of Atomic Physics, Romania; Joint Institute for Nuclear Research (JINR), Ministry of Education and Science of the Russian Federation, National Research Centre Kurchatov Institute, Russian Science Foundation and Russian Foundation for Basic Research, Russia; Ministry of Education, Science, Research and Sport of the Slovak Republic, Slovakia; National Research Foundation of South Africa, South Africa; Swedish Research Council (VR) and Knut & Alice Wallenberg Foundation (KAW), Sweden; European Organization for Nuclear Research, Switzerland; Suranaree University of Technology (SUT), National Science and Technology Development Agency (NSDTA) and Office of the Higher Education Commission under NRU project of Thailand, Thailand; Turkish Atomic Energy Agency (TAEK), Turkey; National Academy of Sciences of Ukraine, Ukraine; Science and Technology Facilities Council (STFC), United Kingdom; National Science Foundation of the United States of America (NSF) and United States Department of Energy, Office of Nuclear Physics (DOE NP), United States of America.

A List of observables

In this section the complete list of the measured observables is presented. By root-mean-squaring the equations in eq. (1.3), one obtains a starting point for the definitions presented in this section. Provided that the linear and non-linear parts are uncorrelated, the following harmonic projections are obtained

$$\begin{aligned}
 v_{4,22} &= \frac{\Re\langle V_4(V_2^*)^2 \rangle}{\sqrt{\langle |V_2|^4 \rangle}} & v_{5,23} &= \frac{\Re\langle V_5 V_2^* V_3^* \rangle}{\sqrt{\langle |V_2|^2 |V_3|^2 \rangle}} \\
 &\approx \langle v_4 \cos(4\psi_4 - 4\psi_2) \rangle, & &\approx \langle v_5 \cos(5\psi_5 - 3\psi_3 - 2\psi_2) \rangle, \\
 v_{6,222} &= \frac{\Re\langle V_6(V_2^*)^3 \rangle}{\sqrt{\langle |V_2|^6 \rangle}} & v_{6,24} &= \frac{\Re\langle V_6 V_2^* V_4^* \rangle}{\sqrt{\langle |V_2|^2 |V_4|^2 \rangle}} \\
 &\approx \langle v_6 \cos(6\psi_6 - 6\psi_2) \rangle, & &\approx \langle v_6 \cos(6\psi_6 - 4\psi_4 - 2\psi_2) \rangle, \\
 v_{6,33} &= \frac{\Re\langle V_6(V_3^*)^2 \rangle}{\sqrt{\langle |V_3|^4 \rangle}} & v_{7,223} &= \frac{\Re\langle V_7(V_2^*)^2 V_3^* \rangle}{\sqrt{\langle |V_2|^4 |V_3|^2 \rangle}} \\
 &\approx \langle v_6 \cos(6\psi_6 - 6\psi_3) \rangle, & &\approx \langle v_7 \cos(7\psi_7 - 4\psi_2 - 3\psi_3) \rangle, \\
 v_{8,233} &= \frac{\Re\langle V_8 V_2^* (V_3^*)^2 \rangle}{\sqrt{\langle |V_2|^2 |V_3|^4 \rangle}} \\
 &\approx \langle v_8 \cos(8\psi_8 - 2\psi_2 - 6\psi_3) \rangle,
 \end{aligned} \tag{A.1}$$

with $v_{4,22}^2 = \chi_{4,22}^2 \langle |V_2|^4 \rangle$, $v_{5,23}^2 = \chi_{5,23}^2 \langle |V_2|^2 |V_3|^2 \rangle$, \dots . The rest of the observables we define using the harmonic projections in eq. (A.1). The symmetry plane correlations are defined as

$$\begin{aligned}
 \rho_{4,22} &= \frac{v_{4,22}}{v_4}, & \rho_{5,23} &= \frac{v_{5,23}}{v_5}, \\
 \rho_{6,222} &= \frac{v_{6,222}}{v_6}, & \rho_{7,223} &= \frac{v_{7,334}}{v_7}, \\
 \rho_{6,33} &= \frac{v_{6,33}}{v_6},
 \end{aligned} \tag{A.2}$$

and the non-linear mode coefficients

$$\begin{aligned}
 \chi_{4,22} &= \frac{v_{4,22}}{\sqrt{\langle v_2^4 \rangle}}, & \chi_{5,23} &= \frac{v_{5,23}}{\sqrt{\langle v_2^2 v_3^2 \rangle}}, \\
 \chi_{6,222} &= \frac{v_{6,222}}{\sqrt{\langle v_2^6 \rangle}}, & \chi_{7,223} &= \frac{v_{7,223}}{\sqrt{\langle v_2^4 v_3^2 \rangle}}, \\
 \chi_{6,33} &= \frac{v_{6,33}}{\sqrt{\langle v_3^4 \rangle}}, \\
 \chi_{6,24} &= \Re \frac{\langle V_6 V_2^* V_4^* \rangle \langle v_2^4 \rangle - \langle V_6 (V_2^*)^3 \rangle \langle V_4 (V_2^*)^2 \rangle}{(\langle v_4^2 \rangle \langle v_2^4 \rangle - \langle V_4 (V_2^*)^2 \rangle^2) \langle v_2^2 \rangle}.
 \end{aligned} \tag{A.3}$$

The higher order superpositions in eq. (1.3) include the coupling constants for the higher order linear responses. In a more complete treatment [100], the extraction of the higher order non-linear flow mode coefficients are performed by correlating the corresponding superpositions with those of the relevant harmonics, effectively resulting in a more general projection. The results agree with the expressions in eq. (2.4), and generate additional high order linear coupling coefficients

$$\begin{aligned}
 \chi_{6,24} &= \Re \frac{\langle V_6 V_2^* V_4^* \rangle \langle v_2^4 \rangle - \langle V_6 (V_2^*)^3 \rangle \langle V_4 (V_2^*)^2 \rangle}{(\langle v_4^2 \rangle \langle v_2^4 \rangle - \langle V_4 (V_2^*)^2 \rangle^2) \langle v_2^2 \rangle}, \\
 \chi_{7,25} &= \Re \frac{\langle V_7 V_2^* V_5^* \rangle \langle v_2^2 v_3^2 \rangle - \langle V_7 (V_2^*)^2 V_3^* \rangle \langle V_5 V_2^* V_3^* \rangle}{(\langle v_5^2 \rangle \langle v_2^2 v_3^2 \rangle - \langle V_5 V_2^* V_3^* \rangle^2) \langle v_2^2 \rangle}, \\
 \chi_{7,34} &= \Re \frac{\langle V_7 V_3^* V_4^* \rangle \langle v_2^4 \rangle - \langle V_7 (V_2^*)^2 V_3^* \rangle \langle V_4 (V_2^*)^2 \rangle}{(\langle v_4^2 \rangle \langle v_2^4 \rangle - \langle V_4 (V_2^*)^2 \rangle^2) \langle v_3^2 \rangle}.
 \end{aligned} \tag{A.4}$$

Open Access. This article is distributed under the terms of the Creative Commons Attribution License ([CC-BY 4.0](https://creativecommons.org/licenses/by/4.0/)), which permits any use, distribution and reproduction in any medium, provided the original author(s) and source are credited.

References

- [1] J.-Y. Ollitrault, *Anisotropy as a signature of transverse collective flow*, *Phys. Rev. D* **46** (1992) 229 [[INSPIRE](#)].
- [2] S.A. Voloshin, A.M. Poskanzer and R. Snellings, *Collective phenomena in non-central nuclear collisions*, *Landolt-Bornstein* **23** (2010) 293 [[arXiv:0809.2949](#)] [[INSPIRE](#)].
- [3] S. Voloshin and Y. Zhang, *Flow study in relativistic nuclear collisions by Fourier expansion of Azimuthal particle distributions*, *Z. Phys. C* **70** (1996) 665 [[hep-ph/9407282](#)] [[INSPIRE](#)].
- [4] A.M. Poskanzer and S.A. Voloshin, *Methods for analyzing anisotropic flow in relativistic nuclear collisions*, *Phys. Rev. C* **58** (1998) 1671 [[nucl-ex/9805001](#)] [[INSPIRE](#)].
- [5] B. Alver and G. Roland, *Collision geometry fluctuations and triangular flow in heavy-ion collisions*, *Phys. Rev. C* **81** (2010) 054905 [Erratum *ibid.* **C 82** (2010) 039903] [[arXiv:1003.0194](#)] [[INSPIRE](#)].
- [6] ALICE collaboration, *Higher harmonic anisotropic flow measurements of charged particles in Pb-Pb collisions at $\sqrt{s_{NN}} = 2.76$ TeV*, *Phys. Rev. Lett.* **107** (2011) 032301 [[arXiv:1105.3865](#)] [[INSPIRE](#)].

- [7] ALICE collaboration, *Elliptic flow of charged particles in Pb-Pb collisions at 2.76 TeV*, *Phys. Rev. Lett.* **105** (2010) 252302 [[arXiv:1011.3914](#)] [[INSPIRE](#)].
- [8] ALICE collaboration, *Anisotropic flow of charged hadrons, pions and (anti-)protons measured at high transverse momentum in Pb-Pb collisions at $\sqrt{s_{NN}} = 2.76$ TeV*, *Phys. Lett. B* **719** (2013) 18 [[arXiv:1205.5761](#)] [[INSPIRE](#)].
- [9] ALICE collaboration, *Elliptic flow of identified hadrons in Pb-Pb collisions at $\sqrt{s_{NN}} = 2.76$ TeV*, *JHEP* **06** (2015) 190 [[arXiv:1405.4632](#)] [[INSPIRE](#)].
- [10] ALICE collaboration, *Higher harmonic flow coefficients of identified hadrons in Pb-Pb collisions at $\sqrt{s_{NN}} = 2.76$ TeV*, *JHEP* **09** (2016) 164 [[arXiv:1606.06057](#)] [[INSPIRE](#)].
- [11] ALICE collaboration, *Anisotropic flow of charged particles in Pb-Pb collisions at $\sqrt{s_{NN}} = 5.02$ TeV*, *Phys. Rev. Lett.* **116** (2016) 132302 [[arXiv:1602.01119](#)] [[INSPIRE](#)].
- [12] ALICE collaboration, *Searches for transverse momentum dependent flow vector fluctuations in Pb-Pb and p-Pb collisions at the LHC*, *JHEP* **09** (2017) 032 [[arXiv:1707.05690](#)] [[INSPIRE](#)].
- [13] ALICE collaboration, *Anisotropic flow of identified particles in Pb-Pb collisions at $\sqrt{s_{NN}} = 5.02$ TeV*, *JHEP* **09** (2018) 006 [[arXiv:1805.04390](#)] [[INSPIRE](#)].
- [14] D.A. Teaney, *Viscous Hydrodynamics and the Quark Gluon Plasma*, in *Quark-gluon plasma 4*, R.C. Hwa and X.-N. Wang eds., pp. 207–266, (2010) [[DOI](#)] [[arXiv:0905.2433](#)] [[INSPIRE](#)].
- [15] D. Molnar and M. Gyulassy, *Saturation of elliptic flow and the transport opacity of the gluon plasma at RHIC*, *Nucl. Phys. A* **697** (2002) 495 [*Erratum ibid.* **A 703** (2002) 893] [[nucl-th/0104073](#)] [[INSPIRE](#)].
- [16] D. Teaney, *The Effects of viscosity on spectra, elliptic flow and HBT radii*, *Phys. Rev. C* **68** (2003) 034913 [[nucl-th/0301099](#)] [[INSPIRE](#)].
- [17] R.A. Lacey et al., *Has the QCD Critical Point been Signaled by Observations at RHIC?*, *Phys. Rev. Lett.* **98** (2007) 092301 [[nucl-ex/0609025](#)] [[INSPIRE](#)].
- [18] H.-J. Drescher, A. Dumitru, C. Gombeaud and J.-Y. Ollitrault, *The Centrality dependence of elliptic flow, the hydrodynamic limit and the viscosity of hot QCD*, *Phys. Rev. C* **76** (2007) 024905 [[arXiv:0704.3553](#)] [[INSPIRE](#)].
- [19] Z. Xu, C. Greiner and H. Stoecker, *PQCD calculations of elliptic flow and shear viscosity at RHIC*, *Phys. Rev. Lett.* **101** (2008) 082302 [[arXiv:0711.0961](#)] [[INSPIRE](#)].
- [20] D. Molnar and P. Huovinen, *Dissipative effects from transport and viscous hydrodynamics*, *J. Phys. G* **35** (2008) 104125 [[arXiv:0806.1367](#)] [[INSPIRE](#)].
- [21] U. Heinz and R. Snellings, *Collective flow and viscosity in relativistic heavy-ion collisions*, *Ann. Rev. Nucl. Part. Sci.* **63** (2013) 123 [[arXiv:1301.2826](#)] [[INSPIRE](#)].
- [22] H. Song, Y. Zhou and K. Gajdosova, *Collective flow and hydrodynamics in large and small systems at the LHC*, *Nucl. Sci. Tech.* **28** (2017) 99 [[arXiv:1703.00670](#)] [[INSPIRE](#)].
- [23] P. Kovtun, D.T. Son and A.O. Starinets, *Viscosity in strongly interacting quantum field theories from black hole physics*, *Phys. Rev. Lett.* **94** (2005) 111601 [[hep-th/0405231](#)] [[INSPIRE](#)].
- [24] D. Teaney and L. Yan, *Triangularity and Dipole Asymmetry in Heavy Ion Collisions*, *Phys. Rev. C* **83** (2011) 064904 [[arXiv:1010.1876](#)] [[INSPIRE](#)].

- [25] H. Niemi, K.J. Eskola and R. Paatelainen, *Event-by-event fluctuations in a perturbative QCD + saturation + hydrodynamics model: Determining QCD matter shear viscosity in ultrarelativistic heavy-ion collisions*, *Phys. Rev. C* **93** (2016) 024907 [[arXiv:1505.02677](#)] [[INSPIRE](#)].
- [26] H. Niemi, G.S. Denicol, H. Holopainen and P. Huovinen, *Event-by-event distributions of azimuthal asymmetries in ultrarelativistic heavy-ion collisions*, *Phys. Rev. C* **87** (2013) 054901 [[arXiv:1212.1008](#)] [[INSPIRE](#)].
- [27] STAR collaboration, *Identified particle elliptic flow in Au + Au collisions at $\sqrt{s_{NN}} = 130$ GeV*, *Phys. Rev. Lett.* **87** (2001) 182301 [[nucl-ex/0107003](#)] [[INSPIRE](#)].
- [28] STAR collaboration, *Elliptic flow from two and four particle correlations in Au+Au collisions at $\sqrt{s_{NN}} = 130$ GeV*, *Phys. Rev. C* **66** (2002) 034904 [[nucl-ex/0206001](#)] [[INSPIRE](#)].
- [29] PHENIX collaboration, *Elliptic flow of identified hadrons in Au+Au collisions at $\sqrt{s_{NN}} = 200$ GeV*, *Phys. Rev. Lett.* **91** (2003) 182301 [[nucl-ex/0305013](#)] [[INSPIRE](#)].
- [30] STAR collaboration, *Azimuthal anisotropy at RHIC: The First and fourth harmonics*, *Phys. Rev. Lett.* **92** (2004) 062301 [[nucl-ex/0310029](#)] [[INSPIRE](#)].
- [31] STAR collaboration, *Azimuthal anisotropy in U+U and Au+Au collisions at RHIC*, *Phys. Rev. Lett.* **115** (2015) 222301 [[arXiv:1505.07812](#)] [[INSPIRE](#)].
- [32] PHOBOS collaboration, *Event-by-Event Fluctuations of Azimuthal Particle Anisotropy in Au + Au Collisions at $\sqrt{s_{NN}} = 200$ GeV*, *Phys. Rev. Lett.* **104** (2010) 142301 [[nucl-ex/0702036](#)] [[INSPIRE](#)].
- [33] T. Hirano, U.W. Heinz, D. Kharzeev, R. Lacey and Y. Nara, *Hadronic dissipative effects on elliptic flow in ultrarelativistic heavy-ion collisions*, *Phys. Lett. B* **636** (2006) 299 [[nucl-th/0511046](#)] [[INSPIRE](#)].
- [34] P. Romatschke and U. Romatschke, *Viscosity Information from Relativistic Nuclear Collisions: How Perfect is the Fluid Observed at RHIC?*, *Phys. Rev. Lett.* **99** (2007) 172301 [[arXiv:0706.1522](#)] [[INSPIRE](#)].
- [35] A.K. Chaudhuri, *Saturation of elliptic flow and shear viscosity*, [arXiv:0708.1252](#) [[INSPIRE](#)].
- [36] H. Song, S.A. Bass, U. Heinz, T. Hirano and C. Shen, *200 A GeV Au+Au collisions serve a nearly perfect quark-gluon liquid*, *Phys. Rev. Lett.* **106** (2011) 192301 [*Erratum ibid.* **109** (2012) 139904] [[arXiv:1011.2783](#)] [[INSPIRE](#)].
- [37] M. Luzum and J.-Y. Ollitrault, *Extracting the shear viscosity of the quark-gluon plasma from flow in ultra-central heavy-ion collisions*, *Nucl. Phys. A* **904–905** (2013) 377c [[arXiv:1210.6010](#)] [[INSPIRE](#)].
- [38] C. Shen et al., *The QGP shear viscosity: Elusive goal or just around the corner?*, *J. Phys. G* **38** (2011) 124045 [[arXiv:1106.6350](#)] [[INSPIRE](#)].
- [39] ALICE collaboration, *Correlated event-by-event fluctuations of flow harmonics in Pb-Pb collisions at $\sqrt{s_{NN}} = 2.76$ TeV*, *Phys. Rev. Lett.* **117** (2016) 182301 [[arXiv:1604.07663](#)] [[INSPIRE](#)].
- [40] ALICE collaboration, *Systematic studies of correlations between different order flow harmonics in Pb-Pb collisions at $\sqrt{s_{NN}} = 2.76$ TeV*, *Phys. Rev. C* **97** (2018) 024906 [[arXiv:1709.01127](#)] [[INSPIRE](#)].

- [41] P. Bozek, *Flow and interferometry in 3+1 dimensional viscous hydrodynamics*, *Phys. Rev. C* **85** (2012) 034901 [[arXiv:1110.6742](#)] [[INSPIRE](#)].
- [42] J.-B. Rose et al., *Extracting the bulk viscosity of the quark-gluon plasma*, *Nucl. Phys. A* **931** (2014) 926 [[arXiv:1408.0024](#)] [[INSPIRE](#)].
- [43] S. Ryu et al., *Importance of the Bulk Viscosity of QCD in Ultrarelativistic Heavy-Ion Collisions*, *Phys. Rev. Lett.* **115** (2015) 132301 [[arXiv:1502.01675](#)] [[INSPIRE](#)].
- [44] S. Ryu et al., *Effects of bulk viscosity and hadronic rescattering in heavy ion collisions at energies available at the BNL Relativistic Heavy Ion Collider and at the CERN Large Hadron Collider*, *Phys. Rev. C* **97** (2018) 034910 [[arXiv:1704.04216](#)] [[INSPIRE](#)].
- [45] J.E. Bernhard, J.S. Moreland, S.A. Bass, J. Liu and U. Heinz, *Applying Bayesian parameter estimation to relativistic heavy-ion collisions: simultaneous characterization of the initial state and quark-gluon plasma medium*, *Phys. Rev. C* **94** (2016) 024907 [[arXiv:1605.03954](#)] [[INSPIRE](#)].
- [46] A. Dubla, S. Masciocchi, J.M. Pawłowski, B. Schenke, C. Shen and J. Stachel, *Towards QCD-assisted hydrodynamics for heavy-ion collision phenomenology*, *Nucl. Phys. A* **979** (2018) 251 [[arXiv:1805.02985](#)] [[INSPIRE](#)].
- [47] J.E. Bernhard, J.S. Moreland and S.A. Bass, *Bayesian estimation of the specific shear and bulk viscosity of quark-gluon plasma*, *Nature Phys.* **15** (2019) 1113.
- [48] B.H. Alver, C. Gombeaud, M. Luzum and J.-Y. Ollitrault, *Triangular flow in hydrodynamics and transport theory*, *Phys. Rev. C* **82** (2010) 034913 [[arXiv:1007.5469](#)] [[INSPIRE](#)].
- [49] ATLAS collaboration, *Measurement of the azimuthal anisotropy of charged particles produced in $\sqrt{s_{NN}} = 5.02$ TeV Pb+Pb collisions with the ATLAS detector*, *Eur. Phys. J. C* **78** (2018) 997 [[arXiv:1808.03951](#)] [[INSPIRE](#)].
- [50] F.G. Gardim, F. Grassi, M. Luzum and J.-Y. Ollitrault, *Mapping the hydrodynamic response to the initial geometry in heavy-ion collisions*, *Phys. Rev. C* **85** (2012) 024908 [[arXiv:1111.6538](#)] [[INSPIRE](#)].
- [51] F.G. Gardim, J. Noronha-Hostler, M. Luzum and F. Grassi, *Effects of viscosity on the mapping of initial to final state in heavy ion collisions*, *Phys. Rev. C* **91** (2015) 034902 [[arXiv:1411.2574](#)] [[INSPIRE](#)].
- [52] D. Teaney and L. Yan, *Event-plane correlations and hydrodynamic simulations of heavy ion collisions*, *Phys. Rev. C* **90** (2014) 024902 [[arXiv:1312.3689](#)] [[INSPIRE](#)].
- [53] ALICE collaboration, *Linear and non-linear flow modes in Pb-Pb collisions at $\sqrt{s_{NN}} = 2.76$ TeV*, *Phys. Lett. B* **773** (2017) 68 [[arXiv:1705.04377](#)] [[INSPIRE](#)].
- [54] M.L. Miller, K. Reygers, S.J. Sanders and P. Steinberg, *Glauber modeling in high energy nuclear collisions*, *Ann. Rev. Nucl. Part. Sci.* **57** (2007) 205 [[nucl-ex/0701025](#)] [[INSPIRE](#)].
- [55] Z. Qiu and U.W. Heinz, *Event-by-event shape and flow fluctuations of relativistic heavy-ion collision fireballs*, *Phys. Rev. C* **84** (2011) 024911 [[arXiv:1104.0650](#)] [[INSPIRE](#)].
- [56] H.-J. Drescher and Y. Nara, *Eccentricity fluctuations from the color glass condensate at RHIC and LHC*, *Phys. Rev. C* **76** (2007) 041903 [[arXiv:0707.0249](#)] [[INSPIRE](#)].
- [57] S. McDonald, C. Shen, F. Fillion-Gourdeau, S. Jeon and C. Gale, *Hydrodynamic predictions for Pb+Pb collisions at 5.02 TeV*, *Phys. Rev. C* **95** (2017) 064913 [[arXiv:1609.02958](#)] [[INSPIRE](#)].

- [58] ALICE collaboration, *Energy dependence and fluctuations of anisotropic flow in Pb-Pb collisions at $\sqrt{s_{NN}} = 5.02$ and 2.76 TeV*, *JHEP* **07** (2018) 103 [[arXiv:1804.02944](#)] [[INSPIRE](#)].
- [59] L. Yan and J.-Y. Ollitrault, $\nu_4, \nu_5, \nu_6, \nu_7$: *nonlinear hydrodynamic response versus LHC data*, *Phys. Lett.* **B 744** (2015) 82 [[arXiv:1502.02502](#)] [[INSPIRE](#)].
- [60] D. Teaney and L. Yan, *Non linearities in the harmonic spectrum of heavy ion collisions with ideal and viscous hydrodynamics*, *Phys. Rev.* **C 86** (2012) 044908 [[arXiv:1206.1905](#)] [[INSPIRE](#)].
- [61] J. Jia and S. Mohapatra, *A Method for studying initial geometry fluctuations via event plane correlations in heavy ion collisions*, *Eur. Phys. J.* **C 73** (2013) 2510 [[arXiv:1203.5095](#)] [[INSPIRE](#)].
- [62] M. Luzum, *Flow fluctuations and long-range correlations: elliptic flow and beyond*, *J. Phys.* **G 38** (2011) 124026 [[arXiv:1107.0592](#)] [[INSPIRE](#)].
- [63] Z. Qiu and U. Heinz, *Hydrodynamic event-plane correlations in Pb+Pb collisions at $\sqrt{s} = 2.76$ ATeV*, *Phys. Lett.* **B 717** (2012) 261 [[arXiv:1208.1200](#)] [[INSPIRE](#)].
- [64] ATLAS collaboration, *Measurement of event-plane correlations in $\sqrt{s_{NN}} = 2.76$ TeV lead-lead collisions with the ATLAS detector*, *Phys. Rev.* **C 90** (2014) 024905 [[arXiv:1403.0489](#)] [[INSPIRE](#)].
- [65] CMS collaboration, *Measurement of Higher-Order Harmonic Azimuthal Anisotropy in PbPb Collisions at $\sqrt{s_{NN}} = 2.76$ TeV*, *Phys. Rev.* **C 89** (2014) 044906 [[arXiv:1310.8651](#)] [[INSPIRE](#)].
- [66] M. Luzum and J.-Y. Ollitrault, *Eliminating experimental bias in anisotropic-flow measurements of high-energy nuclear collisions*, *Phys. Rev.* **C 87** (2013) 044907 [[arXiv:1209.2323](#)] [[INSPIRE](#)].
- [67] ALICE collaboration, *The ALICE experiment at the CERN LHC, 2008* *JINST* **3** S08002 [[INSPIRE](#)].
- [68] ALICE collaboration, *Performance of the ALICE Experiment at the CERN LHC*, *Int. J. Mod. Phys.* **A 29** (2014) 1430044 [[arXiv:1402.4476](#)] [[INSPIRE](#)].
- [69] ALICE collaboration, *ALICE: Physics performance report, volume I*, *J. Phys.* **G 30** (2004) 1517 [[INSPIRE](#)].
- [70] ALICE collaboration, *ALICE: Physics performance report, volume II*, *J. Phys.* **G 32** (2006) 1295 [[INSPIRE](#)].
- [71] ALICE collaboration, *Performance of the ALICE VZERO system, 2013* *JINST* **8** P10016 [[arXiv:1306.3130](#)] [[INSPIRE](#)].
- [72] ALICE collaboration, *Alignment of the ALICE Inner Tracking System with cosmic-ray tracks, 2010* *JINST* **5** P03003 [[arXiv:1001.0502](#)] [[INSPIRE](#)].
- [73] ALICE collaboration, *Performance of the ALICE Time-Of-Flight detector at the LHC, 2019* *JINST* **14** C06023 [[arXiv:1806.03825](#)] [[INSPIRE](#)].
- [74] ALICE collaboration, *Centrality determination of Pb-Pb collisions at $\sqrt{s_{NN}} = 2.76$ TeV with ALICE*, *Phys. Rev.* **C 88** (2013) 044909 [[arXiv:1301.4361](#)] [[INSPIRE](#)].
- [75] J. Alme et al., *The ALICE TPC, a large 3-dimensional tracking device with fast readout for ultra-high multiplicity events*, *Nucl. Instrum. Meth.* **A 622** (2010) 316 [[arXiv:1001.1950](#)] [[INSPIRE](#)].

- [76] ALICE collaboration, *The ALICE definition of primary particles*, [ALICE-PUBLIC-2017-005](#).
- [77] X.-N. Wang and M. Gyulassy, *HIJING: A Monte Carlo model for multiple jet production in $p p$, $p A$ and $A A$ collisions*, *Phys. Rev. D* **44** (1991) 3501 [[INSPIRE](#)].
- [78] M. Gyulassy and X.-N. Wang, *HIJING 1.0: A Monte Carlo program for parton and particle production in high-energy hadronic and nuclear collisions*, *Comput. Phys. Commun.* **83** (1994) 307 [[nucl-th/9502021](#)] [[INSPIRE](#)].
- [79] R. Brun et al., *GEANT Detector Description and Simulation Tool*, [DOI](#) [[INSPIRE](#)].
- [80] A. Bilandzic, C.H. Christensen, K. Gulbrandsen, A. Hansen and Y. Zhou, *Generic framework for anisotropic flow analyses with multiparticle azimuthal correlations*, *Phys. Rev. C* **89** (2014) 064904 [[arXiv:1312.3572](#)] [[INSPIRE](#)].
- [81] H. Niemi, K.J. Eskola, R. Paatelainen and K. Tuominen, *Predictions for 5.023 TeV Pb + Pb collisions at the CERN Large Hadron Collider*, *Phys. Rev. C* **93** (2016) 014912 [[arXiv:1511.04296](#)] [[INSPIRE](#)].
- [82] W. Zhao, H.-j. Xu and H. Song, *Collective flow in 2.76 and 5.02 A TeV Pb+Pb collisions*, *Eur. Phys. J. C* **77** (2017) 645 [[arXiv:1703.10792](#)] [[INSPIRE](#)].
- [83] C. Shen, Z. Qiu, H. Song, J. Bernhard, S. Bass and U. Heinz, *The iEBE-VISHNU code package for relativistic heavy-ion collisions*, *Comput. Phys. Commun.* **199** (2016) 61 [[arXiv:1409.8164](#)] [[INSPIRE](#)].
- [84] R.S. Bhalerao, A. Jaiswal and S. Pal, *Collective flow in event-by-event partonic transport plus hydrodynamics hybrid approach*, *Phys. Rev. C* **92** (2015) 014903 [[arXiv:1503.03862](#)] [[INSPIRE](#)].
- [85] L. Pang, Q. Wang and X.-N. Wang, *Effects of initial flow velocity fluctuation in event-by-event (3+1)D hydrodynamics*, *Phys. Rev. C* **86** (2012) 024911 [[arXiv:1205.5019](#)] [[INSPIRE](#)].
- [86] H.-j. Xu, Z. Li and H. Song, *High-order flow harmonics of identified hadrons in 2.76A TeV Pb + Pb collisions*, *Phys. Rev. C* **93** (2016) 064905 [[arXiv:1602.02029](#)] [[INSPIRE](#)].
- [87] J.S. Moreland, J.E. Bernhard and S.A. Bass, *Alternative ansatz to wounded nucleon and binary collision scaling in high-energy nuclear collisions*, *Phys. Rev. C* **92** (2015) 011901 [[arXiv:1412.4708](#)] [[INSPIRE](#)].
- [88] B. Schenke, S. Jeon and C. Gale, *Elliptic and triangular flow in event-by-event (3+1)D viscous hydrodynamics*, *Phys. Rev. Lett.* **106** (2011) 042301 [[arXiv:1009.3244](#)] [[INSPIRE](#)].
- [89] B. Schenke, P. Tribedy and R. Venugopalan, *Fluctuating Glasma initial conditions and flow in heavy ion collisions*, *Phys. Rev. Lett.* **108** (2012) 252301 [[arXiv:1202.6646](#)] [[INSPIRE](#)].
- [90] Z. Qiu, C. Shen and U. Heinz, *Hydrodynamic elliptic and triangular flow in Pb-Pb collisions at $\sqrt{s} = 2.76 A TeV$* , *Phys. Lett. B* **707** (2012) 151 [[arXiv:1110.3033](#)] [[INSPIRE](#)].
- [91] C. Shen, U. Heinz, P. Huovinen and H. Song, *Systematic parameter study of hadron spectra and elliptic flow from viscous hydrodynamic simulations of Au+Au collisions at $\sqrt{s_{NN}} = 200 GeV$* , *Phys. Rev. C* **82** (2010) 054904 [[arXiv:1010.1856](#)] [[INSPIRE](#)].
- [92] C. Shen, U. Heinz, P. Huovinen and H. Song, *Radial and elliptic flow in Pb+Pb collisions at the Large Hadron Collider from viscous hydrodynamic*, *Phys. Rev. C* **84** (2011) 044903 [[arXiv:1105.3226](#)] [[INSPIRE](#)].

- [93] G.S. Denicol, T. Kodama, T. Koide and P. Mota, *Effect of bulk viscosity on Elliptic Flow near QCD phase transition*, *Phys. Rev. C* **80** (2009) 064901 [[arXiv:0903.3595](#)] [[INSPIRE](#)].
- [94] F. Karsch, D. Kharzeev and K. Tuchin, *Universal properties of bulk viscosity near the QCD phase transition*, *Phys. Lett. B* **663** (2008) 217 [[arXiv:0711.0914](#)] [[INSPIRE](#)].
- [95] J. Noronha-Hostler, J. Noronha and C. Greiner, *Transport Coefficients of Hadronic Matter near $T(c)$* , *Phys. Rev. Lett.* **103** (2009) 172302 [[arXiv:0811.1571](#)] [[INSPIRE](#)].
- [96] E. Molnar, H. Niemi and D.H. Rischke, *Numerical tests of causal relativistic dissipative fluid dynamics*, *Eur. Phys. J. C* **65** (2010) 615 [[arXiv:0907.2583](#)] [[INSPIRE](#)].
- [97] E. Shuryak, *The sounds of the Little and Big Bangs*, *Universe* **3** (2017) 75 [[arXiv:1710.03776](#)] [[INSPIRE](#)].
- [98] P. Staig and E. Shuryak, *The Fate of the Initial State Fluctuations in Heavy Ion Collisions. III The Second Act of Hydrodynamics*, *Phys. Rev. C* **84** (2011) 044912 [[arXiv:1105.0676](#)] [[INSPIRE](#)].
- [99] R.A. Lacey et al., *Is anisotropic flow really acoustic?*, [arXiv:1301.0165](#) [[INSPIRE](#)].
- [100] J. Qian, U.W. Heinz and J. Liu, *Mode-coupling effects in anisotropic flow in heavy-ion collisions*, *Phys. Rev. C* **93** (2016) 064901 [[arXiv:1602.02813](#)] [[INSPIRE](#)].

The ALICE collaboration

S. Acharya¹⁴¹, D. Adamová⁹⁴, A. Adler⁷⁴, J. Adolfsson⁸⁰, M.M. Aggarwal⁹⁹, G. Aglieri Rinella³³, M. Agnello³⁰, N. Agrawal^{10,53}, Z. Ahammed¹⁴¹, S. Ahmad¹⁶, S.U. Ahn⁷⁶, A. Akindinov⁹¹, M. Al-Turany¹⁰⁶, S.N. Alam¹⁴¹, D.S.D. Albuquerque¹²², D. Aleksandrov⁸⁷, B. Alessandro⁵⁸, H.M. Alfanda⁶, R. Alfaro Molina⁷¹, B. Ali¹⁶, Y. Ali¹⁴, A. Alici^{10,26,53}, A. Alkin², J. Alme²¹, T. Alt⁶⁸, L. Altenkamper²¹, I. Altsybeev¹¹², M.N. Anaam⁶, C. Andrei⁴⁷, D. Andreou³³, H.A. Andrews¹¹⁰, A. Andronic¹⁴⁴, M. Angeletti³³, V. Anguelov¹⁰³, C. Anson¹⁵, T. Antičić¹⁰⁷, F. Antinori⁵⁶, P. Antonioli⁵³, N. Apadula⁷⁹, L. Aphecetche¹¹⁴, H. Appelshäuser⁶⁸, S. Arcelli²⁶, R. Arnaldi⁵⁸, M. Arratia⁷⁹, I.C. Arsene²⁰, M. Arslandok¹⁰³, A. Augustinus³³, R. Averbeck¹⁰⁶, S. Aziz⁶¹, M.D. Azmi¹⁶, A. Badalà⁵⁵, Y.W. Baek⁴⁰, S. Bagnasco⁵⁸, X. Bai¹⁰⁶, R. Bailhache⁶⁸, R. Bala¹⁰⁰, A. Balbino³⁰, A. Baldisseri¹³⁷, M. Ball⁴², S. Balouza¹⁰⁴, R. Barbera²⁷, L. Barioglio²⁵, G.G. Barnaföldi¹⁴⁵, L.S. Barnby⁹³, V. Barret¹³⁴, P. Bartalini⁶, K. Barth³³, E. Bartsch⁶⁸, F. Baruffaldi²⁸, N. Bastid¹³⁴, S. Basu¹⁴³, G. Batigne¹¹⁴, B. Batyunya⁷⁵, D. Bauri⁴⁸, J.L. Bazo Alba¹¹¹, I.G. Bearden⁸⁸, C. Beattie¹⁴⁶, C. Bedda⁶³, N.K. Behera⁶⁰, I. Belikov¹³⁶, A.D.C. Bell Hechavarria¹⁴⁴, F. Bellini³³, R. Bellwied¹²⁵, V. Belyaev⁹², G. Bencedi¹⁴⁵, S. Beole²⁵, A. Bercuci⁴⁷, Y. Berdnikov⁹⁷, D. Berenyi¹⁴⁵, R.A. Bertens¹³⁰, D. Berzano⁵⁸, M.G. Besoiu⁶⁷, L. Betev³³, A. Bhasin¹⁰⁰, I.R. Bhat¹⁰⁰, M.A. Bhat³, H. Bhatt⁴⁸, B. Bhattacharjee⁴¹, A. Bianchi²⁵, L. Bianchi²⁵, N. Bianchi⁵¹, J. Bielčík³⁶, J. Bielčíková⁹⁴, A. Bilandzic^{104,117}, G. Biro¹⁴⁵, R. Biswas³, S. Biswas³, J.T. Blair¹¹⁹, D. Blau⁸⁷, C. Blume⁶⁸, G. Boca¹³⁹, F. Bock^{33,95}, A. Bogdanov⁹², L. Boldizsár¹⁴⁵, A. Bolozdynya⁹², M. Bombara³⁷, G. Bonomi¹⁴⁰, H. Borel¹³⁷, A. Borissov^{92,144}, H. Bossi¹⁴⁶, E. Botta²⁵, L. Bratrud⁶⁸, P. Braun-Munzinger¹⁰⁶, M. Bregant¹²¹, M. Broz³⁶, E. Bruna⁵⁸, G.E. Bruno¹⁰⁵, M.D. Buckland¹²⁷, D. Budnikov¹⁰⁸, H. Buesching⁶⁸, S. Bufalino³⁰, O. Bugnon¹¹⁴, P. Buhler¹¹³, P. Buncic³³, Z. Buthelezi^{72,131}, J.B. Butt¹⁴, J.T. Buxton⁹⁶, S.A. Bysiak¹¹⁸, D. Caffarri⁸⁹, A. Caliva¹⁰⁶, E. Calvo Villar¹¹¹, R.S. Camacho⁴⁴, P. Camerini²⁴, A.A. Capon¹¹³, F. Carnesecchi^{10,26}, R. Caron¹³⁷, J. Castillo Castellanos¹³⁷, A.J. Castro¹³⁰, E.A.R. Casula⁵⁴, F. Catalano³⁰, C. Ceballos Sanchez⁵², P. Chakraborty⁴⁸, S. Chandra¹⁴¹, W. Chang⁶, S. Chapeland³³, M. Chartier¹²⁷, S. Chattopadhyay¹⁴¹, S. Chattopadhyay¹⁰⁹, A. Chauvin²³, C. Cheshkov¹³⁵, B. Cheynis¹³⁵, V. Chibante Barroso³³, D.D. Chinellato¹²², S. Cho⁶⁰, P. Chochula³³, T. Chowdhury¹³⁴, P. Christakoglou⁸⁹, C.H. Christensen⁸⁸, P. Christiansen⁸⁰, T. Chujo¹³³, C. Cicalo⁵⁴, L. Cifarelli^{10,26}, F. Cindolo⁵³, G. Clai^{53, ii}, J. Cleymans¹²⁴, F. Colamaria⁵², D. Colella⁵², A. Collu⁷⁹, M. Colocci²⁶, M. Concas^{58, iii}, G. Conesa Balbastre⁷⁸, Z. Conesa del Valle⁶¹, G. Contin^{24,127}, J.G. Contreras³⁶, T.M. Cormier⁹⁵, Y. Corrales Morales²⁵, P. Cortese³¹, M.R. Cosentino¹²³, F. Costa³³, S. Costanza¹³⁹, P. Crochet¹³⁴, E. Cuautle⁶⁹, P. Cui⁶, L. Cunqueiro⁹⁵, D. Dabrowski¹⁴², T. Dahms^{104,117}, A. Dainese⁵⁶, F.P.A. Damas^{114,137}, M.C. Danisch¹⁰³, A. Danu⁶⁷, D. Das¹⁰⁹, I. Das¹⁰⁹, P. Das⁸⁵, P. Das³, S. Das³, A. Dash⁸⁵, S. Dash⁴⁸, S. De⁸⁵, A. De Caro²⁹, G. de Cataldo⁵², J. de Cuveland³⁸, A. De Falco²³, D. De Gruttola¹⁰, N. De Marco⁵⁸, S. De Pasquale²⁹, S. Deb⁴⁹, B. Debjani³, H.F. Degenhardt¹²¹, K.R. Deja¹⁴², A. Deloff⁸⁴, S. Delsanto^{25,131}, W. Deng⁶, D. Devetak¹⁰⁶, P. Dhankher⁴⁸, D. Di Bari³², A. Di Mauro³³, R.A. Diaz⁸, T. Dietel¹²⁴, P. Dillenseger⁶⁸, Y. Ding⁶, R. Divià³³, D.U. Dixit¹⁹, Ø. Djuvsland²¹, U. Dmitrieva⁶², A. Dobrin^{33,67}, B. Dönigus⁶⁸, O. Dordic²⁰, A.K. Dubey¹⁴¹, A. Dubla¹⁰⁶, S. Dudi⁹⁹, M. Dukhishyam⁸⁵, P. Dupieux¹³⁴, R.J. Ehlers^{95,146}, V.N. Eikeland²¹, D. Elia⁵², E. Eppele¹⁴⁶, B. Erazmus¹¹⁴, F. Erhardt⁹⁸, A. Erokhin¹¹², M.R. Ersdal²¹, B. Espagnon⁶¹, G. Eulisse³³, D. Evans¹¹⁰, S. Evdokimov⁹⁰, L. Fabbietti^{104,117}, M. Faggin²⁸, J. Faivre⁷⁸, F. Fan⁶, A. Fantoni⁵¹, M. Fasel⁹⁵, P. Fecchio³⁰, A. Feliciello⁵⁸, G. Feofilov¹¹², A. Fernández Téllez⁴⁴, A. Ferrero¹³⁷, A. Ferretti²⁵, A. Festanti³³, V.J.G. Feuillard¹⁰³, J. Figiel¹¹⁸, S. Filchagin¹⁰⁸, D. Finogeev⁶², F.M. Fionda²¹, G. Fiorenza⁵², F. Flor¹²⁵, S. Foertsch⁷², P. Foka¹⁰⁶, S. Fokin⁸⁷, E. Fragiaco⁵⁹,

U. Frankenfeld¹⁰⁶, U. Fuchs³³, C. Furget⁷⁸, A. Furs⁶², M. Fusco Girard²⁹, J.J. Gaardhøje⁸⁸,
 M. Gagliardi²⁵, A.M. Gago¹¹¹, A. Gal¹³⁶, C.D. Galvan¹²⁰, P. Ganoti⁸³, C. Garabatos¹⁰⁶,
 E. Garcia-Solis¹¹, K. Garg²⁷, C. Gargiulo³³, A. Garibli⁸⁶, K. Garner¹⁴⁴, P. Gasik^{104,117},
 E.F. Gauger¹¹⁹, M.B. Gay Ducati⁷⁰, M. Germain¹¹⁴, J. Ghosh¹⁰⁹, P. Ghosh¹⁴¹, S.K. Ghosh³,
 M. Giacalone²⁶, P. Gianotti⁵¹, P. Giubellino^{58,106}, P. Giubilato²⁸, P. Glässel¹⁰³, A. Gomez
 Ramirez⁷⁴, V. Gonzalez¹⁰⁶, P. González-Zamora⁴⁴, S. Gorbunov³⁸, L. Görlich¹¹⁸, S. Gotovac³⁴,
 V. Grabski⁷¹, L.K. Graczykowski¹⁴², K.L. Graham¹¹⁰, L. Greiner⁷⁹, A. Grelli⁶³, C. Grigoras³³,
 V. Grigoriev⁹², A. Grigoryan¹, S. Grigoryan⁷⁵, O.S. Groettvik²¹, F. Grosa³⁰,
 J.F. Grosse-Oetringhaus³³, R. Grosso¹⁰⁶, R. Guernane⁷⁸, M. Guittiere¹¹⁴, K. Gulbrandsen⁸⁸,
 T. Gunji¹³², A. Gupta¹⁰⁰, R. Gupta¹⁰⁰, I.B. Guzman⁴⁴, R. Haake¹⁴⁶, M.K. Habib¹⁰⁶,
 C. Hadjidakis⁶¹, H. Hamagaki⁸¹, G. Hamar¹⁴⁵, M. Hamid⁶, R. Hannigan¹¹⁹, M.R. Haque^{63,85},
 A. Harlenderova¹⁰⁶, J.W. Harris¹⁴⁶, A. Harton¹¹, J.A. Hasenbichler³³, H. Hassan⁹⁵,
 D. Hatzifotiadiou^{10,53}, P. Hauer⁴², S. Hayashi¹³², S.T. Heckel^{68,104}, E. Hellbär⁶⁸, H. Helstrup³⁵,
 A. Herghelegiu⁴⁷, T. Herman³⁶, E.G. Hernandez⁴⁴, G. Herrera Corral⁹, F. Herrmann¹⁴⁴,
 K.F. Hetland³⁵, H. Hillemanns³³, C. Hills¹²⁷, B. Hippolyte¹³⁶, B. Hohlweger¹⁰⁴, J. Honermann¹⁴⁴,
 D. Horak³⁶, A. Hornung⁶⁸, S. Hornung¹⁰⁶, R. Hosokawa¹⁵, P. Hristov³³, C. Huang⁶¹,
 C. Hughes¹³⁰, P. Huhn⁶⁸, T.J. Humanic⁹⁶, H. Hushnud¹⁰⁹, L.A. Husova¹⁴⁴, N. Hussain⁴¹,
 S.A. Hussain¹⁴, D. Hutter³⁸, J.P. Iddon^{33,127}, R. Ilkaev¹⁰⁸, M. Inaba¹³³, G.M. Innocenti³³,
 M. Ippolitov⁸⁷, A. Isakov⁹⁴, M.S. Islam¹⁰⁹, M. Ivanov¹⁰⁶, V. Ivanov⁹⁷, V. Izucheev⁹⁰, B. Jacak⁷⁹,
 N. Jacazio⁵³, P.M. Jacobs⁷⁹, S. Jadlovská¹¹⁶, J. Jadlovsky¹¹⁶, S. Jaelani⁶³, C. Jahnke¹²¹,
 M.J. Jakubowska¹⁴², M.A. Janik¹⁴², T. Janson⁷⁴, M. Jercic⁹⁸, O. Jevons¹¹⁰, M. Jin¹²⁵,
 F. Jonas^{95,144}, P.G. Jones¹¹⁰, J. Jung⁶⁸, M. Jung⁶⁸, A. Jusko¹¹⁰, P. Kalinak⁶⁴, A. Kalweit³³,
 V. Kaplin⁹², S. Kar⁶, A. Karasu Uysal⁷⁷, O. Karavichev⁶², T. Karavicheva⁶², P. Karczmarczyk³³,
 E. Karpechev⁶², U. Keschull⁷⁴, R. Keidel⁴⁶, M. Keil³³, B. Ketzer⁴², Z. Khabanova⁸⁹,
 A.M. Khan⁶, S. Khan¹⁶, S.A. Khan¹⁴¹, A. Khanzadeev⁹⁷, Y. Kharlov⁹⁰, A. Khatun¹⁶,
 A. Khuntia¹¹⁸, B. Kileng³⁵, B. Kim⁶⁰, B. Kim¹³³, D. Kim¹⁴⁷, D.J. Kim¹²⁶, E.J. Kim⁷³,
 H. Kim^{17,147}, J. Kim¹⁴⁷, J.S. Kim⁴⁰, J. Kim¹⁰³, J. Kim¹⁴⁷, J. Kim⁷³, M. Kim¹⁰³, S. Kim¹⁸,
 T. Kim¹⁴⁷, T. Kim¹⁴⁷, S. Kirsch^{38,68}, I. Kisel³⁸, S. Kiselev⁹¹, A. Kisiel¹⁴², J.L. Klay⁵, C. Klein⁶⁸,
 J. Klein⁵⁸, S. Klein⁷⁹, C. Klein-Bösing¹⁴⁴, M. Kleiner⁶⁸, A. Kluge³³, M.L. Knichel³³,
 A.G. Knospe¹²⁵, C. Kobdaj¹¹⁵, M.K. Köhler¹⁰³, T. Kollegger¹⁰⁶, A. Kondratyev⁷⁵,
 N. Kondratyeva⁹², E. Kondratyuk⁹⁰, J. König⁶⁸, P.J. Konopka³³, L. Koska¹¹⁶, O. Kovalenko⁸⁴,
 V. Kovalenko¹¹², M. Kowalski¹¹⁸, I. Králik⁶⁴, A. Kravčáková³⁷, L. Kreis¹⁰⁶, M. Krivda^{64,110},
 F. Krizek⁹⁴, K. Krizkova Gajdosova³⁶, M. Krüger⁶⁸, E. Kryshen⁹⁷, M. Krzewicki³⁸,
 A.M. Kubera⁹⁶, V. Kučera⁶⁰, C. Kuhn¹³⁶, P.G. Kuijjer⁸⁹, L. Kumar⁹⁹, S. Kundu⁸⁵,
 P. Kurashvili⁸⁴, A. Kurepin⁶², A.B. Kurepin⁶², A. Kuryakin¹⁰⁸, S. Kushpil⁹⁴, J. Kvapil¹¹⁰,
 M.J. Kweon⁶⁰, J.Y. Kwon⁶⁰, Y. Kwon¹⁴⁷, S.L. La Pointe³⁸, P. La Rocca²⁷, Y.S. Lai⁷⁹,
 R. Langoy¹²⁹, K. Lapidus³³, A. Lardeux²⁰, P. Larionov⁵¹, E. Laudi³³, R. Lavicka³⁶,
 T. Lazareva¹¹², R. Lea²⁴, L. Leardini¹⁰³, J. Lee¹³³, S. Lee¹⁴⁷, F. Lehas⁸⁹, S. Lehner¹¹³,
 J. Leibrach³⁸, R.C. Lemmon⁹³, I. León Monzón¹²⁰, E.D. Lesser¹⁹, M. Lettrich³³, P. Lévai¹⁴⁵,
 X. Li¹², X.L. Li⁶, J. Lien¹²⁹, R. Lietava¹¹⁰, B. Lim¹⁷, V. Lindenstruth³⁸, S.W. Lindsay¹²⁷,
 C. Lippmann¹⁰⁶, M.A. Lisa⁹⁶, A. Liu¹⁹, J. Liu¹²⁷, S. Liu⁹⁶, W.J. Llope¹⁴³, I.M. Lofnes²¹,
 V. Loginov⁹², C. Loizides⁹⁵, P. Loncar³⁴, J.A.L. Lopez¹⁰³, X. Lopez¹³⁴, E. López Torres⁸,
 J.R. Luhder¹⁴⁴, M. Lunardon²⁸, G. Luparello⁵⁹, Y.G. Ma³⁹, A. Maevskaya⁶², M. Mager³³,
 S.M. Mahmood²⁰, T. Mahmoud⁴², A. Maire¹³⁶, R.D. Majka¹⁴⁶, M. Malaev⁹⁷, Q.W. Malik²⁰,
 L. Malinina^{75, iv}, D. Mal'Kevich⁹¹, P. Malzacher¹⁰⁶, G. Mandaglio⁵⁵, V. Manko⁸⁷, F. Manso¹³⁴,
 V. Manzari⁵², Y. Mao⁶, M. Marchisone¹³⁵, J. Mareš⁶⁶, G.V. Margagliotti²⁴, A. Margotti⁵³,
 J. Margutti⁶³, A. Marín¹⁰⁶, C. Markert¹¹⁹, M. Marquard⁶⁸, N.A. Martin¹⁰³, P. Martinengo³³,
 J.L. Martinez¹²⁵, M.I. Martínez⁴⁴, G. Martínez García¹¹⁴, M. Martinez Pedreira³³,

S. Masciocchi¹⁰⁶, M. Masera²⁵, A. Masoni⁵⁴, L. Massacrier⁶¹, E. Masson¹¹⁴, A. Mastroserio^{52,138},
 A.M. Mathis^{104,117}, O. Matonoha⁸⁰, P.F.T. Matuoka¹²¹, A. Matyja¹¹⁸, C. Mayer¹¹⁸,
 F. Mazzaschi²⁵, M. Mazzilli⁵², M.A. Mazzoni⁵⁷, A.F. Mechler⁶⁸, F. Meddi²², Y. Melikyan^{62,92},
 A. Menchaca-Rocha⁷¹, C. Mengke⁶, E. Meninno^{29,113}, M. Meres¹³, S. Mhlanga¹²⁴, Y. Miake¹³³,
 L. Micheletti²⁵, D.L. Mihaylov¹⁰⁴, K. Mikhaylov^{75,91}, A.N. Mishra⁶⁹, D. Miśkowiec¹⁰⁶,
 A. Modak³, N. Mohammadi³³, A.P. Mohanty⁶³, B. Mohanty⁸⁵, M. Mohisin Khan^{16,v},
 C. Mordasini¹⁰⁴, D.A. Moreira De Godoy¹⁴⁴, L.A.P. Moreno⁴⁴, I. Morozov⁶², A. Morsch³³,
 T. Mrnjavac³³, V. Muccifora⁵¹, E. Mudnic³⁴, D. Mühlheim¹⁴⁴, S. Muhuri¹⁴¹, J.D. Mulligan⁷⁹,
 M.G. Munhoz¹²¹, R.H. Munzer⁶⁸, H. Murakami¹³², S. Murray¹²⁴, L. Musa³³, J. Musinsky⁶⁴,
 C.J. Myers¹²⁵, J.W. Myrcha¹⁴², B. Naik⁴⁸, R. Nair⁸⁴, B.K. Nandi⁴⁸, R. Nania^{10,53}, E. Nappi⁵²,
 M.U. Naru¹⁴, A.F. Nassirpour⁸⁰, C. Nattrass¹³⁰, R. Nayak⁴⁸, T.K. Nayak⁸⁵, S. Nazarenko¹⁰⁸,
 A. Neagu²⁰, R.A. Negrao De Oliveira⁶⁸, L. Nellen⁶⁹, S.V. Nesbo³⁵, G. Neskovic³⁸, D. Nesterov¹¹²,
 L.T. Neumann¹⁴², B.S. Nielsen⁸⁸, S. Nikolaev⁸⁷, S. Nikulin⁸⁷, V. Nikulin⁹⁷, F. Noferini^{10,53},
 P. Nomokonov⁷⁵, J. Norman^{78,127}, N. Novitzky¹³³, P. Nowakowski¹⁴², A. Nyanin⁸⁷, J. Nystrand²¹,
 M. Ogino⁸¹, A. Ohlson^{80,103}, J. Oleniacz¹⁴², A.C. Oliveira Da Silva^{121,130}, M.H. Oliver¹⁴⁶,
 C. Oppedisano⁵⁸, R. Orava⁴³, A. Ortiz Velasquez⁶⁹, A. Oskarsson⁸⁰, J. Otwinowski¹¹⁸,
 K. Oyama⁸¹, Y. Pachmayer¹⁰³, V. Pacik⁸⁸, D. Pagano¹⁴⁰, G. Paic⁶⁹, J. Pan¹⁴³, A.K. Pandey⁴⁸,
 S. Panebianco¹³⁷, P. Pareek^{49,141}, J. Park⁶⁰, J.E. Parkkila¹²⁶, S. Parmar⁹⁹, S.P. Pathak¹²⁵,
 R.N. Patra¹⁴¹, B. Paul²³, H. Pei⁶, T. Peitzmann⁶³, X. Peng⁶, L.G. Pereira⁷⁰, H. Pereira Da
 Costa¹³⁷, D. Peresunko⁸⁷, G.M. Perez⁸, E. Perez Lezama⁶⁸, V. Peskov⁶⁸, Y. Pestov⁴,
 V. Petráček³⁶, M. Petrovici⁴⁷, R.P. Pezzi⁷⁰, S. Piano⁵⁹, M. Pikna¹³, P. Pillot¹¹⁴, O. Pinazza^{33,53},
 L. Pinsky¹²⁵, C. Pinto²⁷, S. Pisano^{10,51}, D. Pistone⁵⁵, M. Płoskoń⁷⁹, M. Planinic⁹⁸, F. Pliquett⁶⁸,
 S. Pochybova^{145,i}, M.G. Poghosyan⁹⁵, B. Polichtchouk⁹⁰, N. Poljak⁹⁸, A. Pop⁴⁷,
 H. Poppenborg¹⁴⁴, S. Porteboeuf-Houssais¹³⁴, V. Pozdniakov⁷⁵, S.K. Prasad³, R. Preghenella⁵³,
 F. Prino⁵⁸, C.A. Pruneau¹⁴³, I. Pshenichnov⁶², M. Puccio^{25,33}, J. Putschke¹⁴³, L. Quaglia²⁵,
 R.E. Quishpe¹²⁵, S. Ragoni¹¹⁰, S. Raha³, S. Rajput¹⁰⁰, J. Rak¹²⁶, A. Rakotozafindrabe¹³⁷,
 L. Ramello³¹, F. Rami¹³⁶, R. Raniwala¹⁰¹, S. Raniwala¹⁰¹, S.S. Räsänen⁴³, R. Rath⁴⁹, V. Ratza⁴²,
 I. Ravasenga⁸⁹, K.F. Read^{95,130}, A.R. Redelbach³⁸, K. Redlich^{84,vi}, A. Rehman²¹, P. Reichelt⁶⁸,
 F. Reidt³³, X. Ren⁶, R. Renfordt⁶⁸, Z. Rescakova³⁷, J.-P. Revol¹⁰, K. Reygers¹⁰³, V. Riabov⁹⁷,
 T. Richert^{80,88}, M. Richter²⁰, P. Riedler³³, W. Riegler³³, F. Riggi²⁷, C. Ristea⁶⁷, S.P. Rode⁴⁹,
 M. Rodríguez Cahuantzi⁴⁴, K. Røed²⁰, R. Rogalev⁹⁰, E. Rogochaya⁷⁵, D. Rohr³³, D. Röhrich²¹,
 P.S. Rokita¹⁴², F. Ronchetti⁵¹, E.D. Rosas⁶⁹, K. Roslon¹⁴², A. Rossi^{28,56}, A. Rotondi¹³⁹,
 A. Roy⁴⁹, P. Roy¹⁰⁹, O.V. Rueda⁸⁰, R. Rui²⁴, B. Rumyantsev⁷⁵, A. Rustamov⁸⁶, E. Ryabinkin⁸⁷,
 Y. Ryabov⁹⁷, A. Rybicki¹¹⁸, H. Rytkonen¹²⁶, O.A.M. Saarimaki⁴³, S. Sadhu¹⁴¹, S. Sadovsky⁹⁰,
 K. Šafařík³⁶, S.K. Saha¹⁴¹, B. Sahoo⁴⁸, P. Sahoo⁴⁸, R. Sahoo⁴⁹, S. Sahoo⁶⁵, P.K. Sahu⁶⁵,
 J. Saini¹⁴¹, S. Sakai¹³³, S. Sambyal¹⁰⁰, V. Samsonov^{92,97}, D. Sarkar¹⁴³, N. Sarkar¹⁴¹, P. Sarma⁴¹,
 V.M. Sarti¹⁰⁴, M.H.P. Sas⁶³, E. Scapparone⁵³, B. Schaefer⁹⁵, J. Schambach¹¹⁹, H.S. Scheid⁶⁸,
 C. Schiaua⁴⁷, R. Schicker¹⁰³, A. Schmah¹⁰³, C. Schmidt¹⁰⁶, H.R. Schmidt¹⁰², M.O. Schmidt¹⁰³,
 M. Schmidt¹⁰², N.V. Schmidt^{68,95}, A.R. Schmier¹³⁰, J. Schukraft⁸⁸, Y. Schutz^{33,136},
 K. Schwarz¹⁰⁶, K. Schweda¹⁰⁶, G. Scioli²⁶, E. Scomparin⁵⁸, M. Šefčík³⁷, J.E. Seger¹⁵,
 Y. Sekiguchi¹³², D. Sekihata¹³², I. Selyuzhenkov^{92,106}, S. Senyukov¹³⁶, D. Serebryakov⁶²,
 E. Serradilla⁷¹, A. Sevcenco⁶⁷, A. Shabanov⁶², A. Shabetai¹¹⁴, R. Shahoyan³³, W. Shaikh¹⁰⁹,
 A. Shangaraev⁹⁰, A. Sharma⁹⁹, A. Sharma¹⁰⁰, H. Sharma¹¹⁸, M. Sharma¹⁰⁰, N. Sharma⁹⁹,
 S. Sharma¹⁰⁰, A.I. Sheikh¹⁴¹, K. Shigaki⁴⁵, M. Shimomura⁸², S. Shirinkin⁹¹, Q. Shou³⁹,
 Y. Sibiriak⁸⁷, S. Siddhanta⁵⁴, T. Siemiarczuk⁸⁴, D. Silvermyr⁸⁰, G. Simatovic⁸⁹,
 G. Simonetti^{33,104}, R. Singh⁸⁵, R. Singh¹⁰⁰, R. Singh⁴⁹, V.K. Singh¹⁴¹, V. Singhal¹⁴¹, T. Sinha¹⁰⁹,
 B. Sitar¹³, M. Sitta³¹, T.B. Skaali²⁰, M. Slupecki¹²⁶, N. Smirnov¹⁴⁶, R.J.M. Snellings⁶³,
 T.W. Snellman^{43,126}, C. Soncco¹¹¹, J. Song^{60,125}, A. Songmoolnak¹¹⁵, F. Soramel²⁸,

S. Sorensen¹³⁰, I. Sputowska¹¹⁸, J. Stachel¹⁰³, I. Stan⁶⁷, P. Stankus⁹⁵, P.J. Steffanic¹³⁰, E. Stenlund⁸⁰, D. Stocco¹¹⁴, M.M. Storetvedt³⁵, L.D. Stritto²⁹, A.A.P. Suaide¹²¹, T. Sugitate⁴⁵, C. Suire⁶¹, M. Suleymanov¹⁴, M. Suljic³³, R. Sultanov⁹¹, M. Šumbera⁹⁴, V. Sumberia¹⁰⁰, S. Sumowidagdo⁵⁰, S. Swain⁶⁵, A. Szabo¹³, I. Szarka¹³, U. Tabassam¹⁴, S.F. Taghavi¹⁰⁴, G. Taillepied¹³⁴, J. Takahashi¹²², G.J. Tambave²¹, S. Tang^{6,134}, M. Tarhini¹¹⁴, M.G. Tarzila⁴⁷, A. Tauro³³, G. Tejada Muñoz⁴⁴, A. Telesca³³, L. Terlizzi²⁵, C. Terrevoli¹²⁵, D. Thakur⁴⁹, S. Thakur¹⁴¹, D. Thomas¹¹⁹, F. Thoresen⁸⁸, R. Tieulent¹³⁵, A. Tikhonov⁶², A.R. Timmins¹²⁵, A. Toia⁶⁸, N. Topilskaya⁶², M. Toppi⁵¹, F. Torales-Acosta¹⁹, S.R. Torres^{36,120}, A. Trifiro⁵⁵, S. Tripathy⁴⁹, T. Tripathy⁴⁸, S. Trogolo²⁸, G. Trombetta³², L. Tropp³⁷, V. Trubnikov², W.H. Trzaska¹²⁶, T.P. Trzcinski¹⁴², B.A. Trzeciak^{36,63}, T. Tsuji¹³², A. Tumkin¹⁰⁸, R. Turrisi⁵⁶, T.S. Tveter²⁰, K. Ullaland²¹, E.N. Umaka¹²⁵, A. Uras¹³⁵, G.L. Usai²³, A. Utrobicic⁹⁸, M. Vala³⁷, N. Valle¹³⁹, S. Vallero⁵⁸, N. van der Kolk⁶³, L.V.R. van Doremalen⁶³, M. van Leeuwen⁶³, P. Vande Vyvre³³, D. Varga¹⁴⁵, Z. Varga¹⁴⁵, M. Varga-Kofarago¹⁴⁵, A. Vargas⁴⁴, M. Vasileiou⁸³, A. Vasiliev⁸⁷, O. Vázquez Doce^{104,117}, V. Vechernin¹¹², A.M. Veen⁶³, E. Vercellin²⁵, S. Vergara Limón⁴⁴, L. Vermunt⁶³, R. Vernet⁷, R. Vértesi¹⁴⁵, L. Vickovic³⁴, Z. Vilakazi¹³¹, O. Villalobos Baillie¹¹⁰, A. Villatoro Tello⁴⁴, G. Vino⁵², A. Vinogradov⁸⁷, T. Virgili²⁹, V. Vislavicius⁸⁸, A. Vodopyanov⁷⁵, B. Volkel³³, M.A. Völkl¹⁰², K. Voloshin⁹¹, S.A. Voloshin¹⁴³, G. Volpe³², B. von Haller³³, I. Vorobyev¹⁰⁴, D. Voscek¹¹⁶, J. Vrláková³⁷, B. Wagner²¹, M. Weber¹¹³, A. Wegrzynek³³, D.F. Weiser¹⁰³, S.C. Wenzel³³, J.P. Wessels¹⁴⁴, J. Wiechula⁶⁸, J. Wikne²⁰, G. Wilk⁸⁴, J. Wilkinson^{10,53}, G.A. Willems¹⁴⁴, E. Willsher¹¹⁰, B. Windelband¹⁰³, M. Winn¹³⁷, W.E. Witt¹³⁰, Y. Wu¹²⁸, R. Xu⁶, S. Yalcin⁷⁷, Y. Yamaguchi⁴⁵, K. Yamakawa⁴⁵, S. Yang²¹, S. Yano¹³⁷, Z. Yin⁶, H. Yokoyama⁶³, I.-K. Yoo¹⁷, J.H. Yoon⁶⁰, S. Yuan²¹, A. Yuncu¹⁰³, V. Yurchenko², V. Zaccolo²⁴, A. Zaman¹⁴, C. Zampolli³³, H.J.C. Zanoli⁶³, N. Zardoshti³³, A. Zarochentsev¹¹², P. Závada⁶⁶, N. Zaviyalov¹⁰⁸, H. Zbroszczyk¹⁴², M. Zhalov⁹⁷, S. Zhang³⁹, X. Zhang⁶, Z. Zhang⁶, V. Zhrebchevskii¹¹², D. Zhou⁶, Y. Zhou⁸⁸, Z. Zhou²¹, J. Zhu^{6,106}, Y. Zhu⁶, A. Zichichi^{10,26}, M.B. Zimmermann³³, G. Zinovjev², N. Zurlo¹⁴⁰,

ⁱ Deceased

ⁱⁱ Italian National Agency for New Technologies, Energy and Sustainable Economic Development (ENEA), Bologna, Italy

ⁱⁱⁱ Dipartimento DET del Politecnico di Torino, Turin, Italy

^{iv} M.V. Lomonosov Moscow State University, D.V. Skobeltsyn Institute of Nuclear Physics, Moscow, Russia

^v Department of Applied Physics, Aligarh Muslim University, Aligarh, India

^{vi} Institute of Theoretical Physics, University of Wrocław, Poland

¹ A.I. Alikhanyan National Science Laboratory (Yerevan Physics Institute) Foundation, Yerevan, Armenia

² Bogolyubov Institute for Theoretical Physics, National Academy of Sciences of Ukraine, Kiev, Ukraine

³ Bose Institute, Department of Physics and Centre for Astroparticle Physics and Space Science (CAPSS), Kolkata, India

⁴ Budker Institute for Nuclear Physics, Novosibirsk, Russia

⁵ California Polytechnic State University, San Luis Obispo, California, United States

⁶ Central China Normal University, Wuhan, China

⁷ Centre de Calcul de l'IN2P3, Villeurbanne, Lyon, France

⁸ Centro de Aplicaciones Tecnológicas y Desarrollo Nuclear (CEADEN), Havana, Cuba

⁹ Centro de Investigación y de Estudios Avanzados (CINVESTAV), Mexico City and Mérida, Mexico

¹⁰ Centro Fermi — Museo Storico della Fisica e Centro Studi e Ricerche “Enrico Fermi”, Rome, Italy

- 11 *Chicago State University, Chicago, Illinois, United States*
- 12 *China Institute of Atomic Energy, Beijing, China*
- 13 *Comenius University Bratislava, Faculty of Mathematics, Physics and Informatics, Bratislava, Slovakia*
- 14 *COMSATS University Islamabad, Islamabad, Pakistan*
- 15 *Creighton University, Omaha, Nebraska, United States*
- 16 *Department of Physics, Aligarh Muslim University, Aligarh, India*
- 17 *Department of Physics, Pusan National University, Pusan, Republic of Korea*
- 18 *Department of Physics, Sejong University, Seoul, Republic of Korea*
- 19 *Department of Physics, University of California, Berkeley, California, United States*
- 20 *Department of Physics, University of Oslo, Oslo, Norway*
- 21 *Department of Physics and Technology, University of Bergen, Bergen, Norway*
- 22 *Dipartimento di Fisica dell'Università 'La Sapienza' and Sezione INFN, Rome, Italy*
- 23 *Dipartimento di Fisica dell'Università and Sezione INFN, Cagliari, Italy*
- 24 *Dipartimento di Fisica dell'Università and Sezione INFN, Trieste, Italy*
- 25 *Dipartimento di Fisica dell'Università and Sezione INFN, Turin, Italy*
- 26 *Dipartimento di Fisica e Astronomia dell'Università and Sezione INFN, Bologna, Italy*
- 27 *Dipartimento di Fisica e Astronomia dell'Università and Sezione INFN, Catania, Italy*
- 28 *Dipartimento di Fisica e Astronomia dell'Università and Sezione INFN, Padova, Italy*
- 29 *Dipartimento di Fisica 'E.R. Caianiello' dell'Università and Gruppo Collegato INFN, Salerno, Italy*
- 30 *Dipartimento DISAT del Politecnico and Sezione INFN, Turin, Italy*
- 31 *Dipartimento di Scienze e Innovazione Tecnologica dell'Università del Piemonte Orientale and INFN Sezione di Torino, Alessandria, Italy*
- 32 *Dipartimento Interateneo di Fisica 'M. Merlin' and Sezione INFN, Bari, Italy*
- 33 *European Organization for Nuclear Research (CERN), Geneva, Switzerland*
- 34 *Faculty of Electrical Engineering, Mechanical Engineering and Naval Architecture, University of Split, Split, Croatia*
- 35 *Faculty of Engineering and Science, Western Norway University of Applied Sciences, Bergen, Norway*
- 36 *Faculty of Nuclear Sciences and Physical Engineering, Czech Technical University in Prague, Prague, Czech Republic*
- 37 *Faculty of Science, P.J. Šafárik University, Košice, Slovakia*
- 38 *Frankfurt Institute for Advanced Studies, Johann Wolfgang Goethe-Universität Frankfurt, Frankfurt, Germany*
- 39 *Fudan University, Shanghai, China*
- 40 *Gangneung-Wonju National University, Gangneung, Republic of Korea*
- 41 *Gauhati University, Department of Physics, Guwahati, India*
- 42 *Helmholtz-Institut für Strahlen- und Kernphysik, Rheinische Friedrich-Wilhelms-Universität Bonn, Bonn, Germany*
- 43 *Helsinki Institute of Physics (HIP), Helsinki, Finland*
- 44 *High Energy Physics Group, Universidad Autónoma de Puebla, Puebla, Mexico*
- 45 *Hiroshima University, Hiroshima, Japan*
- 46 *Hochschule Worms, Zentrum für Technologietransfer und Telekommunikation (ZTT), Worms, Germany*
- 47 *Horia Hulubei National Institute of Physics and Nuclear Engineering, Bucharest, Romania*
- 48 *Indian Institute of Technology Bombay (IIT), Mumbai, India*
- 49 *Indian Institute of Technology Indore, Indore, India*
- 50 *Indonesian Institute of Sciences, Jakarta, Indonesia*
- 51 *INFN, Laboratori Nazionali di Frascati, Frascati, Italy*
- 52 *INFN, Sezione di Bari, Bari, Italy*
- 53 *INFN, Sezione di Bologna, Bologna, Italy*
- 54 *INFN, Sezione di Cagliari, Cagliari, Italy*

- 55 *INFN, Sezione di Catania, Catania, Italy*
- 56 *INFN, Sezione di Padova, Padova, Italy*
- 57 *INFN, Sezione di Roma, Rome, Italy*
- 58 *INFN, Sezione di Torino, Turin, Italy*
- 59 *INFN, Sezione di Trieste, Trieste, Italy*
- 60 *Inha University, Incheon, Republic of Korea*
- 61 *Institut de Physique Nucléaire d’Orsay (IPNO), Institut National de Physique Nucléaire et de Physique des Particules (IN2P3/CNRS), Université de Paris-Sud, Université Paris-Saclay, Orsay, France*
- 62 *Institute for Nuclear Research, Academy of Sciences, Moscow, Russia*
- 63 *Institute for Subatomic Physics, Utrecht University/Nikhef, Utrecht, Netherlands*
- 64 *Institute of Experimental Physics, Slovak Academy of Sciences, Košice, Slovakia*
- 65 *Institute of Physics, Homi Bhabha National Institute, Bhubaneswar, India*
- 66 *Institute of Physics of the Czech Academy of Sciences, Prague, Czech Republic*
- 67 *Institute of Space Science (ISS), Bucharest, Romania*
- 68 *Institut für Kernphysik, Johann Wolfgang Goethe-Universität Frankfurt, Frankfurt, Germany*
- 69 *Instituto de Ciencias Nucleares, Universidad Nacional Autónoma de México, Mexico City, Mexico*
- 70 *Instituto de Física, Universidade Federal do Rio Grande do Sul (UFRGS), Porto Alegre, Brazil*
- 71 *Instituto de Física, Universidad Nacional Autónoma de México, Mexico City, Mexico*
- 72 *iThemba LABS, National Research Foundation, Somerset West, South Africa*
- 73 *Jeonbuk National University, Jeonju, Republic of Korea*
- 74 *Johann-Wolfgang-Goethe Universität Frankfurt Institut für Informatik, Fachbereich Informatik und Mathematik, Frankfurt, Germany*
- 75 *Joint Institute for Nuclear Research (JINR), Dubna, Russia*
- 76 *Korea Institute of Science and Technology Information, Daejeon, Republic of Korea*
- 77 *KTO Karatay University, Konya, Turkey*
- 78 *Laboratoire de Physique Subatomique et de Cosmologie, Université Grenoble-Alpes, CNRS-IN2P3, Grenoble, France*
- 79 *Lawrence Berkeley National Laboratory, Berkeley, California, United States*
- 80 *Lund University Department of Physics, Division of Particle Physics, Lund, Sweden*
- 81 *Nagasaki Institute of Applied Science, Nagasaki, Japan*
- 82 *Nara Women’s University (NWU), Nara, Japan*
- 83 *National and Kapodistrian University of Athens, School of Science, Department of Physics, Athens, Greece*
- 84 *National Centre for Nuclear Research, Warsaw, Poland*
- 85 *National Institute of Science Education and Research, Homi Bhabha National Institute, Jatni, India*
- 86 *National Nuclear Research Center, Baku, Azerbaijan*
- 87 *National Research Centre Kurchatov Institute, Moscow, Russia*
- 88 *Niels Bohr Institute, University of Copenhagen, Copenhagen, Denmark*
- 89 *Nikhef, National institute for subatomic physics, Amsterdam, Netherlands*
- 90 *NRC Kurchatov Institute IHEP, Protvino, Russia*
- 91 *NRC “Kurchatov Institute” — ITEP, Moscow, Russia*
- 92 *NRNU Moscow Engineering Physics Institute, Moscow, Russia*
- 93 *Nuclear Physics Group, STFC Daresbury Laboratory, Daresbury, United Kingdom*
- 94 *Nuclear Physics Institute of the Czech Academy of Sciences, Řež u Prahy, Czech Republic*
- 95 *Oak Ridge National Laboratory, Oak Ridge, Tennessee, United States*
- 96 *Ohio State University, Columbus, Ohio, United States*
- 97 *Petersburg Nuclear Physics Institute, Gatchina, Russia*
- 98 *Physics department, Faculty of science, University of Zagreb, Zagreb, Croatia*
- 99 *Physics Department, Panjab University, Chandigarh, India*
- 100 *Physics Department, University of Jammu, Jammu, India*
- 101 *Physics Department, University of Rajasthan, Jaipur, India*

- 102 *Physikalisches Institut, Eberhard-Karls-Universität Tübingen, Tübingen, Germany*
 103 *Physikalisches Institut, Ruprecht-Karls-Universität Heidelberg, Heidelberg, Germany*
 104 *Physik Department, Technische Universität München, Munich, Germany*
 105 *Politecnico di Bari, Bari, Italy*
 106 *Research Division and ExtreMe Matter Institute EMMI, GSI Helmholtzzentrum für
Schwerionenforschung GmbH, Darmstadt, Germany*
 107 *Rudjer Bošković Institute, Zagreb, Croatia*
 108 *Russian Federal Nuclear Center (VNIIEF), Sarov, Russia*
 109 *Saha Institute of Nuclear Physics, Homi Bhabha National Institute, Kolkata, India*
 110 *School of Physics and Astronomy, University of Birmingham, Birmingham, United Kingdom*
 111 *Sección Física, Departamento de Ciencias, Pontificia Universidad Católica del Perú, Lima, Peru*
 112 *St. Petersburg State University, St. Petersburg, Russia*
 113 *Stefan Meyer Institut für Subatomare Physik (SMI), Vienna, Austria*
 114 *SUBATECH, IMT Atlantique, Université de Nantes, CNRS-IN2P3, Nantes, France*
 115 *Suranaree University of Technology, Nakhon Ratchasima, Thailand*
 116 *Technical University of Košice, Košice, Slovakia*
 117 *Technische Universität München, Excellence Cluster ‘Universe’, Munich, Germany*
 118 *The Henryk Niewodniczanski Institute of Nuclear Physics, Polish Academy of Sciences,
Cracow, Poland*
 119 *The University of Texas at Austin, Austin, Texas, United States*
 120 *Universidad Autónoma de Sinaloa, Culiacán, Mexico*
 121 *Universidade de São Paulo (USP), São Paulo, Brazil*
 122 *Universidade Estadual de Campinas (UNICAMP), Campinas, Brazil*
 123 *Universidade Federal do ABC, Santo Andre, Brazil*
 124 *University of Cape Town, Cape Town, South Africa*
 125 *University of Houston, Houston, Texas, United States*
 126 *University of Jyväskylä, Jyväskylä, Finland*
 127 *University of Liverpool, Liverpool, United Kingdom*
 128 *University of Science and Technology of China, Hefei, China*
 129 *University of South-Eastern Norway, Tonsberg, Norway*
 130 *University of Tennessee, Knoxville, Tennessee, United States*
 131 *University of the Witwatersrand, Johannesburg, South Africa*
 132 *University of Tokyo, Tokyo, Japan*
 133 *University of Tsukuba, Tsukuba, Japan*
 134 *Université Clermont Auvergne, CNRS/IN2P3, LPC, Clermont-Ferrand, France*
 135 *Université de Lyon, Université Lyon 1, CNRS/IN2P3, IPN-Lyon, Villeurbanne, Lyon, France*
 136 *Université de Strasbourg, CNRS, IPHC UMR 7178, F-67000 Strasbourg, France, Strasbourg, France*
 137 *Université Paris-Saclay Centre d’Etudes de Saclay (CEA), IRFU, Département de Physique
Nucléaire (DPhN), Saclay, France*
 138 *Università degli Studi di Foggia, Foggia, Italy*
 139 *Università degli Studi di Pavia, Pavia, Italy*
 140 *Università di Brescia, Brescia, Italy*
 141 *Variable Energy Cyclotron Centre, Homi Bhabha National Institute, Kolkata, India*
 142 *Warsaw University of Technology, Warsaw, Poland*
 143 *Wayne State University, Detroit, Michigan, United States*
 144 *Westfälische Wilhelms-Universität Münster, Institut für Kernphysik, Münster, Germany*
 145 *Wigner Research Centre for Physics, Budapest, Hungary*
 146 *Yale University, New Haven, Connecticut, United States*
 147 *Yonsei University, Seoul, Republic of Korea*



II

BAYESIAN ESTIMATION OF THE SPECIFIC SHEAR AND BULK VISCOSITY OF THE QUARK-GLUON PLASMA WITH ADDITIONAL FLOW HARMONIC OBSERVABLES

by




J. E. Parkkila, A. Onnerstad, and D. J. Kim, 2021

Phys.Rev.C 104 (2021) 054904

<https://doi.org/10.1103/PhysRevC.104.054904>

Published by the American Physical Society under the terms of
the [Creative Commons Attribution 4.0 International](https://creativecommons.org/licenses/by/4.0/) license.

Bayesian estimation of the specific shear and bulk viscosity of the quark-gluon plasma with additional flow harmonic observables

J. E. Parkkila ,* A. Onnerstad , and D. J. Kim 

*University of Jyväskylä, Department of Physics, P.O. Box 35, FI-40014 University of Jyväskylä, Finland
and Helsinki Institute of Physics, P.O. Box 64, FI-00014 University of Helsinki, Finland*



(Received 8 July 2021; accepted 26 October 2021; published 8 November 2021)

The transport properties of the strongly coupled quark-gluon plasma created in ultrarelativistic heavy-ion collisions are extracted by Bayesian parameter estimate methods with the latest collision beam energy data from the CERN Large Hadron Collider. This Bayesian analysis includes sophisticated flow harmonic observables for the first time. We found that the temperature dependence of specific shear viscosity appears weaker than in the previous studies. The results prefer a lower value of specific bulk viscosity and a higher switching temperature to reproduce additional observables. However, the improved statistical uncertainties both on the experimental data and hydrodynamic calculations with additional observables do not help to reduce the final credibility ranges much, indicating a need for improving the dynamical collision model before the hydrodynamic takes place. In addition, the sensitivities of experimental observables to the parameters in hydrodynamic model calculations are quantified. It is found that the analysis benefits most from the symmetric cumulants and nonlinear flow modes, which mostly reflect nonlinear hydrodynamic responses, in constraining the temperature dependence of the specific shear and bulk viscosities in addition to the previously used flow coefficients.

DOI: [10.1103/PhysRevC.104.054904](https://doi.org/10.1103/PhysRevC.104.054904)

I. INTRODUCTION

The primary goal of heavy-ion physics is to investigate and understand the strongly coupled color-deconfined matter, quark-gluon plasma (QGP), which is produced in ultrarelativistic collisions between heavy ions. The QGP is believed to be the predominant form of matter during the first phases of the early universe. This matter behaves like a near-perfect fluid with the smallest specific shear viscosity, the ratio of the shear viscosity to the entropy density (η/s), of any known substance in nature [1].

The most important remaining open questions in the field are the location of the critical point (T_c) in the QCD phase diagram and temperature dependence of specific shear (η) and bulk (ζ) viscosities of the QGP. The flow analysis at the CERN Large Hadron Collider (LHC) has been very successful and provides valuable information to the field [2–6]. For example, the main constraints for the QGP properties using the Bayesian analysis [7] in the theory came from the ALICE measurements [2,8,9] with both low and high beam energy data. Even though the Bayesian analyses [7,10–13] were successful, the current uncertainties from these works

are large because of statistical limitations of the data, limited observables used for the analysis, and computational constraints. In addition to the aforementioned limitations, pinning down the absolute value of η/s at T_c has a few challenges. First, a principle calculation to describe the initial conditions (IC) is still under development. Second, extracting the temperature dependence of $\eta/s(T)$ has been complicated with the existence of the bulk viscosity [14,15]. However, large flow found in small systems like proton-proton (pp) collisions was striking and opened up the importance of gluon fluctuations within protons, and certainly the experimental data would help to improve the understanding of IC both for small and large systems [16]. There are newer observables that give much stronger constraints to the theory [3,4], showing good sensitivities especially to $\eta/s(T)$ and $\zeta/s(T)$. The correlation strength measured in [3,4] was experimentally decomposed into two components of linear and nonlinear flow modes in [5,17] for the first time in the field, which gives a better understanding of our harmonic analysis and its origin with both LHC Run 1 (2009–2013) and Run 2 (2015–2018) data.

In this work, we extend the Bayesian parameter estimation methods employed in [7] with larger statistic LHC Run 2 results [18,19] as well as a few additional observables [5,6] for the first time which require substantial computational power. This work also allows us to quantify the sensitivity of each observable to the hydrodynamic model parameters in a controlled way. In Sec. II, we present a brief overview of Bayesian analysis methods and model setups. The experimental observables are described in Sec. III. Model parameters and calibrations are explained in Sec. IV. The results are presented in Sec. V, after which Sec. VI summarizes our results and findings.

*jasper.parkkila@cern.ch

Published by the American Physical Society under the terms of the Creative Commons Attribution 4.0 International license. Further distribution of this work must maintain attribution to the author(s) and the published article's title, journal citation, and DOI. Funded by SCOAP³.

II. BAYESIAN ANALYSIS

There have been a number of studies that utilized Bayesian methods for heavy ion collisions [20–24]. We employ the recent state-of-the-art development in [7] for our present study. We define a vector of model parameters \mathbf{x} , and a set of experimental data \mathbf{y} that will be compared with model calculations. Bayes's theorem gives the posterior distributions for the model parameters as

$$P(\mathbf{x}|\mathbf{y}) \propto P(\mathbf{y}|\mathbf{x})P(\mathbf{x}). \quad (1)$$

Here $P(\mathbf{y}|\mathbf{x})$ is the likelihood, which quantifies the model agreement with the data. The prior $P(\mathbf{x})$ encapsulates initial knowledge on the parameters.

The model parameters are then extracted from the posterior distributions. We follow the same procedures as [7], where the model is first evaluated at a small $O(10^2)$ number of “design” parameter points. The resulting discrete set of model predictions is then made continuous by the use of a Gaussian process (GP) emulator, which thereby can be used to systematically probe the parameter space with Markov chain Monte Carlo (MCMC) methods.

A. Hydrodynamic model and parameters

The model used in this analysis consists of the T_RENTO model [25] for the initial condition, which is connected with free streaming to a 2 + 1 dimensional causal hydrodynamic model VISH(2 + 1) [26,27]. The evolution continues after particlization via the UrQMD model [28,29]. This hybrid model, denoted T_RENTO + VISH(2 + 1) + UrQMD, has successfully described the previous ALICE measurements [7].

A hydrodynamic modeling relies on the energy and momentum conservation laws of the fluid dynamics. The conservation is expressed in terms of

$$\partial_\mu T^{\mu\nu}(x) = 0, \quad (2)$$

where $T^{\mu\nu}(x)$ is the energy-momentum tensor. In the case of viscous hydrodynamics, the energy-momentum tensor becomes

$$T^{\mu\nu} = \epsilon u^\mu u^\nu - (P + \Pi)\Delta^{\mu\nu} + \pi^{\mu\nu}, \quad (3)$$

where ϵ is the energy density, P is the local pressure given by the equation of state, and $\Delta^{\mu\nu} = g^{\mu\nu} - u^\mu u^\nu$ is a projector onto the transverse four-velocity. The shear and bulk viscosities are encoded into $\pi^{\mu\nu}$ and Π , respectively.

Free parameters of this model include the initial conditions, $\eta/s(T)$ and $\zeta/s(T)$, characterized by a total of 14 model parameters, which together control the prominent features of the model. The parameter set, described in detail in later sections, will enable simultaneous characterization of the initial state and medium response, including any correlations.

Each event consists of a single initial condition given energy density profile and a hydrodynamic simulation followed by multiple samples of the freeze-out hypersurface. The parameter estimation is conducted using 500 parameter design points, sampled evenly from the parameter space using the Latin hypercube scheme [30,31]. At each design point, the model is used to generate around 3×10^5 events with

the corresponding parametrization, with each event surface sampled ten times to produce a total of 3×10^6 events for 0–60% centrality ranges. A large number of events is generated to ensure a better accuracy for high harmonic observables. A GP emulator is then trained to produce predictions for the observables in between the design points, after which the predictions are validated against a validation set. See [7] for details of the emulator. Using the emulator to produce predictions in continuous parameter space, the final posterior distribution is created using MCMC sampling.

B. Calibrating the model parameters

The parameter estimation attempts to calibrate the model parameters for the model to optimally reproduce experimental observables. With Bayesian methods, the optimal parameters are characterized by probability distributions for their true values. As given by Bayes's theorem, the probability for the true parameters \mathbf{x}_* is

$$P(\mathbf{x}_*|X, Y, \mathbf{y}_{\text{exp}}) \propto P(X, Y, \mathbf{y}_{\text{exp}}|\mathbf{x}_*)P(\mathbf{x}_*). \quad (4)$$

The left-hand side is the *posterior*: the probability of \mathbf{x}_* given the design X , computed observables Y , and the experimental data \mathbf{y}_{exp} . On the right-hand side, $P(\mathbf{x}_*)$ is the *prior* probability, encapsulating the initial knowledge of \mathbf{x}_* , and $P(X, Y, \mathbf{y}_{\text{exp}}|\mathbf{x}_*)$ is the likelihood: the probability of observing $(X, Y, \mathbf{y}_{\text{exp}})$ given a proposal \mathbf{x}_* .

The likelihood may be computed using the principal component GP emulators as

$$\begin{aligned} P &= P(X, Y, \mathbf{y}_{\text{exp}}|\mathbf{x}_*) \\ &= P(X, Z, \mathbf{z}_{\text{exp}}|\mathbf{x}_*) \\ &\propto \exp\left\{-\frac{1}{2}(\mathbf{z}_* - \mathbf{z}_{\text{exp}})^\top \Sigma_z^{-1}(\mathbf{z}_* - \mathbf{z}_{\text{exp}})\right\}, \end{aligned} \quad (5)$$

where $\mathbf{z}_* = \mathbf{z}_*(\mathbf{x}_*)$ are the principal components predicted by the emulators, \mathbf{z}_{exp} is the principal component transform of the experimental data \mathbf{y}_{exp} , and Σ_z is the covariance (uncertainty) matrix. The covariance matrix encodes all the experimental and model uncertainties [32]. In the principal component space, the covariance matrix can be expressed as

$$\Sigma_z = \Sigma_z^{\text{exp}} + \Sigma_z^{\text{GP}} + (\sigma_m^{\text{sys}})^2 I, \quad (6)$$

where Σ_z^{exp} is the matrix for experimental errors and $\Sigma_z^{\text{GP}} = \text{diag}(\sigma_{z,1}(\mathbf{z}_*)^2, \sigma_{z,2}(\mathbf{z}_*)^2, \dots, \sigma_{z,k}(\mathbf{z}_*)^2)$ is the diagonal GP emulator covariance matrix, representing the model statistical and GP predictive uncertainty. Additionally, σ_m^{sys} is a free parameter ranging from zero to one, with the purpose of including all remaining uncertainties arising from the model imperfections. All model parameters are given a uniform prior. Together with the likelihood (5) and Bayes' theorem (4), the posterior probability can be evaluated at an arbitrary point in the parameter space. To construct the posterior distribution, an MCMC method can be used, which generates random walks through parameter space by accepting or rejecting proposal points based on the posterior probability.

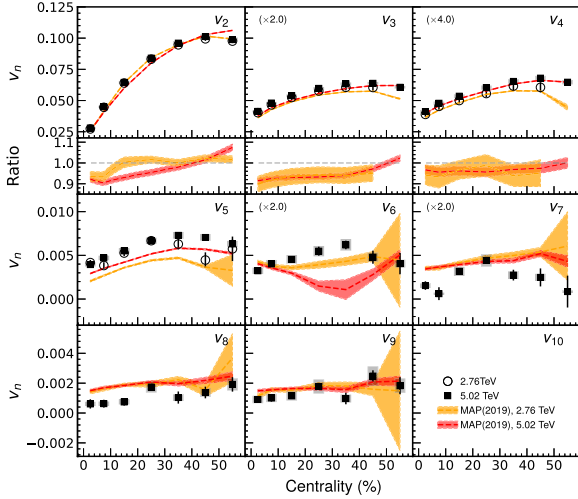


FIG. 1. Model calculations of flow coefficients compared to experimental data at center-of-mass energies of 2.76 and 5.02 TeV. The systematic error for the higher energy data points is shown as a grey band around them. This band is not shown for the lower energy data points since they have combined errors.

III. EXPERIMENTAL OBSERVABLES

In the previous studies, the centrality dependence of identified particle yields dN/dy and mean transverse momenta $\langle p_T \rangle$ for charged pions, kaons, and protons as well as two-particle anisotropic flow coefficients v_n for $n = 2, 3, 4$ were used. The observables are measured by the ALICE Collaboration in Pb-Pb collisions at $\sqrt{s_{NN}} = 2.76$ TeV [2,8,9]. In this work, we mainly focus on the larger statistic higher beam energy collisions at $\sqrt{s_{NN}} = 5.02$ TeV, which give better precision. In addition to the above mentioned observables, we include higher harmonic flow coefficients v_n [5] (up to $n = 9$), the normalized symmetric cumulants NSC(m, n) [6], and the nonlinear flow mode coefficients $\chi_{n,mk}$ [5].

The anisotropic pressure-driven expansion of the QGP, commonly referred to as anisotropic flow, can be characterized by a Fourier decomposition of the azimuthal particle distributions as

$$\frac{dN}{d\phi} \propto 1 + 2 \sum_{n=1}^{\infty} v_n \cos[n(\phi - \psi_n)], \quad (7)$$

where v_n quantifies the magnitude of the n th harmonic flow, and ψ_n its direction. NSC(m, n) quantifies the correlations between event-by-event fluctuations of flow harmonics of different orders, $\text{NSC}(m, n) = (\langle v_m^2 v_n^2 \rangle - \langle v_m^2 \rangle \langle v_n^2 \rangle) / (\langle v_m^2 \rangle \langle v_n^2 \rangle)$ [3,6], and $\chi_{n,mk}$ measures the contribution of lower order harmonic flows to higher order harmonics (i.e., $\chi_{4,22}$ is the nonlinear contribution of v_4 originating from v_2 ; see the details in [5]). These additional observables give better sensitivity to the medium properties and initial conditions, as demonstrated in Refs. [3–6].

As shown in Figs. 1 and 2, a model calculation with the best-fit parametrization given by maximum *a posteriori* (MAP) from the previous Bayesian analysis [7] shows deviations of the measurements for the flow coefficients from

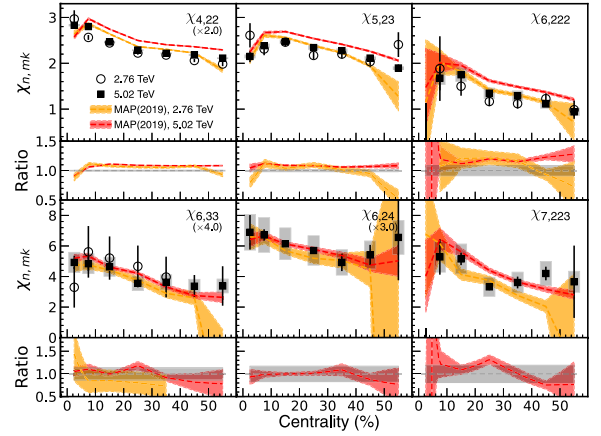


FIG. 2. Model calculations of nonlinear flow mode coefficients compared to experimental data. Most calculations reproduce $\chi_{4,22}$ within the uncertainties of the measurement and calculations. The systematic error for the higher energy data points is shown as a grey band around them. This band is not shown for the lower energy data points since they have combined errors.

$n = 5$ and the nonlinear flow mode coefficients from $\chi_{n,mk}$ ($n = 4$). The black filled and open circles represent the higher ($\sqrt{s_{NN}} = 5.02$ TeV) and lower ($\sqrt{s_{NN}} = 2.76$ TeV) energy data points, respectively, whereas the red and orange bands represent the higher and lower energy model calculations. The v_2 – v_4 values calculated from data were used in model calibration, and, as seen in Fig. 1, the calculations agrees well for v_4 . However, a discrepancy is seen for v_3 with an underestimation of the calculations for the centrality up to $\approx 45\%$ for both energies, and an even larger discrepancy in v_2 for the higher energy calculation, while the lower energy calculation agrees well except for the low centrality of 0–10%. For higher harmonics ($\geq v_5$) the deviation is still visible.

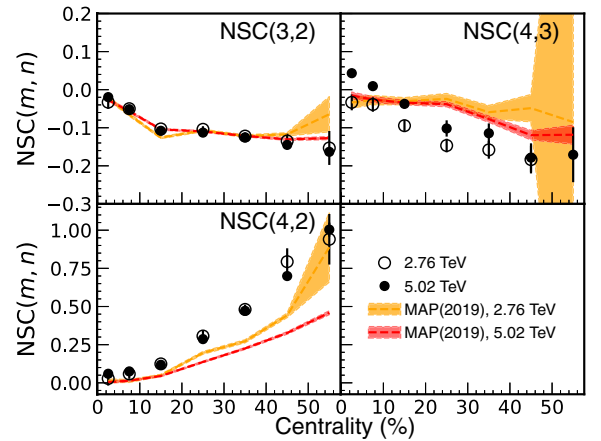


FIG. 3. Model calculations of the normalized symmetric cumulants [NSC(m, n)] compared to experimental data at center-of-mass energies of 2.76 and 5.02 TeV. The systematic error for the higher energy data points is shown as a grey band around them. This band is not shown for the lower energy data points since they have combined errors.

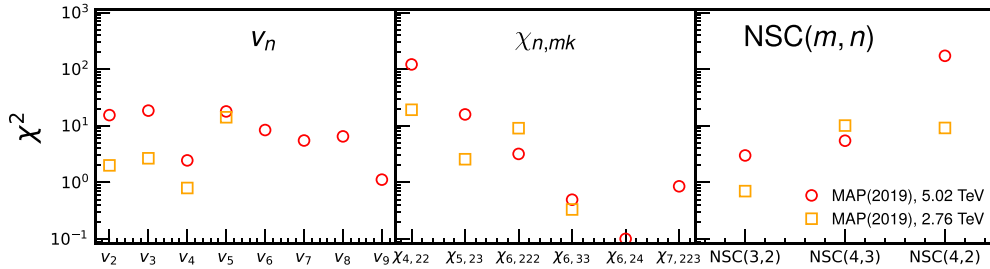


FIG. 4. The χ^2 values calculated between the data and model calculations for both beam energies are shown for v_n , $\chi_{n,mk}$, and $NSC(m, n)$.

The model calculations for the nonlinear flow mode coefficients in Fig. 2 agree within $\pm 15\%$ for $\chi_{4,22}$ and $+15\%$ for the higher energy model calculation of $\chi_{5,23}$, while the lower energy model calculation goes to -30% in central collisions and even larger than 50% at high centrality ranges. The discrepancies between data and model calculations are significantly larger from $\chi_{6,222}$; however, for $\chi_{6,24}$, most of the higher energy data points agree with the calculations within systematic uncertainties.

Model calculations reproduce the value for $NSC(3, 2)$ up to the 40–50% centrality class, which is shown in Fig. 3. Both model predictions underestimate the values of $NSC(4, 2)$ for all centrality classes presented. The model calculations overestimate $NSC(4, 3)$ for the lower energy data and give similar results for the higher energy. However, the results show clear differences between the two beam energies. The differences get larger toward the central collisions. While it is negative for the lower energy data and the model calculations, the measurement at 5.02 TeV shows the change of the signs in central collisions. Also, the magnitudes are smaller in lower energy collisions, which is attributed to the increasing contribution from the nonlinear hydrodynamic response in v_4 [6].

In order to quantify the agreement of the models with the data, the χ^2 test was performed in the same way as in Eq. (5) in Ref. [4] for the centrality range 5–50%. The results are shown in Fig. 4 for the flow coefficients, non-linear flow mode coefficients, and the normalized symmetric cumulants. A significant difference is observed between the χ^2 values for v_n of higher and lower energies at $n \leq 4$. The χ^2 values for v_5 are larger for both beam energies with similar magnitudes. The higher energy χ^2 value for $\chi_{4,22}$ is significantly larger than the one from the lower energy as shown in Fig. 4. The disagreement is still significant for $\chi_{5,23}$ and $\chi_{6,222}$. For $NSC(m, n)$, the χ^2 values are larger for higher harmonics at

both beam energies. The χ^2 is especially large for the higher beam energy $NSC(4, 3)$.

In our calculations of the observables, we used the same methods also used in experimental analysis in Refs. [3–6]. Our centrality classes in this study are chosen to match those used for the experimental data. We define the multiplicity range for each centrality class by simulating events using the MAP parameterization from [7], and sorting the resulting minimum-bias events by charged-particle multiplicity $dN/d\eta$ at midrapidity ($|\eta| < 0.5$). The identified $dN/d\eta$ and $\langle p_T \rangle$ were evaluated by counting and averaging the particle species at midrapidity ($|\eta| < 0.5$). The experimental data are readily corrected and extrapolated to zero p_T [9], and therefore no additional processing is required while preparing the comparison. For the identified $dN/d\eta$, only protons were used in model calibration, as the model did not reproduce the spectra of the other species with any of the parametrizations. Finally, we calculated flow coefficients and other observables for charged particles within the kinematic range of the ALICE detector using the same methods as in the data analyses [5,6]. A summary of all the observables that are included in the Bayesian analysis is given in Table I. The table presents the particle species, kinematic cuts, and centrality classes for each observable.

IV. PARAMETER ESTIMATION USING NEW LHC MEASUREMENTS

The model to be evaluated in this analysis consists of multiple stages, of which a brief overview will be given next. Altogether, the model setup includes the parametric TRENTo initial conditions, free-streaming preequilibrium dynamics, and the VISH(2 + 1) hydrodynamic model for medium evolution. Furthermore, the model performs the hadronization

TABLE I. Experimental data included in Bayesian analysis.

Observable	Particle species	Kinematic cuts	Centrality classes (%)	Ref.
Yields dN/dy	$h^\pm, p\bar{p}$	$ \eta < 0.5$	0–5, 5–10, 10–20, ..., 50–60	[18]
Mean transverse momentum $\langle p_T \rangle$	$\pi^\pm, K^\pm, p\bar{p}$	$ \eta < 0.5$	0–5, 5–10, 10–20, ..., 50–60	[19]
Two-particle flow cumulants $n = 2-8$	h^\pm	$ \eta < 0.8$ $0.2 < p_T < 5.0$ GeV	0–5, 5–10, 10–20, ..., 50–60	[5]
Non-linear flow mode $n = 2-8$	h^\pm	$ \eta < 0.8$ $0.2 < p_T < 5.0$ GeV	0–5, 5–10, 10–20, ..., 50–60	[5]
Symmetric cumulants $n = 2-8$	h^\pm	$ \eta < 0.8$ $0.2 < p_T < 5.0$ GeV	0–5, 5–10, 10–20, ..., 50–60	[6]

TABLE II. Input parameter ranges for the initial condition and hydrodynamic models.

Parameter	Description	Range
Norm	Overall normalization	16.542–25
p	Entropy deposition parameter	0.0042–0.0098
σ_k	Std. dev. of nucleon multiplicity fluctuations	0.5508–1.2852
d_{\min}^3	Minimum volume per nucleon	0.889^3 – 1.524^3
τ_{fs}	Free-streaming time	0.03–1.5
T_c	Temperature of const. $\eta/s(T)$, $T < T_c$	0.135–0.165
$\eta/s(T_c)$	Minimum $\eta/s(T)$	0–0.2
$(\eta/s)_{\text{slope}}$	Slope of $\eta/s(T)$ above T_c	0–4
$(\eta/s)_{\text{crv}}$	Curvature of $\eta/s(T)$ above T_c	–1.3–1
$(\zeta/s)_{\text{peak}}$	Temperature of $\zeta/s(T)$ maximum	0.15–0.2
$(\zeta/s)_{\text{max}}$	Maximum $\zeta/s(T)$	0–0.1
$(\zeta/s)_{\text{width}}$	Width of $\zeta/s(T)$ peak	0–0.1
T_{switch}	Switching/particlization temperature	0.135–0.165

and includes UrQMD hadronic cascade. The model setup used is identical to the one developed and used in [7], except for the number of hypersurface samples taken after evolution. In this work, exactly ten events are sampled from the hypersurface regardless of the cumulative number of particles. The centrality definition is shared for all parametrizations. With close to fixed initial stage parameters, the possible effects of a shared centrality definition should be negligible.

Our main focus will be to investigate the effects of the higher harmonic observables on the temperature dependence of the transport coefficients. The parametrizations of the transport coefficients are [7]

$$(\eta/s)(T) = (\eta/s)(T_c) + (\eta/s)_{\text{slope}}(T - T_c) \left(\frac{T}{T_c} \right)^{(\eta/s)_{\text{crv}}} \quad (8)$$

and

$$(\zeta/s)(T) = \frac{(\zeta/s)_{\text{max}}}{1 + \left(\frac{T - (\zeta/s)_{\text{peak}}}{(\zeta/s)_{\text{width}}} \right)^2} \quad (9)$$

for the ratios of shear viscosity and bulk viscosity over entropy, respectively. Based on previous work, it is known that the lowest value of $\eta/s(T)$ is around the critical temperature T_c , close to the universal minimum $1/(4\pi)$. The temperature dependence of $\eta/s(T)$ is moderate, and increasing with higher values of temperature. Within close proximity of 150 to 500 MeV, the slope of $\eta/s(T)$ is approximately linear. The bulk viscosity over entropy ratio $\zeta/s(T)$ is expected to peak around T_c and to decrease at higher values of temperature.

With this knowledge, we may construct our priors, and assume the initial parameter ranges. The chosen parameter ranges are loosely based on the optimal parameters found in [7]. It was found that in most cases, by taking the optimal parameters in [7] as the center points of the prior range and expanding the range slightly based on a reasonable σ value, those parameters could be further optimized with the additional observables. In this study, we have kept the initial stage parameter ranges narrow around the MAP values found in [7] with the assumption that the additional observables affect mostly the transport coefficients. Very small variation

was allowed to give the parameters space to adjust for minor differences.

The included and varied parameters, of which there are 14 in total, are summarized in Table II. The parametric TRENTo initial conditions comprise an ansatz in terms of five parameters: a normalization factor Norm, entropy deposition parameter p , standard deviation of the nuclear multiplicity fluctuations σ_{fluct} , Gaussian-shaped nucleon width w , and minimum allowed distance between nucleons d_{\min} . The initial conditions are assumed to be already well constrained and presumably not affected by the addition of medium effect

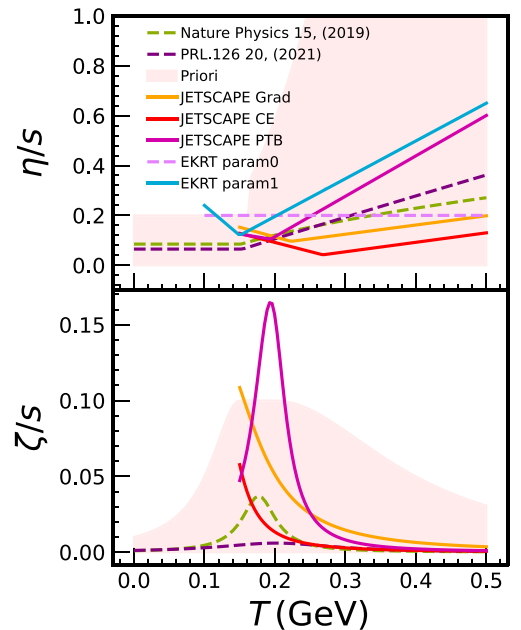


FIG. 5. The specific shear (η/s) and bulk (ζ/s) viscosity ratios as a function of temperature. The region plotted in red visualizes the prior range used in this study. Other curves represent some of the parametrizations found in previous studies: the best-fit $\eta/s(T)$ with EKRT initial conditions [33,34], parametrizations from the JETSCAPE Collaboration with three different particlization distributions [13], and a recent parametrization found in [7].

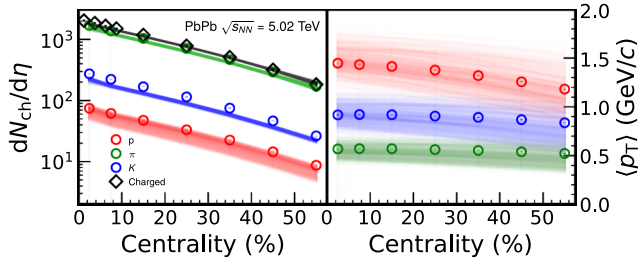


FIG. 6. Charged and identified particle multiplicity and mean transverse momenta $\langle p_T \rangle$ as given by the design parametrizations.

sensitive observables. The range for free-streaming time τ_{fs} characterizing the allotted time for preequilibrium dynamics was kept relatively large.

The rest of the parameters are the components of the transport coefficient parametrizations, and the switching temperature T_{switch} describing the temperature at which the hadronization begins to take place. The initial ranges given for these parameters are more generous, although large deviations in the final parameters compared to the previous study are not expected. The prior range for the transport coefficients is plotted in Fig. 5 among some parametrizations from other related studies [7,13,33,34]. The parametrizations are valid only up to the corresponding limits of the model: 100 MeV in the case of EKRT and 150 MeV for JETSCAPE. We note that the parametrizations EKRT+param0 and EKRT+param1 were not obtained through Bayesian analysis and we do not consider the slightly higher η/s at around $T = 100$ MeV in our prior. Furthermore, we do not consider the large ζ/s reported with the PTB particlization by the JETSCAPE Collaboration [13]. Nevertheless, the ζ/s obtained using the Grad or CE particlization distributions are within our prior, considering the temperature limit $T_{switch} > 150$ MeV.

The model is calibrated to the latest Pb-Pb collision data at $\sqrt{s_{NN}} = 5.02$ TeV from the ALICE Collaboration [5,6,18,19]. Figures 6–9 show the calculations of each observable using the design parametrizations obtained from the prior

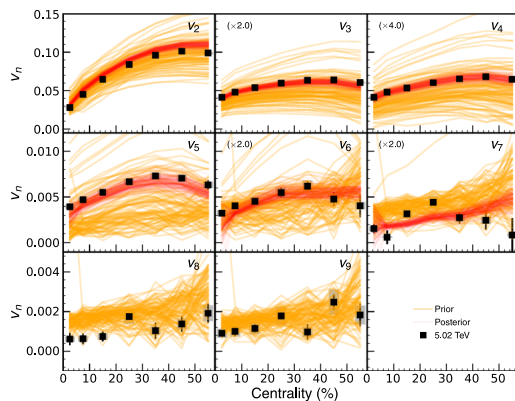


FIG. 7. Flow coefficients v_n as given by the design parametrizations are presented in yellow curves. All harmonics are simultaneously covered by the design parametrizations. The red curves represent a number of curves sampled from the posterior distribution, and are as given by the emulator.

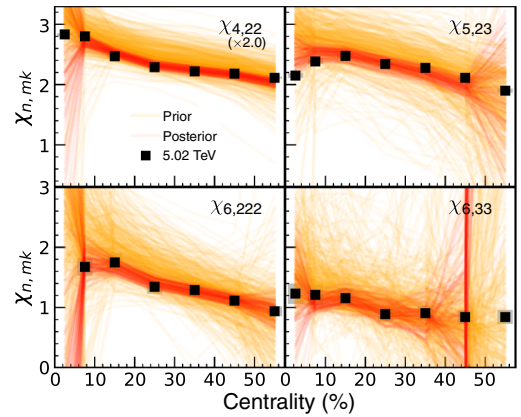


FIG. 8. Design parametrizations for nonlinear flow mode coefficients $\chi_{n,mk}$ (in yellow) and a number of posterior sample curves as given by the emulator (in red).

distribution. The yellow curves represent the calculations corresponding to each design point parametrization, which are used in training the GP emulator, whereas the red curves represent emulator predictions corresponding to random points sampled from the posterior distribution.

V. RESULTS

Figure 10 highlights the posterior and marginal distributions for select components of the transport parameters. The primary components, η/s slope, $\eta/s(T_c)$, $(\zeta/s)_{max}$ in the transport parametrizations, are well constrained. The initial condition parameters are well constrained within the narrow prior range.

Figure 11 presents the estimated temperature dependence of $\eta/s(T)$ and $\zeta/s(T)$ according to the parametrizations from Eqs. (8) and (9), respectively. The shaded region around the curves represents the 90%-credibility region. This region reflects all uncertainties coming from the finite width of the posterior distribution, experimental statistical and systematic uncertainties, statistical uncertainties in model calculations, predictive uncertainty from the GP emulator, and systematic

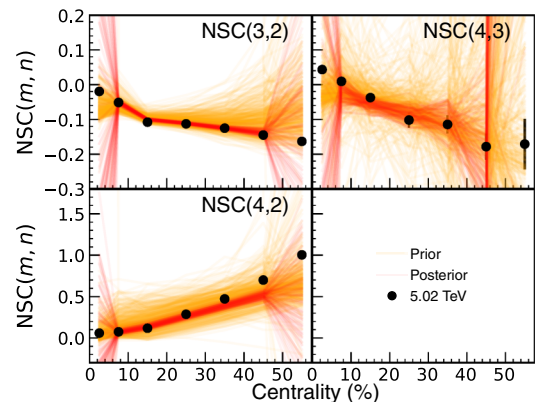


FIG. 9. Design parametrizations for normalized symmetric cumulants (in yellow) and a number of posterior sample curves as given by the emulator (in red).

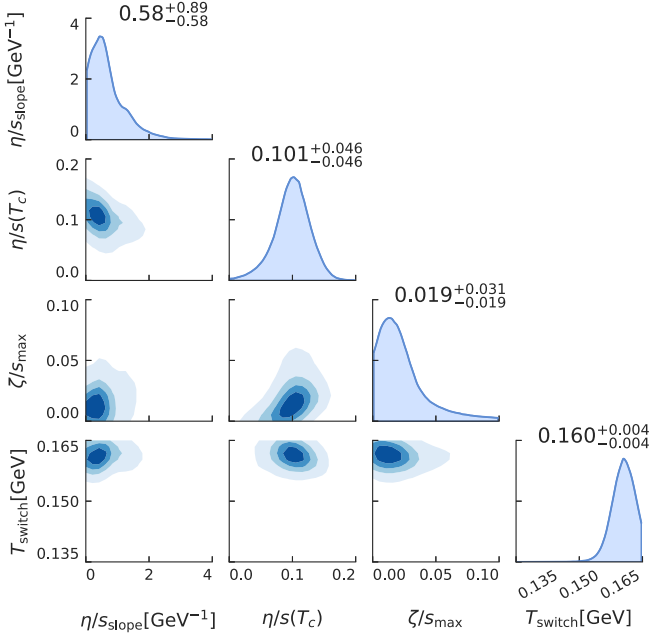


FIG. 10. Dimensionally reduced posterior probability for select transport parameters. The diagonal histograms represent the marginal distributions for the corresponding parameters. The accompanying numbers are the median values, as well as the limits of the 90%-credibility range.

model bias. With high probability, the true curve is located within this region.

Table III presents the best-fit MAP parameters from our analysis. We list here the important findings:

- (1) While the temperature dependence of $\eta/s(T)$ is similar to what was obtained in [7], the curvature of $\eta/s(T)$ is slightly stronger, resulting in lower values at higher temperatures above T_c .
- (2) A notable change is the lower $(\zeta/s(T))_{\max}$ in order to reproduce the additional observables. The obtained $\zeta/s(T)$ is smaller than those found in the previous Bayesian analyses [7,13] where the additional observables were not included. A similar value was reported in Ref. [11]. On average this represents a value an order of magnitude lower compared to the lattice QCD calculation [35] and the parametrizations used

TABLE III. The best-fit MAP parameters.

Initial conditions		Transport	
Parameter	MAP value	Parameter	MAP value
Norm	21.06	$\eta/s(T_c)$	0.104
p	0.0077	$(\eta/s)_{\text{slope}}$	0.425
σ_k	0.881	$(\eta/s)_{\text{erv}}$	0.738
d_{\min}^3	0.975	$(\zeta/s)_{\text{peak}}$	0.170
τ_{fs}	0.901	$(\zeta/s)_{\text{max}}$	0.010
T_c	0.147	$(\zeta/s)_{\text{width}}$	0.057
T_{switch}	0.160		

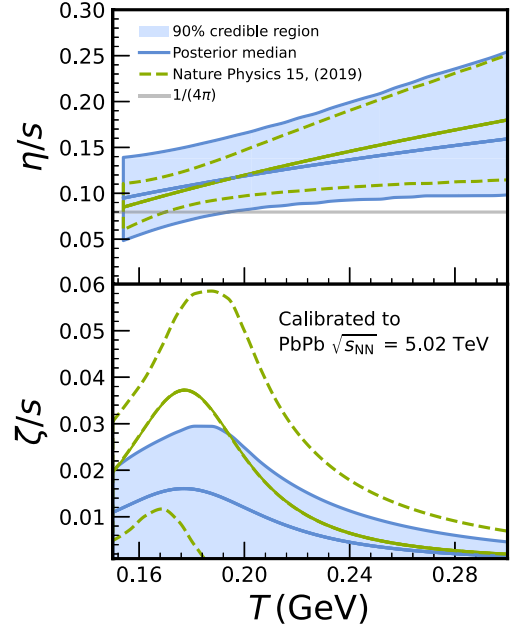


FIG. 11. The 90%-credibility region for the shear (top) and bulk (bottom) viscosity to entropy ratio is given as a blue band. The blue line represents the median of the credible range. The MAP parametrization from [7] as well as the corresponding 90%-credibility range are plotted as green dashed curves.

in [36,37], where the parametrizations were tuned to simultaneously reproduce lower harmonic v_n as well as the charged particle multiplicity and the low- p_T region of the charged hadron spectra.

- (3) The switching temperature on the other hand is higher than the one found in the aforementioned studies, where on average T_{switch} is located around ≈ 0.150 GeV. As discussed in [4,5,17], the additional observables, the nonlinear response modes and the correlations between flow harmonics are sensitive to viscous corrections to the equilibrium distribution at hadronic freeze-out [38–41] and seem to prefer the higher switching temperature.

We performed high-statistics hydrodynamic calculations with the new parametrization. Figures 12 and 13 present the calculations for the flow coefficients v_n and nonlinear flow mode coefficients, respectively. The v_n is reproduced within 10% agreement for $n = 2$ up to $n = 4$. For the fifth harmonic, the calculations underestimate the data. The new parametrization estimates the data better in central and peripheral collisions but deviates significantly in the peripheral region. The magnitude of the successive harmonics from v_6 is not quite captured by the calculations within the statistical uncertainty. Furthermore, with our new parametrization, the predictions for the nonlinear flow mode coefficients have also improved compared to the parametrization from [7], as indicated by the ratio plots. In this case, the lower harmonic nonlinear flow mode coefficients are no longer overestimated, and the magnitude and centrality dependence are correctly captured. We note that the nonlinear flow mode coefficients

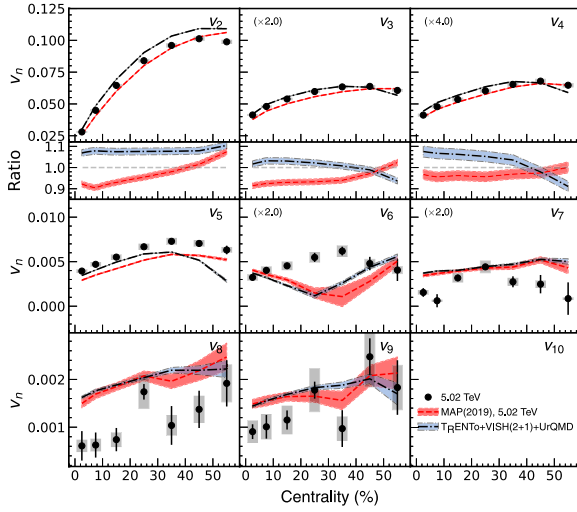


FIG. 12. Flow coefficients from two hydrodynamical calculations are compared to the experimental data [5] at center-of-mass energy 5.02 TeV. The blue band is calculated with the MAP parametrization from this work, whereas the red band uses the parametrization from [7].

have not been included in the model calibration in [7], whereas, coefficients up to $\chi_{6,33}$ and $\chi_{6,222}$ were used in this analysis. Figure 14 presents the calculation of the normalized SC using our obtained parametrization. The performances of the new parametrization and the one from [7] are comparable for NSC(3, 2). For NSC(4, 2) and NSC(4, 3), the centrality dependence is better described by the new parametrization. However, both parametrizations are unable to reproduce the strong centrality dependence of NSC(4, 2), underestimating the most data points in the most peripheral collisions. The multiplicity and the mean- p_T calculations are compared to the results from [7] in Fig. 15. Our parametrization improves the

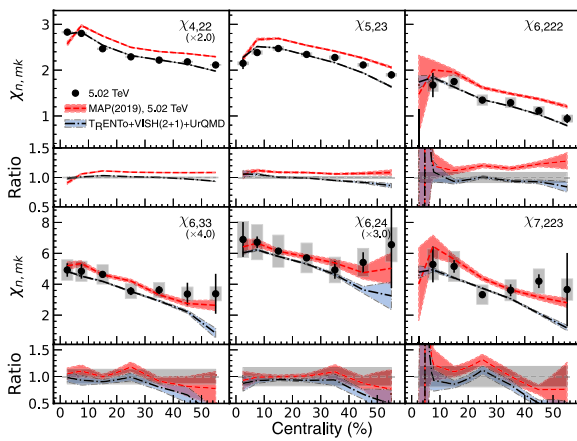


FIG. 13. Nonlinear flow mode coefficients from two hydrodynamical calculations are compared to the experimental data [5] at center-of-mass energy 5.02 TeV. The blue band is calculated with the MAP parametrization from this work, whereas the red band uses the parametrization from [7].

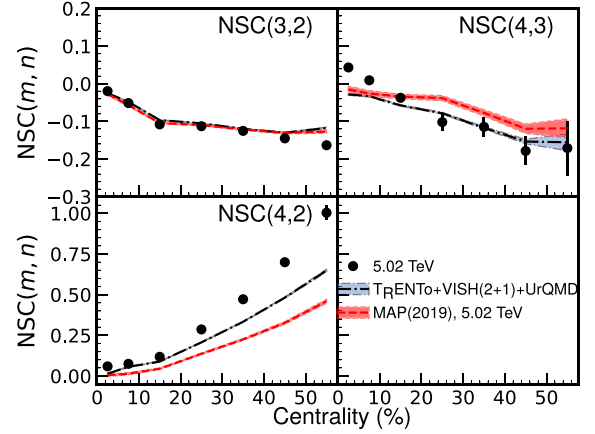


FIG. 14. Normalized symmetric cumulants [NSC(m, n)] from two hydrodynamical calculations are compared to the experimental data [6] at center-of-mass energy 5.02 TeV. The blue band is calculated with the MAP parametrization from this work, whereas the red band uses the parametrization from [7].

estimate of the proton multiplicity and gives the same charged particle multiplicity for 5.02 TeV collisions, while the pion and kaon multiplicities are not in good agreement with the experimental data, as similarly found in [7] for 2.76 TeV calculations. Interestingly, the parametrizations from [7] mainly utilizing 2.76 TeV data give better agreement with pions and kaons in 5.02 TeV collisions than our results while overestimating the proton yields approximately 10%. Agreement of the calculated mean p_T with the experimental data is good for all particle species, as well as with the results from [7] for both beam energies. Refining this analysis by including low beam energy data in the future will help us to understand the beam energy dependence on various observables.

Finally, Fig. 16 shows the χ^2 values with the best-fit MAP parameters extracted from this study for each observable. They are compared to the ones from [7]. The χ^2 values for our new calculation only seem to improve v_3 and v_5 for the v_n observable. For the nonlinear flow mode coefficients the χ^2 values are improved up to $\chi_{6,222}$ with our new parametrization, while the χ^2 values for the higher harmonics are worse than in [7]. For NSC, the χ^2 from the new calculation is worse for

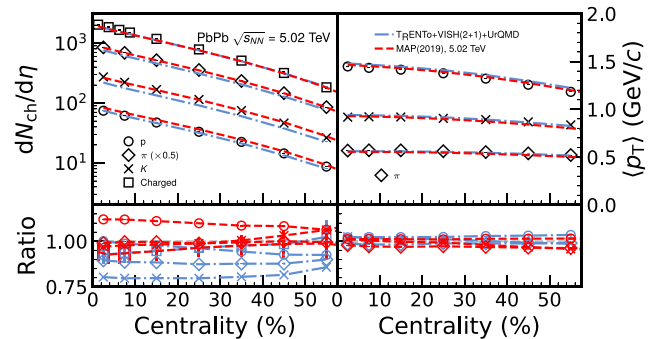


FIG. 15. Charged and identified particle multiplicity and mean p_T from two hydrodynamical calculations are compared to the experimental data at center-of-mass energy 5.02 TeV.

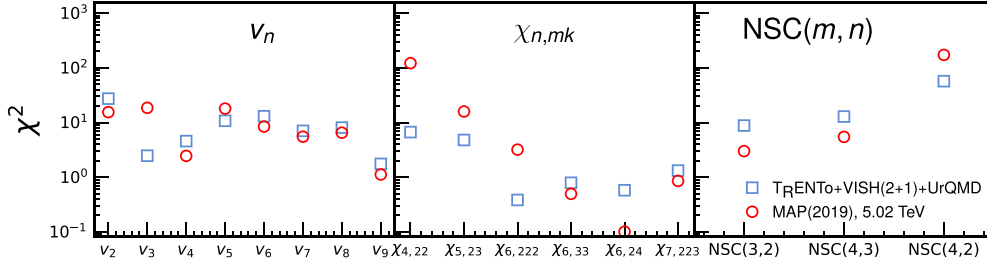


FIG. 16. The χ^2 values with the best-fit MAP parameters extracted from this study are compared to the ones from [7].

NSC(3, 2) and NSC(4, 3), but is improved for NSC(4, 2). We note that the larger statistical error in the calculations using the parametrization of Ref. [7] lowers the corresponding χ^2 values, slightly affecting the direct comparison between the two parametrizations. The sign change of NSC(4, 3) in most central collisions is not reproduced by the models while the beam-energy-dependent magnitudes are better described with new parametrizations. We leave those differences for future research work where the present results should be refined by including experimental data from the lower energy beam data. As a final study in this analysis, we conduct a simple sensitivity analysis of the included observables to the model transport parameters. The sensitivity of each observable is evaluated using the GP emulator by observing the relative difference in the magnitude of the observable between two parameter points in the parameter space. The difference can be formulated as

$$\Delta = \frac{|\hat{O}(\mathbf{x}') - \hat{O}(\mathbf{x})|}{\hat{O}(\mathbf{x})}, \quad (10)$$

where $\hat{O}(\mathbf{x})$ and $\hat{O}(\mathbf{x}')$ represent the values of an observable at parameter points \mathbf{x} and \mathbf{x}' , respectively [13].

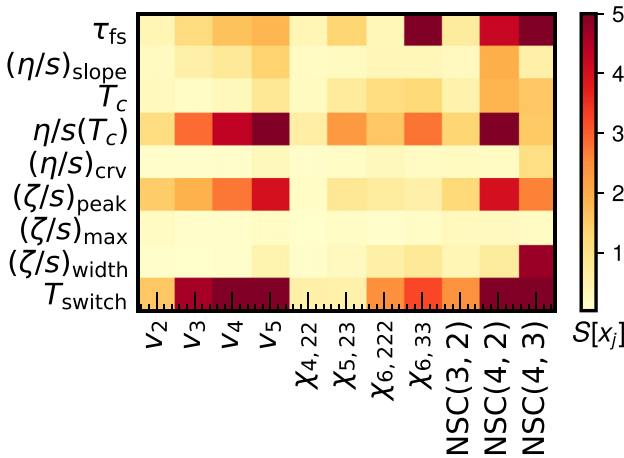


FIG. 17. Sensitivity of the observables to the model parameters visualized as a color map. The sensitivity index is averaged over four centrality classes, from 5% to 40%. Light yellow shades represent a very limited sensitivity or no sensitivity, whereas orange and darker red colors represent moderate or strong sensitivities to the corresponding model parameter, respectively.

In this study, we choose a reference parameter point \mathbf{x} to be the one representing the MAP values obtained in this analysis (see Table III). To probe the sensitivity of a parameter j , another point is defined as $\mathbf{x}' = (x_1, x_2, \dots, (1 + \delta)x_j, \dots, x_p)$, where δ is a small value representing a percentile change in the parameter space. We have used a value $\delta = 0.1$, although larger values were observed to yield similar results.

We then calculate a final sensitivity index for each observable and parameter pair in various centrality classes as

$$S[x_j] = \Delta/\delta. \quad (11)$$

Figure 17 presents the evaluated sensitivity for each observable against the transport parameters. The sensitivity was evaluated over four centrality classes from 5% to 40% and averaged for the final plot. We did not observe large differences in the sensitivity between the individual centrality classes.

For v_n , we can verify a known fact that the sensitivity of the flow coefficients is generally very limited to the temperature dependence of $\eta/s(T)$ [33], although, as expected, the sensitivity to the average $\langle \eta/s \rangle$, in this case, represented by $\eta/s(T_c)$, is very strong, and increasing at higher harmonics. The sensitivity of the v_n to the $(\zeta/s)_{\text{peak}}$ is visible, and also in this case the higher harmonics provide stronger constraints. Based on previous studies, the nonlinear flow mode coefficients $\chi_{n,mk}$ are known to be sensitive to $\eta/s(T)$ at the freeze-out temperature. This is reflected by the observed sensitivity to $\eta/s(T_c)$ as well as T_c . By far, the normalized symmetric

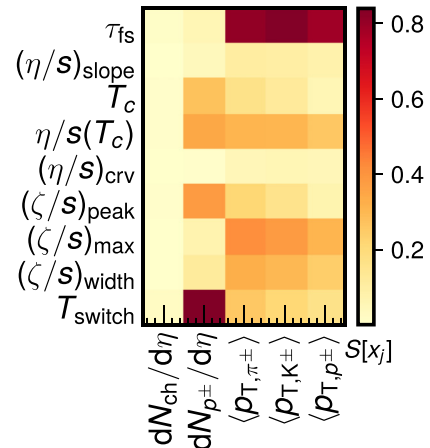


FIG. 18. Sensitivity of the mean multiplicity yields and mean transverse momenta ($\langle p_T \rangle$) to the model parameters.

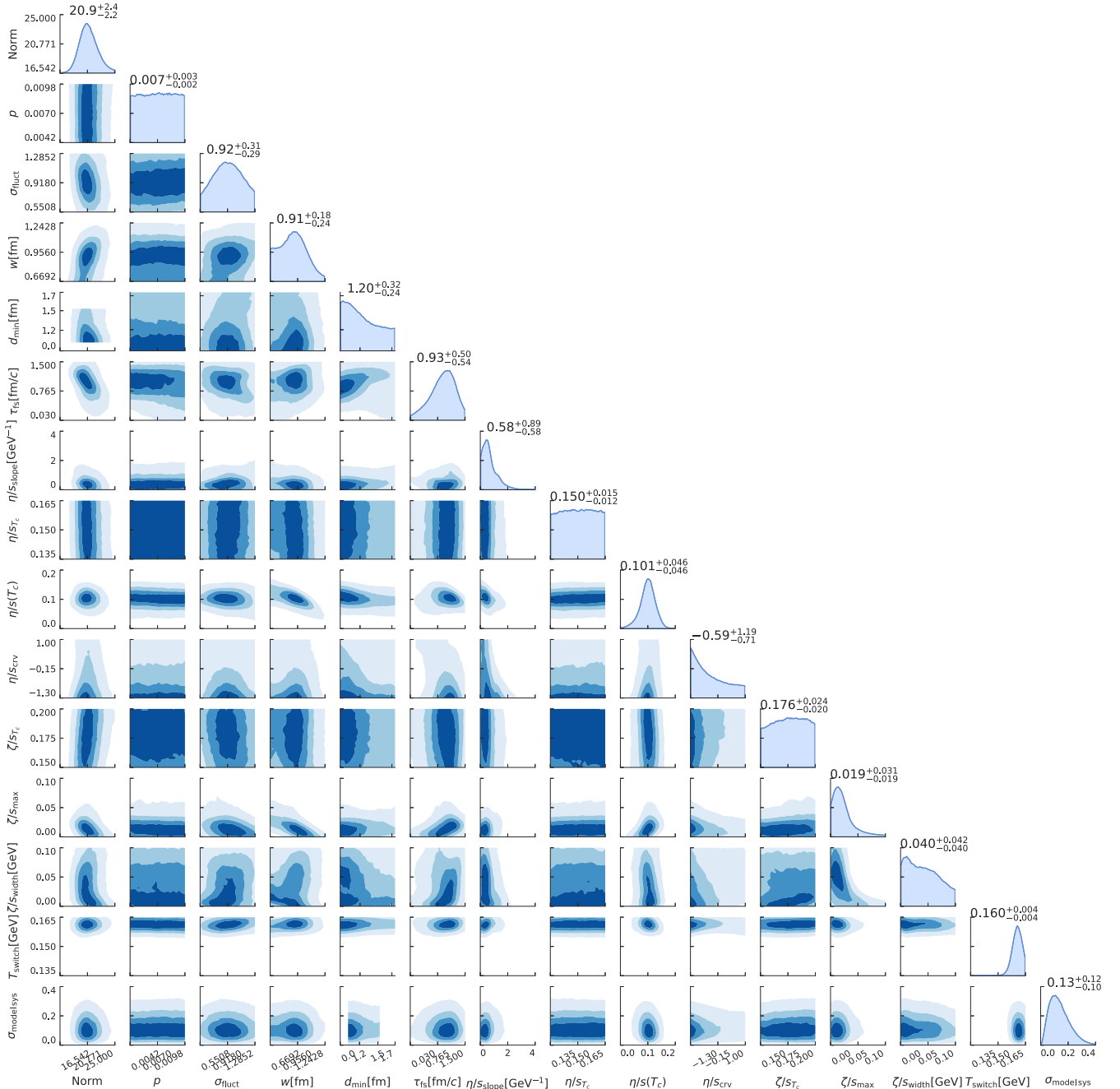


FIG. 19. Dimensionally reduced posterior distribution for all parameters in the analysis. The diagonally placed histograms represent the marginal distributions for each corresponding parameter. For each marginal distribution, a number and a range is given, denoting the median and limits of the 90%-credibility region, respectively.

cumulants provide the strongest constraints to the temperature dependence of $\eta/s(T)$. This is confirmed by higher sensitivity for the other components of $\eta/s(T)$, and not only $\eta/s(T_c)$, which is also higher.

Two other parameters have also been included in this study: the free-streaming time scale τ_{fs} and the switching temperature T_{switch} . On average, the observables are reported to be generally weakly sensitive to τ_{fs} , apart from the symmetric cumulants and $\chi_{6,33}$. Furthermore, most of the observables, such as v_n , $\chi_{6,mk}$ and the NSC(m, n), are seen to be highly

sensitive to the switching temperature T_{switch} . In both cases, the results reported here regarding τ_{fs} and T_{switch} are not compatible with what has been observed in [13].

Figure 18 presents the sensitivity of the multiplicity and the $\langle p_T \rangle$ to the model parametrizations. Most prominently, the switching temperature affects the proton multiplicity. Furthermore, we observe a comparatively large sensitivity of $\langle p_T \rangle$ to the free-streaming timescale τ_{fs} . In the case of the transport parameters, the effect on the observables is relatively small. It is observed that $\langle p_T \rangle$ acts as a subtle

constraint to the parameters describing the specific bulk viscosity. The posterior distribution for all parameters is shown in Fig. 19.

VI. DISCUSSIONS

In summary, we performed a Bayesian analysis with the recently available data from ALICE Collaboration [5,6,18,19] as an extension of the work [7]. We found that the temperature dependence of $\eta/s(T)$ is similar to what was obtained in [7] and that the curvature of $\eta/s(T)$ above T_c is slightly lower at higher temperatures, showing weak temperature dependence of η/s . Notable changes include the lower $(\zeta/s(T))_{\max}$ and the higher switching temperature T_{switch} to reproduce additional observables such as symmetric cumulants and nonlinear flow coefficients. However, the improved statistical uncertainties on both the experimental data and hydrodynamic calculations do not help to reduce the final credibility ranges. It is also noticeable that v_5 is still underestimated as observed in [7]. It is worthwhile to mention that the differences for v_2 , v_3 and NSC(4, 2) still remain about 5–10% for 5.02 TeV. The sign change of NSC(4, 3) in most central collisions is not reproduced by the models while the beam-energy-dependent magnitudes are better described with new parametrizations. We leave those differences for future research work in which the present results should be refined by including the lower energy beam data. The parameter sensitivity analysis for the observables conducted in this study

indicates that observables such as the symmetric cumulants and nonlinear flow modes provide a strong constraining power which, however, is still underutilized in [7] as well as the other Bayesian analyses [10,11,13]. In our study, we confirm that the flow coefficients alongside the symmetric cumulants and nonlinear flow mode can provide some of the strongest constraints for the temperature dependence of $\eta/s(T)$ and T_{switch} . Improving aspects of the collision model, for example by replacing the initial state model with others like EKRT [33,34], IP-Glasma [42], and AMPT [43,44], with incorporation of nucleon substructure [45] in the initial conditions through an improved dynamical collision model before the hydrodynamic takes place [46,47], might help to improve the understanding of the uncertainties of the extracted QGP properties and/or the model building blocks.

ACKNOWLEDGMENTS

We would like to thank Harri Niemi, Kari J. Eskola and Sami Räsänen for fruitful discussions. We thank Jonah E. Bernhard, J. Scott Moreland, and Steffen A. Bass for the use of their viscous relativistic hydrodynamics softwares and their valuable comments on various processes of this work. We acknowledge Victor Gonzalez for his crosscheck for various technical parts of the event generation. We acknowledge CSC-IT Center for Science in Espoo, Finland, for the allocation of the computational resources. This research was completed using ≈ 24 million CPU hours provided by CSC.

-
- [1] P. K. Kovtun, D. T. Son, and A. O. Starinets, Viscosity in Strongly Interacting Quantum Field Theories from Black Hole Physics, *Phys. Rev. Lett.* **94**, 111601 (2005).
 - [2] K. Aamodt *et al.* (ALICE Collaboration), Higher Harmonic Anisotropic Flow Measurements of Charged Particles in Pb-Pb collisions at $\sqrt{s_{NN}} = 2.76$ TeV, *Phys. Rev. Lett.* **107**, 032301 (2011).
 - [3] J. Adam *et al.* (ALICE Collaboration), Correlated Event-by-Event Fluctuations of Flow Harmonics in Pb-Pb Collisions at $\sqrt{s_{NN}} = 2.76$ TeV, *Phys. Rev. Lett.* **117**, 182301 (2016).
 - [4] S. Acharya *et al.* (ALICE Collaboration), Systematic studies of correlations between different order flow harmonics in Pb-Pb collisions at $\sqrt{s_{NN}} = 2.76$ TeV, *Phys. Rev. C* **97**, 024906 (2018).
 - [5] S. Acharya *et al.* (ALICE Collaboration), Higher harmonic non-linear flow modes of charged hadrons in Pb-Pb collisions at $\sqrt{s_{NN}} = 5.02$ TeV, *J. High Energy Phys.* **05** (2020) 085.
 - [6] S. Acharya *et al.* (ALICE Collaboration), Measurements of mixed harmonic cumulants in Pb-Pb collisions at $\sqrt{s_{NN}} = 5.02$ TeV, *Phys. Lett. B* **818**, 136354 (2021).
 - [7] J. E. Bernhard, J. S. Moreland, and S. A. Bass, Bayesian estimation of the specific shear and bulk viscosity of quark-gluon plasma, *Nat. Phys.* **15**, 1113 (2019).
 - [8] K. Aamodt *et al.* (ALICE Collaboration), Centrality Dependence of the Charged-Particle Multiplicity Density at Midrapidity in Pb-Pb Collisions at $\sqrt{s_{NN}} = 2.76$ TeV, *Phys. Rev. Lett.* **106**, 032301 (2011).
 - [9] B. Abelev *et al.* (ALICE Collaboration), Centrality dependence of π , K , p production in Pb-Pb collisions at $\sqrt{s_{NN}} = 2.76$ TeV, *Phys. Rev. C* **88**, 044910 (2013).
 - [10] J. Auvinen, K. J. Eskola, P. Huovinen, H. Niemi, R. Paatelainen, and P. Petreczky, Temperature dependence of η/s of strongly interacting matter: Effects of the equation of state and the parametric form of $(\eta/s)(T)$, *Phys. Rev. C* **102**, 044911 (2020).
 - [11] G. Nijs, W. van der Schee, U. Gürsoy, and R. Snellings, Transverse Momentum Differential Global Analysis of Heavy-Ion Collisions, *Phys. Rev. Lett.* **126**, 202301 (2021).
 - [12] G. Nijs, W. van der Schee, U. Gürsoy, and R. Snellings, Bayesian analysis of heavy ion collisions with the heavy ion computational framework TRAJETUM, *Phys. Rev. C* **103**, 054909 (2021).
 - [13] D. Everett *et al.* (JETSCAPE Collaboration), Multisystem Bayesian constraints on the transport coefficients of QCD matter, *Phys. Rev. C* **103**, 054904 (2021).
 - [14] S. Ryu, J.-F. Paquet, C. Shen, G. Denicol, B. Schenke, S. Jeon, and C. Gale, Effects of bulk viscosity and hadronic rescattering in heavy ion collisions at energies available at the BNL Relativistic Heavy Ion Collider and at the CERN Large Hadron Collider, *Phys. Rev. C* **97**, 034910 (2018).
 - [15] G. S. Denicol, T. Kodama, T. Koide, and P. Mota, Effect of bulk viscosity on elliptic flow near QCD phase transition, *Phys. Rev. C* **80**, 064901 (2009).
 - [16] S. Acharya *et al.* (ALICE Collaboration), Investigations of Anisotropic Flow Using Multiparticle Azimuthal Correlations in pp , p -Pb, Xe-Xe, and Pb-Pb Collisions at the LHC, *Phys. Rev. Lett.* **123**, 142301 (2019).

- [17] S. Acharya *et al.* (ALICE Collaboration), Linear and non-linear flow modes in Pb-Pb collisions at $\sqrt{s_{NN}} = 2.76$ TeV, *Phys. Lett. B* **773**, 68 (2017).
- [18] J. Adam *et al.* (ALICE Collaboration), Centrality dependence of the pseudorapidity density distribution for charged particles in Pb-Pb collisions at $\sqrt{s_{NN}} = 5.02$ TeV, *Phys. Lett. B* **772**, 567 (2017).
- [19] S. Acharya *et al.* (ALICE Collaboration), Production of charged pions, kaons, and (anti-)protons in Pb-Pb and inelastic *pp* collisions at $\sqrt{s_{NN}} = 5.02$ TeV, *Phys. Rev. C* **101**, 044907 (2020).
- [20] H. Petersen, C. Coleman-Smith, S. A. Bass, and R. Wolpert, Constraining the initial state granularity with bulk observables in Au+Au collisions at $\sqrt{s_{NN}} = 200$ GeV, *J. Phys. G* **38**, 045102 (2011).
- [21] J. Novak, K. Novak, S. Pratt, J. Vredevoogd, C. E. Coleman-Smith, and R. L. Wolpert, Determining fundamental properties of matter created in ultrarelativistic heavy-ion collisions, *Phys. Rev. C* **89**, 034917 (2014).
- [22] S. Pratt, E. Sangaline, P. Sorensen, and H. Wang, Constraining the Equation of State of Superhadronic Matter from Heavy-Ion Collisions, *Phys. Rev. Lett.* **114**, 202301 (2015).
- [23] E. Sangaline and S. Pratt, Toward a deeper understanding of how experiments constrain the underlying physics of heavy-ion collisions, *Phys. Rev. C* **93**, 024908 (2016).
- [24] U. Heinz and J. Liu, Pre-equilibrium dynamics and heavy-ion observables, *Nucl. Phys. A* **956**, 549 (2016).
- [25] J. S. Moreland, J. E. Bernhard, and S. A. Bass, Alternative ansatz to wounded nucleon and binary collision scaling in high-energy nuclear collisions, *Phys. Rev. C* **92**, 011901(R) (2015).
- [26] C. Shen, Z. Qiu, H. Song, J. Bernhard, S. Bass, and U. Heinz, The iEBE-VISHNU code package for relativistic heavy-ion collisions, *Comput. Phys. Commun.* **199**, 61 (2016).
- [27] H. Song and U. W. Heinz, Causal viscous hydrodynamics in 2+1 dimensions for relativistic heavy-ion collisions, *Phys. Rev. C* **77**, 064901 (2008).
- [28] S. A. Bass *et al.*, Microscopic models for ultrarelativistic heavy ion collisions, *Prog. Part. Nucl. Phys.* **41**, 255 (1998).
- [29] M. Bleicher *et al.*, Relativistic hadron hadron collisions in the ultrarelativistic quantum molecular dynamics model, *J. Phys. G* **25**, 1859 (1999).
- [30] B. Tang, Orthogonal array-based latin hypercubes, *J. Am. Stat. Assoc.* **88**, 1392 (1993).
- [31] M. D. Morris and T. J. Mitchell, Exploratory designs for computational experiments, *J. Stat. Plann. Inference* **43**, 381 (1995).
- [32] J. E. Bernhard, Bayesian parameter estimation for relativistic heavy-ion collisions, [arXiv:1804.06469](https://arxiv.org/abs/1804.06469).
- [33] H. Niemi, K. J. Eskola, and R. Paatelainen, Event-by-event fluctuations in a perturbative QCD+saturation+hydrodynamics model: Determining QCD matter shear viscosity in ultrarelativistic heavy-ion collisions, *Phys. Rev. C* **93**, 024907 (2016).
- [34] H. Niemi, K. J. Eskola, R. Paatelainen, and K. Tuominen, Predictions for 5.023 TeV Pb+Pb collisions at the CERN Large Hadron Collider, *Phys. Rev. C* **93**, 014912 (2016).
- [35] A. Nakamura and S. Sakai, Transport Coefficients of Gluon Plasma, *Phys. Rev. Lett.* **94**, 072305 (2005).
- [36] S. McDonald, C. Shen, F. Fillion-Gourdeau, S. Jeon, and C. Gale, Hydrodynamic predictions for Pb+Pb collisions at 5.02 TeV, *Phys. Rev. C* **95**, 064913 (2017).
- [37] W. Zhao, H.-J. Xu, and H. Song, Collective flow in 2.76 and 5.02 A TeV Pb+Pb collisions, *Eur. Phys. J. C* **77**, 645 (2017).
- [38] M. Luzum and J.-Y. Ollitrault, Constraining the viscous freeze-out distribution function with data obtained at the BNL Relativistic Heavy Ion Collider (RHIC), *Phys. Rev. C* **82**, 014906 (2010).
- [39] M. Luzum, C. Gombeaud, and J.-Y. Ollitrault, v_4 in ideal and viscous hydrodynamics simulations of nuclear collisions at the BNL Relativistic Heavy Ion Collider (RHIC) and the CERN Large Hadron Collider (LHC), *Phys. Rev. C* **81**, 054910 (2010).
- [40] D. Teaney and L. Yan, Nonlinearities in the harmonic spectrum of heavy ion collisions with ideal and viscous hydrodynamics, *Phys. Rev. C* **86**, 044908 (2012).
- [41] L. Yan and J.-Y. Ollitrault, v_4, v_5, v_6, v_7 : nonlinear hydrodynamic response versus LHC data, *Phys. Lett. B* **744**, 82 (2015).
- [42] B. Schenke, P. Tribedy, and R. Venugopalan, Fluctuating Glasma Initial Conditions and Flow in Heavy Ion Collisions, *Phys. Rev. Lett.* **108**, 252301 (2012).
- [43] R. S. Bhalerao, A. Jaiswal, and S. Pal, Collective flow in event-by-event partonic transport plus hydrodynamics hybrid approach, *Phys. Rev. C* **92**, 014903 (2015).
- [44] L. Pang, Q. Wang, and X.-N. Wang, Effects of initial flow velocity fluctuation in event-by-event (3+1)D hydrodynamics, *Phys. Rev. C* **86**, 024911 (2012).
- [45] H. Mäntysaari, B. Schenke, C. Shen, and P. Tribedy, Imprints of fluctuating proton shapes on flow in proton-lead collisions at the LHC, *Phys. Lett. B* **772**, 681 (2017).
- [46] W. van der Schee, P. Romatschke, and S. Pratt, Fully Dynamical Simulation of Central Nuclear Collisions, *Phys. Rev. Lett.* **111**, 222302 (2013).
- [47] P. Romatschke and U. Romatschke, *Relativistic Fluid Dynamics In and Out of Equilibrium*, Cambridge Monographs on Mathematical Physics (Cambridge University Press, Cambridge, 2019).



III

LONG- AND SHORT-RANGE CORRELATIONS AND THEIR EVENT-SCALE DEPENDENCE IN HIGH- MULTIPLICITY PP COLLISIONS AT $\sqrt{s} = 13$ TeV,

by

ALICE Collaboration, S. Acharya et al. 2020

JHEP 05 (2021) 290

<https://arxiv.org/abs/2101.03110>

[https://doi.org/10.1007/JHEP05\(2021\)290](https://doi.org/10.1007/JHEP05(2021)290)

Reproduced with kind permission by Springer.

Long- and short-range correlations and their event-scale dependence in high-multiplicity pp collisions at $\sqrt{s} = 13$ TeV



ALICE

The ALICE collaboration

E-mail: ALICE-publications@cern.ch

ABSTRACT: Two-particle angular correlations are measured in high-multiplicity proton-proton collisions at $\sqrt{s} = 13$ TeV by the ALICE Collaboration. The yields of particle pairs at short- ($\Delta\eta \sim 0$) and long-range ($1.6 < |\Delta\eta| < 1.8$) in pseudorapidity are extracted on the near-side ($\Delta\varphi \sim 0$). They are reported as a function of transverse momentum (p_T) in the range $1 < p_T < 4$ GeV/c. Furthermore, the event-scale dependence is studied for the first time by requiring the presence of high- p_T leading particles or jets for varying p_T thresholds. The results demonstrate that the long-range “ridge” yield, possibly related to the collective behavior of the system, is present in events with high- p_T processes as well. The magnitudes of the short- and long-range yields are found to grow with the event scale. The results are compared to EPOS LHC and PYTHIA 8 calculations, with and without string-shoving interactions. It is found that while both models describe the qualitative trends in the data, calculations from EPOS LHC show a better quantitative agreement for the p_T dependency, while overestimating the event-scale dependency.

KEYWORDS: Heavy Ion Experiments

ARXIV EPRINT: [2101.03110](https://arxiv.org/abs/2101.03110)

Contents

1	Introduction	1
2	Experimental setup	3
3	Analysis procedure	4
4	Systematic uncertainties of the measured yields	5
5	Results	7
5.1	Ridge yield	7
5.2	Event-scale dependence of the ridge yield	10
6	Conclusions	11
	The ALICE collaboration	20

1 Introduction

In high-energy nucleus-nucleus collisions at RHIC [1–4] and LHC [5–7], significant correlations are observed between particles emitted over a wide pseudorapidity range. The origin of these observations are collective effects, which are related to the formation of a strongly interacting quark-gluon plasma (QGP), which exhibits hydrodynamic behavior (see the reviews [8–10]). Recent theoretical [11–13] and experimental [14–17] advancements have contributed significantly to the understanding of the transport properties of the QGP. Similar long-range correlations are also observed in high-multiplicity proton-proton (pp) [18–21], proton-nucleus (pA) [22–25], and light nucleus-nucleus collisions [26, 27]. The fact that these correlations extend over a large range in pseudorapidity implies that they originate from early times in these collisions and thus suggest that hydrodynamic behavior is present even in these small systems, although the volume and lifetime of the medium produced in such a collision system are expected to be small, and there are other mechanisms which can produce similar flow-like signals [28, 29].

Measurements of two-particle angular correlations provide information on many physical effects, including collectivity, hadronization, fragmentation, and femtoscopic effects [30], and are typically quantified as a function of $\Delta\eta$, the relative pseudorapidity, and $\Delta\varphi$, the separation in azimuthal angle, of particle pairs. The long-range structure of two-particle angular correlations is well suited to analyze collective effects, since it is not created by resonance decays nor fragmentation of high-momentum partons. A typical source of long-range correlations in Monte Carlo pp generators is the momentum conservation. The enhancement in the yield of two-particle correlations at small $\Delta\varphi$ that extends over a large $\Delta\eta$ is

dubbed “ridge” due to its characteristic shape in the $\Delta\eta$ - $\Delta\varphi$ plane. The shape of these $\Delta\varphi$ correlations can be studied via a Fourier decomposition [31, 32]. The second and third order terms are the dominant harmonic coefficients. In heavy-ion collisions, harmonic coefficients can be related to the collision geometry and density fluctuations of the colliding nuclei [33–35] and to transport properties of the QGP in relativistic viscous hydrodynamic models [11–13, 36, 37].

The ridge structures in high-multiplicity pp and p-Pb events have been attributed to initial-state or final-state effects. Initial-state effects, usually attributed to gluon saturation [38, 39], can form long-range correlations along the longitudinal direction. The final-state effects might be parton-induced interactions [40] or collective phenomena due to hydrodynamic behavior of the produced matter arising in a high-density system possibly formed in these collisions [41, 42]. Hybrid models implementing both effects are generally used in hydrodynamic simulations [43, 44]. EPOS LHC describes collectivity in small systems with a parameterized hydrodynamic evolution of the high-energy density region, so called “core”, formed by many color string fields [45]. The proton shape and its fluctuations are also important to model small systems [44]. To understand the influence of initial- or final-state effects, and to possibly disentangle the two, a quantitative description of the measurements in small systems [46, 47] needs to account for details of the initial state. Systematic studies of these correlation effects from small to large systems are being performed, both experimentally [21] and theoretically [47]. However, the quantitative description of the full set of experimental data has not been achieved yet. A summary of various explanations for the observed correlations in small systems is given in [29, 48, 49].

Besides the hybrid models mentioned above, alternative approaches were developed to describe collectivity in small systems. A microscopic model for collectivity was implemented in the PYTHIA 8 event generator, which is based on interacting strings (string shoving) and is called the “string shoving model” [50]. In this model, strings repel each other in the transverse direction, which results in microscopic transverse pressure and, consequently, in long-range correlations. PYTHIA 8 with string shoving can qualitatively reproduce the near-side ($\Delta\varphi \sim 0$) ridge yield measured by the CMS Collaboration [20]. This challenges the hydrodynamic picture and predicts modifications of the jet fragmentation properties [51].

It is expected that final-state interactions affect also produced jets if they are the source of collectivity in small systems. Proving the presence of jet quenching [52, 53] would be another crucial evidence of the existence of a high-density strongly-interacting system, possibly a QGP, in high-multiplicity pp collisions. However, there is no evidence observed so far for the jet quenching effect in high-multiplicity pp and p-Pb collisions [54–57]. Jet fragmentation can be studied in two-particle angular correlations in short-range correlations around $(\Delta\eta, \Delta\varphi) = (0, 0)$ [58].

To further investigate the interplay of jet production and collective effects in small systems, long- and short-range correlations are studied simultaneously in high-multiplicity pp collisions at $\sqrt{s} = 13$ TeV using the ALICE LHC Run 2 data collected with the high-multiplicity event trigger in 2016–2018. In this article, the near-side per-trigger yield at large pseudorapidity separation is presented as a function of transverse momentum.

The results are compared with previous measurements by the CMS Collaboration [19]. In addition, the ridge yield and near-side jet-like correlations with the event-scale selection are reported. The event-scale selection is done by requiring a minimum transverse momentum of the leading particle or the reconstructed jet at midrapidity, which is expected to bias the impact parameter of pp collisions to be smaller on average [59, 60]. At the same time, the transverse momentum of the leading particle or the reconstructed jet is a measure of the momentum transfer in the hard parton scattering [61, 62]. The event-scale dependence of the second-flow harmonic v_2 has previously been studied in pp collisions with and without a tagged Z boson, where little or no dependence was observed [63].

The experimental setup and analysis method are described in section 2 and 3, respectively. The sources of systematic uncertainties are discussed in section 4. The results and comparisons with model calculations of the measurements are presented in section 5. Finally, results are summarized in section 6.

2 Experimental setup

The analysis is carried out with data samples of pp collisions at $\sqrt{s} = 13$ TeV collected from 2016 to 2018 during the LHC Run 2 period. The full description of the ALICE detector and its performance in the LHC Run 2 can be found in [64, 65]. The present analysis utilizes the V0 [66], the Inner Tracking System (ITS) [67], and the Time Projection Chamber (TPC) [68] detectors.

The V0 detector consists of two stations placed on both sides of the interaction point, V0A and V0C, each made of 32 plastic scintillator tiles, covering the full azimuthal angle within the pseudorapidity intervals $2.8 < \eta < 5.1$ and $-3.7 < \eta < -1.7$, respectively. The V0 is used to provide a minimum bias (MB) and a high-multiplicity (HM) trigger. The minimum bias trigger is obtained by a time coincidence of V0A and V0C signals. The charged particle multiplicity selection is done on the sum of the V0A and V0C signals, which is denoted as V0M. The high-multiplicity trigger requires that the V0M signal exceeds 5 times the mean value measured in minimum bias collisions, selecting the 0.1% of MB events that have the largest V0 multiplicity. The analyzed data samples of minimum bias and high-multiplicity pp events at $\sqrt{s} = 13$ TeV correspond to integrated luminosities of 19 nb^{-1} and 11 pb^{-1} , respectively [69].

The primary vertex position is reconstructed from the measured signals in the Silicon Pixel Detector (SPD), which forms the innermost two layers of the ITS. Reconstructed primary vertices of selected events are required to be located within 8 cm from the center of the detector along the beam direction. The probability of pileup events is about 0.6% in MB events. Pileup events can be resolved and are rejected if the longitudinal displacement of their primary vertices is larger than 0.8 cm.

Charged-particle tracks are reconstructed by the ITS and TPC, which are operated in a uniform solenoidal magnetic field of 0.5 T along the beam direction. The ITS is a silicon tracker with six layers of silicon sensors where the SPD [70] comprises the two innermost layers, the next two layers called the Silicon Drift Detector (SDD), and the outermost layers named the Silicon Strip Detector (SSD). The ITS and TPC, covering the

full azimuthal range, have acceptances up to $|\eta| < 1.4$ and 0.9 , respectively, for detection of charged particles emitted within 8 cm from the primary vertex position (z_{vtx}) along the beam direction. The tracking of charged particles is done with the combined information of the ITS and TPC that enables the reconstruction of tracks down to $0.15 \text{ GeV}/c$, where the efficiency is about 65%. The efficiency reaches 80% for intermediate p_{T} , 1 to 5 GeV/c . The p_{T} resolution is around 1% for primary tracks with $p_{\text{T}} < 1 \text{ GeV}/c$, and linearly increases up to 6% at $p_{\text{T}} \sim 40 \text{ GeV}/c$ [71].

The charged particle selection criteria are optimized to make the efficiency uniform over the full TPC volume to mitigate the effect of small regions where some of the ITS layers are inactive. The selection consists of two track classes. Those belonging to the first class are required to have at least one hit in the SPD. Tracks from the second class do not have any SPD associated hit and their initial point is instead constrained to the primary vertex [72].

3 Analysis procedure

The two-particle correlation function is measured as a function of the relative pseudorapidity ($\Delta\eta$) and the azimuthal angle difference ($\Delta\varphi$) between the trigger and the associated particles,

$$\frac{1}{N_{\text{trig}}} \frac{d^2 N_{\text{pair}}}{d\Delta\eta d\Delta\varphi} = B(0, 0) \frac{S(\Delta\eta, \Delta\varphi)}{B(\Delta\eta, \Delta\varphi)} \Big|_{p_{\text{T, trig}}, p_{\text{T, assoc}}}, \quad (3.1)$$

where $p_{\text{T, trig}}$ and $p_{\text{T, assoc}}$ ($p_{\text{T, trig}} > p_{\text{T, assoc}}$) are the transverse momenta of the trigger and associated particles, respectively, N_{trig} is the number of trigger particles, and N_{pair} is the number of trigger-associated particle pairs. The average number of pairs in the same event and in mixed events are denoted as $S(\Delta\eta, \Delta\varphi)$ and $B(\Delta\eta, \Delta\varphi)$, respectively. Normalization of $B(\Delta\eta, \Delta\varphi)$ is done with its value at $\Delta\eta$ and $\Delta\varphi = 0$, represented as $B(0, 0)$. Acceptance effects are corrected by dividing $S(\Delta\eta, \Delta\varphi)$ with $B(\Delta\eta, \Delta\varphi)/B(0, 0)$. The right-hand side of eq. (1) is corrected for the track reconstruction efficiency, which is mainly relevant for the associated particles, as a function of p_{T} and pseudorapidity. Primary vertices of events to be mixed are required to be within the same, 2 cm wide, z_{vtx} interval [58, 73] for each multiplicity class. The final per-trigger yield is constructed by averaging correlation functions over these primary vertex bins.

Ridge yields at large $\Delta\eta$ are extracted for various multiplicity classes and p_{T} intervals. The large $\Delta\eta$ range is selected as $1.6 < |\Delta\eta| < 1.8$, which is the range where the tracking quality — efficiency and precision — is the best. The ridge yield is only reported for $p_{\text{T}} > 1 \text{ GeV}/c$. Below $1 \text{ GeV}/c$, the jet-like contribution to the correlation function extends into the region where the ridge yield is measured, $1.6 < |\Delta\eta| < 1.8$. In this region, the $\Delta\varphi$ distribution, or the so-called per-trigger yield, is expressed as

$$\frac{1}{N_{\text{trig}}} \frac{dN_{\text{pair}}}{d\Delta\varphi} = \int_{1.6 < |\Delta\eta| < 1.8} \left(\frac{1}{N_{\text{trig}}} \frac{d^2 N_{\text{pair}}}{d\Delta\eta d\Delta\varphi} \right) \frac{1}{\delta_{\Delta\eta}} d\Delta\eta - C_{\text{ZYAM}}, \quad (3.2)$$

where $\delta_{\Delta\eta} = 0.4$ is the normalization factor to get the per-trigger yield per unit of pseudorapidity.

The baseline of the correlation is subtracted by means of the Zero-Yield-At-Minimum (ZYAM) procedure [74]. The minimum yield (C_{ZYAM}) at $\Delta\varphi = \Delta\varphi_{\min}$ in the $\Delta\varphi$ projection (note that the value of $\Delta\varphi_{\min}$ can be different in data and in models) is obtained from a fit function, which fits the data with a Fourier series up to the third harmonic. By construction, the yield at $\Delta\varphi_{\min}$ is zero after subtracting C_{ZYAM} from the $\Delta\varphi$ projection. The ridge yield (Y^{ridge}) is obtained by integrating the near-side peak of the $\Delta\varphi$ projection over $|\Delta\varphi| < |\Delta\varphi_{\min}|$ after the ZYAM procedure,

$$Y^{\text{ridge}} = \int_{|\Delta\varphi| < |\Delta\varphi_{\min}|} \frac{1}{N_{\text{trig}}} \frac{dN_{\text{pair}}}{d\Delta\varphi} d\Delta\varphi. \quad (3.3)$$

The ridge yield is further studied in events having a hard jet or a high- p_T leading particle in the midrapidity region. This event scale is set by requiring a minimum p_T of the leading track ($p_{T,LP}$) or the reconstructed jet ($p_{T,jet}^{\text{ch}}$) at midrapidity. The leading track is selected within $|\eta| < 0.9$ and the full azimuthal angle. Jets are reconstructed with charged particles only (track-based jets) with the anti- k_T algorithm [75, 76] and the resolution parameter $R = 0.4$. The recombination scheme used in this article is the p_T scheme. Jets are selected in $|\eta_{jet}| < 0.4$ and in the full azimuthal angle. The p_T of jets $p_{T,jet}^{\text{ch}}$ is corrected for the underlying event density that is measured using the k_T algorithm with $R = 0.2$ [77].

To quantify the variation of the near-side jet-like peak with event-scale selections with a minimum $p_{T,LP}$ or $p_{T,jet}^{\text{ch}}$, the near-side jet-like peak yield is extracted from the near-side $\Delta\eta$ correlations. The near-side is defined as $|\Delta\varphi| < 1.28$, where the correlation function is projected on the $\Delta\eta$ axis. The projection range, 1.28, is chosen to fully cover $\Delta\varphi_{\min}$. The near-side $\Delta\eta$ correlations are then constructed as

$$\frac{1}{N_{\text{trig}}} \frac{dN_{\text{pair}}}{d\Delta\eta} = \int_{|\Delta\varphi| < 1.28} \left(\frac{1}{N_{\text{trig}}} \frac{d^2 N_{\text{pair}}}{d\Delta\eta d\Delta\varphi} \right) \frac{1}{\delta_{\Delta\varphi}} d\Delta\varphi - D_{ZYAM}, \quad (3.4)$$

where $\delta_{\Delta\varphi} = 2.56$ is the normalization factor to get per-trigger yield per unit of azimuthal angle. The minimum yield (D_{ZYAM}) of the $\Delta\eta$ correlations is found within $|\Delta\eta| < 1.6$ and used for the subtraction from the $\Delta\eta$ correlations, which results in zero-yield at the minimum. The near-side jet-like peak yield (Y^{near}) is measured by integrating the $\Delta\eta$ correlations over $|\Delta\eta| < 1.6$,

$$Y^{\text{near}} = \int_{|\Delta\eta| < 1.6} \left(\frac{1}{N_{\text{trig}}} \frac{dN_{\text{pair}}}{d\Delta\eta} \right) d\Delta\eta \quad (3.5)$$

4 Systematic uncertainties of the measured yields

The systematic uncertainties of Y^{ridge} and Y^{near} are estimated by varying the analysis selection criteria and corrections and are summarized in table 1.

The systematic uncertainties are independent of the event-scale selection except for D_{ZYAM} (see below), as expected, since the multiplicity is weakly dependent on the event scale and the ALICE detector is optimized for much higher multiplicities (Pb-Pb collisions), this is in agreement with our expectations.

Sources	Systematic uncertainty (%)	
	Y^{ridge}	Y^{near}
Pileup rejection	$\pm 0.8\text{--}3.9$	$\pm 0.2\text{--}2.2$
Primary vertex	$\pm 0.5\text{--}2.4$	± 1.1
Tracking	$\pm 2.0\text{--}4.0$	$\pm 1.5\text{--}3.4$
ZYAM	$\pm 2.1\text{--}5.1$	$\pm 2.2\text{--}4.8$
Event mixing	$\pm 1.0\text{--}4.4$	$\pm 0.5\text{--}1.7$
Efficiency correction	± 2.5	± 3.1
Jet contamination	$-18.8\text{--}25.9$ ($p_T < 2 \text{ GeV}/c$)	N.A.
Total (in quadrature)	$^{+4.9\text{--}9.4}_{-19.4\text{--}21.0}$	$\pm 3.9\text{--}7.3$

Table 1. The relative systematic uncertainty of Y^{ridge} and Y^{near} . Numbers given in ranges correspond to minimum and maximum uncertainties.

The uncertainty associated to the pileup rejection is estimated by measuring the changes of results with different rejection criteria from the default one. It is mainly estimated by varying the minimal number of track contributors required for reconstruction of pileup event vertices from 3 to 5. The estimated uncertainty of Y^{ridge} is 0.8–3.9%. The corresponding uncertainty of Y^{near} is estimated to be 0.2–2.2%.

Another source of systematic uncertainty is related to the selected range of the primary vertex. The accepted range is changed from $|z_{\text{vtx}}| < 8 \text{ cm}$ to $|z_{\text{vtx}}| < 6 \text{ cm}$. The narrower primary vertex selection allows one to test acceptance effects on the measurement. The estimated uncertainty of Y^{ridge} is 0.5–2.4%. The uncertainty for Y^{near} is estimated to be 1.1%.

An additional source of systematic uncertainty is related to the track selection criteria. The corresponding uncertainty is estimated by employing other track selection criteria, denoted global tracks, which are optimized for particle identification. The selection criteria of the global tracks are almost identical to the hybrid tracks. Each global track is required to have at least one SPD hit. Due to inefficient parts of the SPD, the azimuthal distribution of global tracks is not uniform. The uncertainties associated with the track selection are estimated to be 2.0–4.0% and 1.5–3.4% for Y^{ridge} and Y^{near} , respectively.

The systematic uncertainty of Y^{ridge} resulting from the ZYAM procedure is estimated by varying the range of the fit, which is used to find the minimum, from $|\Delta\varphi| < \pi/2$ down to $|\Delta\varphi| < 1.2$. The estimated uncertainty of Y^{ridge} is 2.1–5.1%. The corresponding uncertainty on Y^{near} is estimated by varying the range from $|\Delta\eta| < 1.6$ to $|\Delta\eta| < 1.5$ and 1.7. The estimated uncertainty of Y^{near} is 2.2% for the unbiased case and increases to 4.8% for the largest event-scale selections. This is the only systematic uncertainty for which a significant dependence on the event scale is observed, reflecting a non-negligible dependence of the near-side magnitude and shape on the event-scale selection.

The source of systematic uncertainty is associated to the choice of the width of z_{vtx} bins that are used in the event mixing method. The default value of 2 cm is changed to 1 cm. The resulting uncertainty of Y^{ridge} is 1.0–4.4%. The uncertainty for Y^{near} is about 0.5–

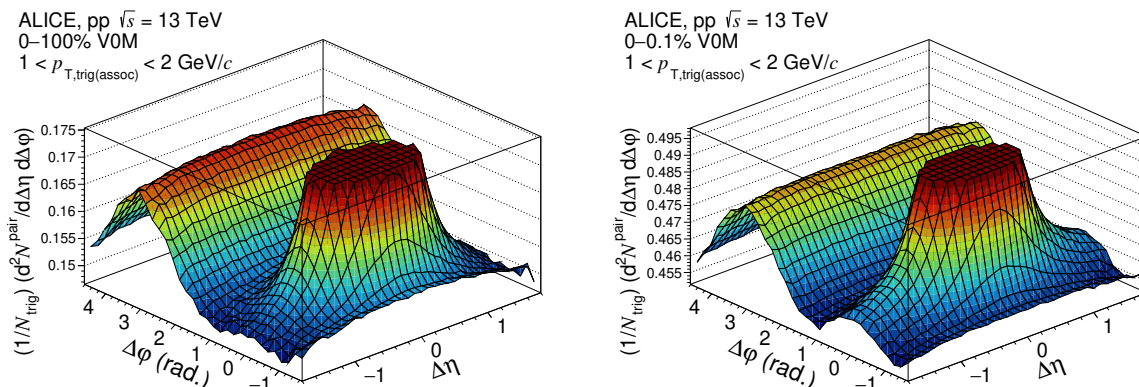


Figure 1. Two-particle correlation functions as functions of $\Delta\eta$ and $\Delta\varphi$ in minimum-bias events (0–100%, left) and high-multiplicity (0–0.1%, right). Note that the near-side jet peaks exceed the chosen range of the z -axis. The intervals of $p_{T, \text{trig}}$ and $p_{T, \text{assoc}}$ are $1 < p_T < 2 \text{ GeV}/c$ in both cases.

1.7%. The uncertainty from the efficiency correction for charged particles is estimated by comparing correlation functions of true particles with correlation functions of reconstructed tracks with the efficiency correction in simulation. The estimated uncertainties are 2.5% and 3.1% for Y^{ridge} and Y^{near} , respectively.

In the limited η -acceptance of ALICE, the ridge structure is not flat in $\Delta\eta$ suggesting that jet-like correlations (non-flow) could contribute, implying that they would impact the ridge-yield extraction. We stress that the models used for comparisons also contain such a non-flow effect, but differences in jet-like correlations between data and MC models could influence the interpretation. To account for the related uncertainty, the variation of the yield with $\Delta\eta$ between 1.5 and 1.8, which should be an upper limit of the residual jet-like contamination, is used as a systematic uncertainty of the ridge yield. The estimated upper limit of the uncertainty is -25.9% for the $1.0 < p_T < 1.5 \text{ GeV}/c$ range, -18.8% for the $1.5 < p_T < 2.0 \text{ GeV}/c$ range, -18.9% for the $1.0 < p_T < 2.0 \text{ GeV}/c$ range, and negligible for $p_T > 2.0 \text{ GeV}/c$. This uncertainty is considered only for the measured ridge yields.

5 Results

5.1 Ridge yield

Figure 1 shows the per-trigger yield obtained from eq. (1) for $1 < p_{T, \text{trig}} (p_{T, \text{assoc}}) < 2 \text{ GeV}/c$ in pp collisions at $\sqrt{s}=13 \text{ TeV}$ for minimum bias events (left) and high-multiplicity events (right). It is worth noting that the z -axes for the yield of the correlations is properly scaled in order to zoom in the ridge yield, as a result, the jet peaks are sheared off in both figures. The ridge structure is clearly observed in the high-multiplicity class while it is less significant in the minimum bias events. The away-side yield is populated mostly by back-to-back jet correlations.

Figure 2 shows $\Delta\varphi$ projections of the two-particle correlation functions obtained in the range $1.6 < |\Delta\eta| < 1.8$ for several track p_T intervals after the ZYAM subtraction (see eq. (2)). The results are shown for various p_T intervals in the minimum bias class (upper)

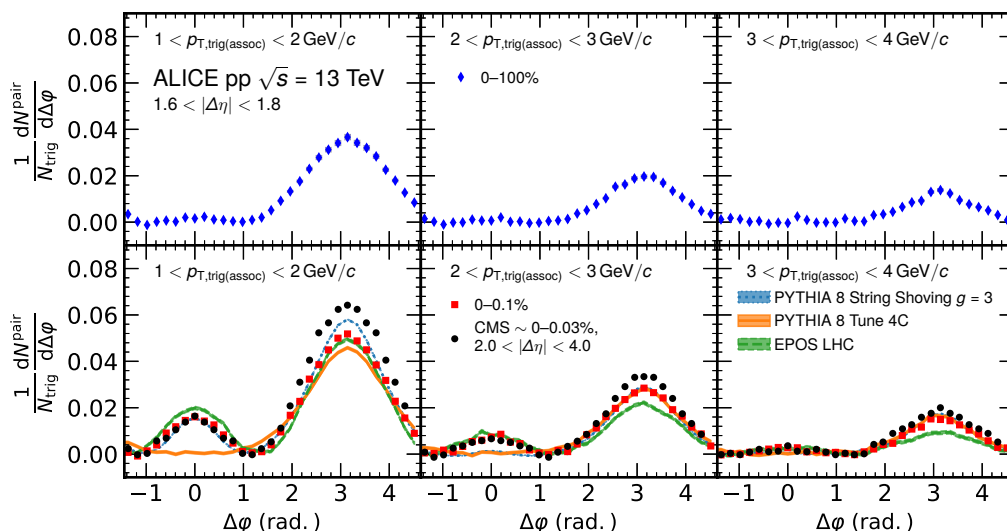


Figure 2. One-dimensional $\Delta\phi$ distribution in the large $\Delta\eta$ projection for three transverse momentum intervals in minimum bias (upper panels) and high-multiplicity (lower panels) events after ZYAM subtraction. Transverse momentum intervals of the trigger particles and associated particles are $1 < p_T < 2$ (left), $2 < p_T < 3$ (middle) and, $3 < p_T < 4$ GeV/c (right), respectively. The presented model predictions were calculated using PYTHIA 8 String Shoving, PYTHIA 8 Tune 4C, and EPOS LHC.

and the high-multiplicity class (lower) down to 1 GeV/c where the non-flow contamination is negligible. The near-side ($\Delta\phi \sim 0$) ridge in the high-multiplicity class is clearly observed for $p_T < 3$ GeV/c while there is no definitive signal in the minimum bias class. Within the range of analyzed particle p_T , the yield in the near-side ridge decreases with increasing p_T in the high-multiplicity class.

The measurements in the high-multiplicity class are compared with the results published by the CMS Collaboration [19]. In case of the CMS measurement, the charged particle multiplicity was obtained by counting the number of particles satisfying $p_T > 0.4$ GeV/c in $|\eta| < 2.4$. In our analysis, event multiplicity is determined from the forward V0 detectors. The difference in multiplicity selection between ALICE (forward) and CMS (midrapidity) is studied using PYTHIA 8 simulations and it is found that the calculated multiplicity using the CMS procedure is about 20% larger than the one from ALICE when compared in the acceptance region of the measurements reported in this article, $|\eta| < 0.9$. Near-side ridges in all transverse momentum ranges are comparable. The larger away-side yields observed in figure 2 for the CMS results can be attributed to the overlap in η acceptance between the multiplicity selection and the correlation function measurement.

In figure 2, the ALICE measurements are also compared with model predictions where a comparable high-multiplicity selection and $\Delta\eta$ projection range are applied. The selection of high-multiplicity events in the models is done by requiring a minimal number of charged particles emitted within the V0M detector acceptance. In case of PYTHIA 8 Tune 4C, the 0–0.1% centrality threshold is 105 charged particles. The threshold for EPOS LHC and PYTHIA 8 String Shoving are 110 and 108, respectively. The magnitude of string

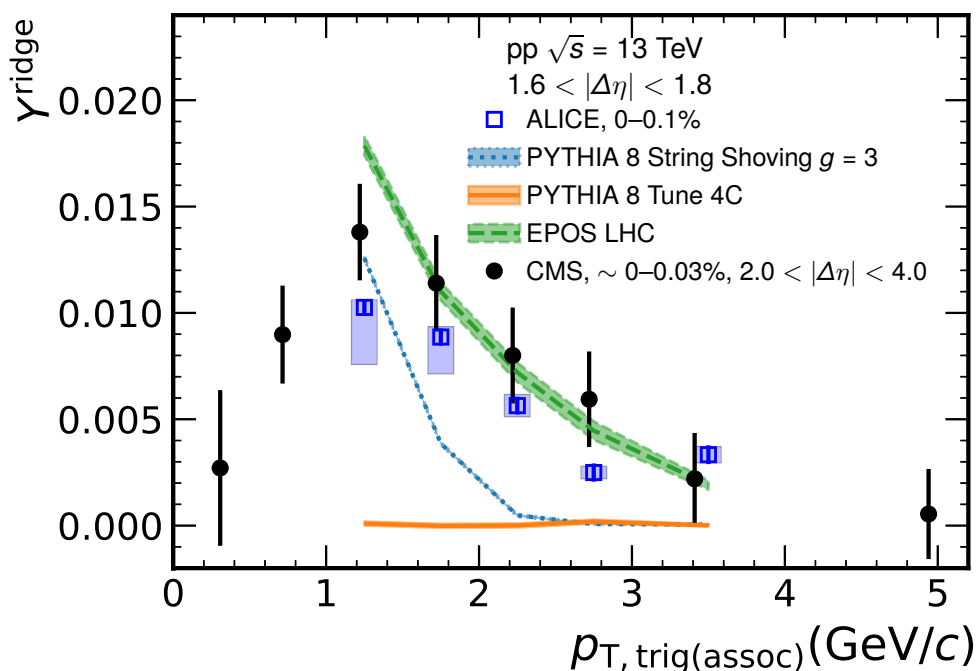


Figure 3. Fully corrected near-side ridge yield as a function transverse momentum. The open blue boxes denote the measurement by ALICE. The statistical and systematic uncertainties are shown as vertical bars and boxes, respectively. The CMS measurement [19] is represented by filled circles and extends down to lower p_T due to the larger $\Delta\eta$ acceptance (see section 3). The three lines show model predictions from PYTHIA 8 Tune 4C (blue dotted line), PYTHIA 8 String Shoving (orange line), and EPOS LHC (green dashed line).

shoving (g) is set to 3.0 in this study. The statistical uncertainties due to the limited number of events for the model calculations are shown as bands in each figure. The PYTHIA 8 String Shoving provides good estimates of the near-side ridge yield and slightly overestimates the away-side yield for the interval $1 < p_T < 2 \text{ GeV}/c$. However, the PYTHIA 8 String Shoving model underestimates the near-side ridge yield for $p_T > 2 \text{ GeV}/c$. The PYTHIA 8 Tune 4C model does not show any near-side ridge as expected. It slightly underestimates the away-side peak for $1 < p_T < 2 \text{ GeV}/c$ and provides good estimates for $p_T > 2 \text{ GeV}/c$. On the other hand, EPOS LHC describes the shape of the ridge yield quantitatively better in the $2 < p_{T, \text{trig}(\text{assoc})} < 4 \text{ GeV}/c$ range, while overestimating the near-side ridge yield for $p_{T, \text{trig}(\text{assoc})} < 2 \text{ GeV}/c$ range.

Figure 3 shows the near-side ridge yield measured in high-multiplicity events as a function of $p_{T, \text{trig}(\text{assoc})}$. The measurement is compared with the result from CMS [19]. Considering the differences in acceptance and the chosen multiplicity estimator of both measurements, perfect agreement between the two sets of results is not expected. The measurement is also compared with model calculations. As expected, the PYTHIA 8 model with Tune 4C does not produce a near-side ridge because it is not designed to account for this effect. The PYTHIA 8 String Shoving model describes the yield qualitatively, however the

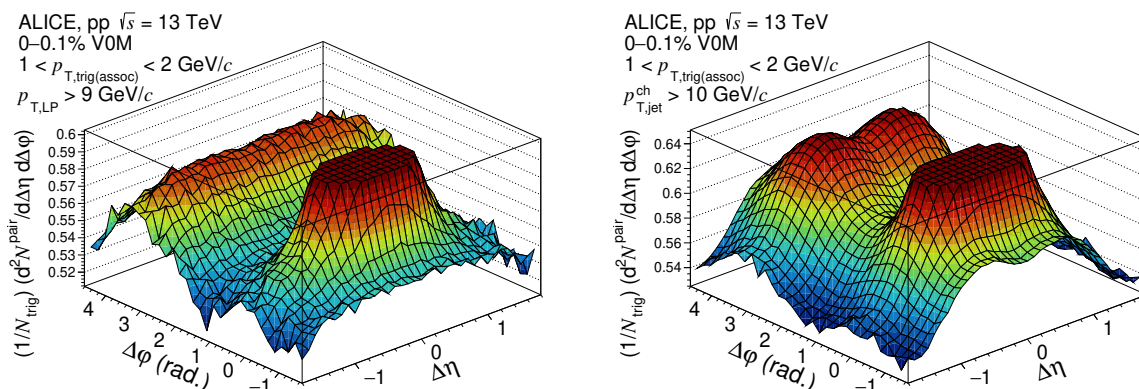


Figure 4. Two-dimensional correlation functions as a function of $\Delta\eta$ and $\Delta\varphi$ in high-multiplicity events including a selection on the event-scale. The interval of $p_{T,\text{trig}}$ and $p_{T,\text{assoc}}$ is $1 < p_{T,\text{trig(assoc)}} < 2 \text{ GeV}/c$. Left: HM events with a $p_{T,\text{LP}} > 9 \text{ GeV}/c$ leading track. Right: HM events with a $p_{T,\text{jet}}^{\text{ch}} > 10 \text{ GeV}/c$.

predicted yield decreases more rapidly than the measured one for increasing $p_{T,\text{trig(assoc)}}$. The EPOS LHC model, unlike the PYTHIA 8 String Shoving model, describes well the p_T dependence of the ridge yield for the range $p_T > 2 \text{ GeV}/c$, while predicting larger yields for $p_T < 2 \text{ GeV}/c$.

5.2 Event-scale dependence of the ridge yield

The ridge yield is further studied with respect to two different event-scales. In the first measurement, the event-scale is set by requiring a minimum p_T on the leading particle in each event (denoted as $p_{T,\text{LP}}$), while in the second measurement, a minimum p_T is imposed on the leading jet (denoted as $p_{T,\text{jet}}^{\text{ch}}$).

Figure 4 shows that the ridge structure for $1 < p_{T,\text{trig}} (p_{T,\text{assoc}}) < 2 \text{ GeV}/c$ still persists in high-multiplicity pp collisions with $p_{T,\text{LP}} > 9 \text{ GeV}/c$ (left) and $p_{T,\text{jet}}^{\text{ch}} > 10 \text{ GeV}/c$ (right). It is worth noting that the correlation function obtained with the minimum $p_{T,\text{jet}}^{\text{ch}}$ selection has a double peak structure which is oriented along the $\Delta\eta$ axis at $\Delta\varphi = \pi$. This structure emerges due to the restricted acceptance of the jet tagging, $|\eta_{\text{jet}}| < 0.4$.

Figure 5 shows projected $\Delta\varphi$ distributions of the correlation functions in $1.6 < |\Delta\eta| < 1.8$ with the minimum $p_{T,\text{LP}}$ (lower) and $p_{T,\text{jet}}^{\text{ch}}$ (upper) requirement. Even with the event-scale selection, the ridge is still visible on the near-side. The near-side ridge peak increases as the thresholds of $p_{T,\text{LP}}$ and $p_{T,\text{jet}}^{\text{ch}}$ increase compared to the one measured in unbiased events in section 5.1. The results are compared with PYTHIA 8 String Shoving, PYTHIA 8 Tune 4C, and EPOS LHC calculations. The near-side ridge peaks are qualitatively reproduced by PYTHIA 8 String Shoving and EPOS LHC models. On the other hand, the PYTHIA 8 Tune 4C does not show the near-side ridge peak for neither of the two event-scale selections, but it gives compatible results for the away-side yield just like the PYTHIA 8 String Shoving model.

The ridge yields as function of the minimum $p_{T,\text{LP}}$ ($p_{T,\text{min}}^{\text{LP}}$) and $p_{T,\text{jet}}^{\text{ch}}$ ($p_{T,\text{min}}^{\text{jet}}$) selections are shown in figure 6. High-multiplicity events with imposed event-scale bias exhibit

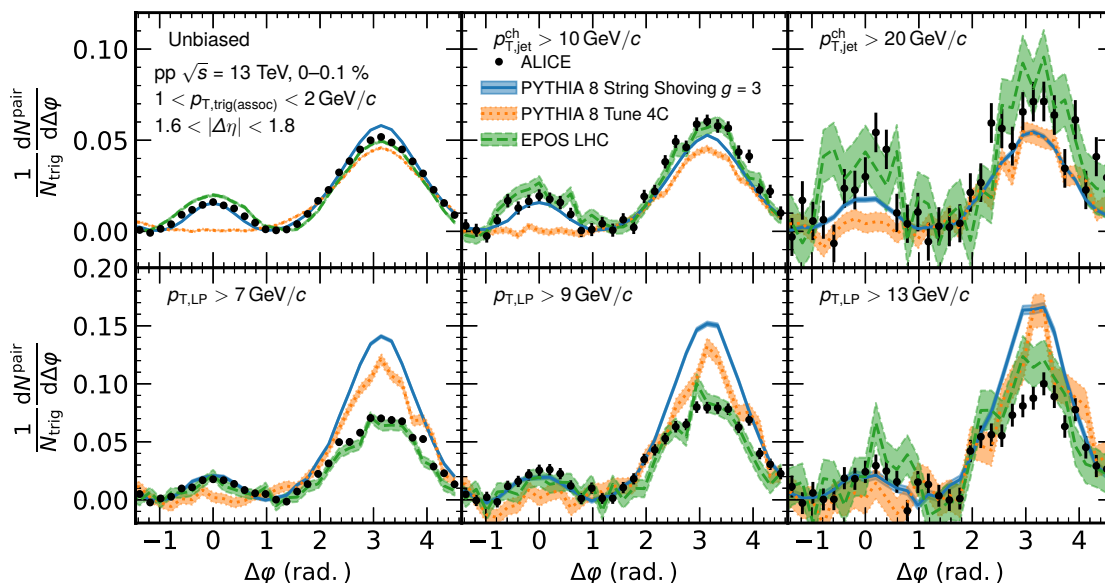


Figure 5. One-dimensional $\Delta\phi$ projections of the correlation functions constrained to $1.6 < |\Delta\eta| < 1.8$ in HM events with an additional event-scale bias. Top: with an imposed selection on the leading jet p_T , bottom: with an imposed selection on the leading particle p_T . ALICE data are compared with prediction of models.

increased ridge yields when compared to unbiased HM events. A small increase of the ridge yields as a function of $p_{T,LP}$ or $p_{T,jet}^{ch}$ is observed and there is no difference between the two event-scale selections within the uncertainties. Comparisons to model calculations show that PYTHIA 8 String Shoving provides a comparable trend with data, but underestimates the ridge yield. On the other hand, EPOS LHC overestimates the ridge yield while providing a trend comparable with the data. The origin of the enhanced ridge yields for higher momentum jet-tagged events is not clear to date but it might be related to the expected smaller impact parameters for dijet or multi-jet production events as studied in [60].

Finally, the near-side jet-like peak yield is measured as a function of minimum $p_{T,LP}$ and $p_{T,jet}^{ch}$ in figure 7 to further test the models that aim to describe the near-side ridge. EPOS LHC provides comparable estimates of the near-side jet-like peak yield, while PYTHIA 8 Tune 4C and PYTHIA 8 String Shoving overestimate the near-side yields for both event selections.

In all models if the ridge is due to final-state interactions, e.g., EPOS LHC and PYTHIA 8 String Shoving, one also expects the near-side jet-like peak yield to be affected. This can be observed when comparing the measured near-side jet yields with PYTHIA 8 calculations with and without String Shoving. The new ALICE results therefore provide constraints beyond traditional ridge measurements that challenge existing models.

6 Conclusions

Long- and short-range correlations for pairs of charged particles with $1 < p_T < 4$ GeV/c are studied in pp collisions at $\sqrt{s} = 13$ TeV with a focus on high-multiplicity events. The ridge

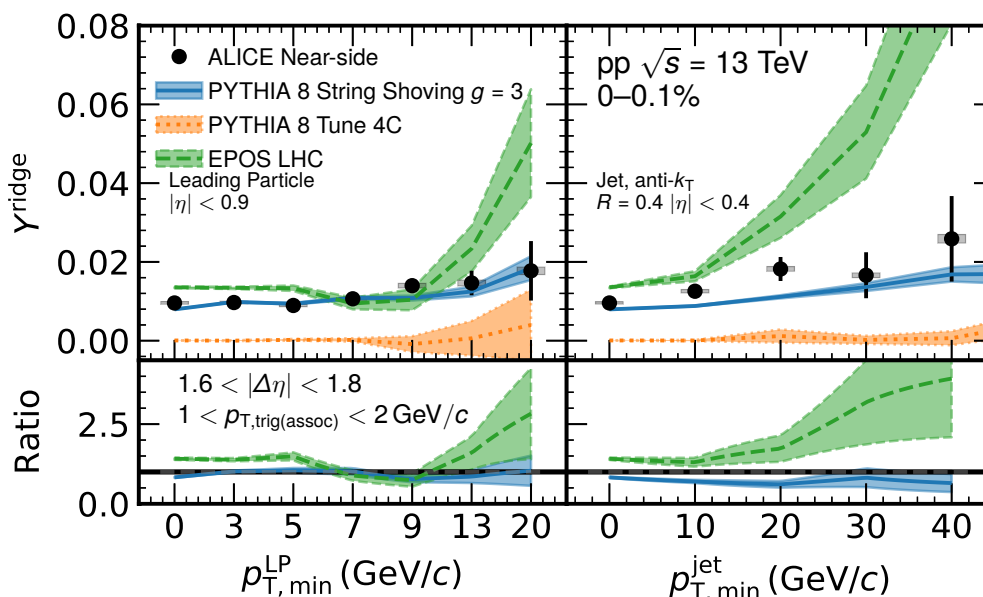


Figure 6. Near-side ridge yield as a function of the $p_{T,\min}^{\text{LP}}$ (left) and $p_{T,\min}^{\text{jet}}$ (right). Data points (filled circles) show the ALICE measurement. The statistical and systematic uncertainties are shown as vertical bars and boxes, respectively. As the ridge yield is obtained in the same operational way for data and models, the upper limit of the systematic uncertainty due to jet contamination, which is 18.9%, is not included in the figure. The data are compared with predictions of models which are represented by colored bands. The bottom panel shows a ratio of the models to the data. The uncertainty of the data is represented by the gray band centered around unity.

and near-side jet yields are extracted and their event scale dependence have been studied. The obtained long-range ridge yields are compatible to those observed by the CMS Collaboration [19]. The PYTHIA 8 String Shoving model describes the observed yields qualitatively but the yields it predicts decrease more rapidly with increasing $p_{T,\text{trig(assoc)}}$ than those measured. On the other hand, the EPOS LHC model gives a better description for the $p_{T,\text{trig(assoc)}}$ dependence while overestimating the ridge yield for $p_{T,\text{trig(assoc)}} < 2 \text{ GeV}/c$. Finally, no long-range ridge is formed in the PYTHIA 8 Tune 4C model.

The ridge yields are further studied in high-multiplicity events biased with additional event-scale selections, which impose a minimum transverse momentum cutoff on a leading track or jet. The ridge structure still persists with both selection criteria. The ridge yield increases as $p_{T,\text{LP}}$ and $p_{T,\text{jet}}^{\text{ch}}$ increase. PYTHIA 8 String Shoving and EPOS LHC estimate qualitatively the trends for the event-scale selections. However, the former underestimates and the latter overestimates it. The model predictions are also compared with the yield of the near-side jet-like correlation measured in the biased events. The evolution of the near-side jet yield as a function of event-scale p_T is better captured by EPOS LHC, while the PYTHIA 8 String Shoving calculation tends to overshoot the data. The results might open a new way of studying the impact parameter dependence of small systems with jet tagged events in the future and will help to constrain the physical origins of long-range correlations.

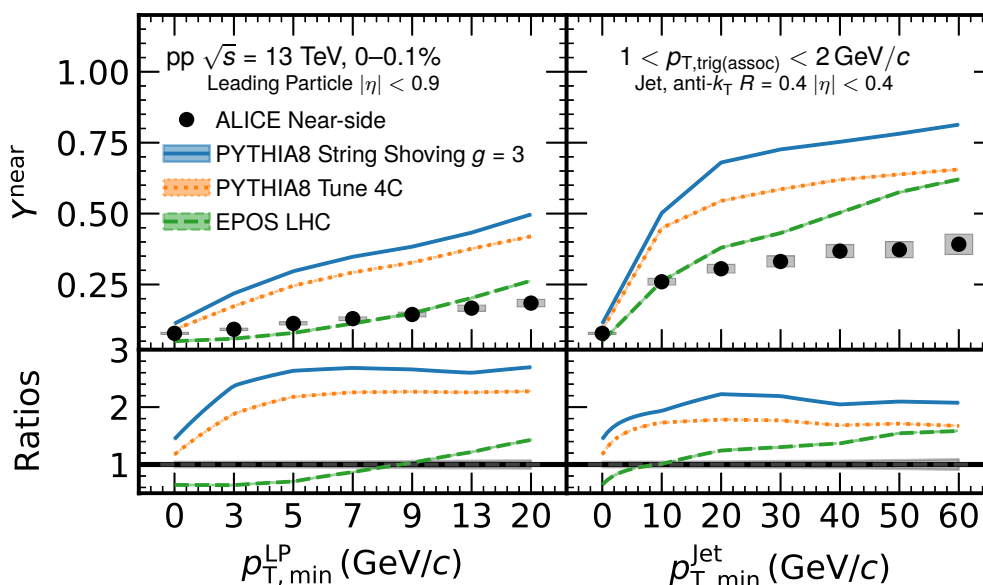


Figure 7. Near-side jet-like peak yield as a function of the $p_{T,\min}^{\text{LP}}$ (left) and $p_{T,\min}^{\text{jet}}$ (right). The filled circles show measurement with ALICE. The statistical and systematic uncertainties are shown as vertical bars and boxes, respectively. The measurements are compared with model descriptions from PYTHIA 8 Tune 4C, PYTHIA 8 String Shoving, and EPOS LHC for both selections. The total uncertainty of the ratio is represented by the gray band centered around unity.

Acknowledgments

The ALICE Collaboration would like to thank Christian Bierlich for providing the PYTHIA8 String Shoving configurations.

The ALICE Collaboration would like to thank all its engineers and technicians for their invaluable contributions to the construction of the experiment and the CERN accelerator teams for the outstanding performance of the LHC complex. The ALICE Collaboration gratefully acknowledges the resources and support provided by all Grid centres and the Worldwide LHC Computing Grid (WLCG) collaboration. The ALICE Collaboration acknowledges the following funding agencies for their support in building and running the ALICE detector: A.I. Alikhanyan National Science Laboratory (Yerevan Physics Institute) Foundation (ANSL), State Committee of Science and World Federation of Scientists (WFS), Armenia; Austrian Academy of Sciences, Austrian Science Fund (FWF): [M 2467-N36] and Nationalstiftung für Forschung, Technologie und Entwicklung, Austria; Ministry of Communications and High Technologies, National Nuclear Research Center, Azerbaijan; Conselho Nacional de Desenvolvimento Científico e Tecnológico (CNPq), Financiadora de Estudos e Projetos (Finep), Fundação de Amparo à Pesquisa do Estado de São Paulo (FAPESP) and Universidade Federal do Rio Grande do Sul (UFRGS), Brazil; Ministry of Education of China (MOEC), Ministry of Science & Technology of China (MSTC) and National Natural Science Foundation of China (NSFC), China; Ministry of Science and Education and Croatian Science Foundation, Croatia; Centro de Aplicaciones Tecnológi-

cas y Desarrollo Nuclear (CEADEN), Cubaenergía, Cuba; Ministry of Education, Youth and Sports of the Czech Republic, Czech Republic; The Danish Council for Independent Research | Natural Sciences, the VILLUM FONDEN and Danish National Research Foundation (DNRF), Denmark; Helsinki Institute of Physics (HIP), Finland; Commissariat à l’Energie Atomique (CEA) and Institut National de Physique Nucléaire et de Physique des Particules (IN2P3) and Centre National de la Recherche Scientifique (CNRS), France; Bundesministerium für Bildung und Forschung (BMBF) and GSI Helmholtzzentrum für Schwerionenforschung GmbH, Germany; General Secretariat for Research and Technology, Ministry of Education, Research and Religions, Greece; National Research, Development and Innovation Office, Hungary; Department of Atomic Energy Government of India (DAE), Department of Science and Technology, Government of India (DST), University Grants Commission, Government of India (UGC) and Council of Scientific and Industrial Research (CSIR), India; Indonesian Institute of Science, Indonesia; Istituto Nazionale di Fisica Nucleare (INFN), Italy; Institute for Innovative Science and Technology, Nagasaki Institute of Applied Science (IIST), Japanese Ministry of Education, Culture, Sports, Science and Technology (MEXT) and Japan Society for the Promotion of Science (JSPS) KAKENHI, Japan; Consejo Nacional de Ciencia (CONACYT) y Tecnología, through Fondo de Cooperación Internacional en Ciencia y Tecnología (FONCICYT) and Dirección General de Asuntos del Personal Académico (DGAPA), Mexico; Nederlandse Organisatie voor Wetenschappelijk Onderzoek (NWO), Netherlands; The Research Council of Norway, Norway; Commission on Science and Technology for Sustainable Development in the South (COMSATS), Pakistan; Pontificia Universidad Católica del Perú, Peru; Ministry of Science and Higher Education, National Science Centre and WUT ID-UB, Poland; Korea Institute of Science and Technology Information and National Research Foundation of Korea (NRF), Republic of Korea; Ministry of Education and Scientific Research, Institute of Atomic Physics and Ministry of Research and Innovation and Institute of Atomic Physics, Romania; Joint Institute for Nuclear Research (JINR), Ministry of Education and Science of the Russian Federation, National Research Centre Kurchatov Institute, Russian Science Foundation and Russian Foundation for Basic Research, Russia; Ministry of Education, Science, Research and Sport of the Slovak Republic, Slovakia; National Research Foundation of South Africa, South Africa; Swedish Research Council (VR) and Knut & Alice Wallenberg Foundation (KAW), Sweden; European Organization for Nuclear Research, Switzerland; Suranaree University of Technology (SUT), National Science and Technology Development Agency (NSDTA) and Office of the Higher Education Commission under NRU project of Thailand, Thailand; Turkish Atomic Energy Agency (TAEK), Turkey; National Academy of Sciences of Ukraine, Ukraine; Science and Technology Facilities Council (STFC), United Kingdom; National Science Foundation of the United States of America (NSF) and United States Department of Energy, Office of Nuclear Physics (DOE NP), United States of America.

Open Access. This article is distributed under the terms of the Creative Commons Attribution License ([CC-BY 4.0](https://creativecommons.org/licenses/by/4.0/)), which permits any use, distribution and reproduction in any medium, provided the original author(s) and source are credited.

References

- [1] STAR collaboration, *Experimental and theoretical challenges in the search for the quark gluon plasma: The STAR Collaboration's critical assessment of the evidence from RHIC collisions*, *Nucl. Phys. A* **757** (2005) 102 [[nucl-ex/0501009](#)] [[INSPIRE](#)].
- [2] PHENIX collaboration, *Formation of dense partonic matter in relativistic nucleus-nucleus collisions at RHIC: Experimental evaluation by the PHENIX collaboration*, *Nucl. Phys. A* **757** (2005) 184 [[nucl-ex/0410003](#)] [[INSPIRE](#)].
- [3] BRAHMS collaboration, *Quark gluon plasma and color glass condensate at RHIC? The Perspective from the BRAHMS experiment*, *Nucl. Phys. A* **757** (2005) 1 [[nucl-ex/0410020](#)] [[INSPIRE](#)].
- [4] PHOBOS collaboration, *The PHOBOS perspective on discoveries at RHIC*, *Nucl. Phys. A* **757** (2005) 28 [[nucl-ex/0410022](#)] [[INSPIRE](#)].
- [5] ALICE collaboration, *Anisotropic flow of charged hadrons, pions and (anti-)protons measured at high transverse momentum in Pb-Pb collisions at $\sqrt{s_{NN}} = 2.76$ TeV*, *Phys. Lett. B* **719** (2013) 18 [[arXiv:1205.5761](#)] [[INSPIRE](#)].
- [6] ALICE collaboration, *Elliptic flow of identified hadrons in Pb-Pb collisions at $\sqrt{s_{NN}} = 2.76$ TeV*, *JHEP* **06** (2015) 190 [[arXiv:1405.4632](#)] [[INSPIRE](#)].
- [7] ATLAS collaboration, *Measurement of the pseudorapidity and transverse momentum dependence of the elliptic flow of charged particles in lead-lead collisions at $\sqrt{s_{NN}} = 2.76$ TeV with the ATLAS detector*, *Phys. Lett. B* **707** (2012) 330 [[arXiv:1108.6018](#)] [[INSPIRE](#)].
- [8] P. Romatschke and U. Romatschke, *Viscosity Information from Relativistic Nuclear Collisions: How Perfect is the Fluid Observed at RHIC?*, *Phys. Rev. Lett.* **99** (2007) 172301 [[arXiv:0706.1522](#)] [[INSPIRE](#)].
- [9] S. Jeon and U. Heinz, *Introduction to Hydrodynamics*, *Int. J. Mod. Phys. E* **24** (2015) 1530010 [[arXiv:1503.03931](#)] [[INSPIRE](#)].
- [10] P. Romatschke and U. Romatschke, *Relativistic Fluid Dynamics In and Out of Equilibrium*, Cambridge Monographs on Mathematical Physics, Cambridge University Press (2019), [[DOI](#)] [[arXiv:1712.05815](#)] [[INSPIRE](#)].
- [11] H. Niemi, K.J. Eskola and R. Paatelainen, *Event-by-event fluctuations in a perturbative QCD + saturation + hydrodynamics model: Determining QCD matter shear viscosity in ultrarelativistic heavy-ion collisions*, *Phys. Rev. C* **93** (2016) 024907 [[arXiv:1505.02677](#)] [[INSPIRE](#)].
- [12] J.E. Bernhard, J.S. Moreland, S.A. Bass, J. Liu and U. Heinz, *Applying Bayesian parameter estimation to relativistic heavy-ion collisions: simultaneous characterization of the initial state and quark-gluon plasma medium*, *Phys. Rev. C* **94** (2016) 024907 [[arXiv:1605.03954](#)] [[INSPIRE](#)].
- [13] J.E. Bernhard, J.S. Moreland and S.A. Bass, *Bayesian estimation of the specific shear and bulk viscosity of quark-gluon plasma*, *Nature Phys.* **15** (2019) 1113.
- [14] ALICE collaboration, *Correlated event-by-event fluctuations of flow harmonics in Pb-Pb collisions at $\sqrt{s_{NN}} = 2.76$ TeV*, *Phys. Rev. Lett.* **117** (2016) 182301 [[arXiv:1604.07663](#)] [[INSPIRE](#)].

- [15] ALICE collaboration, *Systematic studies of correlations between different order flow harmonics in Pb-Pb collisions at $\sqrt{s_{NN}} = 2.76$ TeV*, *Phys. Rev. C* **97** (2018) 024906 [[arXiv:1709.01127](#)] [[INSPIRE](#)].
- [16] ALICE collaboration, *Linear and non-linear flow modes in Pb-Pb collisions at $\sqrt{s_{NN}} = 2.76$ TeV*, *Phys. Lett. B* **773** (2017) 68 [[arXiv:1705.04377](#)] [[INSPIRE](#)].
- [17] ALICE collaboration, *Higher harmonic non-linear flow modes of charged hadrons in Pb-Pb collisions at $\sqrt{s_{NN}} = 5.02$ TeV*, *JHEP* **05** (2020) 085 [[arXiv:2002.00633](#)] [[INSPIRE](#)].
- [18] ATLAS collaboration, *Observation of Long-Range Elliptic Azimuthal Anisotropies in $\sqrt{s} = 13$ and 2.76 TeV pp Collisions with the ATLAS Detector*, *Phys. Rev. Lett.* **116** (2016) 172301 [[arXiv:1509.04776](#)] [[INSPIRE](#)].
- [19] CMS collaboration, *Measurement of long-range near-side two-particle angular correlations in pp collisions at $\sqrt{s} = 13$ TeV*, *Phys. Rev. Lett.* **116** (2016) 172302 [[arXiv:1510.03068](#)] [[INSPIRE](#)].
- [20] CMS collaboration, *Evidence for collectivity in pp collisions at the LHC*, *Phys. Lett. B* **765** (2017) 193 [[arXiv:1606.06198](#)] [[INSPIRE](#)].
- [21] ALICE collaboration, *Investigations of Anisotropic Flow Using Multiparticle Azimuthal Correlations in pp, p-Pb, Xe-Xe, and Pb-Pb Collisions at the LHC*, *Phys. Rev. Lett.* **123** (2019) 142301 [[arXiv:1903.01790](#)] [[INSPIRE](#)].
- [22] ALICE collaboration, *Long-range angular correlations on the near and away side in p-Pb collisions at $\sqrt{s_{NN}} = 5.02$ TeV*, *Phys. Lett. B* **719** (2013) 29 [[arXiv:1212.2001](#)] [[INSPIRE](#)].
- [23] ATLAS collaboration, *Measurement of long-range pseudorapidity correlations and azimuthal harmonics in $\sqrt{s_{NN}} = 5.02$ TeV proton-lead collisions with the ATLAS detector*, *Phys. Rev. C* **90** (2014) 044906 [[arXiv:1409.1792](#)] [[INSPIRE](#)].
- [24] ATLAS collaboration, *Measurements of long-range azimuthal anisotropies and associated Fourier coefficients for pp collisions at $\sqrt{s} = 5.02$ and 13 TeV and p+Pb collisions at $\sqrt{s_{NN}} = 5.02$ TeV with the ATLAS detector*, *Phys. Rev. C* **96** (2017) 024908 [[arXiv:1609.06213](#)] [[INSPIRE](#)].
- [25] CMS collaboration, *Pseudorapidity dependence of long-range two-particle correlations in pPb collisions at $\sqrt{s_{NN}} = 5.02$ TeV*, *Phys. Rev. C* **96** (2017) 014915 [[arXiv:1604.05347](#)] [[INSPIRE](#)].
- [26] PHENIX collaboration, *Creation of quark-gluon plasma droplets with three distinct geometries*, *Nature Phys.* **15** (2019) 214 [[arXiv:1805.02973](#)] [[INSPIRE](#)].
- [27] PHENIX collaboration, *Measurements of Multiparticle Correlations in d + Au Collisions at 200, 62.4, 39, and 19.6 GeV and p + Au Collisions at 200 GeV and Implications for Collective Behavior*, *Phys. Rev. Lett.* **120** (2018) 062302 [[arXiv:1707.06108](#)] [[INSPIRE](#)].
- [28] W. Busza, K. Rajagopal and W. van der Schee, *Heavy Ion Collisions: The Big Picture, and the Big Questions*, *Ann. Rev. Nucl. Part. Sci.* **68** (2018) 339 [[arXiv:1802.04801](#)] [[INSPIRE](#)].
- [29] J.L. Nagle and W.A. Zajc, *Small System Collectivity in Relativistic Hadronic and Nuclear Collisions*, *Ann. Rev. Nucl. Part. Sci.* **68** (2018) 211 [[arXiv:1801.03477](#)] [[INSPIRE](#)].
- [30] M.A. Lisa, S. Pratt, R. Soltz and U. Wiedemann, *Femtoscopy in relativistic heavy ion collisions*, *Ann. Rev. Nucl. Part. Sci.* **55** (2005) 357 [[nucl-ex/0505014](#)] [[INSPIRE](#)].

- [31] A.M. Poskanzer and S.A. Voloshin, *Methods for analyzing anisotropic flow in relativistic nuclear collisions*, *Phys. Rev. C* **58** (1998) 1671 [[nucl-ex/9805001](#)] [[INSPIRE](#)].
- [32] S.A. Voloshin, A.M. Poskanzer and R. Snellings, *Collective phenomena in non-central nuclear collisions*, *Landolt-Bornstein* **23** (2010) 293 [[arXiv:0809.2949](#)] [[INSPIRE](#)].
- [33] B. Alver and G. Roland, *Collision geometry fluctuations and triangular flow in heavy-ion collisions*, *Phys. Rev. C* **81** (2010) 054905 [*Erratum ibid.* **82** (2010) 039903] [[arXiv:1003.0194](#)] [[INSPIRE](#)].
- [34] B.H. Alver, C. Gombeaud, M. Luzum and J.-Y. Ollitrault, *Triangular flow in hydrodynamics and transport theory*, *Phys. Rev. C* **82** (2010) 034913 [[arXiv:1007.5469](#)] [[INSPIRE](#)].
- [35] ALICE collaboration, *Higher harmonic anisotropic flow measurements of charged particles in Pb-Pb collisions at $\sqrt{s_{NN}} = 2.76$ TeV*, *Phys. Rev. Lett.* **107** (2011) 032301 [[arXiv:1105.3865](#)] [[INSPIRE](#)].
- [36] C. Gale, S. Jeon, B. Schenke, P. Tribedy and R. Venugopalan, *Event-by-event anisotropic flow in heavy-ion collisions from combined Yang-Mills and viscous fluid dynamics*, *Phys. Rev. Lett.* **110** (2013) 012302 [[arXiv:1209.6330](#)] [[INSPIRE](#)].
- [37] C. Shen, Z. Qiu, H. Song, J. Bernhard, S. Bass and U. Heinz, *The iEBE-VISHNU code package for relativistic heavy-ion collisions*, *Comput. Phys. Commun.* **199** (2016) 61 [[arXiv:1409.8164](#)] [[INSPIRE](#)].
- [38] K. Dusling and R. Venugopalan, *Evidence for BFKL and saturation dynamics from dihadron spectra at the LHC*, *Phys. Rev. D* **87** (2013) 051502 [[arXiv:1210.3890](#)] [[INSPIRE](#)].
- [39] A. Bzdak, B. Schenke, P. Tribedy and R. Venugopalan, *Initial state geometry and the role of hydrodynamics in proton-proton, proton-nucleus and deuteron-nucleus collisions*, *Phys. Rev. C* **87** (2013) 064906 [[arXiv:1304.3403](#)] [[INSPIRE](#)].
- [40] B.A. Arbuzov, E.E. Boos and V.I. Savrin, *CMS ridge effect at LHC as a manifestation of bremsstrahlung of gluons due to the quark-anti-quark string formation*, *Eur. Phys. J. C* **71** (2011) 1730 [[arXiv:1104.1283](#)] [[INSPIRE](#)].
- [41] R.D. Weller and P. Romatschke, *One fluid to rule them all: viscous hydrodynamic description of event-by-event central p+p, p+Pb and Pb+Pb collisions at $\sqrt{s} = 5.02$ TeV*, *Phys. Lett. B* **774** (2017) 351 [[arXiv:1701.07145](#)] [[INSPIRE](#)].
- [42] W. Zhao, Y. Zhou, H. Xu, W. Deng and H. Song, *Hydrodynamic collectivity in proton-proton collisions at 13 TeV*, *Phys. Lett. B* **780** (2018) 495 [[arXiv:1801.00271](#)] [[INSPIRE](#)].
- [43] M. Greif, C. Greiner, B. Schenke, S. Schlichting and Z. Xu, *Importance of initial and final state effects for azimuthal correlations in p+Pb collisions*, *Phys. Rev. D* **96** (2017) 091504 [[arXiv:1708.02076](#)] [[INSPIRE](#)].
- [44] H. Mäntysaari, B. Schenke, C. Shen and P. Tribedy, *Imprints of fluctuating proton shapes on flow in proton-lead collisions at the LHC*, *Phys. Lett. B* **772** (2017) 681 [[arXiv:1705.03177](#)] [[INSPIRE](#)].
- [45] T. Pierog, I. Karpenko, J.M. Katzy, E. Yatsenko and K. Werner, *EPOS LHC: Test of collective hadronization with data measured at the CERN Large Hadron Collider*, *Phys. Rev. C* **92** (2015) 034906 [[arXiv:1306.0121](#)] [[INSPIRE](#)].
- [46] B. Schenke, C. Shen and P. Tribedy, *Hybrid Color Glass Condensate and hydrodynamic description of the Relativistic Heavy Ion Collider small system scan*, *Phys. Lett. B* **803** (2020) 135322 [[arXiv:1908.06212](#)] [[INSPIRE](#)].

- [47] B. Schenke, C. Shen and P. Tribedy, *Running the gamut of high energy nuclear collisions*, *Phys. Rev. C* **102** (2020) 044905 [[arXiv:2005.14682](#)] [[INSPIRE](#)].
- [48] M. Strickland, *Small system studies: A theory overview*, *Nucl. Phys. A* **982** (2019) 92 [[arXiv:1807.07191](#)] [[INSPIRE](#)].
- [49] C. Loizides, *Experimental overview on small collision systems at the LHC*, *Nucl. Phys. A* **956** (2016) 200 [[arXiv:1602.09138](#)] [[INSPIRE](#)].
- [50] C. Bierlich, G. Gustafson and L. Lönnblad, *Collectivity without plasma in hadronic collisions*, *Phys. Lett. B* **779** (2018) 58 [[arXiv:1710.09725](#)] [[INSPIRE](#)].
- [51] C. Bierlich, *Soft modifications to jet fragmentation in high energy proton-proton collisions*, *Phys. Lett. B* **795** (2019) 194 [[arXiv:1901.07447](#)] [[INSPIRE](#)].
- [52] M. Gyulassy and M. Plumer, *Jet Quenching in Dense Matter*, *Phys. Lett. B* **243** (1990) 432 [[INSPIRE](#)].
- [53] X.-N. Wang and M. Gyulassy, *Gluon shadowing and jet quenching in A + A collisions at $\sqrt{s} = 200$ GeV*, *Phys. Rev. Lett.* **68** (1992) 1480 [[INSPIRE](#)].
- [54] CMS collaboration, *Charged-particle nuclear modification factors in PbPb and pPb collisions at $\sqrt{s_{NN}} = 5.02$ TeV*, *JHEP* **04** (2017) 039 [[arXiv:1611.01664](#)] [[INSPIRE](#)].
- [55] ALICE collaboration, *Centrality dependence of charged jet production in p-Pb collisions at $\sqrt{s_{NN}} = 5.02$ TeV*, *Eur. Phys. J. C* **76** (2016) 271 [[arXiv:1603.03402](#)] [[INSPIRE](#)].
- [56] ALICE collaboration, *Multiplicity dependence of charged pion, kaon, and (anti)proton production at large transverse momentum in p-Pb collisions at $\sqrt{s_{NN}} = 5.02$ TeV*, *Phys. Lett. B* **760** (2016) 720 [[arXiv:1601.03658](#)] [[INSPIRE](#)].
- [57] ALICE collaboration, *Constraints on jet quenching in p-Pb collisions at $\sqrt{s_{NN}} = 5.02$ TeV measured by the event-activity dependence of semi-inclusive hadron-jet distributions*, *Phys. Lett. B* **783** (2018) 95 [[arXiv:1712.05603](#)] [[INSPIRE](#)].
- [58] ALICE collaboration, *Anomalous evolution of the near-side jet peak shape in Pb-Pb collisions at $\sqrt{s_{NN}} = 2.76$ TeV*, *Phys. Rev. Lett.* **119** (2017) 102301 [[arXiv:1609.06643](#)].
- [59] T. Sjöstrand and M. van Zijl, *Multiple Parton-parton Interactions in an Impact Parameter Picture*, *Phys. Lett. B* **188** (1987) 149 [[INSPIRE](#)].
- [60] L. Frankfurt, M. Strikman and C. Weiss, *Transverse nucleon structure and diagnostics of hard parton-parton processes at LHC*, *Phys. Rev. D* **83** (2011) 054012 [[arXiv:1009.2559](#)] [[INSPIRE](#)].
- [61] CMS collaboration, *Measurement of the Underlying Event Activity in pp Collisions at $\sqrt{s} = 0.9$ and 7 TeV with the Novel Jet-Area/Median Approach*, *JHEP* **08** (2012) 130 [[arXiv:1207.2392](#)] [[INSPIRE](#)].
- [62] CMS collaboration, *Measurement of the Underlying Event Activity at the LHC with $\sqrt{s} = 7$ TeV and Comparison with $\sqrt{s} = 0.9$ TeV*, *JHEP* **09** (2011) 109 [[arXiv:1107.0330](#)] [[INSPIRE](#)].
- [63] ATLAS collaboration, *Measurement of long-range two-particle azimuthal correlations in Z-boson tagged pp collisions at $\sqrt{s}=8$ and 13 TeV*, *Eur. Phys. J. C* **80** (2020) 64 [[arXiv:1906.08290](#)] [[INSPIRE](#)].
- [64] ALICE collaboration, *The ALICE experiment at the CERN LHC*, 2008 *JINST* **3** S08002 [[INSPIRE](#)].

- [65] ALICE collaboration, *Performance of the ALICE Experiment at the CERN LHC*, *Int. J. Mod. Phys. A* **29** (2014) 1430044 [[arXiv:1402.4476](#)] [[INSPIRE](#)].
- [66] ALICE collaboration, *Performance of the ALICE VZERO system*, *2013 JINST* **8** P10016 [[arXiv:1306.3130](#)] [[INSPIRE](#)].
- [67] ALICE collaboration, *Alignment of the ALICE Inner Tracking System with cosmic-ray tracks*, *2010 JINST* **5** P03003 [[arXiv:1001.0502](#)] [[INSPIRE](#)].
- [68] J. Alme et al., *The ALICE TPC, a large 3-dimensional tracking device with fast readout for ultra-high multiplicity events*, *Nucl. Instrum. Meth. A* **622** (2010) 316 [[arXiv:1001.1950](#)] [[INSPIRE](#)].
- [69] ALICE collaboration, *ALICE luminosity determination for pp collisions at $\sqrt{s_{NN}} = 13$ TeV*, *ALICE-PUBLIC-2016-002* (2016).
- [70] R. Santoro et al., *The ALICE Silicon Pixel Detector: Readiness for the first proton beam*, *2009 JINST* **4** P03023 [[INSPIRE](#)].
- [71] G. Contin, *Performance of the present ALICE Inner Tracking System and studies for the upgrade*, *2012 JINST* **7** C06007 [[INSPIRE](#)].
- [72] ALICE collaboration, *Measurement of jet suppression in central Pb-Pb collisions at $\sqrt{s_{NN}} = 2.76$ TeV*, *Phys. Lett. B* **746** (2015) 1 [[arXiv:1502.01689](#)] [[INSPIRE](#)].
- [73] G.I. Kopylov, *Like particle correlations as a tool to study the multiple production mechanism*, *Phys. Lett. B* **50** (1974) 472 [[INSPIRE](#)].
- [74] N.N. Ajitanand et al., *Decomposition of harmonic and jet contributions to particle-pair correlations at ultra-relativistic energies*, *Phys. Rev. C* **72** (2005) 011902 [[nucl-ex/0501025](#)] [[INSPIRE](#)].
- [75] M. Cacciari, G.P. Salam and G. Soyez, *The anti- k_t jet clustering algorithm*, *JHEP* **04** (2008) 063 [[arXiv:0802.1189](#)] [[INSPIRE](#)].
- [76] M. Cacciari, G.P. Salam and G. Soyez, *FastJet User Manual*, *Eur. Phys. J. C* **72** (2012) 1896 [[arXiv:1111.6097](#)] [[INSPIRE](#)].
- [77] ALICE collaboration, *Charged jet cross section and fragmentation in proton-proton collisions at $\sqrt{s} = 7$ TeV*, *Phys. Rev. D* **99** (2019) 012016 [[arXiv:1809.03232](#)] [[INSPIRE](#)].

The ALICE collaboration

S. Acharya¹⁴², D. Adamová⁹⁷, A. Adler⁷⁵, J. Adolfsson⁸², G. Aglieri Rinella³⁵, M. Agnello³¹, N. Agrawal⁵⁵, Z. Ahammed¹⁴², S. Ahmad¹⁶, S.U. Ahn⁷⁷, Z. Akbar⁵², A. Akindinov⁹⁴, M. Al-Turany¹⁰⁹, D.S.D. Albuquerque¹²⁴, D. Aleksandrov⁹⁰, B. Alessandro⁶⁰, H.M. Alfanda⁷, R. Alfaro Molina⁷², B. Ali¹⁶, Y. Ali¹⁴, A. Alici²⁶, N. Alizadehvandchali¹²⁷, A. Alkin³⁵, J. Alme²¹, T. Alt⁶⁹, L. Altenkamper²¹, I. Altsybeev¹¹⁵, M.N. Anaam⁷, C. Andrei⁴⁹, D. Andreou⁹², A. Andronic¹⁴⁵, V. Anguelov¹⁰⁶, T. Antičić¹¹⁰, F. Antinori⁵⁸, P. Antonioli⁵⁵, C. Anuj¹⁶, N. Apadula⁸¹, L. Aphecetche¹¹⁷, H. Appelshäuser⁶⁹, S. Arcelli²⁶, R. Arnaldi⁶⁰, M. Arratia⁸¹, I.C. Arsene²⁰, M. Arslanok^{147,106}, A. Augustinus³⁵, R. Averbeck¹⁰⁹, S. Aziz⁷⁹, M.D. Azmi¹⁶, A. Badalà⁵⁷, Y.W. Baek⁴², X. Bai¹⁰⁹, R. Bailhache⁶⁹, R. Bala¹⁰³, A. Balbino³¹, A. Baldisseri¹³⁹, M. Ball⁴⁴, D. Banerjee⁴, R. Barbera²⁷, L. Barioglio²⁵, M. Barlou⁸⁶, G.G. Barnaföldi¹⁴⁶, L.S. Barnby⁹⁶, V. Barret¹³⁶, C. Bartels¹²⁹, K. Barth³⁵, E. Bartsch⁶⁹, F. Baruffaldi²⁸, N. Bastid¹³⁶, S. Basu^{82,144}, G. Batigne¹¹⁷, B. Batyunya⁷⁶, D. Bauri⁵⁰, J.L. Bazo Alba¹¹⁴, I.G. Bearden⁹¹, C. Beattie¹⁴⁷, I. Belikov¹³⁸, A.D.C. Bell Hechavarria¹⁴⁵, F. Bellini³⁵, R. Bellwied¹²⁷, S. Belokurova¹¹⁵, V. Belyaev⁹⁵, G. Bencedi^{70,146}, S. Beole²⁵, A. Bercuci⁴⁹, Y. Berdnikov¹⁰⁰, A. Berdnikova¹⁰⁶, D. Berenyi¹⁴⁶, L. Bergmann¹⁰⁶, M.G. Besoiu⁶⁸, L. Betev³⁵, P.P. Bhaduri¹⁴², A. Bhasin¹⁰³, I.R. Bhat¹⁰³, M.A. Bhat⁴, B. Bhattacharjee⁴³, P. Bhattacharya²³, A. Bianchi²⁵, L. Bianchi²⁵, N. Bianchi⁵³, J. Bielčík³⁸, J. Bielčíková⁹⁷, A. Bilandzic¹⁰⁷, G. Biro¹⁴⁶, S. Biswas⁴, J.T. Blair¹²¹, D. Blau⁹⁰, M.B. Blidaru¹⁰⁹, C. Blume⁶⁹, G. Boca²⁹, F. Bock⁹⁸, A. Bogdanov⁹⁵, S. Boi²³, J. Bok⁶², L. Boldizsár¹⁴⁶, A. Bolozdynya⁹⁵, M. Bombara³⁹, P.M. Bond³⁵, G. Bonomi¹⁴¹, H. Borel¹³⁹, A. Borisso^{83,95}, H. Bossi¹⁴⁷, E. Botta²⁵, L. Bratrud⁶⁹, P. Braun-Munzinger¹⁰⁹, M. Bregant¹²³, M. Broz³⁸, G.E. Bruno^{108,34}, M.D. Buckland¹²⁹, D. Budnikov¹¹¹, H. Buesching⁶⁹, S. Bufalino³¹, O. Bugnon¹¹⁷, P. Buhler¹¹⁶, P. Buncic³⁵, Z. Buthelezi^{73,133}, J.B. Butt¹⁴, S.A. Bysiak¹²⁰, D. Caffarri⁹², A. Caliva¹⁰⁹, E. Calvo Villar¹¹⁴, J.M.M. Camacho¹²², R.S. Camacho⁴⁶, P. Camerini²⁴, F.D.M. Canedo¹²³, A.A. Capon¹¹⁶, F. Carnesecchi²⁶, R. Caron¹³⁹, J. Castillo Castellanos¹³⁹, E.A.R. Casula²³, F. Catalano³¹, C. Ceballos Sanchez⁷⁶, P. Chakraborty⁵⁰, S. Chandra¹⁴², W. Chang⁷, S. Chapeland³⁵, M. Chartier¹²⁹, S. Chattopadhyay¹⁴², S. Chattopadhyay¹¹², A. Chauvin²³, T.G. Chavez⁴⁶, C. Cheshkov¹³⁷, B. Cheynis¹³⁷, V. Chibante Barroso³⁵, D.D. Chinellato¹²⁴, S. Cho⁶², P. Chochula³⁵, P. Christakoglou⁹², C.H. Christensen⁹¹, P. Christiansen⁸², T. Chujo¹³⁵, C. Cicalo⁵⁶, L. Cifarelli²⁶, F. Cindolo⁵⁵, M.R. Ciupek¹⁰⁹, G. Clai^{II,55}, J. Cleymans¹²⁶, F. Colamaria⁵⁴, J.S. Colburn¹¹³, D. Colella^{54,146}, A. Collu⁸¹, M. Colocci^{35,26}, M. Concas^{III,60}, G. Conesa Balbastre⁸⁰, Z. Conesa del Valle⁷⁹, G. Contin²⁴, J.G. Contreras³⁸, T.M. Cormier⁹⁸, P. Cortese³², M.R. Cosentino¹²⁵, F. Costa³⁵, S. Costanza²⁹, P. Crochet¹³⁶, E. Cuautle⁷⁰, P. Cui⁷, L. Cunqueiro⁹⁸, A. Dainese⁵⁸, F.P.A. Damas^{117,139}, M.C. Danisch¹⁰⁶, A. Danu⁶⁸, I. Das¹¹², P. Das⁸⁸, P. Das⁴, S. Das⁴, S. Dash⁵⁰, S. De⁸⁸, A. De Caro³⁰, G. de Cataldo⁵⁴, L. De Cilladi²⁵, J. de Cuveland⁴⁰, A. De Falco²³, D. De Gruttola³⁰, N. De Marco⁶⁰, C. De Martin²⁴, S. De Pasquale³⁰, S. Deb⁵¹, H.F. Degenhardt¹²³, K.R. Deja¹⁴³, L. Dello Stritto³⁰, S. Delsanto²⁵, W. Deng⁷, P. Dhankher¹⁹, D. Di Bari³⁴, A. Di Mauro³⁵, R.A. Diaz⁸, T. Dietel¹²⁶, Y. Ding⁷, R. Divià³⁵, D.U. Dixit¹⁹, Ø. Djuvslund²¹, U. Dmitrieva⁶⁴, J. Do⁶², A. Dobrin⁶⁸, B. Dönigus⁶⁹, O. Dordic²⁰, A.K. Dubey¹⁴², A. Dubla^{109,92}, S. Dudi¹⁰², M. Dukhishyam⁸⁸, P. Dupieux¹³⁶, T.M. Eder¹⁴⁵, R.J. Ehlers⁹⁸, V.N. Eikeland²¹, D. Elia⁵⁴, B. Erazmus¹¹⁷, F. Ercolessi²⁶, F. Erhardt¹⁰¹, A. Erokhin¹¹⁵, M.R. Ersdal²¹, B. Espagnon⁷⁹, G. Eulisse³⁵, D. Evans¹¹³, S. Evdokimov⁹³, L. Fabbietti¹⁰⁷, M. Faggin²⁸, J. Faivre⁸⁰, F. Fan⁷, A. Fantoni⁵³, M. Fasel⁹⁸, P. Fedchio³¹, A. Feliciello⁶⁰, G. Feofilov¹¹⁵, A. Fernández Téllez⁴⁶, A. Ferrero¹³⁹, A. Ferretti²⁵, A. Festanti³⁵, V.J.G. Feuillard¹⁰⁶, J. Figiel¹²⁰, S. Filchagin¹¹¹, D. Finogeev⁶⁴, F.M. Fionda²¹, G. Fiorenza⁵⁴, F. Flor¹²⁷, A.N. Flores¹²¹, S. Foertsch⁷³, P. Foka¹⁰⁹, S. Fokin⁹⁰, E. Fragiaco⁶¹, U. Fuchs³⁵,

N. Funicello³⁰, C. Furget⁸⁰, A. Furs⁶⁴, M. Fusco Girard³⁰, J.J. Gaardhøje⁹¹, M. Gagliardi²⁵, A.M. Gago¹¹⁴, A. Gal¹³⁸, C.D. Galvan¹²², P. Ganoti⁸⁶, C. Garabatos¹⁰⁹, J.R.A. Garcia⁴⁶, E. Garcia-Solis¹⁰, K. Garg¹¹⁷, C. Gargiulo³⁵, A. Garibli⁸⁹, K. Garner¹⁴⁵, P. Gasik¹⁰⁷, E.F. Gauger¹²¹, M.B. Gay Ducati⁷¹, M. Germain¹¹⁷, J. Ghosh¹¹², P. Ghosh¹⁴², S.K. Ghosh⁴, M. Giacalone²⁶, P. Gianotti⁵³, P. Giubellino^{109,60}, P. Giubilato²⁸, A.M.C. Glaenger¹³⁹, P. Glässel¹⁰⁶, V. Gonzalez¹⁴⁴, L.H. González-Trueba⁷², S. Gorbunov⁴⁰, L. Görlich¹²⁰, S. Gotovac³⁶, V. Grabski⁷², L.K. Graczykowski¹⁴³, K.L. Graham¹¹³, L. Greiner⁸¹, A. Grelli⁶³, C. Grigoras³⁵, V. Grigoriev⁹⁵, A. Grigoryan^{1,1}, S. Grigoryan^{76,1}, O.S. Groettvik²¹, F. Grosa⁶⁰, J.F. Grosse-Oetringhaus³⁵, R. Grosso¹⁰⁹, R. Guernane⁸⁰, M. Guilbaud¹¹⁷, M. Guittiere¹¹⁷, K. Gulbrandsen⁹¹, T. Gunji¹³⁴, A. Gupta¹⁰³, R. Gupta¹⁰³, I.B. Guzman⁴⁶, R. Haake¹⁴⁷, M.K. Habib¹⁰⁹, C. Hadjidakis⁷⁹, H. Hamagaki⁸⁴, G. Hamar¹⁴⁶, M. Hamid⁷, R. Hannigan¹²¹, M.R. Haque^{143,88}, A. Harlenderova¹⁰⁹, J.W. Harris¹⁴⁷, A. Harton¹⁰, J.A. Hasenbichler³⁵, H. Hassan⁹⁸, D. Hatzifotiadou⁵⁵, P. Hauer⁴⁴, L.B. Havener¹⁴⁷, S. Hayashi¹³⁴, S.T. Heckel¹⁰⁷, E. Hellbär⁶⁹, H. Helstrup³⁷, T. Herman³⁸, E.G. Hernandez⁴⁶, G. Herrera Corral⁹, F. Herrmann¹⁴⁵, K.F. Hetland³⁷, H. Hillemanns³⁵, C. Hills¹²⁹, B. Hippolyte¹³⁸, B. Hohlweger¹⁰⁷, J. Honermann¹⁴⁵, G.H. Hong¹⁴⁸, D. Horak³⁸, S. Hornung¹⁰⁹, R. Hosokawa¹⁵, P. Hristov³⁵, C. Huang⁷⁹, C. Hughes¹³², P. Huhn⁶⁹, T.J. Humanic⁹⁹, H. Hushnud¹¹², L.A. Husova¹⁴⁵, N. Hussain⁴³, D. Hutter⁴⁰, J.P. Iddon^{35,129}, R. Ilkaev¹¹¹, H. Ilyas¹⁴, M. Inaba¹³⁵, G.M. Innocenti³⁵, M. Ippolitov⁹⁰, A. Isakov^{38,97}, M.S. Islam¹¹², M. Ivanov¹⁰⁹, V. Ivanov¹⁰⁰, V. Izucheev⁹³, B. Jacak⁸¹, N. Jacazio^{35,55}, P.M. Jacobs⁸¹, S. Jadlovska¹¹⁹, J. Jadlovsky¹¹⁹, S. Jaelani⁶³, C. Jahnke¹²³, M.J. Jakubowska¹⁴³, M.A. Janik¹⁴³, T. Janson⁷⁵, M. Jercic¹⁰¹, O. Jevons¹¹³, M. Jin¹²⁷, F. Jonas^{98,145}, P.G. Jones¹¹³, J. Jung⁶⁹, M. Jung⁶⁹, A. Junique³⁵, A. Jusko¹¹³, P. Kalinak⁶⁵, A. Kalweit³⁵, V. Kaplin⁹⁵, S. Kar⁷, A. Karasu Uysal⁷⁸, D. Karatovic¹⁰¹, O. Karavichev⁶⁴, T. Karavicheva⁶⁴, P. Karczmarczyk¹⁴³, E. Karpechev⁶⁴, A. Kazantsev⁹⁰, U. Keschull⁷⁵, R. Keidel⁴⁸, M. Keil³⁵, B. Ketzner⁴⁴, Z. Khabanova⁹², A.M. Khan⁷, S. Khan¹⁶, A. Khanzadeev¹⁰⁰, Y. Kharlov⁹³, A. Khatun¹⁶, A. Khuntia¹²⁰, B. Kileng³⁷, B. Kim⁶², D. Kim¹⁴⁸, D.J. Kim¹²⁸, E.J. Kim⁷⁴, H. Kim¹⁷, J. Kim¹⁴⁸, J.S. Kim⁴², J. Kim¹⁰⁶, J. Kim¹⁴⁸, J. Kim⁷⁴, M. Kim¹⁰⁶, S. Kim¹⁸, T. Kim¹⁴⁸, S. Kirsch⁶⁹, I. Kisel⁴⁰, S. Kiselev⁹⁴, A. Kisiel¹⁴³, J.L. Klay⁶, J. Klein^{35,60}, S. Klein⁸¹, C. Klein-Bösing¹⁴⁵, M. Kleiner⁶⁹, T. Klemenz¹⁰⁷, A. Kluge³⁵, A.G. Knospe¹²⁷, C. Kobdaj¹¹⁸, M.K. Köhler¹⁰⁶, T. Kollegger¹⁰⁹, A. Kondratyev⁷⁶, N. Kondratyeva⁹⁵, E. Kondratyuk⁹³, J. König⁶⁹, S.A. Königstorfer¹⁰⁷, P.J. Konopka^{2,35}, G. Kornakov¹⁴³, S.D. Koryciak², L. Koska¹¹⁹, O. Kovalenko⁸⁷, V. Kovalenko¹¹⁵, M. Kowalski¹²⁰, I. Králik⁶⁵, A. Kravčáková³⁹, L. Kreis¹⁰⁹, M. Krivda^{113,65}, F. Krizek⁹⁷, K. Krizkova Gajdosova³⁸, M. Kroesen¹⁰⁶, M. Krüger⁶⁹, E. Kryshen¹⁰⁰, M. Krzewicki⁴⁰, V. Kučera³⁵, C. Kuhn¹³⁸, P.G. Kuijper⁹², T. Kumaoka¹³⁵, L. Kumar¹⁰², S. Kundu⁸⁸, P. Kurashvili⁸⁷, A. Kurepin⁶⁴, A.B. Kurepin⁶⁴, A. Kuryakin¹¹¹, S. Kushpil⁹⁷, J. Kvapil¹¹³, M.J. Kweon⁶², J.Y. Kwon⁶², Y. Kwon¹⁴⁸, S.L. La Pointe⁴⁰, P. La Rocca²⁷, Y.S. Lai⁸¹, A. Lakrathok¹¹⁸, M. Lamanna³⁵, R. Langoy¹³¹, K. Lapidus³⁵, P. Larionov⁵³, E. Laudi³⁵, L. Lautner³⁵, R. Lavicka³⁸, T. Lazareva¹¹⁵, R. Lea²⁴, J. Lee¹³⁵, J. Lehrbach⁴⁰, R.C. Lemmon⁹⁶, I. León Monzón¹²², E.D. Lesser¹⁹, M. Lettrich³⁵, P. Lévai¹⁴⁶, X. Li¹¹, X.L. Li⁷, J. Lien¹³¹, R. Lietava¹¹³, B. Lim¹⁷, S.H. Lim¹⁷, V. Lindenstruth⁴⁰, A. Lindner⁴⁹, C. Lippmann¹⁰⁹, A. Liu¹⁹, J. Liu¹²⁹, I.M. Lofnes²¹, V. Loginov⁹⁵, C. Loizides⁹⁸, P. Loncar³⁶, J.A. Lopez¹⁰⁶, X. Lopez¹³⁶, E. López Torres⁸, J.R. Luhder¹⁴⁵, M. Lunardon²⁸, G. Luparello⁶¹, Y.G. Ma⁴¹, A. Maevskaya⁶⁴, M. Mager³⁵, S.M. Mahmood²⁰, T. Mahmoud⁴⁴, A. Maire¹³⁸, R.D. Majka^{1,147}, M. Malaev¹⁰⁰, Q.W. Malik²⁰, L. Malinina^{IV,76}, D. Mal'Kevich⁹⁴, N. Mallick⁵¹, P. Malzacher¹⁰⁹, G. Mandaglio^{33,57}, V. Manko⁹⁰, F. Manso¹³⁶, V. Manzari⁵⁴, Y. Mao⁷, J. Mareš⁶⁷, G.V. Margagliotti²⁴, A. Margotti⁵⁵, A. Marín¹⁰⁹, C. Markert¹²¹, M. Marquard⁶⁹, N.A. Martin¹⁰⁶, P. Martinengo³⁵, J.L. Martinez¹²⁷, M.I. Martínez⁴⁶, G. Martínez García¹¹⁷, S. Masciocchi¹⁰⁹, M. Masera²⁵, A. Masoni⁵⁶,

L. Massacrier⁷⁹, A. Mastroserio^{140,54}, A.M. Mathis¹⁰⁷, O. Matonoha⁸², P.F.T. Matuoka¹²³,
 A. Matyja¹²⁰, C. Mayer¹²⁰, A.L. Mazuecos³⁵, F. Mazzaschi²⁵, M. Mazzilli^{35,54}, M.A. Mazzoni⁵⁹,
 A.F. Mechler⁶⁹, F. Meddi²², Y. Melikyan⁶⁴, A. Menchaca-Rocha⁷², C. Mengke^{28,7},
 E. Meninno^{116,30}, A.S. Menon¹²⁷, M. Meres¹³, S. Mhlanga¹²⁶, Y. Miake¹³⁵, L. Micheletti²⁵,
 L.C. Migliorin¹³⁷, D.L. Mihaylov¹⁰⁷, K. Mikhaylov^{76,94}, A.N. Mishra^{146,70}, D. Miśkowiec¹⁰⁹,
 A. Modak⁴, N. Mohammadi³⁵, A.P. Mohanty⁶³, B. Mohanty⁸⁸, M. Mohisin Khan¹⁶,
 Z. Moravcova⁹¹, C. Mordasini¹⁰⁷, D.A. Moreira De Godoy¹⁴⁵, L.A.P. Moreno⁴⁶, I. Morozov⁶⁴,
 A. Morsch³⁵, T. Mrnjavac³⁵, V. Muccifora⁵³, E. Mudnic³⁶, D. Mühlheim¹⁴⁵, S. Muhuri¹⁴²,
 J.D. Mulligan⁸¹, A. Mulliri²³, M.G. Munhoz¹²³, R.H. Munzer⁶⁹, H. Murakami¹³⁴, S. Murray¹²⁶,
 L. Musa³⁵, J. Musinsky⁶⁵, C.J. Myers¹²⁷, J.W. Myrcha¹⁴³, B. Naik⁵⁰, R. Nair⁸⁷, B.K. Nandi⁵⁰,
 R. Nania⁵⁵, E. Nappi⁵⁴, M.U. Naru¹⁴, A.F. Nassirpour⁸², C. Nattrass¹³², S. Nazarenko¹¹¹,
 A. Neagu²⁰, L. Nellen⁷⁰, S.V. Nesbo³⁷, G. Neskovic⁴⁰, D. Nesterov¹¹⁵, B.S. Nielsen⁹¹,
 S. Nikolaev⁹⁰, S. Nikulin⁹⁰, V. Nikulin¹⁰⁰, F. Noferini⁵⁵, S. Noh¹², P. Nomokonov⁷⁶,
 J. Norman¹²⁹, N. Novitzky¹³⁵, P. Nowakowski¹⁴³, A. Nyanin⁹⁰, J. Nystrand²¹, M. Ogino⁸⁴,
 A. Ohlson⁸², J. Oleniacz¹⁴³, A.C. Oliveira Da Silva¹³², M.H. Oliver¹⁴⁷, A. Onnerstad¹²⁸,
 C. Oppedisano⁶⁰, A. Ortiz Velasquez⁷⁰, T. Osako⁴⁷, A. Oskarsson⁸², J. Otwinowski¹²⁰,
 K. Oyama⁸⁴, Y. Pachmayer¹⁰⁶, S. Padhan⁵⁰, D. Pagano¹⁴¹, G. Paic⁷⁰, A. Palasciano⁵⁴, J. Pan¹⁴⁴,
 S. Panebianco¹³⁹, P. Pareek¹⁴², J. Park⁶², J.E. Parkkila¹²⁸, S. Parmar¹⁰², S.P. Pathak¹²⁷,
 B. Paul²³, J. Pazzini¹⁴¹, H. Pei⁷, T. Peitzmann⁶³, X. Peng⁷, L.G. Pereira⁷¹, H. Pereira Da
 Costa¹³⁹, D. Peresunko⁹⁰, G.M. Perez⁸, S. Perrin¹³⁹, Y. Pestov⁵, V. Petráček³⁸, M. Petrovici⁴⁹,
 R.P. Pezzi⁷¹, S. Piano⁶¹, M. Pikna¹³, P. Pillot¹¹⁷, O. Pinazza^{55,35}, L. Pinsky¹²⁷, C. Pinto²⁷,
 S. Pisano⁵³, M. Płoskon⁸¹, M. Planinic¹⁰¹, F. Pliquett⁶⁹, M.G. Poghosyan⁹⁸, B. Polichtchouk⁹³,
 N. Poljak¹⁰¹, A. Pop⁴⁹, S. Porteboeuf-Houssais¹³⁶, J. Porter⁸¹, V. Pozdniakov⁷⁶, S.K. Prasad⁴,
 R. Preghenella⁵⁵, F. Prino⁶⁰, C.A. Pruneau¹⁴⁴, I. Pshenichnov⁶⁴, M. Puccio³⁵, S. Qiu⁹²,
 L. Quaglia²⁵, R.E. Quishpe¹²⁷, S. Ragoni¹¹³, A. Rakotozafindrabe¹³⁹, L. Ramello³², F. Rami¹³⁸,
 S.A.R. Ramirez⁴⁶, A.G.T. Ramos³⁴, R. Raniwala¹⁰⁴, S. Raniwala¹⁰⁴, S.S. Räsänen⁴⁵, R. Rath⁵¹,
 I. Ravasenga⁹², K.F. Read^{98,132}, A.R. Redelbach⁴⁰, K. Redlich^{V,87}, A. Rehman²¹, P. Reichelt⁶⁹,
 F. Reidt³⁵, R. Renfordt⁶⁹, Z. Rescakova³⁹, K. Reygers¹⁰⁶, A. Riabov¹⁰⁰, V. Riabov¹⁰⁰,
 T. Richert^{82,91}, M. Richter²⁰, P. Riedler³⁵, W. Riegler³⁵, F. Riggi²⁷, C. Ristea⁶⁸, S.P. Rode⁵¹,
 M. Rodríguez Cahuantzi⁴⁶, K. Røed²⁰, R. Rogalev⁹³, E. Rogochaya⁷⁶, T.S. Rogoschinski⁶⁹,
 D. Rohr³⁵, D. Röhrich²¹, P.F. Rojas⁴⁶, P.S. Rokita¹⁴³, F. Ronchetti⁵³, A. Rosano^{33,57},
 E.D. Rosas⁷⁰, A. Rossi⁵⁸, A. Rotondi²⁹, A. Roy⁵¹, P. Roy¹¹², N. Rubini²⁶, O.V. Rueda⁸²,
 R. Rui²⁴, B. Rumyantsev⁷⁶, A. Rustamov⁸⁹, E. Ryabinkin⁹⁰, Y. Ryabov¹⁰⁰, A. Rybicki¹²⁰,
 H. Rytönen¹²⁸, W. Rzeska¹⁴³, O.A.M. Saari⁴⁵, R. Sadek¹¹⁷, S. Sadovsky⁹³, J. Saetre²¹,
 K. Šafařík³⁸, S.K. Saha¹⁴², S. Saha⁸⁸, B. Sahoo⁵⁰, P. Sahoo⁵⁰, R. Sahoo⁵¹, S. Sahoo⁶⁶, D. Sahu⁵¹,
 P.K. Sahu⁶⁶, J. Saini¹⁴², S. Sakai¹³⁵, S. Sambyal¹⁰³, V. Samsonov^{I,100,95}, D. Sarkar¹⁴⁴,
 N. Sarkar¹⁴², P. Sarma⁴³, V.M. Sarti¹⁰⁷, M.H.P. Sas^{147,63}, J. Schambach^{98,121}, H.S. Scheid⁶⁹,
 C. Schiaua⁴⁹, R. Schicker¹⁰⁶, A. Schmah¹⁰⁶, C. Schmidt¹⁰⁹, H.R. Schmidt¹⁰⁵, M.O. Schmidt¹⁰⁶,
 M. Schmidt¹⁰⁵, N.V. Schmidt^{98,69}, A.R. Schmier¹³², R. Schotter¹³⁸, J. Schukraft³⁵, Y. Schutz¹³⁸,
 K. Schwarz¹⁰⁹, K. Schweda¹⁰⁹, G. Scioli²⁶, E. Scomparin⁶⁰, J.E. Seger¹⁵, Y. Sekiguchi¹³⁴,
 D. Sekihata¹³⁴, I. Selyuzhenkov^{109,95}, S. Senyukov¹³⁸, J.J. Seo⁶², D. Serebryakov⁶⁴,
 L. Šerkšnytė¹⁰⁷, A. Sevcenco⁶⁸, A. Shabanov⁶⁴, A. Shabetai¹¹⁷, R. Shahoyan³⁵, W. Shaikh¹¹²,
 A. Shangaraev⁹³, A. Sharma¹⁰², H. Sharma¹²⁰, M. Sharma¹⁰³, N. Sharma¹⁰², S. Sharma¹⁰³,
 O. Sheibani¹²⁷, A.I. Sheikh¹⁴², K. Shigaki⁴⁷, M. Shimomura⁸⁵, S. Shirinkin⁹⁴, Q. Shou⁴¹,
 Y. Sibiriak⁹⁰, S. Siddhanta⁵⁶, T. Siemiarczuk⁸⁷, T.F.D. Silva¹²³, D. Silvermyr⁸², G. Simatovic⁹²,
 G. Simonetti³⁵, B. Singh¹⁰⁷, R. Singh⁸⁸, R. Singh¹⁰³, R. Singh⁵¹, V.K. Singh¹⁴², V. Singhal¹⁴²,
 T. Sinha¹¹², B. Sitar¹³, M. Sitta³², T.B. Skaali²⁰, G. Skorodumovs¹⁰⁶, M. Slupecki⁴⁵,
 N. Smirnov¹⁴⁷, R.J.M. Snellings⁶³, C. Soncco¹¹⁴, J. Song¹²⁷, A. Songmoolnak¹¹⁸, F. Soramel²⁸,

S. Sorensen¹³², I. Sputowska¹²⁰, J. Stachel¹⁰⁶, I. Stan⁶⁸, P.J. Steffanic¹³², S.F. Stiefelmaier¹⁰⁶, D. Stocco¹¹⁷, M.M. Storetvedt³⁷, C.P. Stylianidis⁹², A.A.P. Suaide¹²³, T. Sugitate⁴⁷, C. Suire⁷⁹, M. Suljic³⁵, R. Sultanov⁹⁴, M. Šumbera⁹⁷, V. Sumberia¹⁰³, S. Sumowidagdo⁵², S. Swain⁶⁶, A. Szabo¹³, I. Szarka¹³, U. Tabassam¹⁴, S.F. Taghavi¹⁰⁷, G. Taillepied¹³⁶, J. Takahashi¹²⁴, G.J. Tambave²¹, S. Tang^{136,7}, Z. Tang¹³⁰, M. Tarhini¹¹⁷, M.G. Tarzila⁴⁹, A. Tauro³⁵, G. Tejada Muñoz⁴⁶, A. Telesca³⁵, L. Terlizzi²⁵, C. Terrevoli¹²⁷, G. Tersimonov³, S. Thakur¹⁴², D. Thomas¹²¹, R. Tieulent¹³⁷, A. Tikhonov⁶⁴, A.R. Timmins¹²⁷, M. Tkacik¹¹⁹, A. Toia⁶⁹, N. Topilskaya⁶⁴, M. Toppi⁵³, F. Torales-Acosta¹⁹, S.R. Torres³⁸, A. Trifiró^{33,57}, S. Tripathy⁷⁰, T. Tripathy⁵⁰, S. Trogolo²⁸, G. Trombetta³⁴, L. Tropp³⁹, V. Trubnikov³, W.H. Trzaska¹²⁸, T.P. Trzcinski¹⁴³, B.A. Trzeciak³⁸, A. Tumkin¹¹¹, R. Turrisi⁵⁸, T.S. Tveter²⁰, K. Ullaland²¹, E.N. Umaka¹²⁷, A. Uras¹³⁷, M. Urioni¹⁴¹, G.L. Usai²³, M. Vala³⁹, N. Valle²⁹, S. Vallerio⁶⁰, N. van der Kolk⁶³, L.V.R. van Doremalen⁶³, M. van Leeuwen⁹², P. Vande Vyvre³⁵, D. Varga¹⁴⁶, Z. Varga¹⁴⁶, M. Varga-Kofarago¹⁴⁶, A. Vargas⁴⁶, M. Vasileiou⁸⁶, A. Vasiliev⁹⁰, O. Vázquez Doce¹⁰⁷, V. Vechernin¹¹⁵, E. Vercellin²⁵, S. Vergara Limón⁴⁶, L. Vermunt⁶³, R. Vértesi¹⁴⁶, M. Verweij⁶³, L. Vickovic³⁶, Z. Vilakazi¹³³, O. Villalobos Baillie¹¹³, G. Vino⁵⁴, A. Vinogradov⁹⁰, T. Virgili³⁰, V. Vislavicius⁹¹, A. Vodopyanov⁷⁶, B. Volkel³⁵, M.A. Völkl¹⁰⁵, K. Voloshin⁹⁴, S.A. Voloshin¹⁴⁴, G. Volpe³⁴, B. von Haller³⁵, I. Vorobyev¹⁰⁷, D. Voscek¹¹⁹, J. Vrláková³⁹, B. Wagner²¹, M. Weber¹¹⁶, A. Wegrzynek³⁵, S.C. Wenzel³⁵, J.P. Wessels¹⁴⁵, J. Wiechula⁶⁹, J. Wikne²⁰, G. Wilk⁸⁷, J. Wilkinson¹⁰⁹, G.A. Willems¹⁴⁵, E. Willsher¹¹³, B. Windelband¹⁰⁶, M. Winn¹³⁹, W.E. Witt¹³², J.R. Wright¹²¹, Y. Wu¹³⁰, R. Xu⁷, S. Yalcin⁷⁸, Y. Yamaguchi⁴⁷, K. Yamakawa⁴⁷, S. Yang²¹, S. Yano^{47,139}, Z. Yin⁷, H. Yokoyama⁶³, I.-K. Yoo¹⁷, J.H. Yoon⁶², S. Yuan²¹, A. Yuncu¹⁰⁶, V. Yurchenko³, V. Zaccolo²⁴, A. Zaman¹⁴, C. Zampolli³⁵, H.J.C. Zanoli⁶³, N. Zardoshti³⁵, A. Zarochentsev¹¹⁵, P. Závada⁶⁷, N. Zaviyalov¹¹¹, H. Zbroszczyk¹⁴³, M. Zhalov¹⁰⁰, S. Zhang⁴¹, X. Zhang⁷, Y. Zhang¹³⁰, V. Zhrebchevskii¹¹⁵, Y. Zhi¹¹, D. Zhou⁷, Y. Zhou⁹¹, J. Zhu^{7,109}, Y. Zhu⁷, A. Zichichi²⁶, G. Zinovjev³, N. Zurlo¹⁴¹

Affiliation notes

^I Deceased

^{II} Also at: Italian National Agency for New Technologies, Energy and Sustainable Economic Development (ENEA), Bologna, Italy

^{III} Also at: Dipartimento DET del Politecnico di Torino, Turin, Italy

^{IV} Also at: M.V. Lomonosov Moscow State University, D.V. Skobeltsyn Institute of Nuclear Physics, Moscow, Russia

^V Also at: Institute of Theoretical Physics, University of Wrocław, Poland

Collaboration Institutes

¹ A.I. Alikhanyan National Science Laboratory (Yerevan Physics Institute) Foundation, Yerevan, Armenia

² AGH University of Science and Technology, Cracow, Poland

³ Bogolyubov Institute for Theoretical Physics, National Academy of Sciences of Ukraine, Kiev, Ukraine

⁴ Bose Institute, Department of Physics and Centre for Astroparticle Physics and Space Science (CAPSS), Kolkata, India

⁵ Budker Institute for Nuclear Physics, Novosibirsk, Russia

⁶ California Polytechnic State University, San Luis Obispo, California, United States

⁷ Central China Normal University, Wuhan, China

- ⁸ Centro de Aplicaciones Tecnológicas y Desarrollo Nuclear (CEADEN), Havana, Cuba
- ⁹ Centro de Investigación y de Estudios Avanzados (CINVESTAV), Mexico City and Mérida, Mexico
- ¹⁰ Chicago State University, Chicago, Illinois, United States
- ¹¹ China Institute of Atomic Energy, Beijing, China
- ¹² Chungbuk National University, Cheongju, Republic of Korea
- ¹³ Comenius University Bratislava, Faculty of Mathematics, Physics and Informatics, Bratislava, Slovakia
- ¹⁴ COMSATS University Islamabad, Islamabad, Pakistan
- ¹⁵ Creighton University, Omaha, Nebraska, United States
- ¹⁶ Department of Physics, Aligarh Muslim University, Aligarh, India
- ¹⁷ Department of Physics, Pusan National University, Pusan, Republic of Korea
- ¹⁸ Department of Physics, Sejong University, Seoul, Republic of Korea
- ¹⁹ Department of Physics, University of California, Berkeley, California, United States
- ²⁰ Department of Physics, University of Oslo, Oslo, Norway
- ²¹ Department of Physics and Technology, University of Bergen, Bergen, Norway
- ²² Dipartimento di Fisica dell'Università 'La Sapienza' and Sezione INFN, Rome, Italy
- ²³ Dipartimento di Fisica dell'Università and Sezione INFN, Cagliari, Italy
- ²⁴ Dipartimento di Fisica dell'Università and Sezione INFN, Trieste, Italy
- ²⁵ Dipartimento di Fisica dell'Università and Sezione INFN, Turin, Italy
- ²⁶ Dipartimento di Fisica e Astronomia dell'Università and Sezione INFN, Bologna, Italy
- ²⁷ Dipartimento di Fisica e Astronomia dell'Università and Sezione INFN, Catania, Italy
- ²⁸ Dipartimento di Fisica e Astronomia dell'Università and Sezione INFN, Padova, Italy
- ²⁹ Dipartimento di Fisica e Nucleare e Teorica, Università di Pavia and Sezione INFN, Pavia, Italy
- ³⁰ Dipartimento di Fisica 'E.R. Caianiello' dell'Università and Gruppo Collegato INFN, Salerno, Italy
- ³¹ Dipartimento DISAT del Politecnico and Sezione INFN, Turin, Italy
- ³² Dipartimento di Scienze e Innovazione Tecnologica dell'Università del Piemonte Orientale and INFN Sezione di Torino, Alessandria, Italy
- ³³ Dipartimento di Scienze MIFT, Università di Messina, Messina, Italy
- ³⁴ Dipartimento Interateneo di Fisica 'M. Merlin' and Sezione INFN, Bari, Italy
- ³⁵ European Organization for Nuclear Research (CERN), Geneva, Switzerland
- ³⁶ Faculty of Electrical Engineering, Mechanical Engineering and Naval Architecture, University of Split, Split, Croatia
- ³⁷ Faculty of Engineering and Science, Western Norway University of Applied Sciences, Bergen, Norway
- ³⁸ Faculty of Nuclear Sciences and Physical Engineering, Czech Technical University in Prague, Prague, Czech Republic
- ³⁹ Faculty of Science, P.J. Šafárik University, Košice, Slovakia
- ⁴⁰ Frankfurt Institute for Advanced Studies, Johann Wolfgang Goethe-Universität Frankfurt, Frankfurt, Germany
- ⁴¹ Fudan University, Shanghai, China
- ⁴² Gangneung-Wonju National University, Gangneung, Republic of Korea
- ⁴³ Gauhati University, Department of Physics, Guwahati, India
- ⁴⁴ Helmholtz-Institut für Strahlen- und Kernphysik, Rheinische Friedrich-Wilhelms-Universität Bonn, Bonn, Germany
- ⁴⁵ Helsinki Institute of Physics (HIP), Helsinki, Finland
- ⁴⁶ High Energy Physics Group, Universidad Autónoma de Puebla, Puebla, Mexico

- ⁴⁷ Hiroshima University, Hiroshima, Japan
⁴⁸ Hochschule Worms, Zentrum für Technologietransfer und Telekommunikation (ZTT), Worms, Germany
⁴⁹ Horia Hulubei National Institute of Physics and Nuclear Engineering, Bucharest, Romania
⁵⁰ Indian Institute of Technology Bombay (IIT), Mumbai, India
⁵¹ Indian Institute of Technology Indore, Indore, India
⁵² Indonesian Institute of Sciences, Jakarta, Indonesia
⁵³ INFN, Laboratori Nazionali di Frascati, Frascati, Italy
⁵⁴ INFN, Sezione di Bari, Bari, Italy
⁵⁵ INFN, Sezione di Bologna, Bologna, Italy
⁵⁶ INFN, Sezione di Cagliari, Cagliari, Italy
⁵⁷ INFN, Sezione di Catania, Catania, Italy
⁵⁸ INFN, Sezione di Padova, Padova, Italy
⁵⁹ INFN, Sezione di Roma, Rome, Italy
⁶⁰ INFN, Sezione di Torino, Turin, Italy
⁶¹ INFN, Sezione di Trieste, Trieste, Italy
⁶² Inha University, Incheon, Republic of Korea
⁶³ Institute for Gravitational and Subatomic Physics (GRASP), Utrecht University/Nikhef, Utrecht, Netherlands
⁶⁴ Institute for Nuclear Research, Academy of Sciences, Moscow, Russia
⁶⁵ Institute of Experimental Physics, Slovak Academy of Sciences, Košice, Slovakia
⁶⁶ Institute of Physics, Homi Bhabha National Institute, Bhubaneswar, India
⁶⁷ Institute of Physics of the Czech Academy of Sciences, Prague, Czech Republic
⁶⁸ Institute of Space Science (ISS), Bucharest, Romania
⁶⁹ Institut für Kernphysik, Johann Wolfgang Goethe-Universität Frankfurt, Frankfurt, Germany
⁷⁰ Instituto de Ciencias Nucleares, Universidad Nacional Autónoma de México, Mexico City, Mexico
⁷¹ Instituto de Física, Universidade Federal do Rio Grande do Sul (UFRGS), Porto Alegre, Brazil
⁷² Instituto de Física, Universidad Nacional Autónoma de México, Mexico City, Mexico
⁷³ iThemba LABS, National Research Foundation, Somerset West, South Africa
⁷⁴ Jeonbuk National University, Jeonju, Republic of Korea
⁷⁵ Johann-Wolfgang-Goethe Universität Frankfurt Institut für Informatik, Fachbereich Informatik und Mathematik, Frankfurt, Germany
⁷⁶ Joint Institute for Nuclear Research (JINR), Dubna, Russia
⁷⁷ Korea Institute of Science and Technology Information, Daejeon, Republic of Korea
⁷⁸ KTO Karatay University, Konya, Turkey
⁷⁹ Laboratoire de Physique des 2 Infinis, Irène Joliot-Curie, Orsay, France
⁸⁰ Laboratoire de Physique Subatomique et de Cosmologie, Université Grenoble-Alpes, CNRS-IN2P3, Grenoble, France
⁸¹ Lawrence Berkeley National Laboratory, Berkeley, California, United States
⁸² Lund University Department of Physics, Division of Particle Physics, Lund, Sweden
⁸³ Moscow Institute for Physics and Technology, Moscow, Russia
⁸⁴ Nagasaki Institute of Applied Science, Nagasaki, Japan
⁸⁵ Nara Women's University (NWU), Nara, Japan
⁸⁶ National and Kapodistrian University of Athens, School of Science, Department of Physics , Athens, Greece
⁸⁷ National Centre for Nuclear Research, Warsaw, Poland
⁸⁸ National Institute of Science Education and Research, Homi Bhabha National Institute, Jatni, India

- ⁸⁹ National Nuclear Research Center, Baku, Azerbaijan
- ⁹⁰ National Research Centre Kurchatov Institute, Moscow, Russia
- ⁹¹ Niels Bohr Institute, University of Copenhagen, Copenhagen, Denmark
- ⁹² Nikhef, National institute for subatomic physics, Amsterdam, Netherlands
- ⁹³ NRC Kurchatov Institute IHEP, Protvino, Russia
- ⁹⁴ NRC «Kurchatov»Institute - ITEP, Moscow, Russia
- ⁹⁵ NRNU Moscow Engineering Physics Institute, Moscow, Russia
- ⁹⁶ Nuclear Physics Group, STFC Daresbury Laboratory, Daresbury, United Kingdom
- ⁹⁷ Nuclear Physics Institute of the Czech Academy of Sciences, Řež u Prahy, Czech Republic
- ⁹⁸ Oak Ridge National Laboratory, Oak Ridge, Tennessee, United States
- ⁹⁹ Ohio State University, Columbus, Ohio, United States
- ¹⁰⁰ Petersburg Nuclear Physics Institute, Gatchina, Russia
- ¹⁰¹ Physics department, Faculty of science, University of Zagreb, Zagreb, Croatia
- ¹⁰² Physics Department, Panjab University, Chandigarh, India
- ¹⁰³ Physics Department, University of Jammu, Jammu, India
- ¹⁰⁴ Physics Department, University of Rajasthan, Jaipur, India
- ¹⁰⁵ Physikalisches Institut, Eberhard-Karls-Universität Tübingen, Tübingen, Germany
- ¹⁰⁶ Physikalisches Institut, Ruprecht-Karls-Universität Heidelberg, Heidelberg, Germany
- ¹⁰⁷ Physik Department, Technische Universität München, Munich, Germany
- ¹⁰⁸ Politecnico di Bari and Sezione INFN, Bari, Italy
- ¹⁰⁹ Research Division and ExtreMe Matter Institute EMMI, GSI Helmholtzzentrum für Schwerionenforschung GmbH, Darmstadt, Germany
- ¹¹⁰ Rudjer Bošković Institute, Zagreb, Croatia
- ¹¹¹ Russian Federal Nuclear Center (VNIIEF), Sarov, Russia
- ¹¹² Saha Institute of Nuclear Physics, Homi Bhabha National Institute, Kolkata, India
- ¹¹³ School of Physics and Astronomy, University of Birmingham, Birmingham, United Kingdom
- ¹¹⁴ Sección Física, Departamento de Ciencias, Pontificia Universidad Católica del Perú, Lima, Peru
- ¹¹⁵ St. Petersburg State University, St. Petersburg, Russia
- ¹¹⁶ Stefan Meyer Institut für Subatomare Physik (SMI), Vienna, Austria
- ¹¹⁷ SUBATECH, IMT Atlantique, Université de Nantes, CNRS-IN2P3, Nantes, France
- ¹¹⁸ Suranaree University of Technology, Nakhon Ratchasima, Thailand
- ¹¹⁹ Technical University of Košice, Košice, Slovakia
- ¹²⁰ The Henryk Niewodniczanski Institute of Nuclear Physics, Polish Academy of Sciences, Cracow, Poland
- ¹²¹ The University of Texas at Austin, Austin, Texas, United States
- ¹²² Universidad Autónoma de Sinaloa, Culiacán, Mexico
- ¹²³ Universidade de São Paulo (USP), São Paulo, Brazil
- ¹²⁴ Universidade Estadual de Campinas (UNICAMP), Campinas, Brazil
- ¹²⁵ Universidade Federal do ABC, Santo Andre, Brazil
- ¹²⁶ University of Cape Town, Cape Town, South Africa
- ¹²⁷ University of Houston, Houston, Texas, United States
- ¹²⁸ University of Jyväskylä, Jyväskylä, Finland
- ¹²⁹ University of Liverpool, Liverpool, United Kingdom
- ¹³⁰ University of Science and Technology of China, Hefei, China
- ¹³¹ University of South-Eastern Norway, Tonsberg, Norway
- ¹³² University of Tennessee, Knoxville, Tennessee, United States
- ¹³³ University of the Witwatersrand, Johannesburg, South Africa

- ¹³⁴ University of Tokyo, Tokyo, Japan
- ¹³⁵ University of Tsukuba, Tsukuba, Japan
- ¹³⁶ Université Clermont Auvergne, CNRS/IN2P3, LPC, Clermont-Ferrand, France
- ¹³⁷ Université de Lyon, CNRS/IN2P3, Institut de Physique des 2 Infinis de Lyon , Lyon, France
- ¹³⁸ Université de Strasbourg, CNRS, IPHC UMR 7178, F-67000 Strasbourg, France, Strasbourg, France
- ¹³⁹ Université Paris-Saclay Centre d'Etudes de Saclay (CEA), IRFU, Département de Physique Nucléaire (DPhN), Saclay, France
- ¹⁴⁰ Università degli Studi di Foggia, Foggia, Italy
- ¹⁴¹ Università di Brescia and Sezione INFN, Brescia, Italy
- ¹⁴² Variable Energy Cyclotron Centre, Homi Bhabha National Institute, Kolkata, India
- ¹⁴³ Warsaw University of Technology, Warsaw, Poland
- ¹⁴⁴ Wayne State University, Detroit, Michigan, United States
- ¹⁴⁵ Westfälische Wilhelms-Universität Münster, Institut für Kernphysik, Münster, Germany
- ¹⁴⁶ Wigner Research Centre for Physics, Budapest, Hungary
- ¹⁴⁷ Yale University, New Haven, Connecticut, United States
- ¹⁴⁸ Yonsei University, Seoul, Republic of Korea